Sheffield Hallam University

A Sheffield Hallam University thesis

Effects of d^0 and s^2 cations on optical properties of silicate glasses

Benjamin Luke Allsopp

December 2018

A Thesis Submitted to

Materials and Engineering Research Institute (MERI)

Sheffield Hallam University

In partial fulfilment of its requirements for

The Degree of Doctor of Philosophy

Declaration

I hereby declare, that the thesis entitled 'Effects of d^0 and s^2 cations on optical properties of silicate glasses' is a result of my original work and investigation. None of the results presented in the manuscript have been lifted from any other sources and legitimate references are presented where necessary.

Name: Benjamin Luke Allsopp

Date: December 2018

Signature:

Published work and conferences

Aspects of the work described in the thesis were published in:

- Optical and structural properties of d^0 ion doped silicate glasses for photovoltaic applications. B.L. Allsopp, G. Christopoulou, A. Brookfield, S.D. Forder, P.A. Bingham. Physics and Chemistry of Glasses – European Journal of Glass Science and Technology Part B. 59, 4, 2018, 193-202

- Glass composition for solar energy applications. UK Patent Application GB2553163A. B.L. Allsopp, P.A. Bingham, J. Booth, S. Johnson, R. Orman. 2018. 1700981.2

Other works were published in:

- Enhanced thermal stability of high-bismuth borate glasses by addition of iron. N. Mary, M. Rebours, E. Castel, S. Vaishnav, W. Deng, A.M.T. Bell, F. Clegg, B. Allsopp, A. Scrimshire, P.A. Bingham. Journal of Non-Crystalline Solids. 500, 2018, 149-157.

- Non-isothermal crystallization kinetics and stability of leucite and kalsilite from K_2O-Al_2O_3-SiO_2 glasses. G. Christopoulou, F. Modarresifar, B.L. Allsopp. A.H. Jones, P.A. Bingham. Journal of the American Ceramic Society. 102, 2018, 508-523.

Selected results have been presented at various conferences;

- Optical and structural properties of PbO doped silicate glasses. B.L Allsopp, P.A. Bingham. Society of Glass Technology Annual Meeting, 2017, Cambridge, U.K

- The effects of d^0 metal ion doping on the optical properties and structure of soda lime silica glasses for photovoltaic applications. B.L Allsopp, P.A Bingham. Society of Glass Technology Centenary Conference, 2016, Sheffield, U.K

- The effects of Bi_2O_3 doping on the optical properties and structure of soda lime silica glasses for photovoltaic applications. B.L Allsopp, P.A. Bingham. Society of Glass Technology Annual Meeting, 2015, Cambridge, U.K

Glossary of Abbreviations

AM1.5……………………………………………………………………Air Mass 1.5
AR……………………………………………………………………..Antireflective
BO………………………………………………………………Bridging Oxygen
c-Si………………………………………………………………Crystalline Silicon
CdTe…………………………………………………Cadmium Telluride
CIGS……………………………………………Copper Indium Gallium Selenide
CN………………………………………………………Coordination Number
Boro………………………………………………………..Borosilicate
kW…………………………………………………………………Kilowatt
kWh…………………………………………………………Kilowatt Hour
DC…………………………………………………Downconversion
DSC………………………………………Differential Scanning Calorimetry
EPR……………………………………Electron Paramagnetic Resonance
EVA……………………………………………..Ethylene Vinyl Acetate
EXAFS…………………………Extended X-Ray Absorption Fine Structure
GaAs………………………………………………..Gallium Arsenide
HOMO…………………………………Highest Occupied Molecular Orbital
InP……………………………………………Indium Phosphide
IR…………………………………………………………Infrared
J_{sc}………………………………………Short Circuit Current Density
LDS…………………………………Luminescent Downshifting Sheet
LIMES……………………Light Innovative Materials for Enhanced Solar Efficiency
LMCT……………………………………Ligand to Metal Charge Transfer
LUMO……………………………Lowest Unoccupied Molecular Orbital
MAS-NMR………………Magic Angle Spinning – Nuclear Magnetic Resonance
M-L………………………………………………………Metal to Ligand
MLCT…………………………………..Metal to Ligand Charge Transfer
MRN…………………………………..Modified Random Network
NBO……………………………………Non-Bridging Oxygen
NIR……………………………………………..Near Infrared
PMT…………………………………..Photomultiplier Tube
PV……………………………………………Photovoltaic
PVB………………………………………..Polyvinyl Butyral
QE………………………………………..Quantum Efficiency
R_f……………………………………………..Refractive Index
SHU…………………………………..Sheffield Hallam University
SCL…………………………………Supercooled Liquid
SEM…………………………………Scanning Electron Microscopy
SLS……………………………………………..Soda Lime Silica
STM…………………………Scanning Tunnelling Microscopy
STP………………………Standard Temperature and Pressure
T_g……………………………………..Glass Transition Temperature

Abstract

There is a growing requirement worldwide for low-cost, reliable, and green electricity. From 2000 to 2015, the total installed capacity worldwide of solar photovoltaics (PV) increased from 4 GW to 227 GW, and is worth more than £75 billion annually. Solar photovoltaics are available in a multitude of technologies such as various morphologies of silicon, perovskite, organics, and other semiconducting technologies. However, a common issue regardless of technology is a spectral mismatch, where the incident solar irradiance does not equally match the range in which the semiconductor efficiently absorbs photons, and a second issue is degradation of polymeric components from UV photons. Ultimately critical failure of a solar module can occur due to the degradation of polymeric glues in the module, which allows for the ingress of water which rapidly leads to failure. Even before the critical failure, transmission of light is reduced due to the polymeric components becoming discoloured under UV irradiation to a yellow and brown colour due to the formation of organic radicals and short chain alkenes.

Glass front sheets are used for the transmission of light to the active semiconducting material in a PV module whilst providing environmental, chemical and physical protection. Spectral mismatch and polymeric damage can be ameliorated through absorption of ultraviolet (UV) photons in the glass layer of the PV module. Incorporation of particular cations, in specific oxidation states into a glass matrix can afford strong UV absorption, and no visible or infrared (IR) absorption allowing for the protection of the polymeric species within the module with no reduction in transmission of lower-energy photons required by the PV cell for conversion to electric current. Furthermore, broadband visible emission can be induced from the absorption of UV photons with careful selection and preparation of the cations in the glass matrix, which allows a better spectral matching

from the incident (and re-emitted) radiation and the absorption profile of the semiconductor.

This thesis describes the effects of certain cations with d^0, d^{10} and s^2 electron configurations in silicate glasses. Investigations into the optical, structural and chemical properties of doping silicate (soda lime silica and borosilicate) glasses with cations of titanium, zirconium, hafnium, niobium, tantalum, molybdenum, and tungsten (d^0), zinc (d^{10}), bismuth, lead and tin (s^2) ions. Shifts in the absorbance profiles of doped and base glasses were measured by UV Visible IR absorption spectroscopy. These measurements were conducted in conjunction with UV Visible IR fluorescence emission and excitation spectroscopy measurements, by which the oxidation state(s) and fluorescence profiles of the dopants can be elucidated. X-Ray diffraction (XRD) was undertaken to confirm the amorphous nature of the materials prepared. Raman spectroscopy was used to investigate the structure of the glasses and to determine whether changes occurred upon addition of the dopants studied. Electron paramagnetic resonance spectroscopy (EPR) and X-Ray Absorption Near Edge Structure (XANES) measurements were performed to elucidate the oxidation state/s of the dopants within the glasses. X-Ray fluorescence (XRF) spectroscopy was carried out to measure the proportions of oxides within the glasses and confirm that the melt-quench regime did not result in excessive volatilisation of materials or other contamination. Differential scanning calorimetry (DSC) was used to determine the glass transition temperature (T_g) of the prepared glasses.

Keywords: Fluorescence spectroscopy, UV VIS IR spectroscopy, transition metal, post-transition metal, silicate, photovoltaic

Acknowledgements

List of Tables

List of Figures

Contents

1 LIMES Project and Sheffield Hallam University Aims

1.1 LIMES

The LIMES (Light Innovative Materials for Enhanced Solar Efficiency) project was a collaboration between six members, led by RISE (Research Institutes of Sweden) compromising of the former Glafo and SP technical research institute of Sweden. In addition, including Sheffield Hallam University, GB, Johnson Matthey, GB, Solar Capture Technologies, GB, along with Agencia Estatal Consejo Superior de Investigaciones Cientificas (CSIC), ES.

The aim of the project was to develop glass with greater functionality than that which is currently commercially available for PV solar front sheets. One of the major objectives was to transmit / emit more of the desirable wavelengths of light to the active component of a solar module, whilst providing enhanced UV protection and still providing at least the same chemical resistance and mechanical protection that are currently available. The glass used in PV modules is typically 3 mm thick and can comprise up to 97% of the weight of the module. The LIMES project aimed towards developing 1 mm, thermally toughened glass, with enhanced optical, mechanical and chemical properties, and to demonstrate a cost effective PV module with enhanced performance over a 30 year projected life cycle. This comprised five key performance indicators:

1 – Produce 1 mm thick glass applicable for PV solar modules

2 – Measure of the thermal tempering through impact testing according to IEC 61215

3 – Measure of the optical properties with $T_{vis} > 99\%$ and $T_{sol} > 98\%$

4 – Demonstrate high efficiency is retained after accelerated environmental testing with a minimum of 95% of the maximum power point as compared with the efficiency prior to accelerated environmental testing

5 – Decrease the cost of PV modules by 10%, from raw materials through to installation

1.2 Sheffield Hallam University

While the consortium-wide project focussed on the previous key performance indicators, this PhD project completed at Sheffield Hallam University (SHU) comprised optically active doped glasses for photovoltaic applications. This manuscript details the work undertaken at SHU, and not the wider project work.

Glasses with optically active dopant additions have been studied in the LIMES project. These absorb deleterious UV light whilst converting and re-emitting a proportion of those absorbed UV photons as visible light, and subsequently into increased photon energy available for conversion by the solar cells. Glasses have been developed with increased mechanical and chemical resistive properties. Novel glass compositions developed within the LIMES project give enhanced resistance to cracking by a factor of three relative to commercially available glasses, and with enhanced chemical resistance by a factor of four. With the increased optical, chemical and mechanical properties of the glasses developed, the use of thinner glass front sheets is enabled, reducing the weight and cost of PV modules. This has been exploited through a patent application [1] and a publication [2].

Two main bodies of work were completed focussing on d^0 cations comprising transition metal oxides of titanium, zirconium, hafnium, niobium, tantalum, molybdenum and tungsten outlined in Chapter 4. Chapter 5 details a second set of dopants of s^2 configuration such as bismuth, lead and tin oxides, whilst Chapter 6 shows results from prepared PV modules made within the wider LIMES project with glass compositions developed from this PhD project. Chapter 7 describes the additional cost of dopant additions, and suggestions for future work.

The aims of the project outlined within this manuscript are to study the effects of doping silicate glasses with transition and post transition metals to modify the UV absorption edge to protect polymer layers within PV modules. Further to this, visible luminescence of the glasses from the absorption of UV light will be characterised.

2 Solar Energy, Photovoltaics and Silicate Glasses

2.1 Energy and CO_2 Emissions

The Paris accord published in 2016, signed by 195 countries, aimed to prevent the global average temperature raising above $2.0^{\circ}C$ relative to preindustrial levels [3]. To minimize the impact of anthropomorphic climate change, CO_2 emissions must be reduced. This can be achieved, in part, by increased use of solar photovoltaic energy [4]. While there are forms of electricity generation which have lower emissions of CO_2 per kWh [5,6] they are not applicable to every environment. Onshore wind and hydroelectricity both require high initial capital investment of £1000-1700 per kW and £800-6500 per kW respectively [7,8]. Solar energy has a similar barrier to entry with, assuming 14% efficiency for a c-Si PV system with battery storage, £3000-5000 installed cost per kW [9], there are commercial examples exceeding 20% efficiency [10] which reduces the cost per watt over the lifetime of the module.

Energy generated from the sun, via the photoelectric effect, is inexhaustible, clean and widely available. The first demonstration of the photoelectric effect was by Edmund Becquerel in 1839. Little research happened until the 1950's, when development of silicon-based solar cells became a viable method for energy harvesting on satellites. Considerable research took place during and after the oil crisis of the 1970's, this led to the development of new low-cost materials such as III-V thin films (GaAs and InP), amorphous silicon, CIGS ($CuInGaSe_2$) and CdS/CdTe based solar devices. In 1988, the first dye sensitised solar cell (DSSC) was created by Gratzel and O'Regan, with the incorporation of an organic dye affording cost reductions of 50% relative to silicon solar cells [11]. The first demonstration of a perovskite based solar cell occurred in 2009,

initially with an efficiency of 3.8% [12]. As of March 2018, the most efficient perovskite solar cell afforded an efficiency of 22.1% [10,13]. Solar energy has the potential to be completely environmentally friendly, and to increase energy security without the geopolitical issues sometimes arising with fossil fuels such as the Suez Crisis and the 1990's oil crisis as a response to the Iraqi invasion of Kuwait.

From the years 2000 to 2015 total installed solar PV capacity increased from 4 GW to 227 GW, a factor of 57 [14], and is worth more than £75 billion annually [9]. However, it is not without serious limitations at present, generally in the form of energy storage and effective scaling for greater deployment [15]. Even with the dramatic increase of installed capacity, solar PV contributes only 1.5% of all electricity used globally [16]. Other forms of renewable energy also arise primarily from the sun - such as wind, wave, hydropower and biomass.

This section will give an overview of the different parts of the solar spectrum. It will cover how modifying this spectrum can confer a two-fold benefit in the context of PV modules: (i) more efficient use of the solar spectrum; and (ii) increasing the service lifetimes of photovoltaic modules. An overview of the photovoltaic effect will be given, with how different types of PV modules take advantage of this. Finally, this section will discuss the limitations of current PV modules, and methods that are available to overcome or mitigate these issues.

2.1.1 Solar Spectrum

Sunlight in space consists of a continuum of electromagnetic radiation from X-rays through to radio waves (in particular circumstances it may also include gamma rays), however, this study focused on ultraviolet (UV), visible (VIS) and infrared (IR)

wavelengths. Figure 1 shows the solar spectrum, and the variation of intensity as a function of wavelength and height above sea level on Earth. The black line (AM0) shows the wavelengths and intensities of photons emitted by the sun, this closely follows a black body emitting at $5250^\circ C$, with characteristic wavelengths present of hydrogen [17]. The AM1.5 spectrum shows that particular wavelengths are absorbed by molecules in the atmosphere, such as O_2, O_3, H_2O and CO_2. The AM1.5 spectrum which is the average solar energy on the earth's surface at a zenith angle of 48.2° [18]. The solar spectrum is different at high altitude, and in space. Our research has focused on land-based PV modules. Although H_2O absorbs IR photons over a greater range, and therefore has more impact regarding climate change, CO_2 is the primary issue of anthropomorphic emissions. The solar spectrum shown in Figure 1 is at sea level, the relative proportions of wavelengths varies as a function of altitude, and zenith angle on earth relative to the sun, and in outer space UV wavelengths constitute a greater proportion. The research herein focused on silicon based solar modules for terrestrial applications, however, it would also be relevant to any PV module which suffers from UV damage.

This study aims to modify the spectral profile which the contents of a PV module will be exposed to through doping soda lime silica cover glasses with transition and post-transition metal oxides. Importantly, this includes absorbing and converting ultraviolet (UV) photons to photons with longer visible wavelengths and re-emitting a proportion of them, which provides a two-fold benefit; (i) protects the PV module from UV degradation [19–21], (ii) produces photons which are available for absorption by the PV cell and hence provide additional electricity generation [22–24].

Within this study ultraviolet (UV) will be defined as the wavelengths corresponding to 50000 cm^{-1}–26000 cm^{-1} (200 nm-380 nm), visible photons corresponding to 26001 cm^{-1}–12800 cm^{-1} (380 nm–780 nm), and infrared (IR) as 12801 cm^{-1}–3300 cm^{-1} (780 nm–3000 nm). In this study graphs will primarily be presented in wavenumbers for clarity within the UV portion of the graph, and, where appropriate, a second nanometre scale will be added.
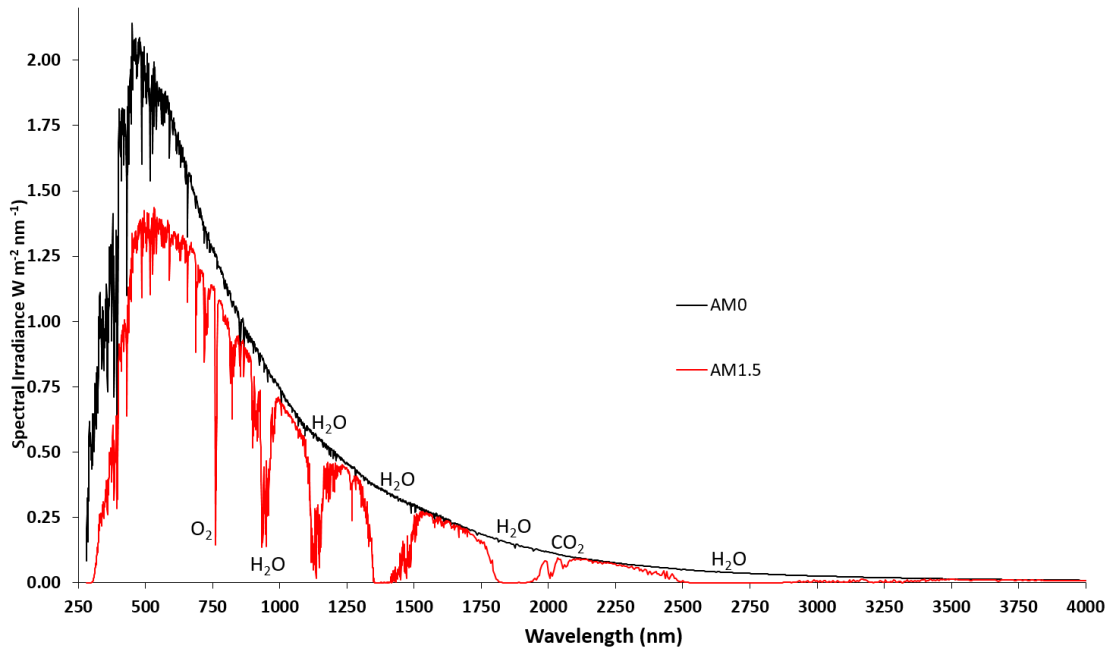
Figure 1 AM1.5 irradiation profile, AM0 is shown for comparison

AM0 is the solar irradiance in space at the top of the atmosphere, this is broadly similar to a blackbody emitter. AM1.5 corresponds to the irradiance at ground level with a solar zenith angle of 48.2°, this approximates the yearly average of latitudes within Europe, North America, China, Japan and Northern India. AM1.5 is used as a standardised measure for testing of photovoltaic module efficiency [18].

2.1.2 Photovoltaic Module Construction

Figure 2 demonstrates a typical crystalline silicon (c-Si) solar cell construction similar to those shown in Figure 4; this study is focused on modifying the front soda lime silica (SLS) glass front sheet as the technology is also applicable to other types of PV materials such as perovskite (shown in Figure 3) and dye sensitised solar cells. Various glues are utilised for the encapsulant layer, notably polyvinyl butyral (PVB), thermoplastic polyurethane (TPU), and ethylene vinyl acetate (EVA), while the back sheets are either aluminium or polyvinyl fluoride (known as Tedlar®) [21]. These backsheets are selected for a combination of aesthetics, protection from the environment, and light reflectivity.

Glass
EVA glue
Silicon absorber
Back metal contact
Backsheet
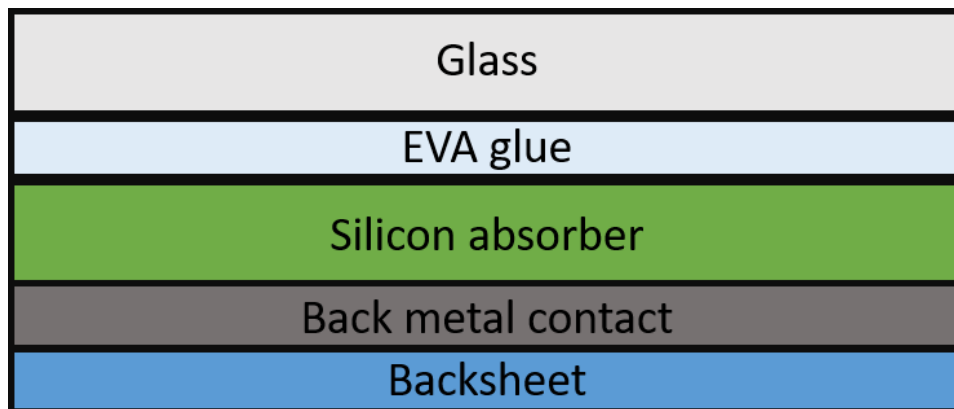
Figure 2 Typical c-Si solar PV module construction
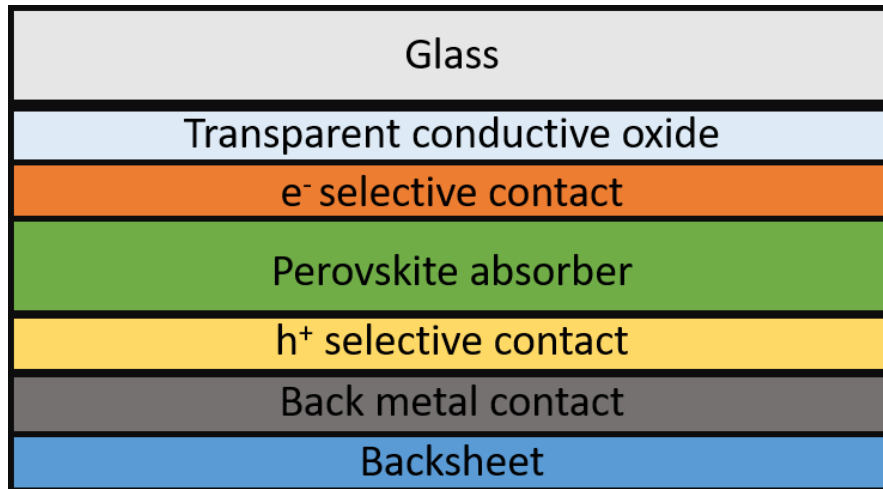
Figure 3 Typical planar n-i-p perovskite solar PV module construction

Figure 4 Solar modules mounted on solar trackers [25]

Table 1 Cost breakdown of silicon solar modules

Component	Cost% [26]
Frame	20.1
Glass	8.3
EVA	2.7
Si Wafer	48.0
Stringing	3.7
Backsheet	7.5
Junction Box	9.7

Silicon based solar modules typically weigh between 15 and 25 kg depending on manufacturer [27]. Typical c-Si panels are $1.4\ m^2 - 1.7\ m^2$ and 4 cm deep, with an average of 72 cells within the entire module [28]. The silicon semiconductor is the most expensive component shown in

Table *1*, while the glass front sheet and frame may be up to 97% of the weight [27]. PV modules have a desired service lifetime of 20-30 years, however, in high UV areas this may be reduced due to polymeric damage [29]. During the service lifetime c-Si PV modules degrade between 0.6 - 2.5% per year depending on service conditions and manufacturer [29,30]. A major cause of failure before the expected service lifetime of PV modules is delamination, due to UV induced degradation of the encapsulant layers, allowing water to ingress and corrode the materials within [19]. Even before delamination occurs, the EVA layer can discolour turning yellow and ultimately brown reducing transmission of incoming light, contributing to reduced efficiency [20]. Absorption of damaging UV photons within the glass front sheet can increase the service lifetimes of PV modules. Absorption of high-energy UV photons can give two effects; (i) the energy converting to phonons (heat), (ii) fluorescence / downconversion to visible photons. Within the module of all commercial modules, there are polymeric components, which undergo UV induced degradation.

2.1.2.1 Photovoltaic Effect

The photovoltaic effect is the process of conversion of a photon into an electron-hole pair, which can then be used to generate electricity.

Four basic steps are required for the generation of energy from light:

1. Absorption of photons in a semiconducting material
2. Creation of charge carriers, an electron-hole pair, by breaking bonds between atoms in the material
3. Separation of these charge carriers before they are able to recombine

4. Transportation of the charge carriers through electrical contacts and movement through a circuit to generate work

A photon of energy equal to or slightly higher than the bandgap of the semiconductor is absorbed (1), exciting an electron to the conduction band (2). Due to the nature of semiconductor junctions, the electron can only move towards the negative terminal and the hole moves in the opposite direction (3). The hole is the propagation of the 'empty' covalent bond to the positive metal contact. The election can pass through a circuit to extract work from the system (4). This process is schematically outlined in Figure 5. Inefficiency or failure of any of these processes will lead to poor, or zero conversion efficiency. This is why production of commercial PV modules is an interdisciplinary challenge, involving multiple selections of materials and components which work harmoniously to produce an effective module that can extract energy from the system.
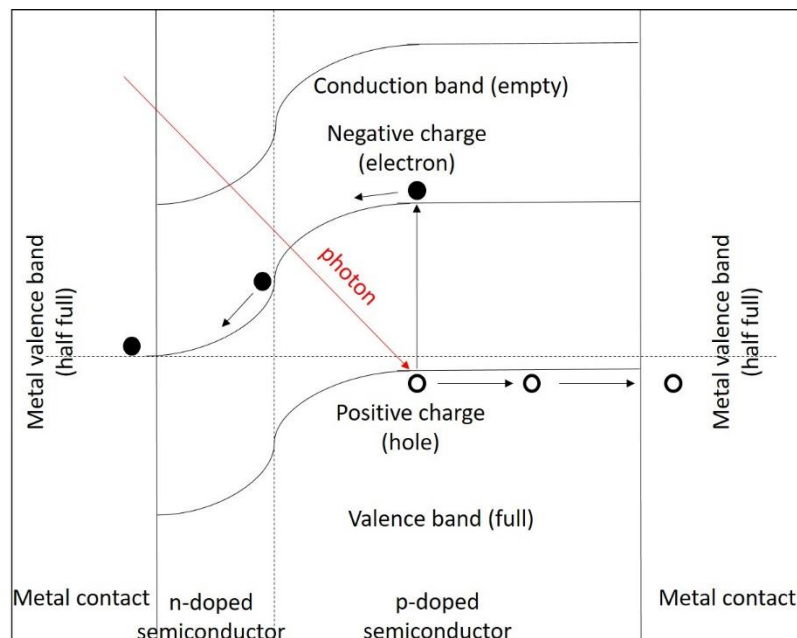
Figure 5 Schematic of photovoltaic effect at a simple p-n junction

2.1.3 Silicon Semiconductors for Photovoltaic Modules

Since silicon is a poor conductor of electricity dopants are added to increase conductivity, through the introduction of phosphorous (n-doping) or boron (p-doping) the conductivity can be increased by a factor of 10^6, Table 2 outlines the differences between p and n-type semiconductors.

Table 2 Comparison of p and n-type semiconductors

p-type semiconductors	n-type semiconductors
• Majority of carriers are holes • Minority of carriers are electrons • Group III dopants (B, Al, Ga, In) • Fermi level is close to valence band	• Majority of carriers are electrons • Minority of carriers are holes • Group V dopants (N, P, As) • Fermi level is close to conduction band

Figure 6 demonstrates the process of developing a depletion region across the p-n junction. Initially at the p-n junction, the free charge carriers, as represented by the torus and rectangle, which combine leading to a depletion zone. Due to the lack of charge carriers within this depletion zone a positive region exists within the n-doped silicon, and a negative region forms in the p-doped silicon, this gradient corresponds to 0.7 V. The internal electric field across the p-n junction causes electrons to direct towards the n-doped silicon and holes towards the p-doped silicon. While this is the most basic interface, commercial semiconductors have more complex architectures, which overcomes the Shockley-Queisser limit. Ojo et al have shown experimentally a single photon can generate more than one electron hole pair, and state a higher short-circuit current density, J_{sc}, above the Shockley-Queisser limit of a single p-n junction is achievable [31]. The

graded bandgap induced by the method by Ojo and Dharmadasa effectively acts as multiple p-n junctions which more efficiently splits the electron-hole pairs, and in turn confers greater efficiency to the PV module.
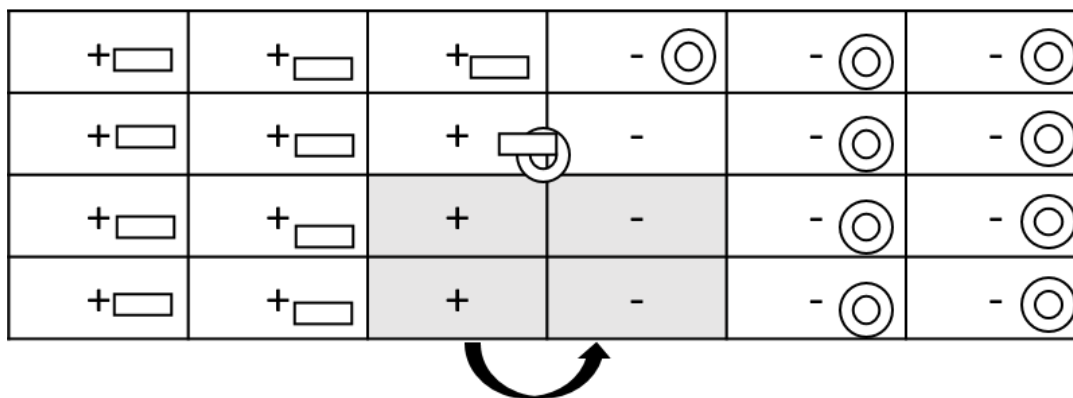
Figure 6 Propagation of a potential gradient at a p-n junction, top is the initial state of the system, an electron and hole combine to create a depletion zone with a positive to negative gradient

At p-i-n junctions, where there is a layer of intrinsic or insulating material sandwiched between the p and n type semiconducting layers, are more advanced than a simple p-n
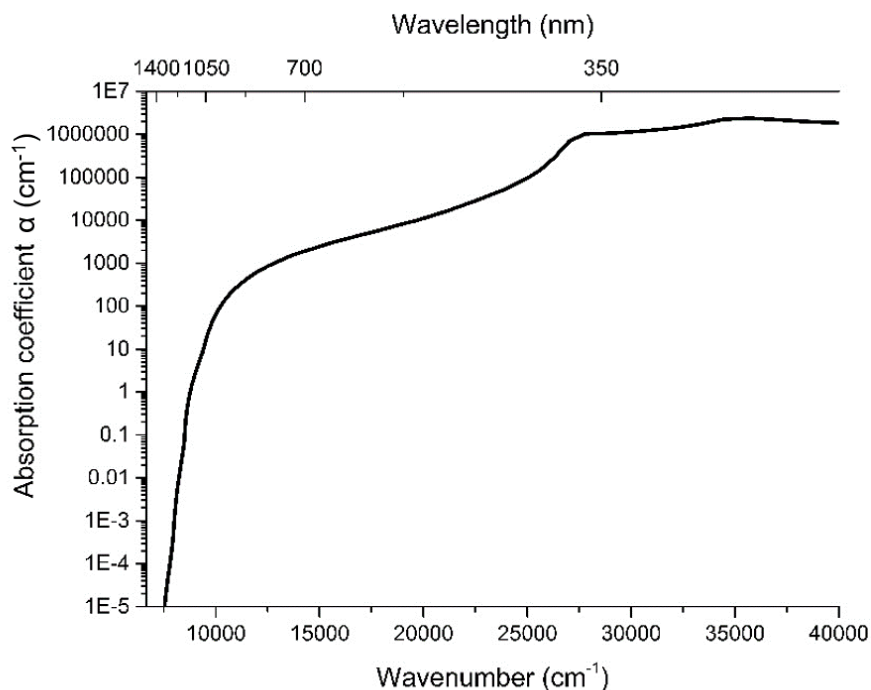
Figure 7 Absorption coefficient of silicon in cm as a function of wavenumber

junction. The p-i-n junction leads to a more effective internal electric field, which reduces the likelihood of recombination of the electron hole pair. Various other junctions have been developed, and while beyond the scope of this project, the reader is directed to the following resources [32–34].

The absorption coefficient of silicon varies with wavelength, with the absorption much weaker in the UV than in the visible and IR regions as shown in Figure 7. Due to the low absorption, low conversion efficiency and harmful effects of UV light on a PV module, there is an urgent need to convert these photons into more efficient and useful wavelengths. There are several properties which are required for effective PV materials and devices. Efficient light absorption over a large wavelength range, with the peak of absorption being close to the bandgap of the material. This provides the greatest conversion efficiency within the PV module.

The materials used within a PV module need to be low cost, and readily available for large-scale production. Silicon solar cells are particularly beneficial due to the high abundance of the metal on earth, and the methods of purification are suitable for the end use. Perovskite materials are beginning to be used as PV devices, while originally they had poor conversion efficiency and had poor environmental stability, modern materials do not suffer these issues. Tandem perovskite - silicon PV modules have been demonstrated to have 9% higher photoconversion efficiency with 30% lower environmental impact [35], and these are particularly suitable to incorporate other technologies such as quantum dots [36].

PV modules are required to have high environmental stability in regard to light, moisture, and temperature, with environmentally friendly technologies for production of the

semiconductor. Thin film technology, especially deposition methods such as electroplating use low temperature, low concentration and readily scalable methods to produce PV modules [37]. Novel work at Sheffield Hallam University has been undertaken in thin film technologies, with graded bandgap CdTe showing efficiencies of up to 18.5% [31]. CdTe is an important material for the future of solar energy harvesting with a 2 μm thick layer able to absorb over 90% of photons with energies higher than 11,700 cm^{-1} (lower than 855 nm) [37]. The morphology of CdTe thin films can be readily controlled and even stir rate of the electroplating solution has a significant impact on the final film, and hence optical properties [38].

The semiconductors used in PV modules are required to have a low recombination level of electron hole pairs. A reduction in the recombination level results in a greater proportion of photons inducing a current, thereby increasing efficiency of the module [39].

2.1.4 Types of Photovoltaic Modules

There is a multitude of available technologies for PV materials, and while silicon based modules dominate the market, emerging technologies such as thin film CdTe or copper-indium-gallium-selenide (CIGS), and organic based PV modules are all available commercially. These were initially developed in the 1970's but recent advancements in their efficiencies are making them more commercially viable. The efficiency of perovskite materials, in particular, has shown dramatic efficiency increases, from 3.8% in 2009 to 22.1% in 2016. Silicon dominates the market for several reasons, firstly it is one of the most abundant elements available on earth, with over 90% of the Earth's crust being composed of silicate minerals [40]. There are various technologies available for the

purification and production of silicon wafers, for example the Czochralski process, that result in comparatively low cost materials with well-defined properties.

Single crystal, non-concentrator, silicon PV modules have efficiencies of up to 25.6% [41] however, efficiencies have stagnated over the last 15 years with only small further efficiency gains. The efficiency rate of change shown in Figure 8 on the emerging PV technologies such as perovskite, quantum dot and dye sensitised solar cells, are much steeper showing significant and rapid advancements, and are poised to become commercially available over the next decade. Tandem solar cells are also to become increasingly efficient and commercialised within the next 5-10 years. Various technologies and their efficiencies are outlined in Figure 8 [10].

2.1.5 First, Second and Third Generation Solar Cell Modules

Solar cell technologies have been divided into three distinct generations. The first generation were typically based on silicon wafers, with an efficiency of between 15-20% [42]. Silicon based solar cells still dominate the market, accounting for 87% of global PV sales [16] due to the mature technology and robustness, with polycrystalline silicon itself accounting for 63% [43]. The silicon wafer used in these PV modules are between 200-250 μm thick, which accounts for 50% of the cost of the module [43]. However, absorption of solar photons occurs within the first tens of microns of the silicon. Therefore, reducing the thickness of the absorbing layer will reduce the cost.

Second generation solar cells employed thin films of absorbing layers to reduce the price and reduce the cost per Watt. Deployment of second-generation solar cells is now happening at significant quantities [44]. The main technologies include amorphous silicon (a-Si), CdTe thin films and copper-indium-gallium-diselenide (CIGS).

Up to 99% less semiconducting material is required to absorb the same amount of light in thin film devices than in a corresponding c-Si cell [16], with layers between 1-4 µm thick [45,46]. a-Si solar cells are the most developed second-generation PV module, due to both the wide availability and comparative ease of fabrication (continuous chemical vapour deposition). However, due to the lower efficiency than traditional c-Si systems [47], it is only suitable for application in specific conditions where curved surfaces are required [48].

Third generation solar cells are primarily in the research and development stage, however some devices are beginning to be commercialised. The new PV systems include concentrating photovoltaics [49,50], dye sensitised solar cells [44] and organic solar cells [51]. Concepts are being developed to complement third generation PV systems such as quantum dot [41,52] and upconversion / downcoversion technology [53,54]. Third generation technologies, on the graph in Figure 8, highlighted as emerging PV, show the sharpest efficiency gradient within the past 10 years. The technology is rapidly developing and shows significant promise.

Multi-junction solar cells, or tandem solar cells, are PV modules with multiple semiconducting materials with differing responses to wavelengths layered together. This allows for a broader absorption of sunlight. While a single junction of Si has a maximum efficiency limit of 33.1% [55], multiple layers in conjunction of different bandgaps can overcome this limit. However, there are still technological hurdles to be bypassed with this approach, and the increased difficulty in manufacture offsets the gains in efficiency. For non-terrestrial purposes tandem PV modules have proven popular where weight is a significant issue such as aerospace [35].

Figure 8 NREL best research cell efficiencies over time. Open blue square denotes multicrystalline silicon solar cells, which are currently 22-23% efficient [10]
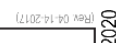
2.1.6 Limitations of Photovoltaic Modules by Component

Each component of a PV module, as illustrated in Figure 2, has limitations that reduce the overall PV module efficiency. The issues are caused either by absorption or transmission being inefficient or non-existent, or by the component having a high cost. Modification of the encapsulant glass layer can improve all of the issues outlined below.

2.1.6.1 Glass Front Sheet

2.1.6.1.1 Absorbance and Transmission

All soda lime silica glass contains some quantity of Fe_2O_3, whether deliberately added or present as an impurity. While section 2.2.4.1.5.5 will give detailed coverage on the theoretical basis for the optical absorption of iron species in glass, for brevity here, Fe^{3+} absorbs in the UV and blue regions and Fe^{2+} absorbs more strongly in the red and IR regions. The precise values of absorptivity are affected by factors including concentration of iron species, the glass composition and the redox ratio – as given by Equation 1;

$$\Sigma \frac{Fe^{2+}}{Fe\ (tot)} = \frac{[Fe^{2+}]}{[Fe^{2+}] + [Fe^{3+}]}$$

Equation 1

Whilst Fe^{2+} and Fe^{3+} in glass strongly shift the UV absorption towards the visible, beneficially protecting the polymeric layers from UV damage, the visible and IR optical transitions parasitically absorb photons that could otherwise be converted by the photovoltaic material. Absorptions in the UV to visible from 27,250 cm^{-1} (366 nm) to 21,550 cm^{-1} (464 nm) corresponding to Fe^{3+}, and strong absorptions within the IR centred at 10,380 cm^{-1} (963 nm), 7490 cm^{-1} (1335 nm), and 4950 cm^{-1} (2020 nm) corresponding

to Fe^{2+} [56,57], limit the effectiveness of doping with iron for solar control. Absorptions such as these from 0.01mol% Fe_2O_3 in silicate glass can cause a 1.1% loss in module output power, and a 9.8% loss for a 0.1mol% Fe_2O_3 doped silicate glass front sheet [58]. Reduction of the concentration of iron oxides in glass is therefore a requirement to more effective photovoltaic panels, and has been employed industrially.

Ti^{3+} gives a strong crystal field band centred at 20,000 cm^{-1} (500 nm) which extends to 10,000 cm^{-1} (1000 nm) [59], directly reducing the transmission properties of soda lime silica front sheets in a PV module. The asymmetry of the band originates from Jahn-Teller effects observed in d^1 and d^6 oxidation states, i.e. Ti^{3+} and Fe^{2+}. When combined into one glass, Fe^{2+} and Ti^{3+} display a charge transfer band at 24,000 cm^{-1} (416 nm), with stronger absorption than the sum of the individual components. However, Ti^{3+} is unlikely to occur under standard float glass melt conditions. The charge transfer band corresponding to $Fe^{2+} \rightarrow Ti^{3+}$ centred at 24,000 cm^{-1} (416 nm) strongly affects the UV absorption edge [59] and is significantly more deleterious for PV module efficiency.

Any absorption by the cover glass of photons able to induce the photovoltaic effect will directly reduce the efficiency of the PV module. Minimising the quantity of iron species and reduced forms of titanium will lower the visible absorption but also reduce the UV absorption leading to increased rate of reaction for UV induced polymeric damage. Therefore alternative compounds need to be introduced into the soda lime silica matrix to fulfil the desirable UV absorption characteristics whilst having minimal or no absorption within the visible and NIR regions.
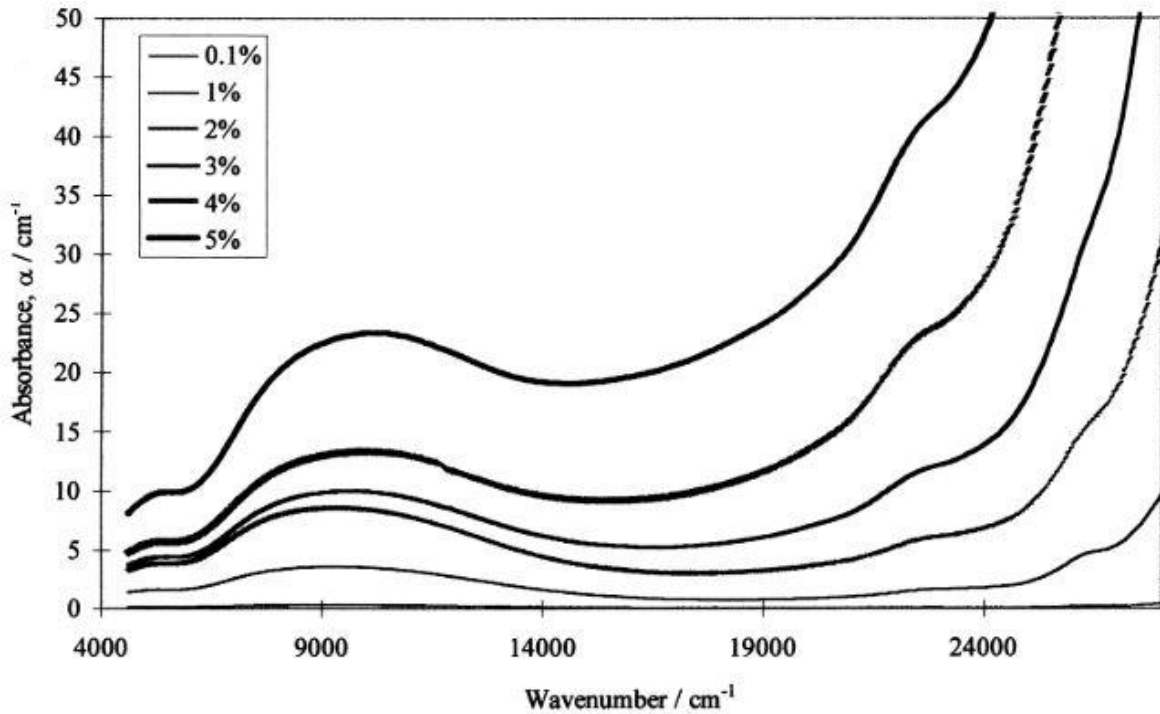
Figure 9 Typical UV VIS IR absorption curves for increasing Fe_2O_3 concentration in soda lime silica glasses [57]

Figure 9 shows the typical absorption profiles of increasing mol% Fe_2O_3 content in SLS glasses [57]. Glass front sheets require low iron content i.e. below 0.09wt% [58,60], with increasing iron content the efficiency of the module is decreased due to competitive absorption of the photons in the cover glass. For glass containing 0.01% Fe_2O_3 this equates to a loss of 1.1% [58]. However, photons of light above 27,500 cm^{-1} (below 360 nm) induce damage to the polymeric components within the PV module [19]. Therefore, removal of all the iron oxides is both technologically difficult [61] and negatively affects the long-term reliability of the PV module. There is therefore a requirement for minimising the quantity of Fe species with the addition of novel optically active dopants to absorb UV photons but without visible or near-IR absorption.

2.1.6.1.2 Reflectivity

Reflectivity of the cover glass also reduces the number of available photons for the generation of energy. In fixed PV systems (without solar tracking) around 20% of the available photons are lost per day due to reflection of the glass [43]. This can be ameliorated with anti-reflective coatings [62], usually processed through a sol-gel route by dip coating or a spinning technique [63]. The long term stability of the coating is highly dependent on the initial surface conditions, and is suitable over a narrow wavelength range and incident angle [63]. For example, for the complete transmission of 18,181 cm^{-1} (550 nm) photons, a coating refractive index of 1.22 with a thickness of 112.7 nm is required; however, photons of different wavelengths will suffer some reflection. Stronger adhesion of the coating to the underlying glass is possible through vacuum processing, however, this is cost prohibitive for large areas and large volumes. Etching of borosilicate glasses has been demonstrated to modulate the reflective properties of a flat panel [64]: as fewer photons were reflected a greater proportion were transmitted, from a maximum transmission (T_{max}) of 92% to a $T_{max\%}$ of 98%.

2.1.6.1.3 Weight

The typical dimensions of a domestic PV panel are 1.4 m^2 – 1.7 m^2, with glass cover layer 3-4 mm thick [28]. The density of commercial PV SLS glass is ~ 2.52 g/cm^3 [65], therefore the average weight of glass may be between 14-24 kg and comprises some 97% of the total module weight [27]. Due to these weight constraints, heavy support structures are required, further adding to the weight and installation costs of the module [15]. The weight restricts exploitation of portable off grid PV modules, and the volume of glass used bears an environmental and energy cost. To melt 1 kg of soda lime silica glass at 1450°C

requires 2500 – 2800 kJ, depending on composition and furnace type [66]. These factors

result in the glass cover layer constituting between 20-30% of the price of a solar module

[9] shown in

Table *1*. To simply reduce the thickness of the glass front sheet is not practical, as the optical properties are directly affected by the thickness of the glass sheet according to Beer-Lambert law, and mechanical properties can also be affected. Common soda lime silica glass products such as float glass have strengths of the order of 14-70 MPa, however, the theoretical strength may be up to 13-14 GPa for fine silica fibres. The large difference arises from surface defects on the glass which act as stress concentrators, allowing a relatively small load to form a crack and ultimately cause critical failure of the glass product. For a thinner piece of glass to have the same crack resistance, the surface must be more pristine than a corresponding thicker piece of glass. Surface flaws typically extend only 1-10 µm, but they reduce the strength of glass to around 1% of the theoretical value [67].

2.1.6.2 First Polymeric Glue Layer

EVA glue is the most commonly used polymer for c-Si based PV modules with 80% of PV modules encapsulated by EVA [68]. The structure of EVA is given in Figure 10. The primary roles of the glue is to offer electrical insulation, structural support and high optical transparency in the visible region with transmission >91%. However, the polymer undergoes UV degradation over time, initially causing discolouration of the polymer due to oxidation and free radical formation, and ultimately to delamination of the PV module [19]. The oxidation and formation of free radicals lead to the production of acetic acid, the formation of aldehydes and ketones, along with volatile gasses such as methane, carbon dioxide and carbon monoxide [19]. Degradation processes form alkenes of various lengths, which have strong absorptions within the UV, fragmentation of the chain lengths

cause a broadening of these absorption bands. The acetic acid formed also has a catalytic effect of the yellowing caused by UV photons in the EVA polymer [69].
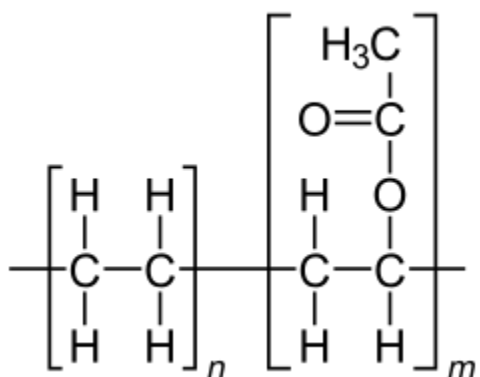
Figure 10 Chemical structure of EVA copolymer

This is the primary cause of efficiency reduction and failure for Si based PV systems [29]. As the EVA becomes brittle, the mechanical structural support between the cover glass and the glue layers begin to fail, eventually leading to water ingress. The dissolved minerals within the water can short the circuit and reduce the effectiveness of the semiconducting layer: this affects all types of semiconductor [39,70,71]. UV filtering glass cover layers which absorb photons of energy greater than 28,500 cm^{-1} (lower than 350 nm) effectively reduce the rate of UV induced discolouration and subsequent degradation of the PV module.

2.1.6.3 Photon Absorbing Layer

All semiconductors have a range of wavelengths close to their bandgap over which they most efficiently convert photons into electricity; photon energies that do not fall within this range are inefficiently converted or not absorbed at all. The bandgap of silicon is 1.1 eV (8872 cm^{-1} or 1127 nm), and as shown in Figure 7 absorption by silicon in the visible and UV is significantly lower. Modulating the number of photons with energies in the range

that can be converted, through upconversion and / or downconversion, is a promising technology in third generation solar modules. This is discussed in section 2.1.4.

The cost of the wafer in c-Si PV modules constitutes around 48% of the total price [9] as shown in

Table *1*, thin film Si based systems use up to 99% less material, and are subsequently cheaper, however the lower efficiency offsets the cost per watt. Promising research into thin film technologies may be found here [32,72]. Electrically conductive layers on glass (indium tin oxide or fluorine doped tin oxide) allows for the growth of thin film semiconductors in a low cost manner such as electrodeposition. Electrodeposition confers several cost saving measures such as self-purification of raw materials [31], it is a low cost and highly scalable method of production.

2.1.6.4 Second Polymeric Glue Layer

The second encapsulant glue layer as shown in Figure 2 undergoes UV induced damage in the same manner as the first encapsulant glue layer, albeit to a lower degree as a proportion of the UV photons have been absorbed either by the first glue layer or reflected by the c-Si layer. However, enough of the photons pass through to induce damage to this glue layer and lead to the same processes outlined in section 2.1.6.2.

2.1.6.5 Backsheet

Backsheets are used to protect the PV module from light and moisture, and act as an electrical insulator. The colour of the backsheet can impact the module efficiency, with white backsheets reflecting light back into the semiconductor, this increasing the current flow [73]. Backsheets are commonly either aluminium or polyvinvyl fluoride (e.g. Tedlar®) [21].

During operation backsheets undergo UV induced degradation, yellowing the polymer over time. An increase in the yellowing increases the overall temperature of the module, giving a two-fold negative effect. Firstly the higher temperatures decrease the efficiency of the module and secondly the heat increases the rate of degradation of the module [21].

As with the EVA layer, as accumulated UV induced damage increases in the backsheet, the likelihood of delamination and water ingress increases, ultimately leading to module failure [29]. UV absorption in the glass cover layer may reduce the damage, leading to longer services lifetimes.

2.1.7 Front Sheet Modifications

Several technologies are being developed for use within PV modules, involving the functionalisation of the glass front sheet, such as the following:

2.1.7.1 UV Control

While it is not technologically or commercially feasible to remove all of the iron content in flat glass production, a reduction in the total quantity of iron can minimise the efficiency loss of the PV module. In order to maintain the UV protection of the polymeric layers dopants, alternative dopants such as d^0 and d^{10} ions may be added [74,75]. Dopants such as Ti^{4+} or Bi^{3+} exhibit strong UV absorption and visible fluorescence emission [76–78], while having no visible or near-IR absorption bands, giving a two-fold benefit to the PV modules' long term stability and efficiency.

Bulk doping of glasses to induce visible fluorescence from absorbed UV light is a method for enhancing the performance of next generation solar cells. Bulk glass doping confers several advantages over coatings or field assisted solid state ion exchange techniques [79,80], in particular ease of fabrication, and it does not require secondary and expensive techniques. Doping of soda lime silica glasses offers multiple advantages; UV control, visible emission, and modulation of the refractive index to reduce reflection losses.

Akin to bulk doping of cover glasses for optical modulation, quantum dots such as bismuth doped aluminosilicates [81,82] or CdSe [54], may be used as downconverting / upconverting materials for PV systems. Quantum dots offer the ability, as with fluorescent cover glass, to be easily retrofitted into existing technology and readily enhance the efficiency of the PV module.

Glass ceramic based encapsulant layers can offer fluorescence [83] giving the same advantages as bulk doped glass and quantum dots. Through control over the size of the crystals, transparency may be high whilst providing enhanced mechanical and chemical properties [84]. Investigations into glass ceramics for photovoltaic applications are beyond the scope of this thesis.

2.1.7.2 Antireflective Coatings

Reflective losses can be minimised by the application of an antireflective (AR) coating. Coatings are applied either through a vapour deposition process [85] or a dip coating or spinning technique [67]. Minimising the reflective losses results in a greater intensity of photons available for PV energy generation. The high cost of coating glasses currently limits the application of this technology. However, advances in AR coatings with added functionality such as self-cleaning and fluorescent systems can offset the high cost through enhanced efficiency and lower maintenance costs [43,85]. Up to 20% of all available photons are reflected in a fixed array PV system [43], however, with antireflective coatings and optical metamaterials, a 4% increase, under standard test conditions, can be observed due to an increased flux of photons available [86].

2.1.7.3 Luminescent Downshifting Front Sheets

Bismuth oxide (Bi_2O_3) has shown promise in phosphate laser glasses for its NIR emission at 7700 cm^{-1} (1300 nm) from 12,500 cm^{-1} (800 nm) excitation [87]. Experiments have shown that this process can be ascribed to transitions of Bi^+, as the isoelectronic compounds Tl^0 and Pb^0 display similar luminescent behaviour [88]. However, for effective UV to visible conversion bismuth must be in the Bi^{3+} valence [89]. Bismuth is a multivalent ion, and can exist in oxidation states from 3^- to 5^+, and therefore, careful control of the oxidation state is required for effective luminescent downshifting sheets.

Luminescent downshifting front sheets (LDS) are a more attractive technology for third generation solar cells compared to improving the electronic components within the module. Various technologies have been developed which improve the efficiency of PV modules such as thin-films or graded bandgap materials, although commercialisation is comparatively low relative to the dominance of silicon based PV modules [90]. LDS front sheets are applicable to be added to any type of solar cell in which UV light degradation occurs [91–93], and the passive approach does not interfere with the architecture of the module. LDS technology was first proposed in 1979 by H.J Hovel, and with non-optimised optical components, plastic sheets containing organic dyes, gave an efficiency increase of between 0.5 and 2.0% in photoconversion [94]. Similar values for the effect of LDS layers on the efficiency increase of PV modules have been calculated by C.P. Thomas at 1.5% [95] with organic dyes using a modified Shockley model. An LDS layer has been utilised in CIGS modules to give a 1.8% efficiency increase in short circuit current density (J_{sc}) [91]. Studies using nanoparticle phosphor coatings on the glass front sheet have been undertaken with silica particles doped with up to 3wt% Eu^{3+}, the combination of the

anti-reflective properties of the nanoparticles and the LDS effect gave a total J_{sc} increase of 5.17% using multiple species of phosphor in Si phosphors [96], and with a YVO$_4$: Bi^{3+} / Eu^{3+} complex coating gave a 4% increase in J_{sc} [97]. LDS technology proves to be particularly beneficial in PV modules and garners much research interest in the solar energy community [98]. Combined with bulk doping of SLS glasses, LDS is the technique utilised in this study.

2.1.7.4 Electrically Conductive Layer for Electrodeposition of Semiconductors

Indium tin oxide (ITO) or fluorine doped tin oxide (FTO) layers coated onto silicate glass allow for the electrodeposition of semiconducting materials directly onto the glass layer. The coated glass is the cathode in the electroplating system, with a Pt wire being the anode. A solution containing the required ions, usually $CdSO_4$ and TeO_2, with a current of around 2 V and 1 mA, is used to reduce the ions onto the glass surface, growing the semiconductor device [32,37]. This method of production allows for lower quantities of expensive semiconductors to be used, while conferring other benefits such as low cost processing methods. It is highly scalable and is self-purifying, allowing for the use of lower purity raw materials [32].

2.1.7.5 Replacement of Backsheet

One possible method to remove issues with backsheet degradation is to replace the polymer backsheet with a second glass sheet. Such modules are called bifacial PV modules, and one is schematically represented in Figure 11. Bifacial PV modules are now beginning to be commercialised. The backsheet in these modules is replaced by a second glass sheet, allowing for absorption of light arriving from both sides. This increases the

efficiency of the module due to the additional absorption of photons. Bifacial PV modules are suitable for vertical installation, reducing the size footprint of the system, and particularly useful for building integrated PV (BIPV) modules.

Glass
EVA
Silicon
EVA
Glass
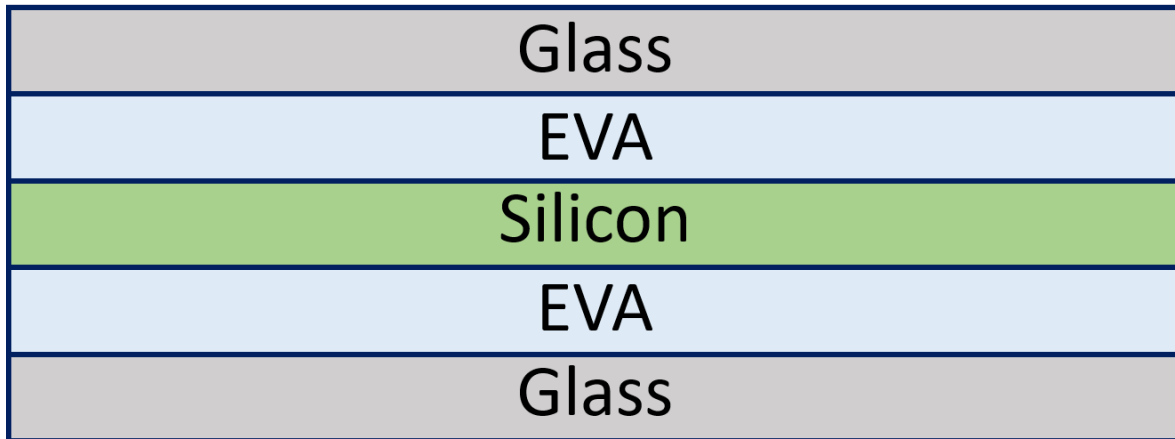
Figure 11 Bifacial PV module, typically installed vertically or at 45°

2.2 Glass Structure and Properties
2.2.1 Definition of Glass

Glass is an often-misunderstood material; in the general public lexicon, glass usually refers to soda lime silica type glasses, namely windows and drinking glasses. However, in the technical sense glass refers to a state of matter and is not specific to any particular material, element or compound. Glasses exist in metallic [99,100], organic [101–103] and non-silica based systems [104]. While there are multiple definitions of a glass, the current definition of 'glass is a non-equilibrium, non-crystalline condensed state of matter that exhibits a glass transition. The structure of glasses is similar to that of their parent supercooled liquid (SCL) and they spontaneously relax towards their SCL state. Their ultimate fate, in the limit of infinite time, is to crystallise' [105] is the most comprehensive definition to date. The formation method to produce the glass is not a defining metric either, glasses can be produced from the traditional melt quench method, or more modern sol-gel [106–108] or vapour deposition methods [109]. Glass has been the driving technology for vital research in many disciplines, including biology (microscope lenses), chemistry (glassware), and astronomy (telescope lenses).

Modern life would not be possible without glass, from communications in the form of fibre optic cables [110] and mobile phone screens, to insulation (fibreglass), to medical applications (bioglass and bone repair [111,112]) and to energy applications (radioactive waste immobilisation [113,114] or solar glass [54,115]). This has led some to postulate the modern world may be defined as the glass age [116] akin to the bronze age or space age. Glass has always had cultural significance, originally in the form of decorative beads from ancient Egypt [117] to renaissance cathedrals stained glass displays [118,119].

Glass art continues to the modern era with artists such as Patchen and Chihuly, as well as books published on the topic [120]. Modern architecture would not be possible without glass; the unique combination of properties glass provides, results in contemporary buildings having large glass facades. Notable examples include the botanical garden of Curitiba, Brazil and 30 St. Mary Axe (the Gherkin), England.

2.2.2 Structure of Glass

In crystalline solids, atoms have a highly ordered structure with the bond angle and bond lengths at specific lengths dependent on the material, and this short-range order extends in all planes of direction. Discrete repeatable units of the crystal are called the unit cell, and these unit cells allow for Bragg diffraction. There are two defining characteristics of a glass: no glass has long-range periodic order (i.e. glasses are amorphous according to their X-ray diffraction patterns). In addition, all glasses exhibit a time dependent glass transition temperature (T_g) which is determined by a reversible transition from a brittle 'glassy' state to a viscous or 'rubbery' state as the temperature is increased. Glasses are thermodynamically unstable and will, in infinite time, revert to a crystalline form. A glass is not a true solid due to its thermodynamic instability: a substance in a true solid state has an atomic configuration that is time independent. Glasses do not retain their shape and will spontaneously start to relax, for soda lime silica glasses ($T_g \sim 550°C$) relax over geological time scales [121], whereas some organic glasses ($T_g \sim 20\text{-}50°C$) relax within hours [105]. The rate of flow of soda lime silica type glasses is in the order of 0.1 nm in 10^{10} years [121].

2.2.2.1 Silicate Glass – Vitreous Silica

Early structural studies relied on studying vitreous silica as a model compound for glasses. The theory of Goldschmidt [122] stated that glasses are likely to form if the ionic radius of the cation in R_nO_m is within the range 0.2-0.4, as this tends to form tetrahedral motifs. However, this theory failed to state why the tetrahedral configuration was favourable for glass formation and it was purely empirical. Following this, Zachariasen wrote a paper explaining why certain coordination numbers favour glass formation behaviour [123]. In this paper, it is stated that silicate crystals readily form glasses instead of devitrifying after a melt-quench process, and thus forming a three dimensional network. This network consists of tetrahedra connected at all four corners, with the bond length essentially the same as in the corresponding SiO_2 crystal, but the bond angle varying as shown in Figure 12.

Figure 13 shows a scanning tunnelling micrograph (STM) of a film of silica displaying both vitreous and crystalline phases, experimentally displaying Figure 12. Zachariasen also stated that no oxygen atom can be linked to more than two cations, and all tetrahedra are corner sharing and not face or edge sharing. This theory has been widely accepted and is known as the *random network theory*. The four rules derived by Zachariasen, for a compound of formula A_mO_n, wherein A is a cation and O is an oxygen, are:

- An oxygen atom is linked to no more than two glass forming atoms of A

- The coordination number of the glass forming atoms is small, either 3 or 4

- The oxygen polyhedra share corners with each other, and do not share edges or faces

- At least three corners are shared

It therefore follows that the oxides of formulas A_2O and AO do not satisfy any of the rules.

Oxides A_2O_3 (e.g. B_2O_3) satisfy the rules providing the oxygen atoms form triangles around each central A atom. For AO_2 (e.g. SiO_2) and A_2O_5 (e.g. P_2O_5) type oxides the rules are satisfied if the oxygen atoms form tetrahedra around each A atom.

crystal   glass
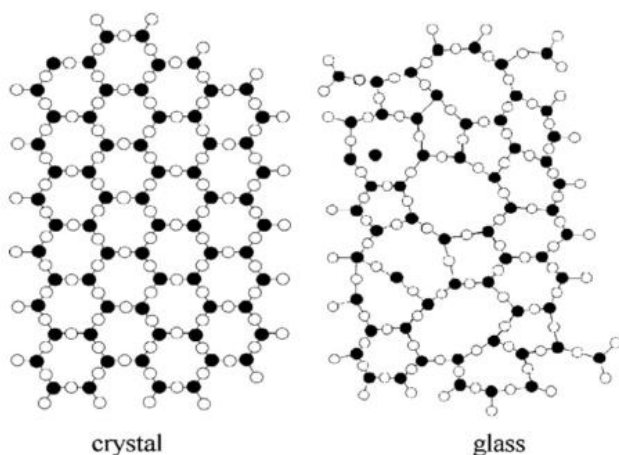
Figure 12 Schematic structures of crystalline and amorphous silica, note the fourth Si-O bond is above the silicon atom. Black circle – Si, White circle – O. [124]

| crystalline | ⟶ | vitreous |
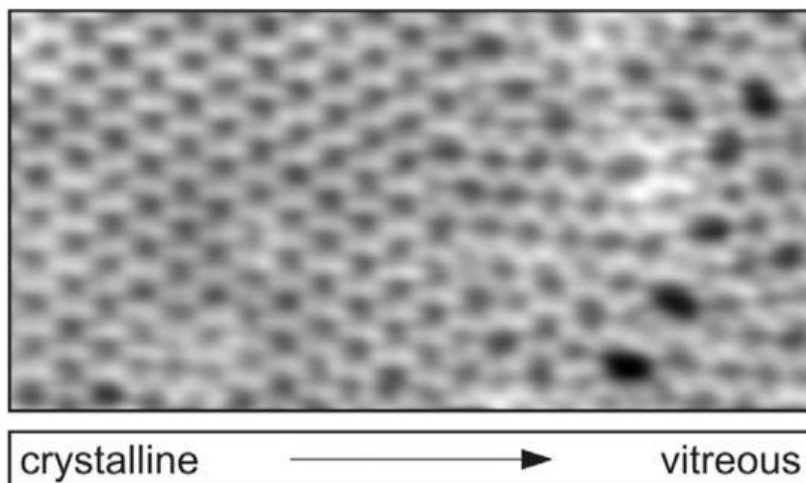
Figure 13 STM image of a silica film, with crystalline (left) and vitreous (right) phases observed [125]

While the lack of long-range periodic order appears to preclude the idea that glasses have a definite structure, it is the short to medium range order which gives rise to the macroscopic properties.

The coordination number of cations within the vitreous network determines how the 'building blocks' or structural motifs will arrange, i.e. into tetrahedra, triangles, octahedra. These structural motifs exhibit order within the range of several atoms [126]. The coordination number (CN) of the cations within a glass structure determine whether they are network formers (CN=3 or 4) such as Si, B, P, Ge, As, Be, or network modifiers (CN≥6) which reduce the connectivity of the network, such as Na, K, Ca or Ba. There also exists a subset of intermediate cations which, depending on their CN, either reinforce the network (CN=4) or loosen the network (CN≥6) but cannot readily form a glass alone [123,124]. The ways in which the individual structural motifs are connected together induce randomness into the network by variation of the bond angles and bond rotation. These structural motifs can be determined through Fourier Transform Infrared (FT-IR) and Raman spectroscopies [126,127].

2.2.2.2 Alkali - Silicate Glass

Due to the prohibitively high temperature required to melt pure silica (2200°C), fluxes and modifiers are added to reduce the melting temperature to more accessible temperatures. These additions modulate the properties (chemical durability, colour, viscosity, and mechanical properties amongst others). In order to reduce the melting temperature sodium oxide (Na_2O) is added: this gives a twofold change to the network. Firstly, it

reduces the connectivity of the glass network by introducing non-bridging oxygens (NBOs) as demonstrated in Figure 14, which significantly reduce the viscosity.
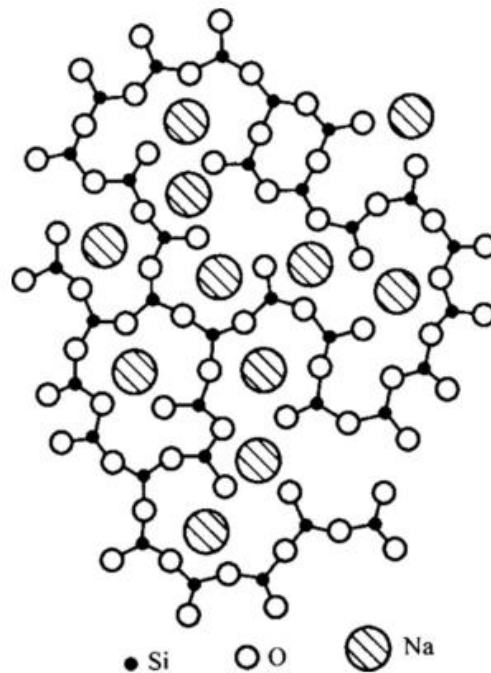
Figure 14 Arrangement of ions in Na_2O-SiO_2 glass. Na_2O ruptures oxygen bridges and the larger Na^+ ions are located within the interstitial cavities [128]
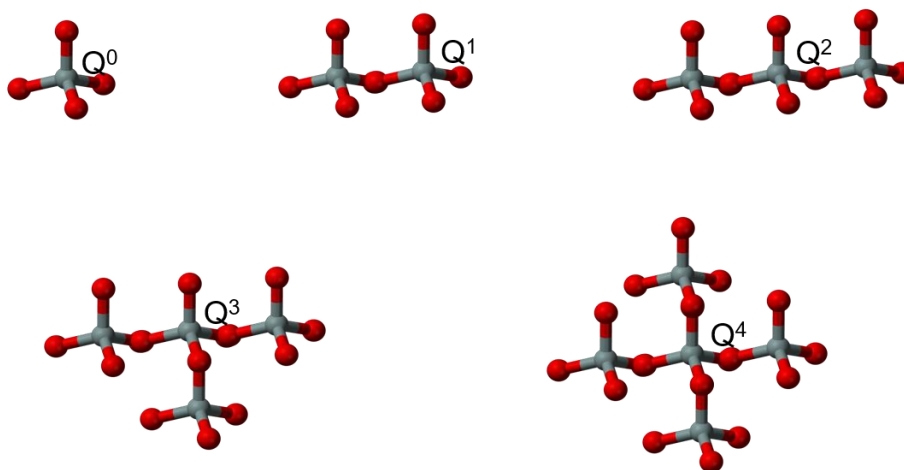
Figure 15 Q^n tetrahedra in a silicate glass, grey = Si, red = O
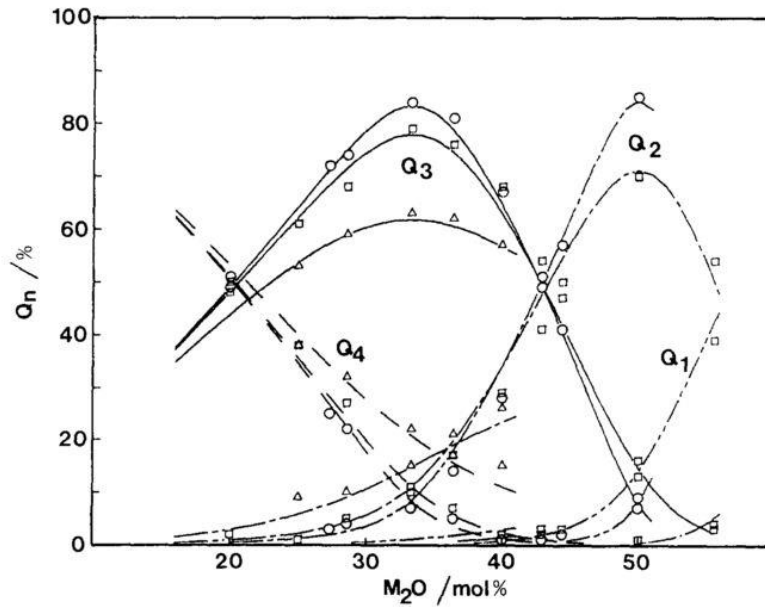
Figure 16 Effect of R_2O concentration on the relative concentration of Q^n units in R_2O-SiO_2 glasses

NBOs reduce the connectivity of the silicate glass network, and thus reduce the viscosity. Through Raman spectroscopy, this reduction in connectivity can be quantified by measuring the Q^n speciation [129]. Q^4 refers to a SiO_4 tetrahedra fully coordinated to four other SiO_4 tetrahedra, and inversely Q^0 indicates that the SiO_4 tetrahedron is bonded to no other SiO_4 tetrahedra, as shown in Figure 15. Determination of the concentration of each of the five possible Q^n units can be used to characterise the connectivity of the network. The relative concentrations of each of the Q^n structures are dependent on the concentration of the modifier ion, as shown in Figure 16 [130]. Between 0 and 15mol% of M_2O (where M= alkali), Q^4 tetrahedra are preponderant. Upon further addition of alkali oxide to 20-40%, the Q^4 concentration decreases while Q^3 concentration increases to a maximum at ca. 32% alkali oxide. Q^1 and Q^2 conformations become dominant towards 50+% concentration of M_2O.

Greaves proposed a *modified random network model* (MRN) [131] suggesting in an alkali silica glass, the overall structure is composed of two interlocking sublattices. One is comprised of network formers (i.e. SiO_2) and the other is inter-network regions or percolation channels, consisting of network modifiers (i.e. Na_2O). This is demonstrated schematically in Figure 17. Structures shown in Figure 17 occur when the volume fraction of the modifier oxide ≥16%. Ionic transport is more readily supported by the percolation channels as the activation energy decreases with increasing modifier content. At low concentrations of modifier oxide the ratio between self-diffusion and ionic conductivity (i.e. correlation factor, f) is not associated. Upon increasing the modifier concentration ≥16%, the correlation factor plateaus at a value close to one. This has been calculated and measured experimentally [131,132].
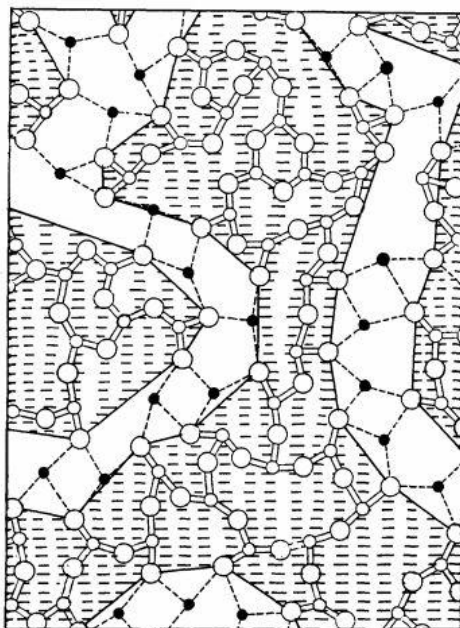
Figure 17 MRN schematic of a 2-dimensional oxide glass. Covalent bonds are shown by the solid lines and ionic bonds are given in dashed lines. The shaded regions represent disclinations (line defects) which pass through the non-bridging bonds. The percolation channels of the modifier are shown with a white background [131]

2.2.2.3 Alkali – Alkaline Earth -Silicate Glass

In order to improve the chemical durability whilst maintaining a technologically available melting temperature ternary silicate glasses (R_2O-RO-SiO_2) are made. Soda lime silica glasses constitute the majority of technological and commercial glasses. Of the order of 95% of commercial glass production is oxide based glasses, with the majority silica based [133]. Generally, the composition for soda lime silica glasses falls within the ranges 10-20mol% Na_2O, 5-15mol% CaO and 70-75mol% SiO_2, and other minor additives modulate the optical, chemical and mechanical properties. These additives are strongly affected by the soda lime silica network and it is therefore imperative to understand the topology of a soda lime silica glass before the structure is further convoluted upon the addition of other components.
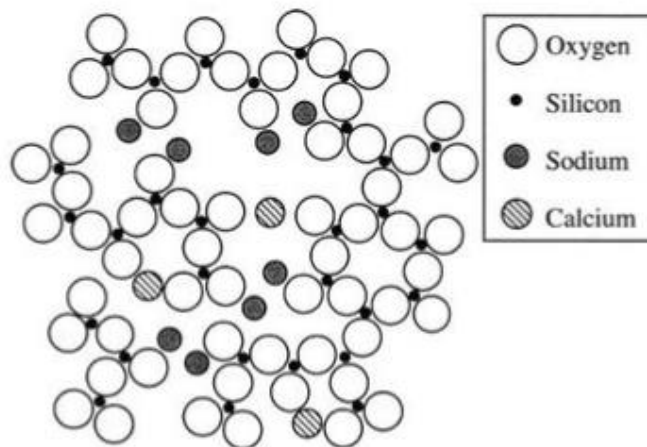
Figure 18 Schematic of 2-dimensional structure for soda lime silica type glass. Note a fourth oxygen atom would be located above each silicon atom in the 3-dimensional structure [147]

As shown in Figure 18 every R^{2+} ion must be connected to two NBOs to balance the local charge. This provides a stronger linkage than the corresponding R^+ ion, and R^{2+} cations are thus bonded more strongly into the network and are relatively immobile. Replacement of the more mobile R^+ ions by less mobile R^{2+} ions reduces the overall mobility of the

network and hence improves the chemical durability significantly, whilst also contributing to decreasing the viscosity of the molten glass.

2.2.2.4 Hydration and Dissolution of SLS glass

The long-term chemical durability of soda lime silica glasses is determined by the rate of exchange and interdiffusion of alkali ions with protonic, generally hydronium ions H_3O^+, species from water. Dissolution behaviour is dependent on both the composition of the glass and the solution in which it resides. Five types of dissolution behaviour were observed by Hench and Clark [134] , type 1 corresponds to inert glasses in a neutral pH solution where there is a very thin (ca. 5 nm) surface hydration layer, this occurs in pure silica in deionised neutral water. Type 2 corresponds to durable glasses which form a diffusion limited hydrated layer in the order of 10 nm to circa 500 nm, which occurs in low alkali silicate glasses in pH < 9 solutions. Type 3 is the same as type 2 in the hydration layer and conditions but is distinguished by an additional layer of secondary phases that are redeposited onto the hydration layer. Type 4 corresponds to glasses with a high alkali content in which the hydration layer is not diffusion limited and leads to further dissolution. Type 5 is characterised by complete dissolution and observed in high pH solutions >10.

The long term performance of glass products depends on the chemical resistance, the importance of chemical durability is shown by four ISO tests [135–138]. Glasses may exhibit strong chemical resistance to one of these tests but be susceptible to corrosion from another.

In glasses containing highly mobile ions, notably alkali ions, ionic exchange between those R^+ and acidic water (H_3O^+) can occur. This is the initial step in the dissolution of sodium silicate glasses [139]. The process is diffusion controlled so the depth of

penetration of hydronium ions into the glass increases with the square root of exposure to the solution. This ion exchange process is predominant initially but becomes self-limiting at increasing hydration thicknesses [140].

As congruent dissolution occurs at a constant rate, while ion exchange processes are proportional to the square root of time, the congruent dissolution process will begin to dominate over longer periods [141].
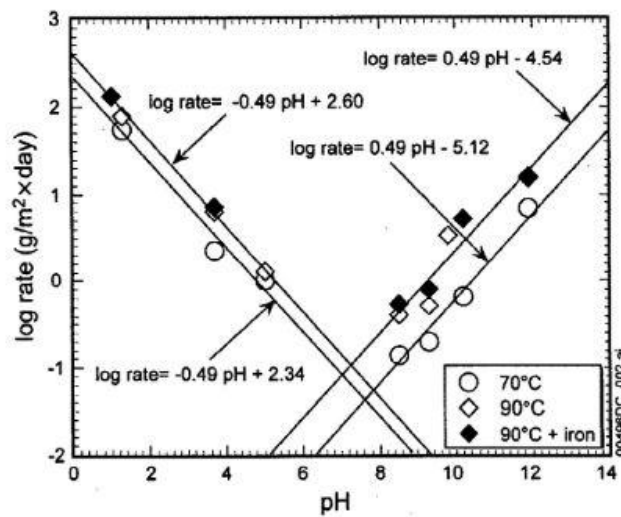
Figure 19 Glass dissolution as a function of pH [142]

The solution conditions affect the rate of dissolution greatly [143]. Factors which favour dissolution include a very large surface area, the solution is replenished constantly (or the volume is infinite), the solution is dilute in dissolved ions, and the pH remains constant at either extreme of the pH scale i.e. greater than 9 or lower than 3 as shown in Figure 19 [142]. At the extremes of pH the Si-O bonds are affected directly resulting in differences in durability becoming negligible. Even the addition of alumina, which typically improves chemical durability, in strongly acidic solutions the Al-O bonds are broken leading to rapid dissolution of the network [140]. While beyond the scope of this work, glasses with phase

69

separation may exhibit different chemical durabilities with different orders of magnitude [144].

2.2.2.5 Minor Additives for SLS glass

2.2.2.5.1 Al^{3+}

In oxide crystals, aluminium ions are found in both tetrahedral and octahedral coordination [145,146]. In SLS type glasses the aluminium ions occur in aluminium-oxygen tetrahedra almost exclusively, providing the R$^+$ and R^{2+} content is eqimolar or in excess [147]. This is required for two reasons; firstly as Al$_2$O$_3$ provides only 1.5 oxygen atoms per aluminium atom, the oxygen provided by the R$^+$ or R^{2+} oxides is needed to complete the two oxygen atoms per tetrahedra (giving Q^4 speciation) [148]. Since the oxygen atom supplied by the R$^+$ or R^{2+} is utilised as a bridging oxygen upon the addition of aluminium ions, it cannot be a NBO. Hence, for every one atom of aluminium one NBO is removed from the network, increasing network connectivity and chemical durability [149,150]. The second reason the R$^+$ and R^{2+} ions need to be in excess for tetrahedral Al^{3+} ions to occur is to balance the local charge, as the effective charge for the AlO$_2$ tetrahedra is -1 distributed over the anion which is balanced by either one R$^+$ or two R^{2+} cations, demonstrated in Equation 2.

$$[AlO_2]^- + R^+ \propto 2[AlO_2]^- + R^{2+}$$
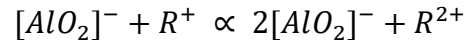
Equation 2 Local charge balances of aluminium-oxygen tetrahedra

2.2.2.5.2 Mg^{2+}

In aluminosilicate glasses modified by R^{2+} ions, Ca^{2+} and Mg^{2+} confer different local environments. Mg^{2+} has a smaller ionic radius than Ca^{2+}, and the coordination number of Ca^{2+} is generally six-fold or seven-fold [151,152], whereas the coordination number of Mg^{2+} has been reported as being four, five or six-fold [153,154]. This suggests that Mg^{2+} may act as a classical network modifier or a network former. Mg^{2+} allows for the formation of more Al-O-Al bonds relative to Ca^{2+} in aluminosilicate glasses [155].

2.2.2.5.3 K$^+$

Potassium has been used as a glassmaking reagent since at least 1000AD [119], primarily in the form of wood ash. The raw materials in the production of wood ash glasses contained a higher amount of Fe$_2$O$_3$ and MnO, the resultant glasses were a deep green – blue colour [156].

Potassium oxide is used as a flux in the same manner as sodium oxide, to lower the viscosity of the main glass former. As K$^+$ has a lower field strength than Na$^{+,}$ the viscosity is higher with the same molar amount [157]. Recently the glass industry has utilised potassium to chemically strengthen the surfaces of glass and induce a stress profile [158]. See section 2.2.3.3.1.

2.2.2.5.3.1 Mixed Alkali Effect

In glasses, containing two different alkali ions the diffusivity of either component is orders of magnitude greater than in the corresponding glass with either of the alkali ions [159,160]. This is termed the *mixed alkali effect*. The mixed alkali effect decreases the

temperature at which viscosity is equal to 10^{12} Pa.S, the annealing temperature as shown by Figure 20. See section 2.2.3.1.2 for viscosity fixed points.
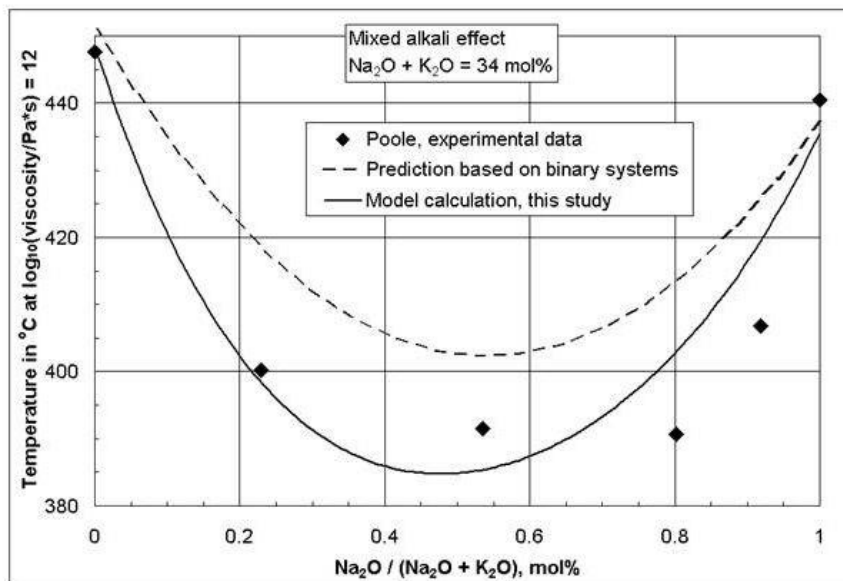
Figure 20 Viscosity at 10^{12}Pa.S at constant alkali molar concentration [161]

2.2.2.6 Non-Negligible Components of Soda Lime Silica Glasses

Since glass is used to transmit visible light into buildings, to transmit light through a PV module cover glass and to transmit photons through optical fibres, the colour of commercial glass is of great importance, with a great deal of research undertaken to fully understand the chromophores present in silicate glasses [61,78,162–164]. The main two chromophores present in soda lime silica glasses are iron and titanium;

2.2.2.6.1 Fe_2O_3

In all commercial glasses Fe_2O_3 is present, either as a deliberate addition or as an impurity, particularly from the silica source [165]. Iron is usually present in glass in the oxidation states Fe^{2+} and Fe^{3+}, with raw materials and melting conditions strongly affecting the Fe^{2+}/Fe^{3+} redox ratio [163]. The content, redox ratio and environment of iron in the glass matrix can modulate the optical absorption in the UV, visible and IR regions [57,166].

2.2.2.6.2 TiO_2

TiO_2 is another polyvalent ion found in commercial glasses, with effects in the UV and visible regions [167]. Ti^{4+} in silicate glasses shifts the UV absorption edge towards the visible region due to the absorption of *2p* orbitals from O^{2-} ions to the d^0 metal ion, inducing a fluorescence effect [74,78]. In the Ti^{3+} oxidation state an optical absorption around 20,000 cm^{-1} (500 nm) occurs due to the $^2T_{2g}$-^2E_g transition of the *3d* electron [167].

2.2.2.6.3 Na_2SO_4

The addition of Na_2SO_4 has several pronounced effects on glass production; it is both a source of Na_2O and SO_3^{2-} in the glass. It promotes the formation of low melting eutectic liquids during the silicate formation portion of the melt [168]. Primarily the addition of sodium sulphate to the melt is to aid in refining, through the decomposition at high temperatures forming large bubbles aiding the removal of seed, and due to the release of oxygen at high temperatures it is an oxidising agent [169].

Refining agents are used in a glass melt to aid homogenisation through the release of large quantities of gas release. The large volume of gas has a two-fold benefit; firstly, the large bubbles rise faster than the small entrapped bubbles. This process is characterised by Stokes' law of rising bubbles through a viscous medium, following Equation 3.

$$F_d = 6\pi\eta Rv$$

Equation 3 Stokes' law on the force of viscosity on a small sphere moving through a viscous medium

Where; F_d = frictional force, η = dynamic viscosity, R = radius of sphere, v = flow velocity relative to the moving object

Utilising Equation 3 it follows there are two methods to increase the speed of the entrapped bubbles to rise to the surface, increase the radius of the bubble or to lower viscosity. Common refining agents include potassium and sodium nitrates, sodium chloride, fluorides of calcium and sodium and sodium sulfate (Na_2SO_4) [164]. Historically oxides of arsenic and antimony were used to aid in bubble removal.

2.2.2.7 Commercial Compositions of Soda Lime Silica Glasses

Glasses that attenuate UV light and have high transmission in the visible are used for PV modules [60]. Critically the composition must fulfil several criteria; high chemical resistance, good mechanical properties, high transmission in the visible and NIR and strong attenuation in the UV [27]. The ranges of compositions are outlined in Table 3. Selection of low iron oxide raw materials is crucial. Commercial soda lime silica glasses are melted at temperatures of between 1450°C to 1550°C [27]. Resultant glasses are frequently tempered to increase the strength and to reduce risk of serious injury [170].

Table 3 Typical compositional ranges of PV solar glasses [171,172]

Oxide	Molar %
SiO_2	70-74
Na_2O	12-16
CaO	5-11
MgO	1-3
Al_2O_3	1-3

2.2.3 Chemistry and Physics of Glass Processing

2.2.3.1 Mechanisms of Glass Melting

Specific details regarding the mechanisms of melting are dependent upon the specific batch materials and the type of glass produced. For silica based glasses, especially the formation of soda-lime-silica glasses, far more information is available in the literature about specific melt processes [124,173]. The major mechanisms in soda lime silica glass melts are:

- Release of adsorbed water around 100°C. Generally, raw oxides and carbonates have been dried before melting in a furnace to obtain a reliable weight. However, some components are hygroscopic (CaO or NaOH) or contain water in their crystalline structure and to remove the water from these components requires extra energy input.

- Release of volatile gases and combustion of organic compounds between 200-600°C [174]. Carbonates also begin to decompose leading to large volumes of CO_2, for one mole of $CaCO_3$ 22,400 cm^3 of CO_2 gas is released, a volume expansion of around 600 times.

- Solid-state reactions occur between components leading to binary or ternary systems. This leads on to the eutectic melting of Na_2O and CaO at 775°C and

sodium disilicate and SiO_2 at 800˚C. Solid state reactions begin to occur over this temperature range. The viscosity is low at this point and the rate of dissolution of silica and alumina rapidly increases with increasing temperature. As the concentration of silica increases in the liquid phase, the viscosity increases, resulting in the required high temperatures to aid in refining.

At high temperatures, fining processes lead to homogenisation of the glass melt where it is subsequently processed.

2.2.3.1.1 Commercial Glass Melting Procedure

Float glass manufacture, or the Pilkington process as named after the inventor, produces parallel flat glass sheets by floating molten soda lime silica glass on a molten tin bath. Although some speciality borosilicate glasses such as Borofloat® by Schott are prepared through this method, the majority of commercial production corresponds to the soda lime silica family of glasses. In 2009 annual flat glass production globally was 52 million tonnes, worth globally £20 billion [175].
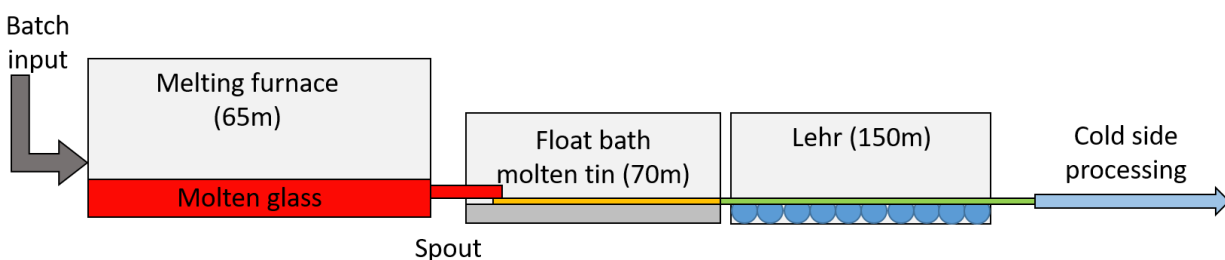
Figure 21 Schematic of float glass furnace, float bath, and lehr

Figure 21 shows a typical float glass 250 tonne per day float glass furnace. Batch input corresponds to the pre-mixed composition of soda lime silica with minor additives and

cullet. The mixture enters the melting furnace with a batch charger, the rate of which is determined by the output and retention time of the furnace. The melting furnace is typically between 1450°C and 1575°C depending on composition [27], desired redox of any constituents and throughput. Typically these are heated through natural gas or oxy-gas, a mixture of hydrogen and oxygen which burns cleaner and hotter [176]. To induce thermal convection currents heating electrodes are frequently used, these are electrically powered and assist in homogenisation of the melt [177].

The furnace is lined with refractory material to withstand the temperature and atmosphere, in the hot end of the furnace thermal regenerators are frequently used to recapture flue exhaust heat [178]. Within the flue are chemical scrubbers to remove SO_x, NO_x and fine particulates which are tightly controlled by EU legislation.

After homogenisation the molten glass flows into a molten tin bath via a spout. The atmosphere is controlled with N_2 and H_2 under positive pressure to minimise oxidation of the tin. Tin diffuses into the glass and oxidises, this can be revealed through reflectivity, fluorescence and ellipsometry measurements [179]. The temperature of the tin is circa 600°C, the viscosity of the glass rapidly increases within this section. At the input the glass is generally 1200°C, and is cooled to above T_g by the end of the float process [180].

The viscosity is sufficiently high to not deform under the weight of the glass, i.e. the Littleton softening point, as it enters the annealing lehr [181], see section 2.2.3.1.2. Over the distance of the lehr the temperature is gradually reduced to remove thermal stresses within the glass where it is subsequently cut and prepared for transport. Within the lehr, coatings can be applied to enhance optical and mechanical properties. Until this portion

the process is referred to as the hot end, and any subsequent post melt and cooling are termed the cold end such as applying labels and cutting.

2.2.3.1.2 Typical Viscosity Curve

In commercial processes, there are four standard viscosity points that must be controlled, and which are essential to ensure a high throughput of glass. These points are shown in a typical viscosity curve in Figure 22 [147] and are as follows:

- Working point – 10^3 Pa.s

- Littleton softening point – $10^{6.65}$ Pa.s

- Annealing point – 10^{12} Pa.s

- Strain point – $10^{13.5}$ Pa.s
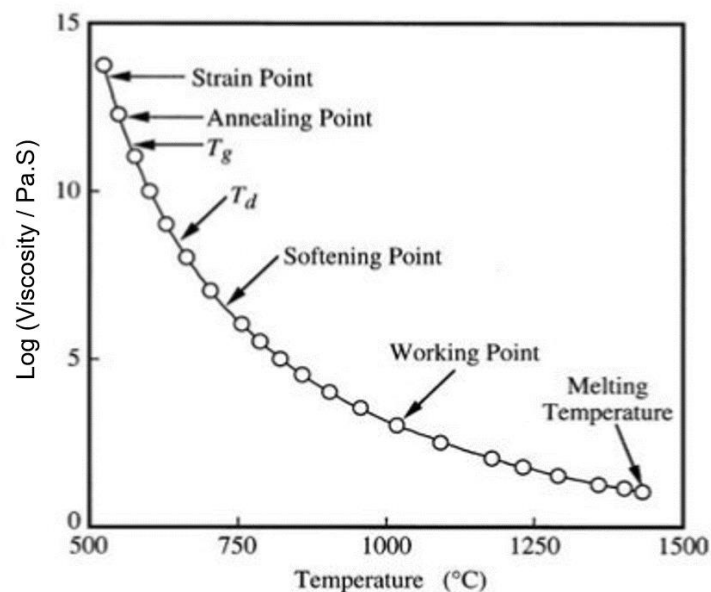
Figure 22 Typical viscosity curve as a function of temperature for a soda lime silica melt

After the melting temperature (of 1-10 Pa.s to aid in refining and homogeneity), the glass is delivered to a machine to be worked, generally a float or bottle forming section, hence the working point. This viscosity allows for the formation of shapes under reasonable and technological stresses but the glass must be supported until below the Littleton softening point. This point is characterised as the temperature which the top 10 cm of a glass fibre of between 0.55-0.75 mm diameter and 23.5 cm length is heated in a furnace at 5°C min^{-1} begins to elongate under its own weight at a rate of 1 mm min^{-1} [181]. Note, the viscosity of $10^{6.65}$ Pa.s only refers to the specific glass which was originally tested by Littleton; if the density of another glass is different the softening point will vary from $10^{6.65}$ Pa.s.

Viscosity is a measure of the resistance of a liquid to shear deformation, given by Equation 4, where viscosity (η) is defined by the force applied (F) between two parallel sheets of (d) distance, divided by the area (A) of those plates and the relative velocity (v) of the two plates.

$$\eta = \frac{Fd}{Av}$$

Equation 4

Glasses most readily form either if the viscosity is high at the melting temperature, or if viscosity increases rapidly upon cooling from the melt to the solid. Both of these high viscosity situations impede the crystallisation of the melt as atomic rearrangement is significantly reduced in a high viscosity liquid. The annealing point is generally defined as 'the temperature at which a glass would release 95% of its stresses within 15 minutes' and the strain point 'the stress release[s] over 6 hours' [133].

2.2.3.2 Crystallisation of Glass

While all glasses will crystallise over a long enough time frame, '[the] ultimate fate, in the limit of infinite time, is to crystallise' [105], uncontrolled bulk crystallisation tends to produce poorly-performing glass-ceramics, as the devitrification process occurs at random times and locations [182]. However, upon addition of a suitable nucleating agent such as TiO_2 [183], ZrO_2, halides [184], phosphates [185], or Ag_2O [186], the nucleation and subsequent crystallisation occurs at a particular time and location within the network and under the right conditions, allowing careful control of the subsequent glass-ceramic.
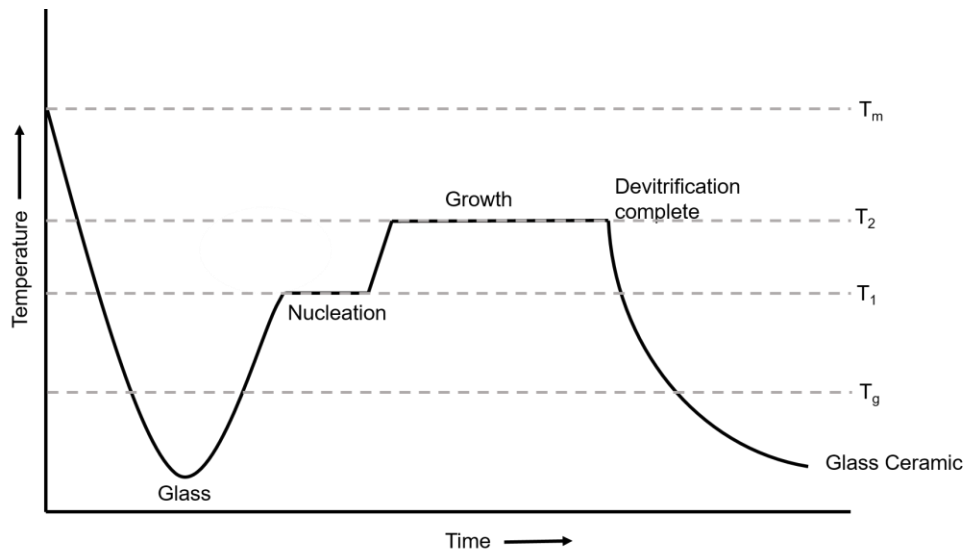
Figure 23 Time - Temperature schematic for the production of glass ceramics

There are several critical steps to produce a suitable glass-ceramic, as shown in Figure 23. The raw materials are melted until a homogeneous liquid is formed, and then cooled and formed into the desired morphology below T_g. The glass must be annealed to remove thermal stresses before reheating to T_1 or above. This is the minimum temperature for (technologically feasible) devitrification, and produces large numbers of small crystallites. T_2 corresponds to the temperature in which growth of the crystallites is at a maximum,

and must be below the liquidus temperature. After the appropriate time the glass-ceramic is slowly cooled to room temperature to remove thermal stresses.

Crystallisation of glasses have been extensively researched and developed since Stookey first proposed glass-ceramics in 1959 [187], leading to novel hybrids overcoming classical drawbacks of glasses. Glasses are readily formed into a multitude of shapes and structures, and the subsequent glass-ceramics have zero porosity. Glass-ceramics have interesting properties that are difficult to achieve with either component. The mechanical [188,189], optical [184,190–192] and electrical [193] properties can be dramatically improved upon partial crystallisation.

2.2.3.3 Mechanical Properties of Glass

Fracture strengths of glasses are generally far lower than the maximal theoretical strength. Various environmental and surface flaws give rise to a large variation in fracture strengths, and hence fracture strength can only be described as a distribution function. The stress required to form two new surfaces is given by Equation 5.

$$\sigma_m = \sqrt{\frac{E\gamma}{r_0}}$$

Equation 5

Where σ_m is the Orowan stress, E is Young's modulus, γ is the fracture surface energy and r_0 is the interatomic distance. The terms in Equation 5 are generally independent of glass composition, resulting in all glasses having a fracture strength within the range of 1-100 GPa. Equation 5 allows for calculation of breaking of individual chemical bonds, and does not allow for surface flaws acting as stress concentrators. The typical practical

fracture strength is around 7-32 MPa for silicate glasses [67]. During manufacture, transport and use of glass products flaws in the surface develop, which act as stress concentrators increasing the local stress to levels higher than the theoretical level and hence causing a fracture. In practical terms, glasses with a higher scratch resistance will have a higher strength (all else being equal) due to the ability to resist the build-up of flaws. However, flaws can occur not just from mechanical actions but also from chemical attack, such as hydration of the surface [141], or from thermal actions. Rapid heating and cooling of glasses reduce the strength of glasses due to the outside of the material being heated faster than the inside, inducing stress due to thermal expansion.

2.2.3.3.1 Strengthening of Glass

Other than producing a pristine glass with near zero surface flaws [67], there are two main methods to increase the strength of glass; both methods rely on the same principle of inducing surface compression and internal tension. Introducing a stress gradient according to Figure 24, allows the surface of the glass to resist scratches and fractures [194]. Typical thermal toughening occurs due to rapid air quenching of glass from above to below its T_g. The surfaces solidify rapidly while the core remains in a relaxed fluid state, upon further cooling the surfaces cannot shrink further while the core shrinks slightly building in the compressive and tensile stresses and balancing the stress distribution.

Tensile stress   Compressive stress
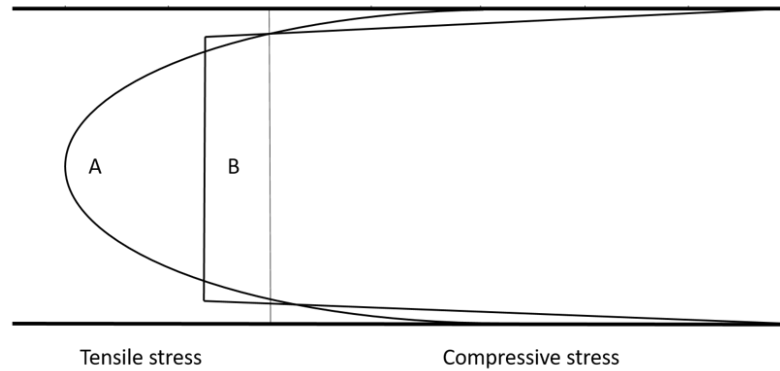
Figure 24 Schematic of residual stress profiles in A) thermally and B) chemically tempered glasses as a function of depth

Chemical toughening occurs through an ion exchange process wherein a larger ionic radius ion replaces a smaller, more mobile ion, usually between alkali ions [195], however various sulphur oxides can also be used to induce stress [196]. Due to the larger, less mobile ion becoming embedded within the network at the surfaces of the glass, a compressive stress layer is built in with greater control over the thickness and with a higher total stress [197]. Fracture toughness of a glass can be controlled through composition, with larger, less mobile alkaline earth ions increasing fracture toughness [198], and between 5-15 vol% Al_2O_3 content in SLS glasses fracture toughness increases [117]. Typical silicate glasses have a fracture toughness of between 0.6 – 0.8 $MPa.m^{1/2}$ [199].

2.2.4 Optical Properties of Glass

Soda lime silica glasses have a unique combination of properties that make their use widespread: perhaps the most important are their optical properties. The ability to transmit visible light allows for illumination of homes and PV modules while the chemical inertness protects from the elements.

The optical properties of glasses may be divided into four categories: (i) bulk properties that refer to refractive index, scattering and optical dispersion; (ii) absorption properties refer to the colour of the glass, UV Vis and IR absorption profiles, colloidal dispersion amongst others; (iii) surface properties including reflection; and (iv) other properties such as photochromism, Faraday rotation of light and luminescence [133].

Silicate glasses are one of the few commonly available materials that allow the transmission of visible light. The optical properties of glass allow communication through optical fibres [200], the refractive index and transmission allows for optical instruments and enhanced solar PV modules [95] and the aesthetics of the material are useful for architecture and glassware. The colour of glass have been studied for many years by technologists understanding chromophores particularly iron and other transition metals [201]. Stained glass has been produced for over 1000 years, due to its aesthetics, for mosques, cathedrals and other buildings of cultural importance.

There are many other optical characteristics that change the properties of the glass such as luminescence, scattering, photochromism and opalescence. In the 1959 book 'Coloured glasses' by Woldemar A. Weyl [202], while a few of the theories outlined have been modified since his book was written, the main bulk of the work is still crucial to the modern glass scientist.

2.2.4.1 Basics of Light

As outlined in section 2.1.1, the wavelength ranges outlined in this study are defined as ultraviolet (UV) have been defined as the wavelengths corresponding to 50000 cm^{-1}–26000 cm^{-1} (200 nm-380 nm), visible photons corresponding to 26001 cm^{-1}–12800 cm^{-1} (380 nm–780 nm), and infrared (IR) as 12801 cm^{-1}–3300 cm^{-1} (780 nm–3000 nm). This

is outlined in Figure 25; the UV VIS IR range is a narrow band of the total electromagnetic spectrum.
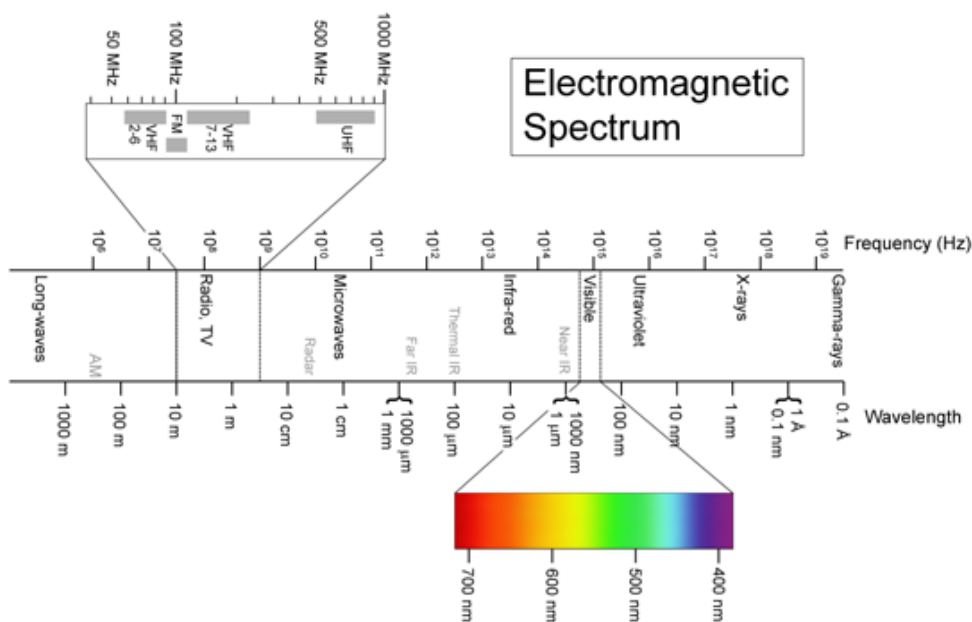
Figure 25 Electromagnetic spectrum. Public domain image from Louis E. Keiner via Wikipedia Creative Commons

Electromagnetic waves transport energy through a vacuum at 2.997×10^8 m s^{-1} (notated by the symbol C). As light passes through a medium the wave is absorbed by the atoms in the material, the electrons undergo non-resonant vibration and then emit the wave. This process is repeated multiple times throughout the material, ultimately slowing the propagation of the wave.

The reduction in speed at an interface leads to a refraction of the wave. A vacuum, by definition, has a refractive index of 1, air at STP has an $R_f=1.00023$, and SLS type glass has an $R_f=1.502-1.557$ depending on composition and treatment [58]. Refractive indices are not constant and vary with wavelength: shorter wavelengths are deviated more

strongly than longer wavelengths, following the derivation given in Equations 6-10, and

shown in Figure 26.
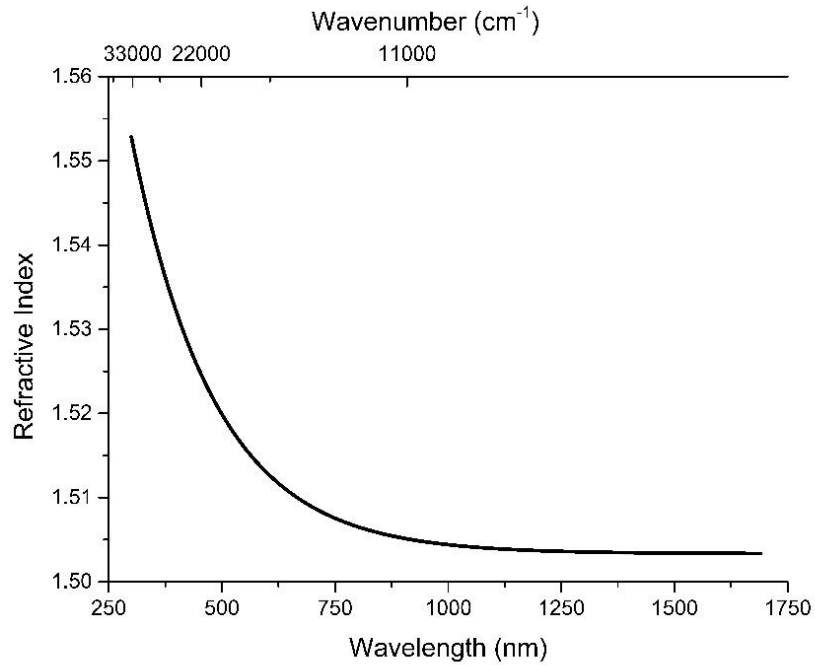
Figure 26 Variation of refractive index by wavelength for soda lime silica glass (data from [58] and smoothed)

$$R_f = \frac{c}{v}$$

Equation 6

Velocity can be defined as;

$$v = \lambda . f$$

Equation 7

Substitution into Equation 6 gives;

$$R_f = \frac{\lambda_{medium1} . f}{\lambda_{medium2} . f}$$

Equation 8

The frequency term cancels leaving;

$$R_f = \frac{\lambda_{medium1}}{\lambda_{medium2}}$$

Equation 9

Therefore,

$$R_f \propto \frac{1}{\lambda}$$

Equation 10

2.2.4.1.1 Refraction

Transmission of light from the air to glass to air interfaces leads to two changes of refractive index, as demonstrated schematically by Figure 27.
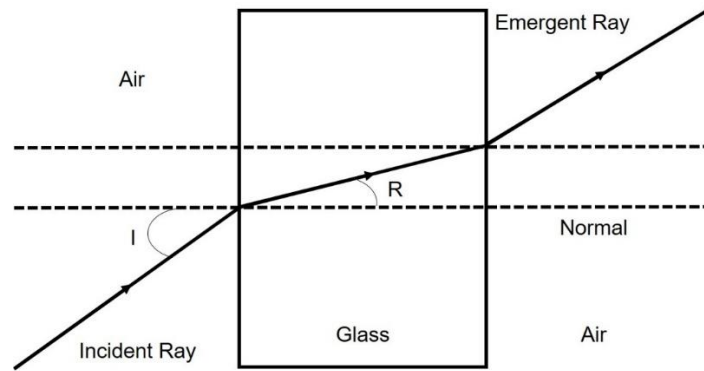
Figure 27 Schematic of refraction and transmission of light

The refractive index is dependent on the photons' interaction with the electrons from the atoms forming the glass. Increases in either the electron density or polarisability of the ions lead to an increase in the refractive index. Glasses with heavy ions such as Pb or Bi have higher refractive indices, generally around 2.0 [203,204]. Lead crystal glassware

87

has been produced for centuries for its brilliance; this is partially attributed to the high refractive index of 24wt% PbO glasses. Anionic contributions such as F$^-$ lower the refractive index. The proportion of non-bridging oxygens (NBOs) to bridging oxygens (BOs) modulates the refractive index as NBOs are more polarisable, leading to higher refractive indices.

2.2.4.1.2 Reflection

Reflection is a change in direction of a photon as it passes through one medium to the surface of a second medium. In glasses, the electric field of the photon interacts with the electrons within the glass, which in turn reradiate the light outward. In the context of solar PV modules, this occurs at several points and must be minimised at each surface, not only for better conversion efficiency but also for air navigation requirements. In fixed PV systems up to 20% of the available photons are lost through reflection per day [43]. Antireflective coatings are frequently applied to glasses which reduce the reflective losses to below 7% in 1986 [205], and have recently been demonstrated to reduce them to below 5% losses, with the additional benefit of having self-cleaning properties [62,206].

Antireflective coatings work most effectively at a particular wavelength, and cause greater refraction for photons of other wavelengths. Antireflective coatings on glass can increase the transmission to above 98% over the visible range. However, long term stability of the coatings is highly dependent upon the initial surface conditions and is most effective over a narrow wavelength range [63].

At any interface with a difference in refractive index, refraction occurs. In photovoltaic modules efficiency can be increased through a refractive index matching of the EVA and

glass front sheet layers, additionally when combined with a luminescence downshifting layer [207].

2.2.4.1.3 Charge Transfer Bands

Silicate glasses have strong absorption of photons in the ultraviolet region; this absorption is termed the *ultraviolet edge*. The ultraviolet edge is caused by a photon exciting a valence electron of an anion (e.g. O^{2-}) to an excited state. NBOs lower the energy required for this excitation process to occur, hence the addition of modifiers (Na^+, Ca^{2+} etc.) shift the ultraviolet edge towards the visible region.

Due to impurities such as iron and titanium, arising from the raw materials and refractories, the inherent ultraviolet edge is infrequently measured. Strong absorption bands occur in $Fe^{3+/2+}$ and Ti^{4+} in silicate glasses due to an oxygen metal transfer band [56,78] from the cation to a network anion. The intensity of these bands is so great as to effectively shift the ultraviolet edge towards the visible.

A charge transfer band is a change in the electron distribution between a metal and ligand. There are two types, which are defined by the direction of electron transfer;

2.2.4.1.3.1 Ligand to Metal Charge Transfer Bands

Ligand to metal charge transfer (LMCT) bands involve the transfer of electron(s) from an orbital of a ligand, to the orbital of a metal. This is favoured where the ligand has high-energy lone pairs (e.g. O^{2-}) and the metal is in a high oxidation state (e.g. d^0 metals) as the acceptor level is low in energy. Metal ions that are more readily reduced tend to have lower energy transitions.

2.2.4.1.3.2 Metal to Ligand Charge Transfer Bands

Inverse to LMCT, metal to ligand charge (MLCT) transfer bands involve the transfer of electron(s) from the orbital of a metal, to the orbital of a ligand. This is favoured with low energy π^* orbitals in aromatic ligands, and if the metal has a low oxidation number.

2.2.4.1.3.3 Transition Metal and Lanthanides Charge Transfer Bands

Particular transition metal ions such as $Fe^{2+/3+}$ [208], $Cr^{5+/6+}$ [209] and lanthanide ions, notably $Ce^{3+/4+}$ [210], absorb strongly in the UV region and their presence in the cover glass will thereby confer protection to polymeric species beneath. However, all of these metal ions in glass produce strong visible absorption. Cerium oxide has been used as a model UV absorbing agent for the protection of polymers in PV modules [28], however CeO_2 solarises over time, resulting in less effective protection over time [211].

2.2.4.1.4 Luminescence

Fluorescence, downconversion and upconversion are types of luminescence with subtle differences. Fluorescence (sometimes referred as downshifting) involves the absorption of one photon and the emission of up to one photon, after losses of non-radiative decay mechanisms. Downconversion (DC) processes involve the absorption of one photon and the emission of more than one photon of lower energy. Upconversion (UC) processes involve absorption of multiple photons (at least two) and release of a photon of higher energy. These three variations of luminescence are schematically shown in Figure 28. Luminescence in silicate glasses can allow a PV module to access a wider range of photons available for conversion to electricity. All solar cells have a range of photons which are able to be absorbed and converted to electricity, c-Si PV modules absorb according to Figure 29, note this follows the solar spectrum as shown in Figure 1.
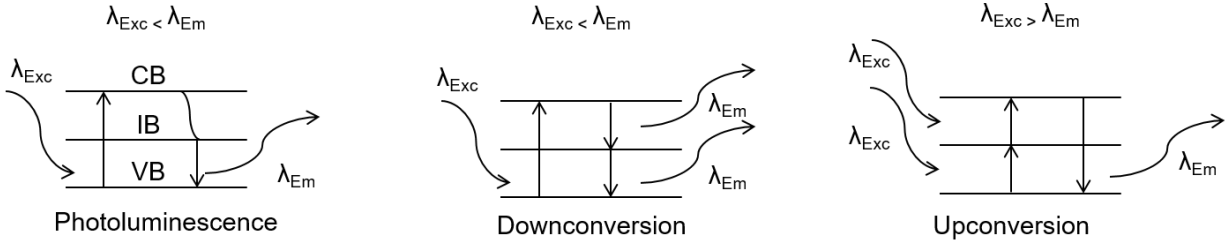
Figure 28 Schematic of absorption and emission processes of photoluminescence (PL), downconversion (DC) and upconversion (UC) [2]
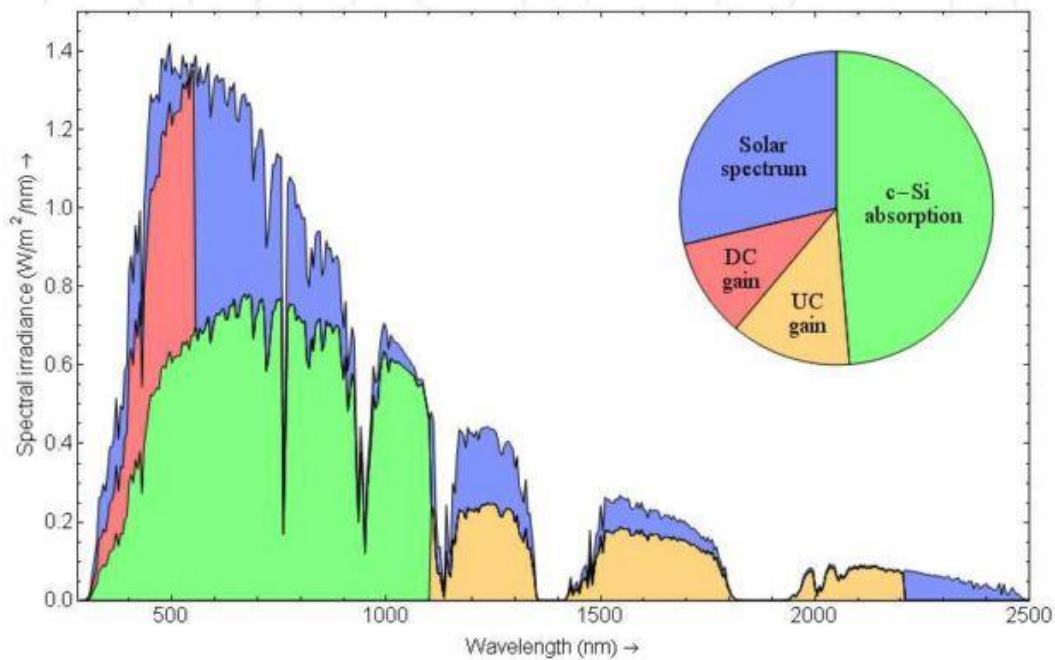
Figure 29 Potential gain of up and downconversion processes for a Si-PV module. Figure considers no other losses than spectral mismatch. DC – downconversion, UC – upconversion. Copied from [212]

Downconversion processes (including fluorescence) can lead to a theoretical efficiency increase in a c-Si solar module of up-to 36.5% [213], upconversion processes can lead to a theoretical efficiency of 37.0% [214].

There are two forms of light emission, blackbody radiation and luminescence. Blackbody radiation was briefly discussed in section 2.1.1, the various forms of luminescence and

their mechanisms will be detailed here. The absorption and emission of light is quantised according to Equation 11;

$$E = hv = \frac{hc}{\lambda}$$

Equation 11

Where; v = frequency, c = speed of light, λ = wavelength and h = Planck constant. As the energy is proportional to the frequency there is a great variation over the electromagnetic spectrum (10^6 eV for gamma rays to 10^{-9} eV for radio waves). Within the scope of this thesis, luminescence discussion is limited to transitions induced by UV and visible photons (12eV – 1.6 eV), which involve the transitions of the outer atomic electrons.

2.2.4.1.4.1 Absorption

There are several possible outcomes after the initial absorption of a photon to dissipate the energy through phonon losses, decomposition, reactions, or by re-emission. The quantum efficiency (QE) factors all the mechanisms and details the statistical chance of photon emission and can never exceed 1 (or 100%) given by;

$$QE = \frac{photons\ emitted}{photons\ absorbed}$$

At room temperature, most electrons are in the ground state (termed S_0) in the lowest vibrational level. Absorption of a photon, of near or equal to the energy of the bandgap, induces an electron to be promoted to either the first (S_1) or second (S_2) excited state as demonstrated schematically in Figure 30.
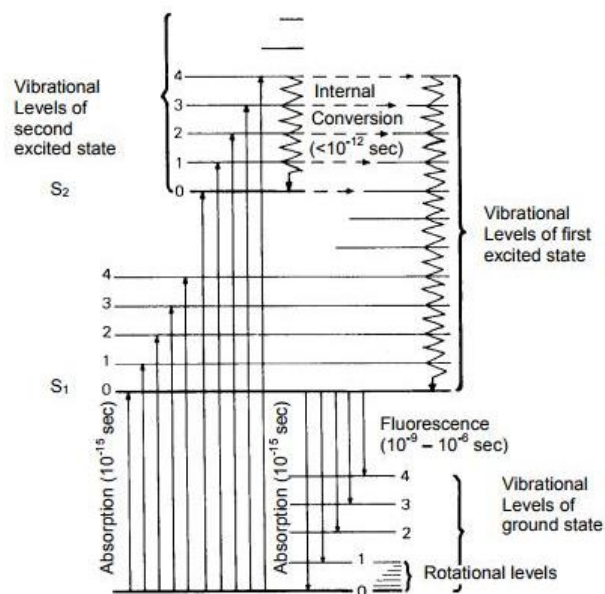
Figure 30 Transitions leading to fluorescence absorption and emission spectra [215]

The Jablonski diagram in Figure 30 shows the energy levels on the vertical axis, the bold lines represent the limit of a particular electronic transition, with the fine lines corresponding to vibrational levels, and between the bold and fine rotational levels can be represented. For clarity, not all lines are shown in Jablonski diagrams. Straight lines show the conversion between a photon and the energy of an electron, with curved or wavy lines representing non-radiative pathways.

Absorption of a photon of a particular energy promotes an electron from the ground state (this is usually the case as statistically most electrons occupy a low-lying energy state at room temperature). The absorption process is in the order of 10^{-15} seconds (1 femtosecond).

2.2.4.1.4.2 Excitation

Excitation can induce an electron into any of the vibrational energy levels associated with each electronic state. Although the energy is quantised, and the resultant absorption and emission bands should therefore be very narrow, this is rarely observed except in molecules that are rotationally inhibited such as planar configurations. In molecules with rotational freedom the number of potential absorption transitions is dramatically increased leading to broad absorption and emission bands (the resolution limits of the instrument does not allow these individual transitions to be detected individually).

As the electron is in an excited state in one of the higher vibrational levels, the excess energy begins to dissipate through intermolecular collisions. This culminates in the electron residing in the lowest vibrational level of the excited electronic state (e.g. S_1). From this state, the electron may return to any of the vibrational levels associated with the ground state (S_0) with the remaining excess energy being released as a photon, i.e. fluorescence.

There is one common transition in the excitation and emission spectra, from the lowest vibrational level in the ground state (S_0) to the lowest vibrational state in the first excited state (S_1). All other transitions require more energy to excite than to emit, i.e. other than the common transition, the emission spectrum will be of lower energy than the excitation spectra.

2.2.4.1.4.3 Emission

In an excited state energy can be dissipated in several ways, either through a radiative or non-radiative mechanism. Non-radiative decay occurs through vibrational relaxation, indicated by the wavy line in Figure 30, where the energy is shifted to the vibrational

modes within the molecule, or transferred to other molecules within the vicinity. This process occurs between 10^{-14} seconds (10 femtoseconds) and 10^{-11} seconds (10 picoseconds). This non-radiative decay occurs through vibrational levels, and only rarely through electronic transitions. If there is overlap between the vibrational levels and electronic level, an internal conversion process may occur. Internal conversion processes have a higher probability of occurring in the higher energy regimes, i.e. S_2, S_3, as the vibrational and energy levels have greater overlap. Due to the large energy, difference between the first excited state and the ground state internal conversion is unlikely to occur between these two energy levels and is therefore a slower process.

Radiative decay, the emission of a photon, or fluorescence occur in the order 10^{-9} seconds (nanoseconds) to 10^{-7} seconds (100 nanoseconds). Emission most frequently occurs between the first energy level and the ground state. Radiative decay and non-radiative decay are competitive processes, as the non-radiative decay mechanisms are orders of magnitude faster than radiative processes these tend to dominate at higher energy levels. Due to a large number of vibrational levels that can be coupled to the electronic levels, emission is distributed over a range of wavelengths.

Upon the promotion of an electron to a higher excited state, the spin of the electron is preserved, as most molecules have an even number of electrons that are arranged in pairs of opposite spin. It is possible for the spin of the promoted electron to be reversed, resulting in the molecule having two electrons of the same spin in different orbitals. In such a state, the molecule may be in three states of slightly different energies, a triplet state. The spin quantum number is $S = 1$ and as such the three values of the spin component correspond to $M_s = -1$, 0, and 1. Similar to fluorescence, phosphorescence

results in the emission of a photon, but involves an *intersystem crossing*. The electron

changes its spin state from an excited singlet to an excited triplet state. This is a slower

process than fluorescence, in the order of 10^{-4} seconds (100 microseconds) to 10^{2}

seconds. A schematic showing absorption, fluorescence, intersystem crossing and

phosphorescence is shown in Figure 31.
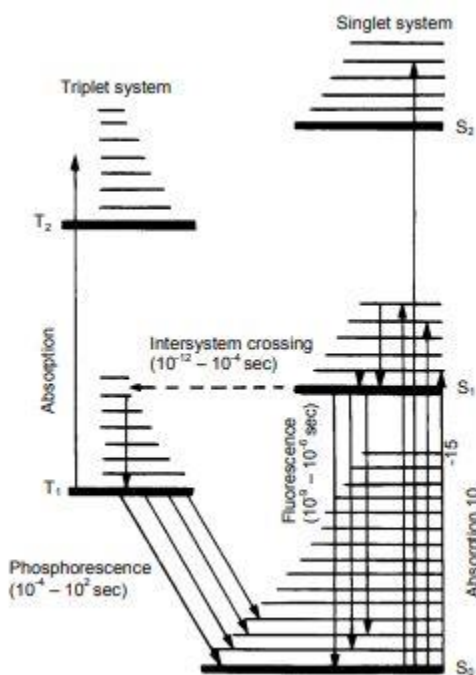
Figure 31 Jablonski diagram showing absorption, fluorescence, intersystem crossing, and phosphorescence

In the triplet state, relaxation to the ground state is a forbidden process, through coupling

of the vibrational modes into the selection rules, the transition becomes weakly allowed.

Intersystem crossing events are reversible and can lead to delayed fluorescence.

Phosphorescence leads to lower energy wavelengths than fluorescence as more energy

is lost during the intersystem crossing, and during the long lifetime in the triplet, state

energy can further dissipate through non-radiative decay mechanisms such as phonon

losses, bimolecular interactions or internal conversion. The difference in maxima between absorption of photons and emission is termed the Stokes shift. Anti-Stokes shift corresponds to an emission of photons of higher energy than the absorbed photon. The extra energy comes from phonon energy leading to a cooling of the sample; it may also arise from the absorption of two or more photons, i.e. an upconversion process.

2.2.4.1.4.4 Quenching

Fluorescence quenching is a process that leads to a reduction in intensity of fluorescence emission. This may occur through an increase of non-radiative decay mechanisms, competitive absorption of photons, bimolecular energy transfer. In silicate glasses, iron ions strongly quench UV induced fluorescence.

2.2.4.1.5 Glass Phonon Interactions

2.2.4.1.5.1 Crystal Field Theory

Absorption in the visible region gives rise to coloured glasses. D or F block elements colour glasses in a predictable way according to ligand field theory, an extension of crystal field theory with considerations of the effect of the metal-ligand covalent bonding.

Crystal field theory suggests a breaking of the orbital degeneracy of metal complexes due to the bonded ligands. The strength of the metal-ligand (M-L) bonds alters the energy of the system, which changes the photon absorption characteristics and ultimately the colour of the complex.

The approach utilised by crystal field theory follows Equation 12, where E is the bond energy between the charges, q_1 and q_2 are the charges of the ions and r is the distance separating them.

97

$$E \propto \frac{q_1 q_2}{r}$$

Equation 12

This leads to accurate predictions for large cations with low charge such as alkali metals as the orbitals are degenerate and symmetrical. However, for transition metals, the orbitals are not degenerate. Ligands interacting with the transition metal ion affect some orbitals more strongly than others dependent upon the geometry of the coordination complex. In a complex with octahedral geometry, ligands coordinate to the metal ion along the x, y, and z axes, thus stabilising the complex. The electrons in the $d_x{}^2\text{-}y^2$ and $d_z{}^2$ orbitals have greater repulsion. More energy is necessary to have an electron in these two orbitals, causing a splitting of energy levels in the d-orbitals shown in Figure 32.
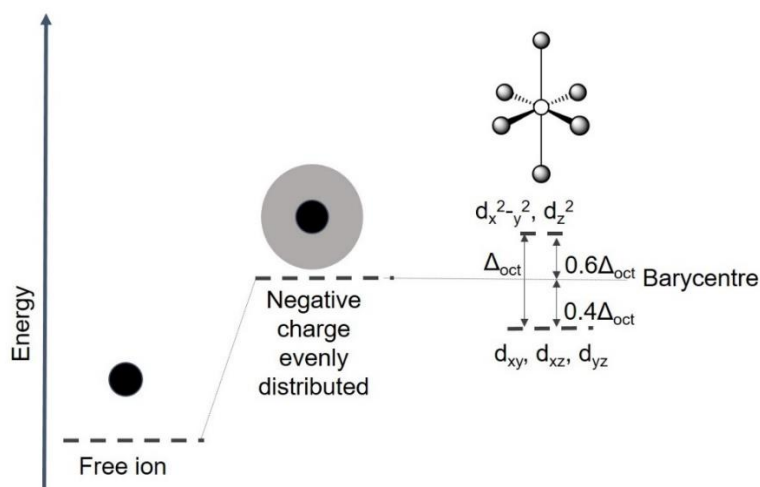
Figure 32 Crystal field stabilisation energy diagram for an octahedral complex

Electrons fill from the lowest energy orbitals to the highest energy orbitals according to the Aufbau principle, therefore the d_{xy}, d_{xz}, and d_{yz} (t_{2g} orbitals) will fill before $d_x{}^2\text{-}y^2$ and $d_z{}^2$ ($e_{.g.}$ orbitals). In a d^3 complex, the t_{2g} orbitals will each contain 1 electron. However, in a d^4 complex the electron may either fill a higher energy $e_{.g.}$ orbital or pair with an electron in the t_{2g} orbitals. If the spin pairing energy is lower than the crystal field, splitting, i.e. Δ

the electron will pair and the complex will be in low spin. Upon Δ being greater than the spin pairing energy the electron would be in a higher energy orbital and the complex be in high spin. The value of Δ is influenced by the cation, anion, ligand, interatomic distance, and the symmetry of the coordination complex.

As the charge on the metal ion increases, the value of Δ increases. The increase of charge on the metal ion causes the ligands to be more strongly attracted, and hence have a greater overlap of orbitals. The spectrochemical series highlights the effect on the value of the value of Δ.

$$I^- < Br^- < S^{2-} < Cl^- < F^- < OH^- < CO_3^{2-} < O^{2-} < SO_3^{2-}$$
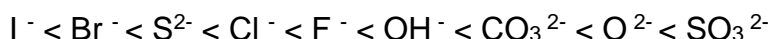
Ligands towards the left of the spectrochemical series are weak field as they are highly polarisable, due to a combination of their large volume and low charge. These produce little change in the value of Δ and generally form high spin complexes. Weak field strength ligands form high spin complexes, which absorb photons of higher wavelengths (red to IR), whereas strong field ligands tend to form low spin complexes with unpaired electrons and absorb low wavelengths (UV to blue photons). Iron in oxide glass tends to form high spin complexes, with different glass compositions and hence different ligands affecting the absorption profiles [208].

The interatomic distance of the metal ligand (M-L) bond affects Δ according to an inverse fifth-power law [216]. Therefore small variations in the M-L bond length strongly affects Δ. The charge, coordination and glass matrix all modulate the M-L interatomic distance. Techniques such as extended X-ray absorption fine structure (EXAFS) and neutron diffraction are used to determine the bond length of M-L bonds. Bismuth is often used

commercially in replacement for Pb due to similar glass forming properties. The stability against chemical reduction allows for control of the optical properties afforded through the incorporation of Bi [217]. EXAFS measurements estimate Bi^{3+} cations have an average coordination of between 5 to 7 with Bi-O bond lengths of typically 286 pm [218], whereas Pb^{2+} tends to have a more ordered structure with a 6-fold octahedral coordination with an average bond length of 233 pm [217]. The complex $[BiO_6]$ may be misleading as studies have shown non-uniform bond lengths relating to a distorted octahedron [219], the variation in bond lengths within such a complex affects the value of Δ.

In tetrahedral complexes, the four ligands are bonded to a central metal ion. The splitting is reversed relative to octahedral splitting due to poor orbital overlap, shown in Figure 33. The bonding orbitals are directed along the axis while the ligands are between the axis, and hence orbitals.

Figure 33 Splitting of d-orbitals due to octahedral ligand field (left) and tetrahedral ligand field (right)

For the same ligands, a tetrahedral complex will have a lower crystal field corresponding to $\Delta_{tet}=0.44\Delta_{oct}$. Due to this, Δ_{tet} is frequently smaller than the spin pairing energy, predominantly forming high spin complexes.

High spin complexes and low spin complexes have different values of Δ. A photon equal to the energy difference, Δ, can be absorbed, which promotes an electron to a higher energy level as demonstrated in Figure 34.
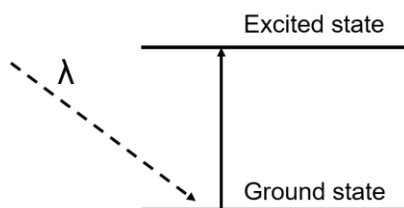
Figure 34 Absorption of a photon, inducing the promotion of an electron from the ground state to the excited state

Certain wavelengths of light are absorbed, causing the complex to appear coloured. A larger Δ results in the absorption of higher energy photons. If ions have a noble gas configuration such as Ti^{4+} ([Ar]) and / or have no unpaired electrons in the outermost shell e.g. Bi^{3+} ([Xe] $4f^{14}$ $5d^{10}$ $6s^2$ $6p^0$) the complex appears colourless as the absorption is centred within the UV portion of the electromagnetic spectrum.

2.2.4.1.5.2 Laporte Selection Rules

Selection rules for electronic transitions in metal complexes are governed by the spin selection rule given in Equation 13 and the orbital rule given in Equation 14;

$$\Delta S = 0$$

Equation 13

$$\Delta L = \pm 1$$

Equation 14

The spin rule dictates that transitions which involve the promotion of electrons which involve a change in their spin states are forbidden. The orbital rule stipulates that transitions within a set of orbitals, e.g. *d-d* or *f-f* transitions can be forbidden in a

centrosymmetric molecule such as in an octahedrally coordinated Fe^{3+} ion bonded to 6 oxygen atoms $[FeO_6]^{3-}$. The π-donating or π-accepting properties of ligands can hybridise with d or f orbitals resulting in transitions that are no longer purely d-d or f-f, and thus no longer violating the spin rule.

Relaxation of the rules can occur through spin-orbit coupling, which allows for the formation of weak, spin forbidden bands to arise. This coupling occurs between the spin and orbital momentum of an electron, giving the total angular orbital momentum quantum number, j. This type of coupling is also known as Russel-Saunders coupling. An electron with spin, S, is spinning upon its own axis inducing a magnetic field corresponding to μ. A second magnetic field is induced by the spinning electron moving around the nucleus. These two magnetic fields interact allowing for the absorption of a photon [220].

An octahedral molecule is never perfectly centrosymmetric due to thermal vibrations of the bonds, absorption of photons is possible during these moments of asymmetric stretching. This vibronic mechanism is only partially allowed according to the Laporte selection rules and therefore weak, but resolvable through luminescence excitation measurements [221]. Tetrahedral molecules have no centre of symmetry and have strong absorption bands due to the greater degree of d and p orbital hybridisation. The resulting absorptions may be 10-100 times more intense than from octahedral sites. Expected values of ε concerning various transitions are outlined in Table 4.

Ligand to metal charge transfer (LMTC) bands arise from the transfer of an electron from a ligand (in silicate glasses this is usually O^{2-}) to a d-orbital of a metal ion. As the distances involved in this transfer are large, there is a large dipole moment. This transition is allowed according to the orbital rule and the transitions are 2-3 orders of magnitude stronger than

d-d or *f-f* transitions. In the case of Fe^{3+} the tail of the LMTC extends into the visible from the UV and obfuscates some *d-d* transitions [56].

Table 4 Expected values of ε based on various transition types

Transition type	Example Complex	ε/m^2mol^{-1}
Spin forbidden, orbital forbidden	$[Mn(OH_2)_6]^{2+}$	~0.1
Spin allowed (octahedral complex), orbital forbidden	$[Ti(OH_2)_6]^{3+}$	1-10
Spin allowed (tetrahedral complex), orbital partially allowed (hybridised)	$[CoCl_4]^{2-}$	50-150
Spin allowed, orbital allowed (charge transfer bands)	MnO_4^-	$1000-10^6$

Inter-valence charge transfer bands involves the exchange of an electron between ions of the same element in different oxidation states, e.g. Fe^{3+} and Fe^{2+}. This occurs when polyhedra are edge sharing, this process can be induced by thermal effects or photon absorption. The strong coupling between the ferric and ferrous iron breaks the symmetry of the *d*-orbitals of the Fe^{2+} ion, allowing for *d-d* transitions and greatly intensifies the absorption.

2.2.4.1.5.3 Quantum Numbers

Four quantum numbers accurately describe the movement and trajectories of each electron within a molecule. The Pauli Exclusion Principle postulates all electrons contained within a molecule must have a unique combination of quantum numbers. The quantum numbers determines the electronic configuration of an atom and the probable location of the atoms electrons.

The principle quantum number, n, described the electron and the most likely distance from the nucleus. This determines the principle electronic shell, with increasing values of n the farther the electron is from the nucleus, and hence the larger the orbital in which the electron populates. The values of n can be any positive integer with $n = 1$ corresponding to the ground state. As an electron absorbs energy from a photon, the electron may be promoted to a higher energy level where $n = 2, 3, 4$ ..., a positive change in energy levels is associated with absorption and a negative change with emission.

2.2.4.1.5.4 Jahn Teller Effect

The Jahn-Teller effect results in a broad and asymmetric band due to distortions in the coordination polyhedra [179]. Orbitals are theoretically degenerate, i.e. have the same energy however, the molecule will spontaneously distort to where the degeneracy is removed and one energy level becomes more stable at the expense of another. Overall, this rearrangement allows a molecule to exist at a lower energy.

Jahn-Teller distortions are small in t_{2g} ground state orbital groups, such as that of Fe^{2+}. The theory allows for predictions in the splitting of energy levels upon absorption of a photon at higher energy levels. During the lifetime of the excited state the upper energy levels are split, this is known as the dynamic Jahn-Teller effect [222]. This leads to further asymmetry and broadening of bands, and is found in Fe^{2+} and Ti^{4+} containing oxide glasses frequently [223].

In the complex $[Fe(H_2O)_6]^{2+}$, the main spin-allowed band arising from the transition of $^5T_2(D) \rightarrow ^5E(D)$ centred at 10,400 cm^{-1} (961 nm) exhibits a dynamic Jahn-Teller effect typical of Fe^{2+} [59]. The peak displays two maxima separated by circa 2000 cm^{-1} (20 nm) [224]. The fine structure splittings arise from a combination of the crystal-field interaction

104

and the spin-orbit coupling of the central metal ion and the ligands, along with the Jahn-Teller couplings.

For octahedral coordination complexes, the expected magnitude of the separation induced by the Jahn Teller effect is given by Table 5.

Table 5 Strength of Jahn-Teller distortions as a function of d-electron count. s = strong, w = weak

Number of d-electrons	1	2	3	4		5		6		7		8	9	10
High / Low Spin				HS	LS	HS	LS	HS	LS	HS	LS			
Strength	w	w	-	s	w	-	w	w	-	w	s	-	s	-

2.2.4.1.5.5 Beer Lambert Law

The Beer-Lambert law given in Equation 15 gives the relation between the extinction coefficient (ε), a measure of the probability of an electronic transition occurring after irradiation, the concentration of the absorbing species (c), and the path length (l).

$$A = -\varepsilon c l$$

Equation 15

The Beer-Lambert law is limited in the range of concentrations available for measurements, >0.01M non-linearity occurs due to electrostatic effects associated with the increasing concentration of absorbing molecules. Further issues giving non-linearity include scattering from particles within the sample and luminescence, and for samples with a high refractive index.

2.2.4.1.5.5.1 Behaviour of Fe^{2+} and Fe^{3+}

As iron is the fourth most abundant element on earth, it is a chronic impurity in the glass making process, either from the raw materials of the glass, or from the refractory in the furnace. The concentration and valence of iron can dominate the resultant colour of silicate glasses. Glass manufacturers must carefully control both the concentration (often from the selection of purity of raw materials), and oxidation state. This is particularly pertinent to the production of solar glasses as visible and IR absorption reduce the efficiency of the module significantly. Only 0.10mol% of iron oxide in a soda lime silica glass can reduce the efficiency of the module by 1.1% [58].

Fe^{2+} dominates relative to the concentration of Fe^{3+} in silicate glasses prepared in a reducing environment (e.g. carbon crucible, H_2-N_2 environment [163]). The resultant glasses have strong IR absorption at ca. 9000 cm^{-1} (1100 nm), which allows for greater heat flux to the glass melt from the gas burners. However, due to the higher IR emission, the glass has a shorter working time than a glass with the equivalent concentration of ferric iron. Silicate glasses containing Fe^{2+} have an LMCT band at 42,400 cm^{-1} (235 nm) [163].

Fe^{3+} in silicate glasses has a complex absorption spectra, with six transitions between 21,200 cm^{-1} (471 nm) and 27,190 cm^{-1} (367 nm) and an LMCT band corresponding to O^{2-} →Fe^{3+} at 36,400 cm^{-1} (274 nm) [163,225].

In commercial glass manufacture a mixed valence of iron species is usually observed with the proportion of Fe^{2+} compromising between ca. 15-30% [163,225] which further complicates the absorption spectra. Solar glasses require low levels of either valence of iron, as Fe^{3+} parasitically absorbs visible photons, (however it does provide useful UV

protection), while Fe^{2+} absorbs IR photons which both increases the heat to the module whilst deleteriously affecting conversion efficiency.

2.2.4.1.5.5.2 Behaviour of Lanthanides

Lanthanides in silicate glasses have been extensively studied for their upconversion properties for solar energy, the reader is directed to the work by T. Fix et al [226] and the book by van Sark et al [53,212]. Lanthanides are used as dopants in glasses for luminescence downconversion front sheets. UV absorption from a codoped Nd^{3+} and Yb^{3+} transparent yttrium aluminium garnet glass ceramic leads to an emission of two NIR photons at 10,200 cm^{-1} (980 nm) [227]. The absorption and emission profiles of lanthanides tends to be narrow relative to *d* or *p* block metal ions, due to the crystal field splitting being small. Transitions between *f* orbitals are also forbidden due to the Laporte rule. However, as the *f-f* transitions are forbidden, upon absorption of a photon and the molecule placed in a higher energy state, decay to the ground state is slow making lanthanide-doped materials particularly useful for lasing applications, as population inversion is relatively easy to achieve.

2.2.4.1.5.6 Optical Basicity Scale

An important development by Duffy [228] aided in characterisation of the quantity of negative charge carried by O^{2-} ligands. Oxide glasses consist of acidic oxides such as SiO_2 and basic oxides such as alkali oxides and alkaline earth oxides. With increasing basicity, i.e. with more alkali and alkaline earth content, there is increasing negative charge on the O^{2-} ion. Probe ions such as Tl^+ or Pb^{2+}, which are isoelectronic, are modulated in their absorption spectra by a quantitative manner by the magnitude of the negative charge they receive from the O^{2-} ions.

Calculation of theoretical optical basicity (Λ_{th}) of an example SLS glass is given by Equation 16.

$$\Lambda_{th} = X_{SiO_2}\Lambda_{SiO_2} + X_{Na_2O}\Lambda_{Na_2O} + X_{CaO}\Lambda_{CaO}$$

Equation 16, Λ = optical basicity, X = molar fraction

The average optical basicity can be calculated for the bulk glass, as well as the local optical basicity to focus on particular sites within a glass [229]. Bridging and non-bridging oxygens have different basicities which can aid in characterisation of site specific phenomena [230].

2.2.4.1.5.7 Phonon

A phonon is a vibrational motion in which a series of atoms oscillates at a particular frequency. The emission of a photon causes an atom to be *pushed back* due to the conservation of momentum. Optical phonons such as these can be measured by Raman spectroscopy, for silicate glasses the phonon peak is considered to be the 1100 cm^{-1} peak corresponding to Q^3 speciation [231]. Phosphate or fluoride glasses have lower phonon losses and therefore a relatively higher fluorescence emission under the same conditions.

2.3 Conclusions

Due to increasing demands for cheap, carbon free electricity, solar photovoltaic energy has seen a dramatic increase in adoption across the world. Crystalline silicon based PV modules remain the dominant type due to the robust technology and sufficient cost per Watt for widespread adoption.

Unfortunately, over time modules containing polymeric compounds such as EVA glue and polymer backsheets undergo UV induced degradation which discolours the material. This

yellowing reduces the transmission of visible photons and subsequently reduces module efficiency. Ultimately, over prolonged time this may lead to critical failure and allow water to ingress into the module.

Absorption of deleterious UV photons within the glass front sheet therefore may protect PV modules from long term yellowing and damage. Incorporation of transition metal oxides in d^0 oxidation or post-transition metal oxides in s^2 oxidation can absorb UV photons in silicate glass front sheets. Furthermore, these oxides do not absorb in the visible region which would critically reduce module efficiency. The oxides emit visible fluorescence from UV excitation and may therefore enhance module efficiency by providing a marginally higher flux of visible photons.

3 Experimental Procedures

3.1 Glass Preparation

The initial glasses melted for this study had the nominal composition listed in Table 6. Raw materials of ≥ 99.9% purity sand (SiO_2), aluminium hydroxide ($Al(OH)_3$), magnesium carbonate ($MgCO_3$), calcium carbonate ($CaCO_3$), sodium carbonate (Na_2CO_3), and potassium carbonate (K_2CO_3) were dried for at least 24 hours at $110°C$ to remove moisture, then weighed and mixed in a polyethylene bag. Batches to produce 100 g of glass of the nominal composition outlined in Table 6 were melted in corundum (Al_2O_3) crucibles by ramping from room temperature to $1450°C$ at $5°C$/min with a dwell of 5 hours, before pouring into moulds on a steel plate and annealing at $530°C$ for 1 hour then cooling to room temperature to remove thermal stresses.

Table 6 Initial nominal glass composition

Oxide	Mol %
SiO_2	70.89
Al_2O_3	0.59
MgO	5.49
CaO	9.27
Na_2O	13.75
K_2O	0.01

The first glass melted (SLS1) corresponds to Figure 35. The glass had significant quantities of bubble remaining and a pink hue, from a selenium oxide impurity in the calcium carbonate as shown in the absorbance spectra in Figure 36 [232]. The peak

centred at 20,000 cm^{-1} (500 nm) corresponds to a characteristic weak absorption for molecular selenium, and calcium in the glass allows for greater retention of elemental selenium [233].

Figure 35 SLS1, pink discolouration and bubbles
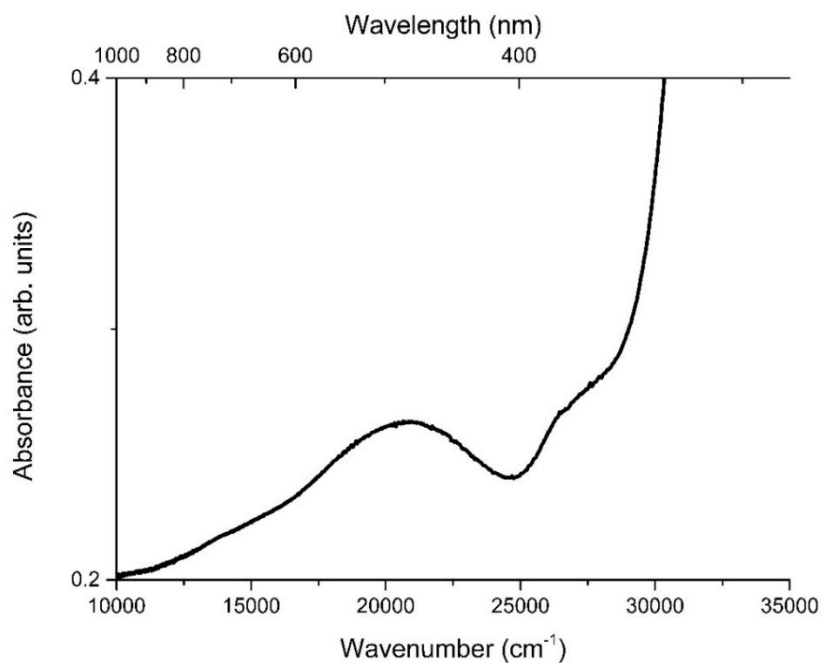
Figure 36 UV VIS NIR absorption spectra of SLS1

Glass produced with the composition in Table 6 melted at 1450°C result in a glass with significant levels of bubbles from a combination of lack of refining agents and bubbles introduced from dissolution of the corundum refractory crucible. Refining agents are utilised in the production of glass to aid in the removal of trapped gas bubbles. A refining agent is a material which thermally decomposes to produce large quantities of gas(ses) at a temperature below the liquidus of the resultant material. The large quantity of gas produced has a two-fold benefit; removal of small bubbles and aiding in homogenisation. A second glass was produced with the same melt quench anneal cycle incorporating 0.22mol% sodium sulfate (Na_2SO_4) into the batch in replacement of silica (SiO_2). A new, more pure source of $CaCO_3$ (≥99.9%, Better Equipped) was used to avoid the pink discolouration found in SLS1. The resultant material SLS2, shown in Figure 37 shows fewer and smaller bubbles relative to that shown in Figure 35.

Figure 37 SLS2, no pink hue, with bubbles remaining

To aid in the homogenisation a third glass was prepared containing two refining agents, sodium sulfate (Na_2SO_4) (0.22mol%) and table sugar ($C_{12}H_{22}O_{11}$) (0.22mol%) in

replacement of silica, were used. The two refining agents decompose at different temperatures, to aid in homogenisation over a wider temperature range. The resultant glass had very few bubbles remaining, shown in Figure 37.

Figure 38 SLS3, with bubbles remaining

A base glass utilizing the refining agent sodium sulfate (Na_2SO_4), with the composition outlined in Table 6 was prepared by melting in a zirconia grain stabilised platinum (ZGS-Pt) crucible. Use of the ZGS-Pt crucible afforded a bubble free and homogenous glass for optical and structural measurements.

3.1.1 Soda Lime Silica Glasses

For all soda lime silica glasses produced herein the standard procedure outlined below was used to prepare the materials unless stated otherwise for a particular glass. Batches to produce 100 g of glass were prepared by drying of the raw materials in a furnace at 120°C for 24 hours, then weighed and mixed in polyethylene bags to two decimal points

precision. The raw batch material was then added to the zirconia grain stabilised platinum (ZGS-Pt) crucible and added directly to the furnace set to 1450°C to melt and homogenise for 5 hours. The resultant glass was poured onto a steel plate in a steel ring and then annealed at 530°C for 1 hour before cooling to room temperature. This was the standard melt quench process for all glasses unless stated otherwise. Glasses for optical measurements were polished on both faces to a mirror finish with decreasing SiC grit sandpaper on a disk polishing machine to 1 μm grit, before a final polish with 1 μm CeO_2 powder in water. The melt quench process is outlined in Figure 39. Top left shows a homogenously mixed bag of constituent powders, top right shows retrieval of the crucible and glass contents after melting. Bottom left shows a recently poured silicate glass on a steel block, and bottom right shows the temperature of the glass cooling ready for annealing.

Figure 39 Melt quench process for the lab scale production of SLS glasses

3.1.1.1 d^0-ion Oxide Doped Soda Lime Silica Glasses

Seven d^0-ion oxide were prepared using the standard method. A doping concentration of 0.20mol% was selected for TiO_2, ZrO_2, HfO_2, Nb_2O_5, Ta_2O_5, MoO_3 and WO_3. TiO_2 and Nb_2O_5 were promising candidates for codoping to enhance fluorescence emission intensity. Nominal compositions are outlined in Table 7.

Table 7 Sample nominal and measured (XRF) compositions (mol%) and measured densities of d^0 SLS glasses

Sample	SiO_2	Al_2O_3	MgO	CaO	Na_2O	SO_3	Dopant	Density (g/cm³)
Base SLS	70.51 (72.00)	0.59 (0.48)	5.48 (5.01)	9.25 (9.13)	13.95 (13.20)	0.22 (0.18)	0.00	2.484
0.20 TiO_2	70.31	0.59	5.48	9.25	13.95	0.22	0.20	2.490
0.20 ZrO_2	70.31	0.59	5.48	9.25	13.95	0.22	0.20	2.497
0.20 HfO_2	70.31	0.59	5.48	9.25	13.95	0.22	0.20	2.501
0.20 Nb_2O_5	70.31	0.59	5.48	9.25	13.95	0.22	0.20	2.504
0.20 Ta_2O_5	70.31	0.59	5.48	9.25	13.95	0.22	0.20	2.518
0.20 MoO_3	70.31	0.59	5.48	9.25	13.95	0.22	0.20	2.493
0.20 WO_3	70.31	0.59	5.48	9.25	13.95	0.22	0.20	2.510

3.1.1.1.1 Codoped Glasses

3.1.1.1.1.1 Al_2O_3

To elucidate the effect of Al_2O_3 on the absorption and emission properties of TiO_2 and Nb_2O_5 in soda lime silica glasses, three glasses with 5.00mol% Al_2O_3 were prepared using the standard melt quench procedure. Nominal compositions of these glasses are given in

Table 8.

Table 8 Sample nominal compositions and measured (XRF) (mol%) and measured densities of Al_2O_3 SLS glasses

Sample	SiO_2	Al_2O_3	MgO	CaO	Na_2O	SO_3	Dopant	Density (g/cm³)
5.00 Al_2O_3	66.10 (68.52)	5.00 (5.03)	5.48 (5.22)	9.25 (8.94)	13.95 (13.55)	0.22 (<0.10)	0.00 (<0.10)	2.511
5.00 Al_2O_3 0.20 TiO_2	65.90	5.00	5.48	9.25	13.95	0.22	0.20	2.513
5.00 Al_2O_3 0.20 Nb_2O_5	65.90	5.00	5.48	9.25	13.95	0.22	0.20	2.522

3.1.1.1.1.2 ZnO

TiO_2 and Nb_2O_5 were codoped with 1.00mol% ZnO in replacement of MgO. A 1.00mol% ZnO base glass was also prepared as shown in Table 9.

Table 9 Sample nominal compositions (mol%) and measured densities of ZnO SLS glasses

Sample	SiO_2	Al_2O_3	MgO	CaO	Na_2O	SO_3	ZnO	Dopant	Density (g/cm³)
1.00 ZnO	70.51 (70.37)	0.59 (0.52)	4.48 (3.12)	9.25 (8.89)	13.95 (14.30)	0.22 (0.31)	1.00 (0.82)	0.00 (<0.10)	2.521
1.00 ZnO / 0.20 TiO_2	70.31	0.59	4.48	9.25	13.95	0.22	1.00	0.20	2.523
1.00 ZnO / 0.20 Nb_2O_5	70.31	0.59	4.48	9.25	13.95	0.22	1.00	0.20	2.521

3.1.1.1 Bi_2O_3 Doped Soda Lime Silica Glasses

Bismuth oxide doped soda lime silica glasses were produced in a ZGS-Pt crucible with the compositions outlined in

Table 10. A low iron (100 ppm Fe_2O_3) sand was used to prepare the series of glasses with different Bi_2O_3 contents.

Table 10 Sample nominal compositions (mol%) and measured densities of Bi_2O_3 doped SLS glasses

Sample	SiO_2	Al_2O_3	MgO	CaO	Na_2O	SO_3	Bi_2O_3	Density (g/cm³)
Bi 0.00	70.51 (72.00)	0.59 (0.48)	5.48 (5.01)	9.25 (9.13)	13.95 (13.20)	0.22 (0.18)	0.00	2.484
Bi 0.01	70.50	0.59	5.48	9.25	13.95	0.22	0.01	2.485
Bi 0.025	70.485	0.59	5.48	9.25	13.95	0.22	0.025	2.487
Bi 0.05	70.46	0.59	5.48	9.25	13.95	0.22	0.05	2.497
Bi 0.10	70.41	0.59	5.48	9.25	13.95	0.22	0.10	2.502
Bi 0.15	70.36	0.59	5.48	9.25	13.95	0.22	0.15	2.513
Bi 0.20	70.31	0.59	5.48	9.25	13.95	0.22	0.20	2.518

3.1.1.2 PbO Doped Soda Lime Silica Glasses

Lead oxide (PbO) was selected as a dopant due to the isoelectronic nature of Pb^{2+} and Bi^{3+}. Five glasses were prepared in Al_2O_3 crucibles ramped at 5°C/min to 1450°C with a dwell of 5 hours, all glasses were poured into a steel mould and annealed at 530°C for 1 hour. Concentrations of PbO, in mol%, were 0.20, 0.50, 1.00, 2.50 and 7.50 as shown in Table 11.

Table 11 Sample nominal compositions (mol%) of PbO SLS glasses

Sample	SiO_2	Al_2O_3	MgO	CaO	Na_2O	SO_3	PbO
0.00 PbO	70.51	0.59	5.48	9.25	13.95	0.22	0.00
0.50 PbO	70.01	0.59	5.48	9.25	13.95	0.22	0.50
1.00 PbO	69.51	0.59	5.48	9.25	13.95	0.22	1.00
2.50 PbO	68.01	0.59	5.48	9.25	13.95	0.22	2.50
7.50 PbO	63.01	0.59	5.48	9.25	13.95	0.22	7.50

3.1.1.3 Fe_2O_3 / Bi_2O_3 Doped Soda Lime Silica Glasses

Three glasses containing 0.20mol% Bi_2O_3 and 0.01mol%, 0.05mol% or 0.10mol% Fe_2O_3 to elucidate doping effects into representative style float glass systems were produced. Glasses were melted with the standard procedure, with the nominal compositions in Table 12.

Table 12 Sample nominal compositions (mol%) and measured densities of Bi_2O_3 / Fe_2O_3 SLS glasses

Sample	SiO_2	Al_2O_3	MgO	CaO	Na_2O	SO_3	ZnO	Dopant	Density (g/cm^3)
0.20 Bi_2O_3 / 0.01 Fe_2O_3	70.30	0.59	5.48	9.25	13.95	0.22	0.20	0.01	2.518
0.20 Bi_2O_3 / 0.05 Fe_2O_3	70.26	0.59	5.48	9.25	13.95	0.22	0.20	0.05	2.519
0.20 Bi_2O_3 / 0.10 Fe_2O_3	70.21	0.59	5.48	9.25	13.95	0.22	0.20	0.10	2.523

3.1.1.4 Fe_2O_3 Doped Soda Lime Silica Glasses

Three iron oxide doped glasses were prepared as models for solar glasses available within the photovoltaic industry. Doping concentrations, in mol%, of 0.01, 0.05 and 0.10 were used in this study, shown in Table 13.

Table 13 Sample nominal compositions (mol%) and measured densities of Fe_2O_3 SLS glasses

Sample	SiO_2	Al_2O_3	MgO	CaO	Na_2O	SO_3	Fe_2O_3	Density (g/cm^3)
0.01 Fe_2O_3	70.50	0.59	5.48	9.25	13.95	0.22	0.01	2.491
0.05 Fe_2O_3	70.46	0.59	5.48	9.25	13.95	0.22	0.05	2.492
0.10 Fe_2O_3	70.41	0.59	5.48	9.25	13.95	0.22	0.10	2.494

3.1.2 Borosilicate Glasses

Raw materials of ≥ 99.9% purity of sand (SiO_2), alumina ($Al(OH)_3$), sodium carbonate (Na_2CO_3), and bismuth oxide (Bi_2O_3) were dried at 120°C for at least 24 hours to remove moisture, then weighed and mixed before melting. H_3BO_3 was not dried at that temperature to avoid decomposition reactions occurring. Batches to produce 100 g of glass of the nominal compositions listed in Table 14 were melted in an alumina (Al_2O_3) crucible at 1450°C for 5 hours, before pouring into moulds on a steel plate and annealing at 500°C for 1 hour then cooling within the furnace to room temperature to remove thermal stresses. Samples were polished with decreasing SiC grit sizes to 1 μm, before a final polish of 1 μm CeO_2 for optical measurements; all other measurements were carried out using powdered glass, prepared in a vibratory disc mill. Due to the transparency of boron to X-rays these glasses were not analysed by XRF.

Table 14 Sample nominal compositions (mol%) of Bi_2O_3 Borosilicate glasses

Sample	SiO_2	Al_2O_3	B_2O_3	Na_2O	Bi_2O_3
Base Boro	65.00	1.00	16.00	18.00	0.00
0.01 Bi Boro	64.99	1.00	16.00	18.00	0.01
0.025 Bi Boro	64.975	1.00	16.00	18.00	0.025
0.05 Bi Boro	64.95	1.00	16.00	18.00	0.05
0.10 Bi Boro	64.90	1.00	16.00	18.00	0.10
0.15 Bi Boro	64.85	1.00	16.00	18.00	0.15
0.20 Bi Boro	64.80	1.00	16.00	18.00	0.20

3.2 Optical Measurements

3.2.1 UV Vis NIR Fluorescence Spectroscopy

3.2.1.1 Schematic of Instrument
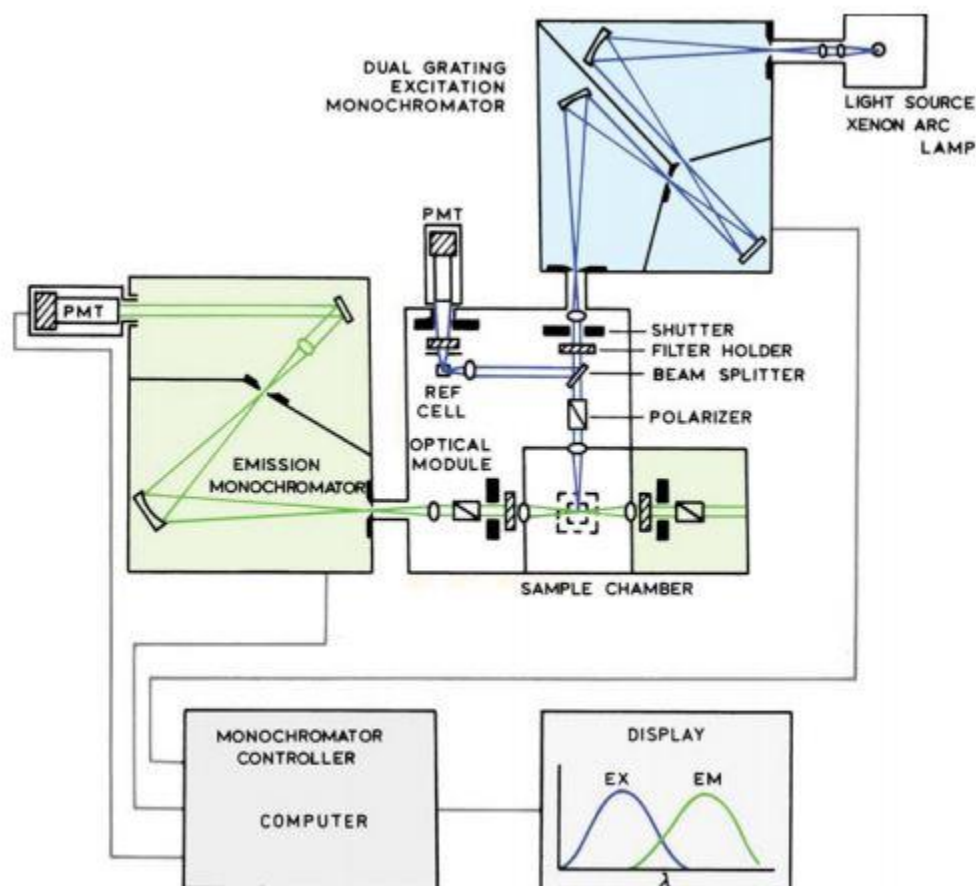
Figure 40 Schematic diagram of a spectrofluorometer (reproduced from [234])

Figure 40 shows a general schematic diagram of a spectrofluorometer, there are five

essential components, a light source, a grating to monochromate the incident source, a

sample holder / chamber, a second grating to filter stray light and a detector. In the case

of the Varian Cary Eclipse spectrofluorometer primarily used in this study the light source

was a xenon flash lamp. Xenon flash lamps confer several advantageous properties for

fluorescence measurements; the spectrum is broad and generally flat over the

wavelength range 50,000 cm^{-1} – 10,000 cm^{-1} (200-1000 nm), the short term stability is in the order of 2-3% difference of maximum power, and the drift or long term stability is in the order of 2000-3500 hours of operation.

The excitation grating minimises stray light, the degree of stray light is determined by the slit width selected, thinner slits result in a more spectrally pure light but with diminished intensity. The monochromators in the Varian Cary Eclipse spectrofluorometer use concave reflective surfaces fitted with a stepwise motor for fine control of the relative angles to control the wavelength of light passing to the sample. Due to small (2-3%) variations in the short term power output, a beam splitter made of quartz is used to direct approximately 4% of the photons to a stable fluorophore, with known emission characteristics which is detected by a photomultiplier tube (PMT). Changes in the short term intensity of the xenon flash lamp are then corrected by the software by dividing the intensity of the sample by the intensity of the fluorophore.

Lasers are often used in spectrofluorometers due to their small spot size and temporal coherence. Tuneable lasers are also frequently used but are limited to a wavelength range in the order of 200-300 nm, whereas flash xenon bulbs or mercury discharge may extend up to 2000 nm. Polarisers are available in some spectofluorometers for the detection of fluorescence anisotropy, as glasses in this study were homogenous this feature was not utilised.

The Varian Cary spectrophotometer used in this study uses photomultiplier tubes (PMT) for the detection of emitted photons. PMTs are current generators with the current proportional to the intensity of light. PMTs are vacuum tubes consisting of a photocathode followed by a series of dynodes shown in Figure 41.
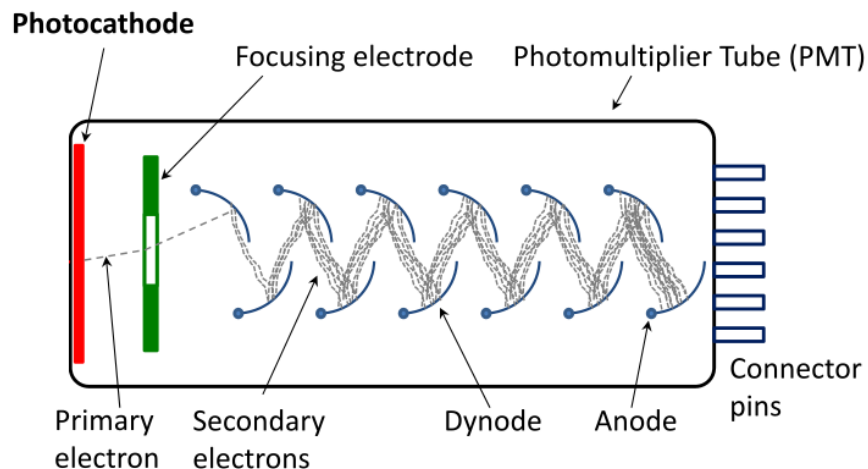
Figure 41 Schematic of a PMT. Modified for clarity from [235]

The photocathode is a thin film of metal, where upon photon absorption an electron is discharged from its surface. The electron is focused and directed towards the first dynode due to the photocathodes high negative potential. The dynodes are held at a negative potential, with each in succession having a potential closer to zero. Upon the primary electron colliding with the first dynode between 5 to 20 electrons are emitted and subsequently directed towards the second dynode. This process is repeated along the chain until the anode which records the current. Between 5^{12} and 20^{12} electrons are generated per single primary electron. This current is proportional to the intensity of incoming photons. To increase the gain, higher voltages can be applied across each dynode; this produces more secondary electrons per dynode, which allows for the detection of weakly emitting samples. However, careful control must be applied as to not increase the voltage and saturate the current carrying capacity of the PMT. This leads to saturation of the signal and meaningful data cannot be measured. An alternative detector would be a charge coupled device (CCD), these typically have 10^6 or more pixels. Since

each pixel acts as a detector, spatial measurements may be done to produce a two dimensional image.

All fluorescence measurements in this study were conducted on glass samples. A solid stage sample holder was used to maintain the sample within the beam pathlength. All samples were held at 30° to the incident beam to maximise signal output and minimise reflections to the detector. Not all samples were perfectly parallel and some degree of wedging was observed in the order of 5° from parallel due to the polishing technique utilised. This effect was minimised by adjusting the angle of the sample holder so all the surface of the sample was held to 30° rather than the sample holder itself. An angle of 45° should not be used due to the high flux of photons reflected directly towards the detector. A second set of monochromators is used to direct particular wavelengths to the PMT detector. The step size of these monochromators defines the resolution of the instrument and the integration time affects the total counts at a given wavelength.

The monochromators in a fluorescence spectrophotometer are used to separate polychromatic light into the desired wavelengths. In most commercially available spectrophotometers diffraction gratings are used rather than prisms. Diffraction gratings are characterised by their efficiency in separating particular wavelengths, and the magnitude of stray light levels. Slits control the intensity of light passing through the monochromators proportional to the square of the slit width. Slit widths are variable, with larger widths allowing for increased photon flux and hence increased signal levels. Conversely, smaller slit widths afford higher resolution at the cost of reduced intensity. Monochromators are either planar or concave gratings, schematically shown in Figure 42. Imperfections in the reflective surfaces are a source of stray light within a

spectrophotometer. A planar monochromator has three reflective surfaces, whereas the architecture for a concave affords one reflective surface, which minimises the stray light propagation, as a concave grating acts as both a diffracting and focusing element as shown schematically in Figure 42.
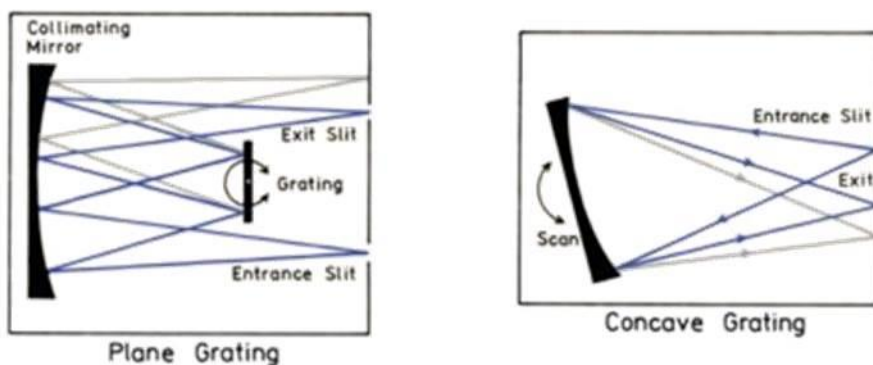
Figure 42 Planar (L) and concave (R) monochromator configurations

3.2.1.2 Stray Light

Stray light is any light that passes through the monochromator other than the wavelengths defined by the program. Reduction in the intensity of stray light is critical for the proper use of a spectrophotometer. The spectral output of a Xenon flash lamp in the visible may be as intense as the fluorescence emission to be measured therefore it is imperative to minimise the stray light through the use of a monochromator and bandpass filters.

3.2.1.3 Second Order Transmission

A particularly problematic source of stray light is second order transmission diffracted by the monochromator. This is where the monochromator cannot distinguish and separate multiples of the excitation wavelength, for example if the excitation wavelength is set to 300 nm, stray light may be detected at 600 nm, 900 nm etc. Bandpass filters are used to remove these undesirable wavelengths from the incident beam, and therefore not allow

their propagation through the instrument. This second order transmission is demonstrated in Figure 43. As multiples of λ propagate at a rate of 1/n times, monochromators cannot separate them through destructive interference.
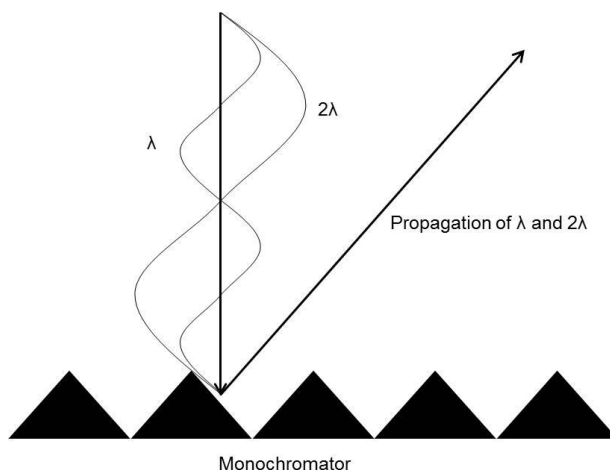
Figure 43 Second order diffraction of λ and 2λ wavelengths from a monochromator

An ideal spectrofluorometer would have a light source with a constant output of photons across the wavelength range required, monochromators which only allow for the wavelength of interest to pass through, and which transmits all photons equally and a detector which is equally sensitive to all photons. As this ideal spectrofluorometer has yet to be realised corrections are made within the instrument or software. However, even though the intensity from the excitation source is not linear and is corrected through the beam splitter and fluorophore, the response of both the detector and the reference material may vary over the excitation wavelengths available. The emission spectra may further be distorted from self-absorption in the sample. However, device independent spectra are rarely reported in the literature as most commercially available spectrophotometers show similar responses over a particular wavelength range due to

their similar components. Corrected spectra are needed for the calculation of quantum yields.

3.2.1.4 Operation of Instrument

An emission spectrum is measured across a range of wavelengths with a fixed excitation wavelength. Conversely, an excitation scan is a measure of the intensity of a fixed emission wavelength over a particular range.

There is a debate over the most appropriate units in which present excitation and emission spectra, either in nanometres (nm) or in wavenumbers (cm^{-1}), for the purposes of this study wavenumbers have been primarily reported, since wavenumbers are linear in energy, the scale of UV absorptions can be more clearly represented in this format. As the primary function of glasses produced in this study is to protect the polymeric components from UV damage the information is best presented in this manner. For convenience a nanometre scale is presented in graphs where appropriate. Wavelengths and wavenumbers are converted by taking the reciprocal of each value, for example 500 nm corresponds to (500×10^{-7} cm^{-1}) which is equal to 20,000 cm^{-1}.

Fluorescence measurements were collected on a Varian Cary Eclipse fluorescence spectrophotometer. Samples were held at 30° to the excitation source and scanned at 240 nm to 330 nm in 10 nm intervals, with the 360-1100 nm filter to remove excitation interference. All samples were scanned with 120 nm/min scan rate, with a data interval of 1 nm, and slit widths of 20 nm for excitation and 20 nm for emission; the detector voltage was set to 400 V. Excitation beyond 330 nm was not possible due to the bandpass filters transmitting wavelengths in the visible in the same magnitude as the fluorescence emission photons.

3.2.1.5 NIR Fluorescence Emission Spectroscopy

NIR fluorescence measurements were conducted on an Edinburgh Instruments FLS1000 spectrophotometer. Excitation between 43,500 cm^{-1} and 10,000 cm^{-1} (230 nm and 1000 nm) was from a 450 W ozone free Xenon arc lamp. Samples were excited between 13,300 cm^{-1} and 11,750 cm^{-1} (750 nm and 850 nm). Bandpass filters were not available on this instrument so second order transmission of the excitation wavelength is superimposed onto the emission spectra.

3.2.2 UV Vis NIR Absorbance Spectroscopy

3.2.2.1 Schematic of Instrument

UV-Vis-NIR absorption spectra were measured on a Varian Cary 50 Scan UV visible spectrophotometer over the range 200-1000 nm, at a scan rate of 60 nm/min with a data interval of 0.5 nm. NIR absorption spectra were measured using a Perkin Elmer Lambda 900 UV VIS NIR spectrophotometer, at a scan rate of 100 nm/min. Background removal for both instruments was carried out through measurement of the empty chamber, subtracted from the measurement. This removed the device interference from the absorption profile.
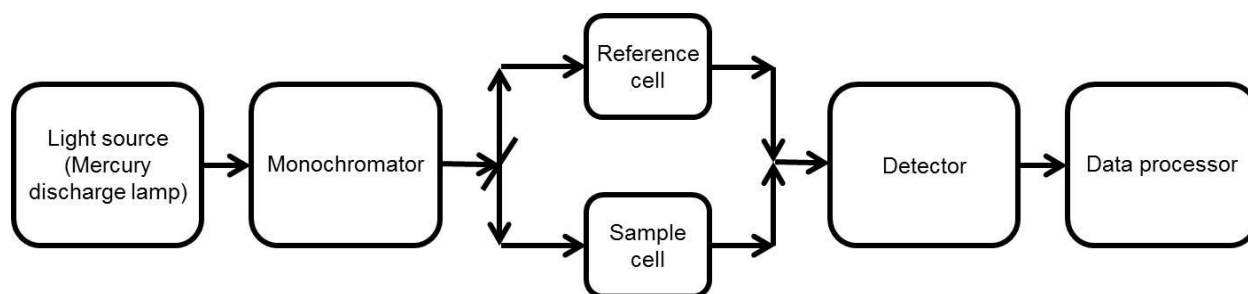
Figure 44 Schematic of a UV-VIS-NIR spectrophotometer

Shown in Figure 44, a UV-Vis-NIR spectrophotometer has a relatively simple design. Photons travel from the left to right in this schematic for the detection of absorbance bands. The Varian Cary 50 spectrophotometer used in this study uses a Xenon flash lamp as the light source which allows for a range between 50,000 cm^{-1} and 9090 cm^{-1} (200 nm to 1100 nm). The white light is then separated with a monochromator, which works identically to those found in a fluorescence spectrophotometer. The beam of photons is split with a beam splitter which sends a portion to a reference cell, the majority of the beam passes through a sample cell which attenuates some of the light. A reduction in intensity from the sample cell, relative to the reference cell, indicates absorption at that particular wavelength which is measured by the detector and sent to a data processor. Conventional UV-Vis spectrophotometers cannot measure above 50,000 cm^{-1} (below 200 nm) due to the absorption of molecular oxygen, measurements in the vacuum UV, as the name suggests, must be carried out under vacuum.

3.2.2.2 Operation of Instrument

UV-Vis absorption spectra were measured using Varian Cary 50 Scan UV visible spectrophotometer over the range 200-1000 nm, at a scan rate of 60 nm/min with a data interval of 0.5 nm.

NIR measurements were carried out using a Perkin Elmer Lambda 900 spectrophotometer over the range of 1000-2200 nm at a scan rate of 100 nm/min.

3.3 Structural Measurements

3.3.1 X-Ray Diffraction

3.3.1.1 Theory and Schematic of Instrument

X-Ray diffraction (XRD) is a technique used to determine the structure of crystalline materials in three dimensions. Diffraction is the slight bending of a wave of light around the edges of an obstacle, this is most pronounced when the wavelength of light and obstacle are of similar sizes. X-rays are able to be diffracted upon the atomic lattice of a crystal. This is because the interatomic distance of the lattice is on the same order of magnitude as the X-ray radiation, in the order of 1 Å.

Diffraction of an X-ray beam occurs when it interacts with the electron cloud of a material, the beam is partially scattered upon interacting with the first layer of the material, the beam is then partially scattered upon interaction with the second and third to n layers as shown in Figure 45.
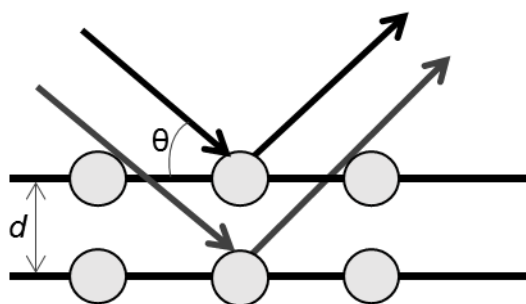
Figure 45 Bragg diffraction of X-rays striking planes spaced d apart at an angle of θ

If the diffracted beams are in phase, constructive interference occurs and a diffraction peak can be detected. However, if the diffracted beams are out of phase they destructively interfere and no peak may be detected. Only certain angles allow for constructive

interference to occur for a particular *d*-spacing according to Bragg's law shown in Equation 17.

$$sin\theta = \frac{n\lambda}{2d}$$

Equation 17 Bragg's equation of diffraction

Where θ is the angle of incidence of the X-ray, *n* is an integer, λ is the wavelength of the X-ray and *d* is the spacing between the atomic layers.

A simplified schematic X-ray diffractometer is shown in Figure 46. There are five essential components to generate a diffractogram. To generate X-rays a tube, containing a tungsten cathode and a water cooled copper anode, is held under vacuum. The cathode and anode have a large potential difference so when electrons are fired from the tungsten cathode they are directed rapidly towards the copper anode. The generated electrons are able to knock out a core electron from the copper atoms, as an electron in a higher valence drops to fill that energy level and emitting an X-ray.

K_α X-ray radiation is dominant from the emission from copper at a wavelength of 1.54 Å, however a second emission of radiation, K_β, with wavelength of 1.39 Å is emitted. K_β radiation is filtered using a nickel or iron filter; otherwise all peaks appear to be doublets in the resultant diffractogram. The K_α signal is monochromated using an appropriate slit, which reduces the intensity but also reduces the line width of the diffracted peaks. The beam is then diffracted due to the sample towards the detector, which are either PMT type detectors or based on semiconductor transducers.
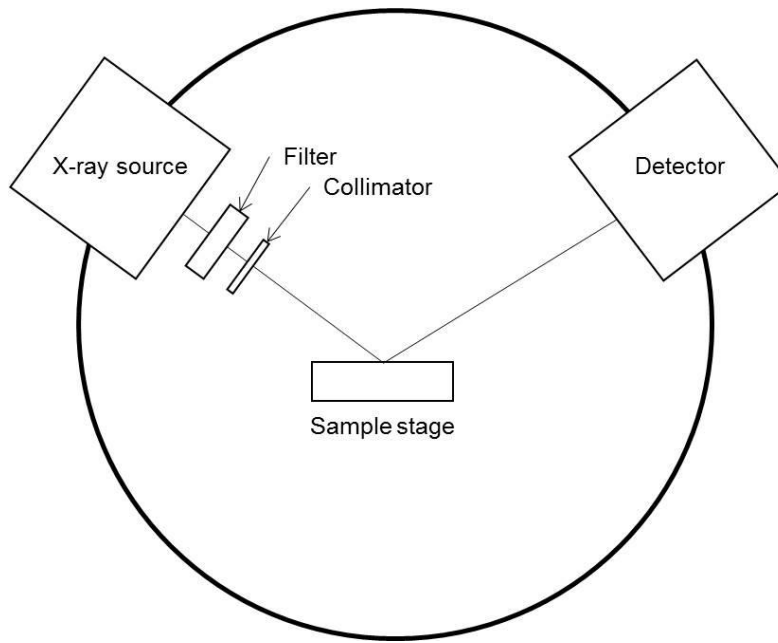
Figure 46 Schematic of an X-ray diffractometer

Amorphous materials do not have long range periodic order, which precludes the diffraction pattern from showing narrow, defined peaks. An X-ray diffraction pattern for a glass cannot be used to quantify the material, as would be possible in crystalline materials, but gives information regarding the glassy state and whether any crystallinity is contained within the material. Resultant diffraction patterns for an amorphous material are described as an 'amorphous hump' with few to no peaks as shown in Figure 47. This is contrasted to the heat treated glass ceramics with clearly defined sharp peaks.
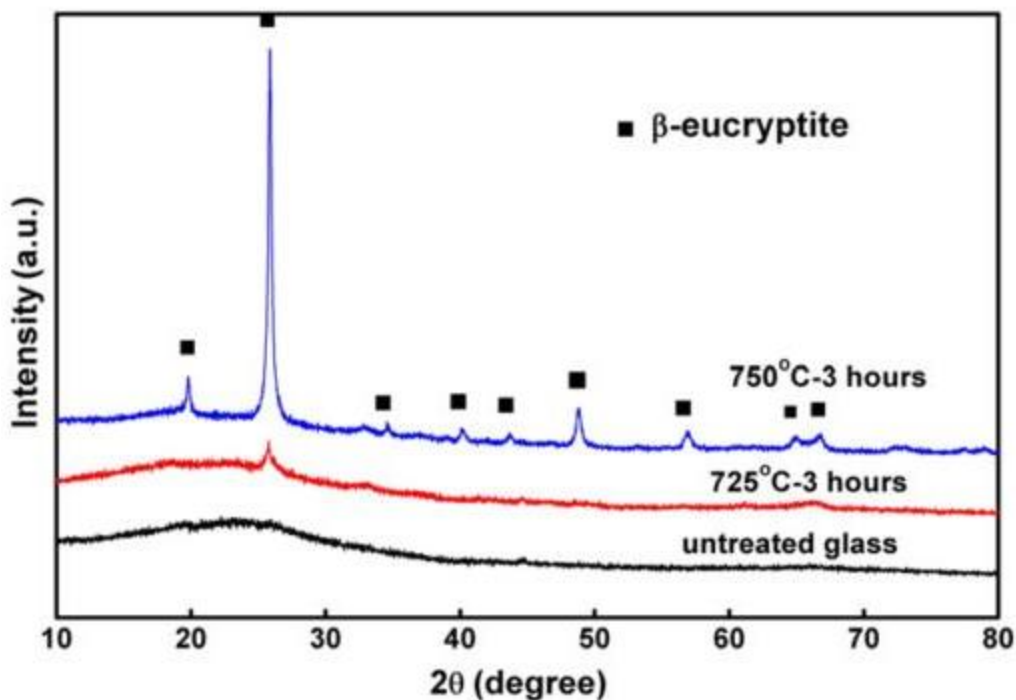
Figure 47 X-ray diffraction patterns of Bi doped glass and heat treated glass ceramics [236]

3.3.1.2 Operation of Instrument

XRD was carried out using a Philips X-Pert X-ray diffractometer, with Cu K_α radiation = 1.54 Å, working at 40 kV and 40 mA on a spinner stage with a step size of $0.001°2\theta$. Samples were measured between $10°$ and $80°$, 2θ. All samples were measured as powders prepared in a vibratory disc mill.

3.3.2 Raman Spectroscopy

3.3.2.1 Theory

Upon a compound being irradiated by a monochromatic intense light source, such as a laser, some of the light is scattered. Most of the light is scattered without a loss in energy, known as Rayleigh scattering, however, additional frequencies are symmetrically imposed above and below the Rayleigh line. The differences between the Rayleigh line

and those bands above and below correspond to Raman scattering from the vibrational frequencies in the compound.

Raman spectroscopy is not an absorption effect but is dependent on the polarisability of a bond. The photon interacts with the bond of a molecule and distorts the electron(s), promoting them to a virtual excited state, see Figure 48. Upon returning to a lower state there is a difference in energy corresponding to a Raman shift. Stoke Raman shifts are more commonly measured than anti-Stokes Raman shifts, as at RT most electrons are in the ground state.
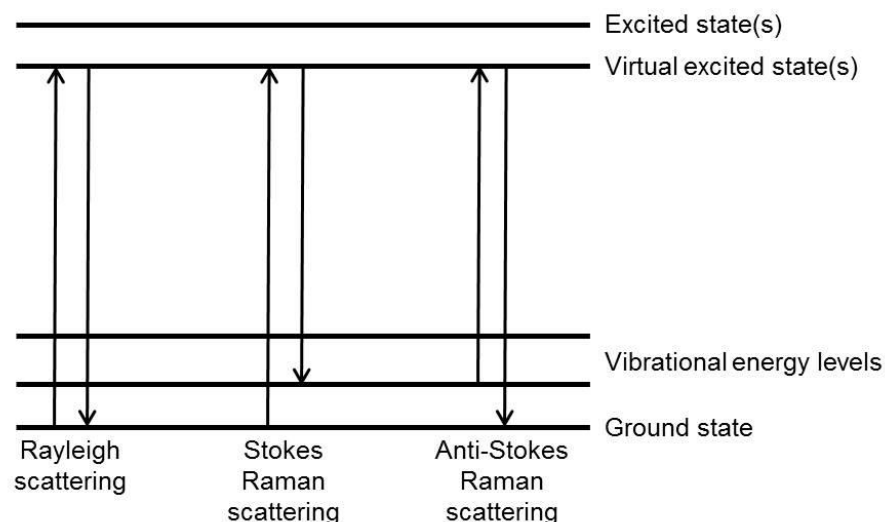
Figure 48 Rayleigh, Stokes Raman and Anti-Stokes Raman scattering energy diagrams

3.3.2.2 Operation of Instrument

Raman spectroscopy was carried out using a Thermo Scientific DXR2 Raman spectrometer, using a 532 nm laser with a power of 10 mW in a depolarised configuration. The aperture was set to 50 µm slit, with an estimated spot size of 0.7 µm. Scans were carried out over 20 seconds with 20 exposures each with a 10x objective lens, with

fluorescence correction. Measurements were done on flat polished samples. Using ThermoFisher Omnic software baseline corrections were done to remove the tilt associated with it. This was done within the software by clicking on portions of the spectra, at both the beginning and end of the spectra and any points between which deviate from a zero line. The software then brings the clicked points to zero and 'pulls' down portions around to more accurately represent a flat spectrum. Through proper use of this function peaks may be more clearly observed. Fluorescence correction was also applied within the software program, this was completed by inputting the emission wavelengths from the excitation from the laser which was subsequently removed to allow clearer observation of peaks. Post processing was done by subtraction to observe any additional peaks by normalising the largest peak in the spectra to 1.0. All traces were done in this manner and doped spectra were subtracted with the base glass spectra.

3.3.3 X-Ray Near Edge Absorption Spectroscopy

3.3.3.1 Theory and Schematic of Instrument

Strong monochromatic X-rays have sufficient energy to excite a core electron within an atom to an excitonic state. Different core electrons require distinct energies to excite due to their binding energies, so element specific measurements can be made. The absorption edge corresponds to the absorption of an X-ray photon by a specific core electron shell as shown by

Table 15.

Table 15 Absorption edges and the corresponding principle quantum number

K Edge	1s			
L Edge	2s	2p		
M Edge	3s	3p	3d	
N Edge	4s	4p	4d	4f

The absorption edge has complexity called pre-edge structure which correspond to 1s to nd (where n=2, 3, 4, or 5) transitions. The pre-edge structures are conventionally within 50 eV of the absorption edge. The pre-edge structure and absorption edge confer information relating to the oxidation state of the atom as with increasing oxidation the absorption energy increases. In an electrostatic model, atoms with a higher oxidation state require X-rays of greater energy to excite the core electron as the nucleus is less shielded and has a higher effective charge. It is also possible to derive 3-dimensional structure of an atoms environment. The XANES pre-edge structure is sensitive to small variations in geometry of the absorbing atom.

As shown in Figure 49 a beam line monochromates the X-ray beam towards an end station which contains the sample holder and then detector, along with shielding for the protection of the user. The X-ray source is most frequently a synchrotron, although laboratory scale X-ray sources have been successfully used in the past. The path of photons passes through mirrors and gratings to modulate the width of the energies available at the end station.
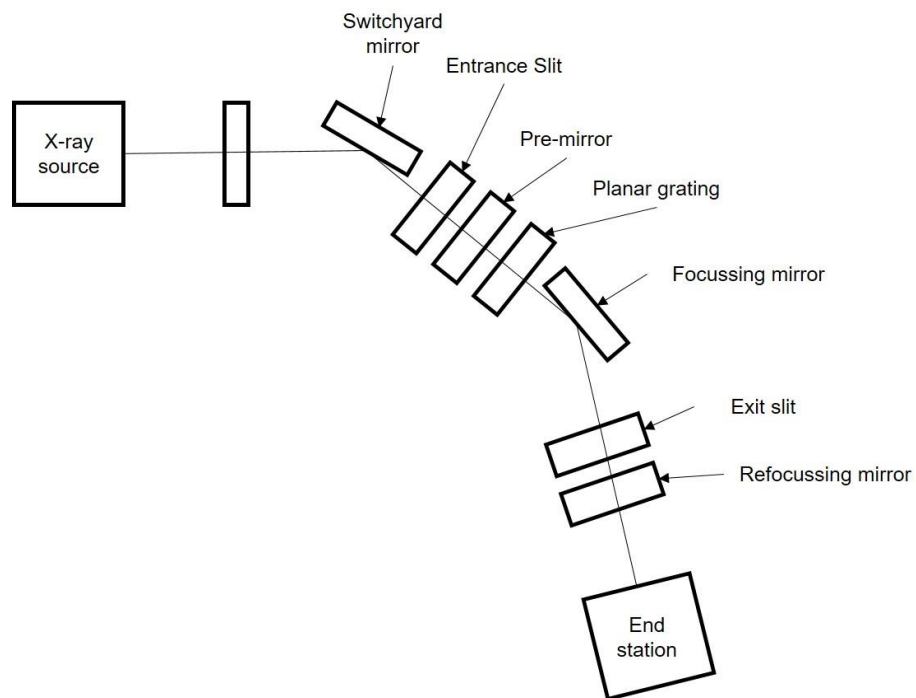
Figure 49 Standard beam line schematic, end station contains sample holders / detectors relevant to experiment

3.3.3.2 Operation of Instrument

The Bi(L_{III}) edge at 13,418 eV XANES measurements were performed at the European Synchrotron Radiation Facility (ESRF) in the BM26A beam line using a Rh harmonic mirror. Transmission measurements were recorded using Bi metal, Bi_2O_3 and $NaBiO_3$ as reference materials indicating Bi^0, Bi^{3+} and Bi^{5+} respectively. All measurements were done on powders diluted with cellulose pressed into pellets. Data was corrected and analysed using the ATHENA and ARTEMIS XAS software package [237]. XANES measurements were collected on behalf of the author by colleagues from SHU.

3.3.4 Electron Paramagnetic Resonance Spectroscopy

3.3.4.1 Theory and Schematic of Instrument

Electron paramagnetic resonance (EPR) is a spectroscopic tool based on the absorption of microwaves by unpaired electron(s) tuned by an external magnetic field. An electron has spin and therefore a magnetic moment, and will precess in an applied magnetic field, and will undergo transitions in spin states upon energy of the correct frequency being applied. An EPR spectrometer can detect molecules containing an electron with unpaired spin. The magnetic moment of an electron is principally contributed by the spin magnetic moment, while the orbital magnetic moment provides a smaller contribution. The spin magnetic moment is shown by Equation 18.

$$M_S = \sqrt{S(S+1)}\frac{h}{2\pi}$$

Equation 18 Electron spin magnetic moment

Where, M_s is the total spin angular moment, S is the spin quantum number and h is Planck's constant. The M_s component has 2S+1 different values, so for a single electron only the two values of M_s equalling +1/2 or -1/2 are possible.

In EPR a sample is held in a magnetic field while microwave radiation is applied monochromatically over a between 300-400 GHz. The microwave energy is monitored to detect absorbance corresponding to an electron the promotion of an electron from the lower energy m_s=-1/2 to the more energetic m_s=+1/2 as shown in Figure 50. In the presence of a magnetic field the difference in energy states is given by Equation 19.

$$\Delta E = h\nu = gu_B B_0$$

Equation 19

Where, g=2.0023 for the free electron, u_B is the Bohr magneton, and B_0 is the external magnetic field.
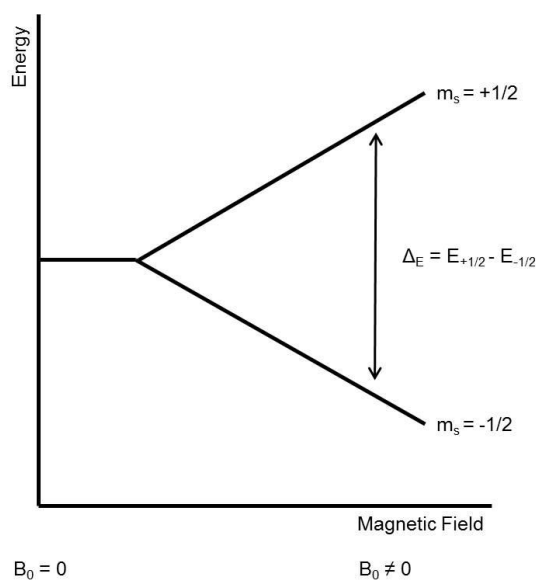
Figure 50 Resonance of a free electron

As shown in Figure 51 an EPR spectrometer has a microwave source which is directed towards the sample, held between two magnets, which is then directed back towards a detector. The magnetic flux experienced by the sample is held constant whilst the microwave radiation is modulated.
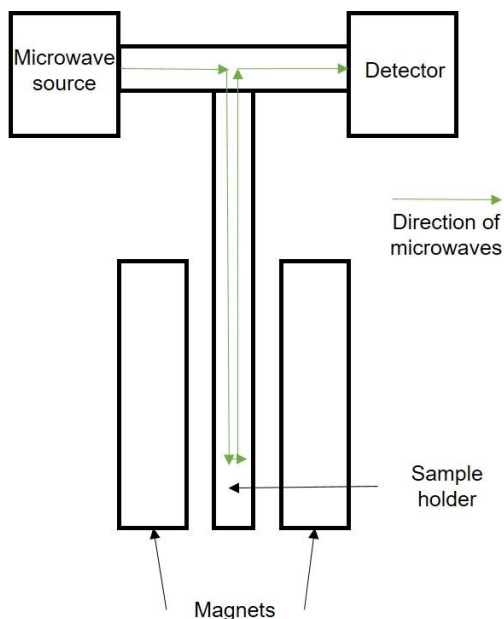
Figure 51 Schematic of an EPR spectrometer

3.3.4.2 Operation of Instrument

There are several commonly used microwave bands used in EPR spectroscopy, in this study all measurements were conducted in the X-band frequencies, circa 9.5 GHz. EPR measurements were obtained using a Bruker EMX Premium X EPR spectrometer at the national EPR facility and service at the University of Manchester. Powdered samples were measured in silica capillary tubes at room temperature (20°C) at X-Band frequencies (~9.80 GHz). Magnetic power was adjusted to collect convenient signal-to-noise ratios without saturation.

3.4 Chemical and Physical Measurements

3.4.1 X-Ray Fluorescence Spectroscopy

3.4.1.1 Theory

X-Ray fluorescence (XRF) is a process wherein X-rays ionise an atom by exciting a core electron, the subsequent cascade of electrons from higher shells and emission of K_α and K_β X-rays is detected as shown in Figure 52. The energy of a particular electron depends on the shell and which element is bound to, the X-ray emission characteristics are determined by the difference in energy levels. The fluorescence emission for a particular element has a discrete energy and hence the concentration of each component can be calculated from the total photon count. In wavelength dispersive XRF the emission is collimated by crystals or monochromators, this step affords greater resolution at the expense of wavelength range.
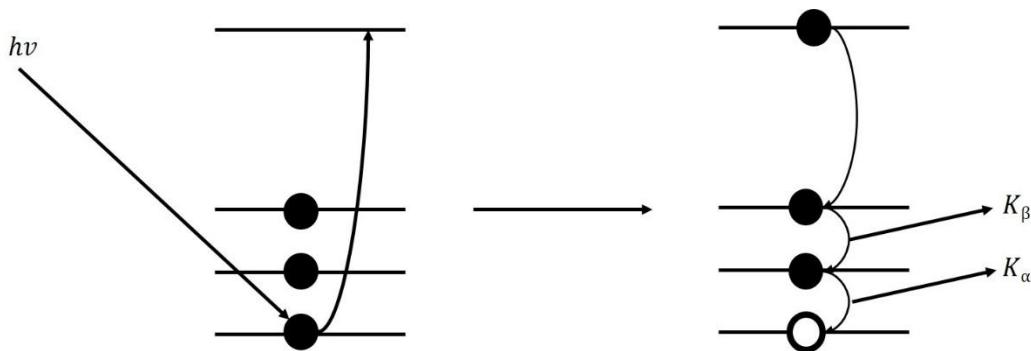
Figure 52 Excitation of a core electron and subsequent cascade and X-ray emission

Wavelength dispersive XRF spectrometers can detect from PPM to 100% elemental analysis from carbon to americium. Lighter elements including boron and lithium are effectively transparent to XRF due to their low energy levels in which the generated photons are reabsorbed readily.

3.4.1.2 Operation of Instrument

The chemical composition of the prepared base glasses were analysed using a Phillips Magix Pro X-Ray fluorescence spectrometer and a Panalytical Axios Fast fluorescence spectrometer in a 1:10 sample to lithium tetraborate flux ratio as a fused bead. Beads were melted in a Pt/5%Au crucible at 1065°C for 15 minutes before being air cooled. Scans were carried out on the SuperQ 3-IQ+ software in the oxide setting. Uncertainties in XRF analysis results are conservatively estimated to be ±2% of the measured concentration.

3.4.2 Density Measurements

Densities of all glasses were measured on samples of 10-30 g bulk glass using the Archimedes method in deionized water. This involved weighing the sample in air and in distilled water at a known temperature (room temperature, 20°C) then performing the calculation given in Equation 20.

$$\rho_{glass} = \frac{W_a}{W_a - W_w} \cdot \rho_{water}$$

Equation 20 Calculation of density of glass by Archimedes method

Where; ρ_{glass} is the density of the glass, ρ_{water} is the density of water at 20°C, W_a is the weight in air of the glass, and W_w is the weight in water of the glass. Samples were measured in triplicate and averaged.

3.4.3 Differential Scanning Calorimetry

3.4.3.1 Theory and Schematic of Instrument

Differential scanning calorimetry (DSC) is used to quantify the heat change during a chemical or physical process. In DSC, as shown in Figure 53, a sample and reference pan are heated equally, as measured by thermocouples. Differences in the required heat flux are shown on a thermogram, corresponding to physical or chemical reactions. In this study the glass transition temperature, T_g, was of most interest.
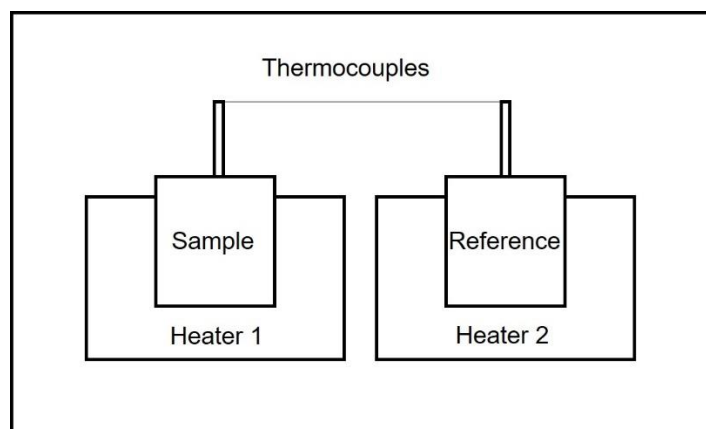
Figure 53 Schematic of a DSC instrument

Thermograms corresponding to the difference in heat flux applied to the sample and reference pans, in an exothermic reaction such as crystal formation less heat energy is applied to the sample pan, the reverse is true for an endothermic reaction such as melting.

3.4.3.2 Operation of Instrument

10-15 mg of powdered sample was heated from 50°C to 725°C at a rate of 10°C/min in a Pt sample pan using a Perkin Elmer DSC 8000 differential scanning calorimeter. An empty Pt sample pan was used as the reference. N_2 flow of 20.0 ml/min was used to aid in heat conductivity whilst remaining inert at higher temperatures.

3.5 Preparation of Photovoltaic Modules

Glasses of the composition outlined in Table 16, were melted in Pt crucibles at 1450°C for 5 hours. A steel mould was heated to 550°C, along with a steel press. The glass was poured into the mould, the schematic of which is outlined in Figure 54. Due to the high viscosity of other SLS melts within this study being prohibitive for the preparation of large 7 cm^2 plates ca. 2mol% of Li_2O was added to reduce the viscosity while maintaining the same melt temperature. Excess glass flowed out of the overflow channels to afford a 70x70x4 mm^3 glass plate. The glass monoliths were then annealed at 530°C. These glasses were prepared at Johnson Matthey, Sonning Common, UK, with B. Allsopp and a consortium member. Following cooling to RT, the samples were polished to 1 μm CeO_2, and sent to Solar Capture Technologies, Blyth, UK.

Table 16 Sample nominal compositions (mol%) of SLS glasses for PV modules

Name	SiO$_2$	Al$_2$O$_3$	MgO	CaO	Na$_2$O	Li$_2$O	Na$_2$SO$_4$	Bi$_2$O$_3$	Gd$_2$O$_3$
LIMES A	69.29	0.58	5.38	9.09	13.48	1.96	0.22	0.00	0.00
LIMES B2	69.09	0.58	5.38	9.09	13.48	1.96	0.22	0.20	0.00
LIMES BG A, B, C	69.09	0.58	5.38	9.09	13.48	1.96	0.22	0.10	0.10
LIMES B2G2	68.89	0.58	5.38	9.09	13.48	1.96	0.22	0.20	0.20
LIMES B2G A, B	69.99	0.58	5.38	9.09	13.48	1.96	0.22	0.20	0.10

A base glass was prepared LIMES A, along with seven other glasses containing proportions of Bi_2O_3 and Gd_2O_3 as outlined in Table 16.

Increasing the temperature to lower the viscosity was considered but not done due to the redox effect of polyvalent elements. The low addition of Li_2O was less likely to affect the redox of Bi_2O_3 than increasing the temperature of the melt.
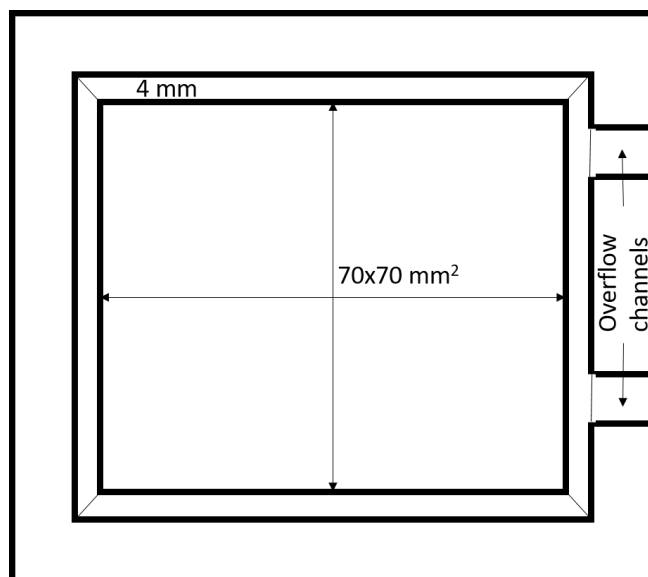
Figure 54 Steel mould schematic

Solar modules were prepared at Solar Capture Technologies. C-Si was tabbed with silver paste, a Tedlar® backsheet, EVA glue, and the glass front sheet were cured together using Solar Capture Technologies standard commercial procedure as shown in Figure 55. As this is commercially sensitive it is not outlined herein. A commercially available float glass SLS was prepared into a PV module in the same manner as a baseline.

Electroluminescence measurements and efficiency measurements were taken on a solar simulator device with 1.5AM illumination as stated in [18]. Both the string and module were measured to compare differences corresponding to the processing. In some cases the lamination process would crack the string resulting in a lower surface area for the collection of photons, and therefore, a lower apparent module efficiency.

Figure 55 Typical PV module prepared at Solar Capture Technologies, Blyth, UK

4 Structural, Chemical and Optical Properties of Doping Silicate Glasses With d^0-Ion Oxide Transition Metals for Photovoltaic Applications

4.1 Introduction

Recent research in spectral modification for photovoltaics has been primarily focussed on glasses doped with lanthanide elements [83,238–240]. This interest has been predominantly in upconversion of IR wavelengths to visible wavelengths [22,53,241]. Rare earth elements tend to have sharp absorption and transmission peaks, and are not particularly beneficial for the protection of polymeric species because of this. Doping of luminescent front sheets with transition metals has been infrequently studied as many transition metals produce strong and broad d-d absorption bands in the visible and near-IR ranges, particularly from Fe_2O_3 [242] and chromium oxides [243]. These absorptions negatively affect the efficiency of PV modules due to parasitic absorption of photons which may have been converted into electricity [58].

Currently critical failure of c-Si PV modules is often caused through the ingress of water after delamination occurs [29,30]. This reduces the total lifetime of PV modules, and therefore increases the cost per watt across the service lifetime of the module. Dependant on manufacturer, location, and other environmental conditions the service lifetime of a PV module is expected to last between 20-25 years. Degradation occurs as soon as the module is mounted and subject to UV irradiation, with module efficiency degrading with a median value of 0.5% per year [244] from the yellowing of the EVA glue [20,68] which reduces the transmission of visible light.

Absorption of UV photons, therefore, may protect PV modules from UV induced degradation. Critically the absorption cannot be within the visible and NIR where the

semiconductor material absorbs as this will lower module efficiency significantly, up to 1.1% for 0.01mol% Fe_2O_3 SLS front sheets due to these absorption [58]. However, particular metals in certain oxidations states, notably those with a d^0 configuration [74,78,245], have a full outer electron shell, which has traditionally been thought to hamper electronic transitions, produce no d-d absorption bands in the visible or near-IR [246,247] but fluoresce in the visible under UV excitation [179,191,248].

From this it was hypothesised that such a dopant at low concentration may prove beneficial for doping PV front sheets as the visible and near-IR absorption would be minimised whilst the beneficial UV absorption would be increased. Furthermore, the glasses would demonstrate a downconversion or fluorescence emission within the visible range to further enhance efficiency of a PV module. Emission of 1mol% d^0 transition metal oxide has been demonstrated to emit within the visible, from UV excitation [74]. However, the comparatively high doping concentration used within that study would prove costly for full scale production for PV front sheets. Only a few studies [74,78,179,245] have investigated the phenomenon of downconversion and fluorescence emission of d^0 ions in silicate glasses. There is extensive literature concerning d^0 fluorescence in crystalline materials [249–253] and thin films for solar harvesting [254–256], which demonstrate broadband visible emission from UV excitation.

The low doping levels used within this study potentially confer two benefits: (i) relatively low additional raw materials cost due to the low level of additions; and (ii) may enable technologically achievable melting in float glass plants due to minimal changes in composition. By modifying the cover glasses in PV modules, an efficiency increase can be envisaged, along with protecting the polymeric glues from UV light degradation. In this

work, the structural, chemical and optical effects of adding low doping levels of d^0 transition metal ions in a representative soda-lime-silicate (SLS) float glass system have been investigated.

4.2 Results
4.2.1 X-Ray Diffraction
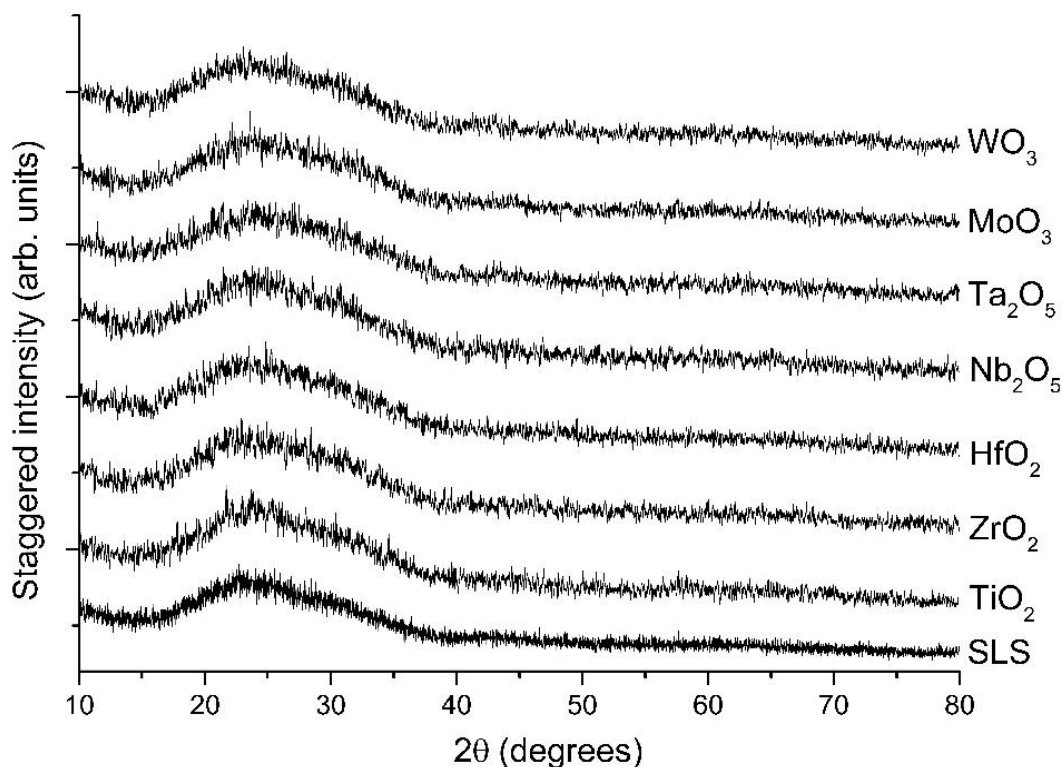
Figure 56 X-ray diffraction patterns of d^0 doped and base SLS glasses

XRD patterns for the base and 0.20mol% d^0 oxide doped glasses are shown in Figure 56, all patterns are consistent with an amorphous silicate structure, with none showing sharp Bragg diffraction peaks. All display a broad amorphous hump centred at ca. 25 °2θ.

Through neutron diffraction and NMR studies it has been shown Si-O bond lengths do not vary greatly relative to SiO_2, however the range of bond angles and different Q^n speciation result in the observed glassy structure. No crystallisation is observed in these glasses, however surface and bulk crystallisation has been demonstrated in $60SiO_2$-$20Al_2O_3$-$20MgO$ glasses incorporating 0.20mol% MoO_3 [257], this glass was melted under reducing conditions and then subsequently heat treated. Transition metals of d^0 electronic configurations have the propensity for crystal nucleation in glasses due to their large ionic radii, high charge density and predilection for clustering [129]. However, the doping concentrations used in this study are below thresholds for crystallisation observed in other studies [258,259]. 0.10mol% Nb_2O_5 in lithium disilicate glass slightly decreases the steady state nucleation rate, resulting in fewer crystals developing relative to the base glass [259]. Crystals are unlikely to form in the glasses produced as the dopants are dilute, the glass was not heat treated, and soda lime silica glasses do not tend to crystallise without sufficient nucleation points (such as lithium disilicate [260]).

4.2.2 Raman Spectroscopy

Raman spectra of base and doped glasses are shown in Figure 57. Each trace is composed of five main peaks, consistent with other float and soda lime silica systems [261,262]. Samples doped with Nb_2O_5 and MoO_3 have an additional peak highlighted by ● and ■ respectively. The peak centred at 875 cm^{-1} corresponds to $[NbO_6]$ octahedra which have a higher Raman cross section relative to the glass matrix. Due to the high Raman cross section of $[NbO_6]$ octahedra the peaks are detectable at low (>0.10mol%) concentrations in SLS glasses [263,264]. The additional bands from NbO_6 octahedra are

also present in both the Al_2O_3 and ZnO co-doped sample Raman spectra, shown in Figure 58 and Figure 59 respectively.
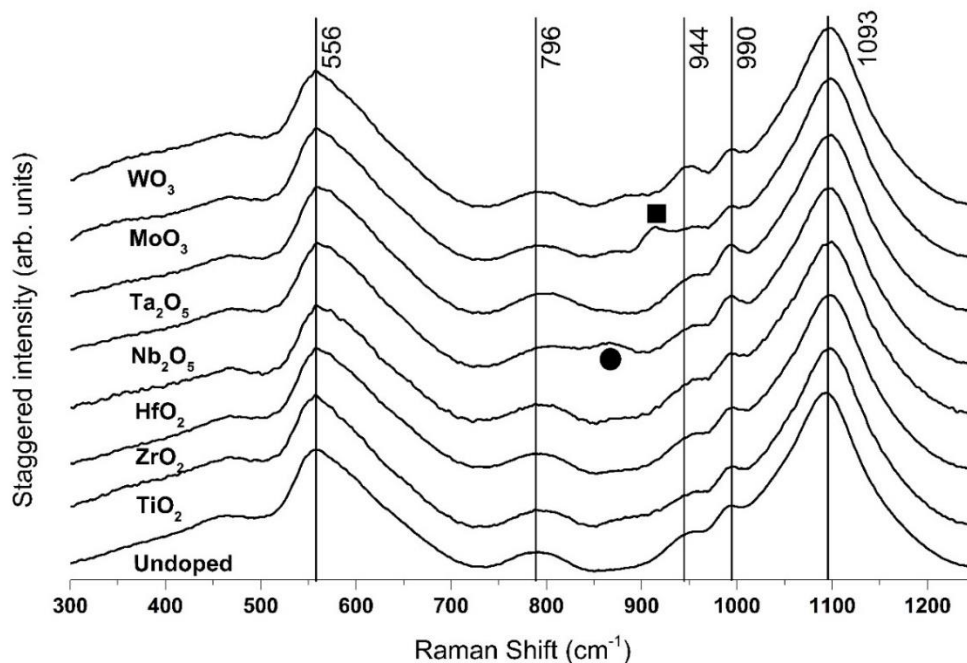
Figure 57 Normalised Raman spectra of base and doped glasses, ● = NbO_6 octahedra (875 cm^{-1}), ■ = $[MoO_4]^{2+}$ tetrahedra (925 cm^{-1})

Molybdate tetrahedra also present strong Raman cross sections, thus giving rise to a stronger signal relative to the corresponding network [265]. The peak at 925 cm^{-1} in Figure 57 corresponds to symmetric stretching of $[MoO_4]^{2-}$ tetrahedral entities in the glassy phase [266,267]. As with the X-ray diffraction patterns in Figure 56 no crystallisation is observed in the d^0 doped glasses Raman spectra shown in Figure 57, Figure 58 and Figure 59.

Within the Raman spectra shown in Figure 57, Figure 58 and Figure 59 there are no major differences suggesting no significant structural changes occur between the different base

systems. This is commensurate to the X-ray diffraction patterns shown in Figure 56 not showing discernible differences between the base glasses.
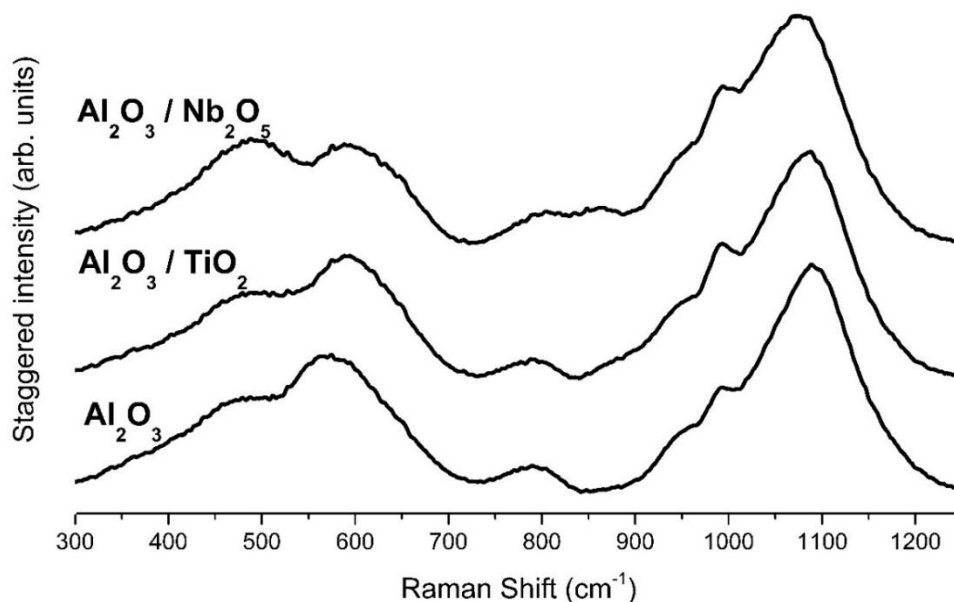
Figure 58 Normalised Raman spectra of Al$_2$O$_3$ base and doped SLS glasses

ZnO crystals provide Raman peaks at 502, 681, 766, 865 and 967 cm^{-1} corresponding to mutiphonon modes [268], a peak at 438 cm^{-1} corresponds to the E$_2$ mode, related to the hexagonal structure of ZnO [269]. The peaks are not apparent in the Raman spectra of ZnO doped and codoped glasses shown in Figure 59. A difference spectra is shown in Figure 60 showing doped glasses with the effect of the base glass removed.

After deconvolution of base SLS and 0.20 mol% Nb$_2$O$_5$ SLS using the program FitYK and applying 5 Gaussian peaks, the ratio of NBO:BO was found to be 0.361±0.025 for the undoped SLS glass and 0.364±0.025 for 0.20mol% Nb$_2$O$_5$ SLS glass shown in Figure 61. As both glass systems contain around 36% NBO and 64% BO this indicates the glasses are well polymerised and the transition metal doping does not significantly alter the

structure. Other dopants were not deconvoluted due to the dilute doping concentration, and the Raman and XRD evidence do not show significant changes from the base glass.
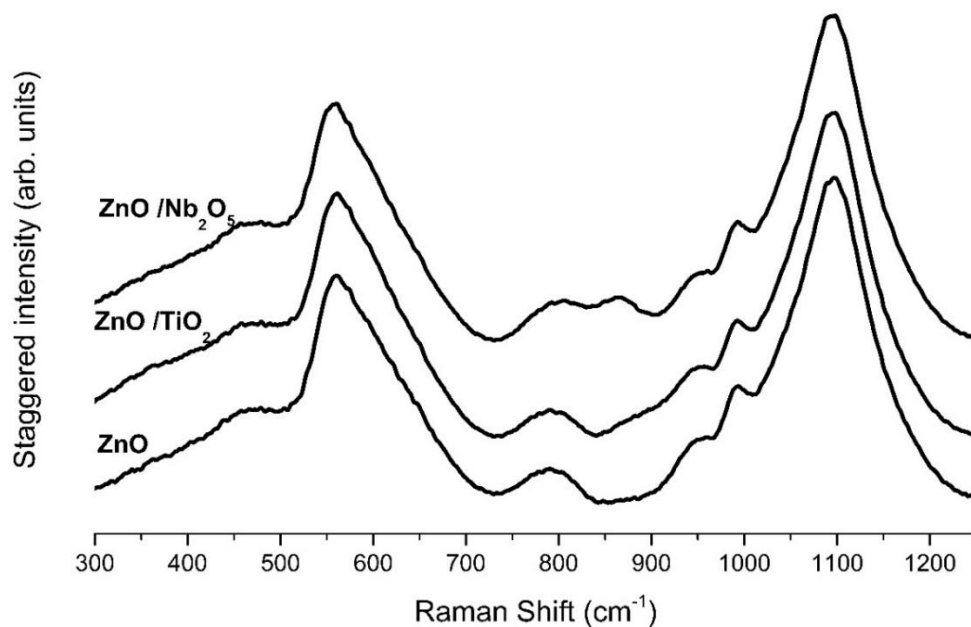
Figure 59 Normalised Raman spectra of ZnO base and doped SLS glasses
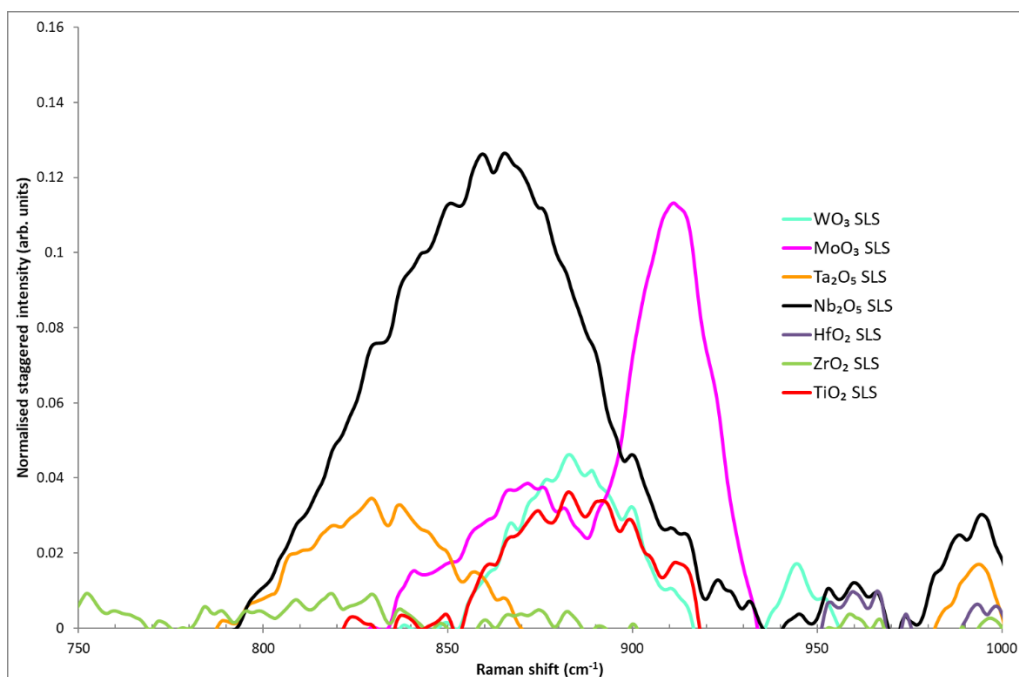
Figure 60 Difference Raman spectra of d^0 doped SLS glasses
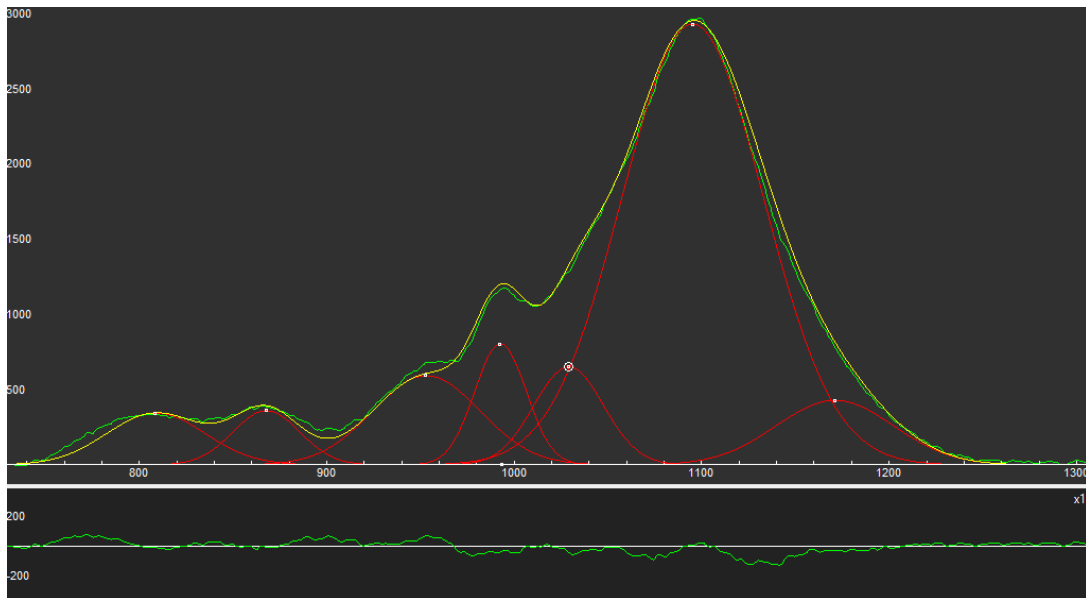
Figure 61 Raman fitting of 0.20mol% Nb_2O_5 SLS

4.2.3 Electron Paramagnetic Resonance Spectroscopy

Figure 62 shows EPR spectra of powdered glass samples, measured in silica tubes at X-band frequencies. Two signals, g=4.3 (1.6T) and g=2.0 (3.4T), correspond to paramagnetic Fe^{3+} in isolated and clustered environments respectively [163], though this is highly contested in the literature. Whilst Mn^{2+} which is isoelectronic to Fe^{3+} results in resonances at g=4.3 and g=2.0 [270,271], the lack of hyperfine structure at g=2.0 further indicates that the observed resonances are due to Fe^{3+}. Furthermore, Fe_2O_3 is a ubiquitous impurity in commercial SLS glass production. Fe_2O_3 was not deliberately added to the glass melts and is present in impurity levels of circa 100 ppm. Doped samples display the same peaks as the base glass, indicating the dopants are in the expected oxidation states of Ti^{4+}, Zr^{4+}, Hf^{4+}, Nb^{5+}, Ta^{5+}, W^{6+}, and Mo^{6+}. In the case of

155

MoO$_3$ doped glass there is an additional weak resonance at g=1.92 (3.7 T) corresponding to Mo^{5+}, shown in the inset of Figure 62.
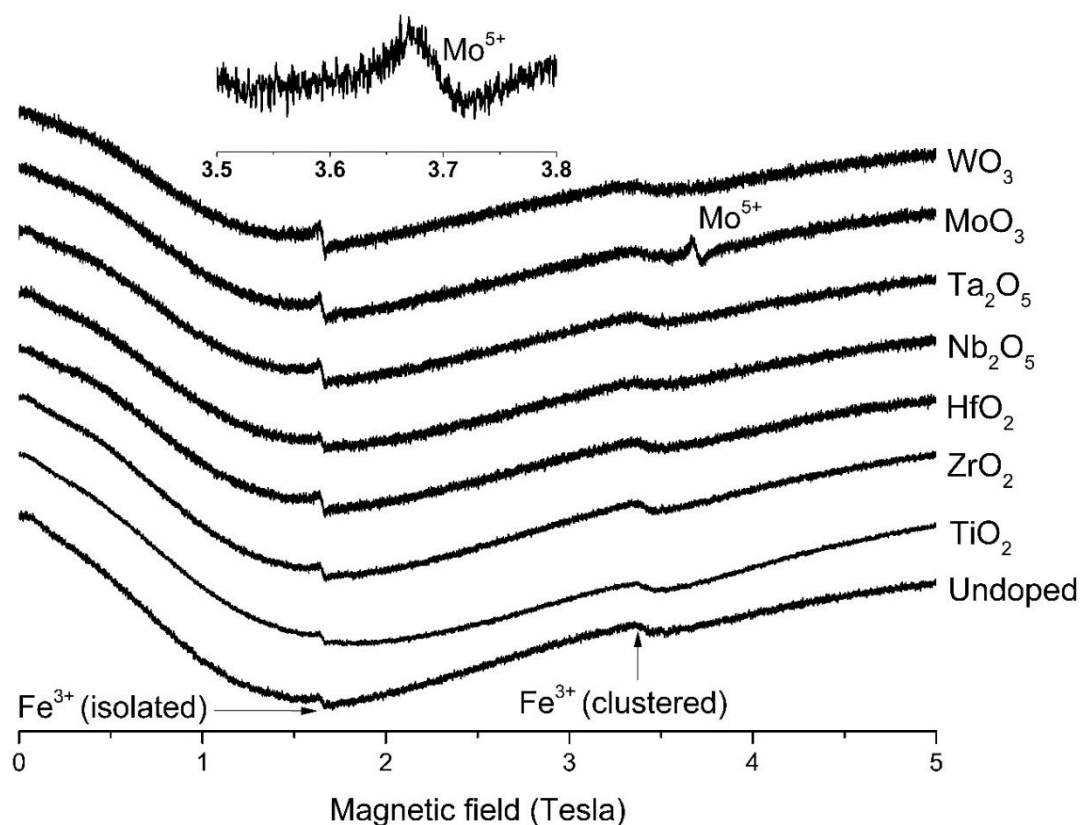
Figure 62 RT X-band EPR of base and d^0 doped SLS glasses

4.2.4 UV Vis NIR Absorption Spectroscopy

UV VIS absorption spectra of base and doped glasses are shown in Figure 63. These spectra all show strong UV absorption edges arising from the Si-O network and network modifying cations such as Na$^+$, Ca^{2+} and Al^{3+}. This band is strongly modified by transition metals including Fe-O bonds. The MoO$_3$ doped spectrum is circa 4,000 cm^{-1} (~40 nm) shifted towards the visible region relative to the base glass. The dotted line is reproduced from Yang et al. [272] and extended with data from Fix et al. [93], giving the absorbance

of EVA glue. With different compositions of the glue and age the absorbance can shift [28], with older, more irradiated glue having absorption shifted towards the visible due to yellowing.
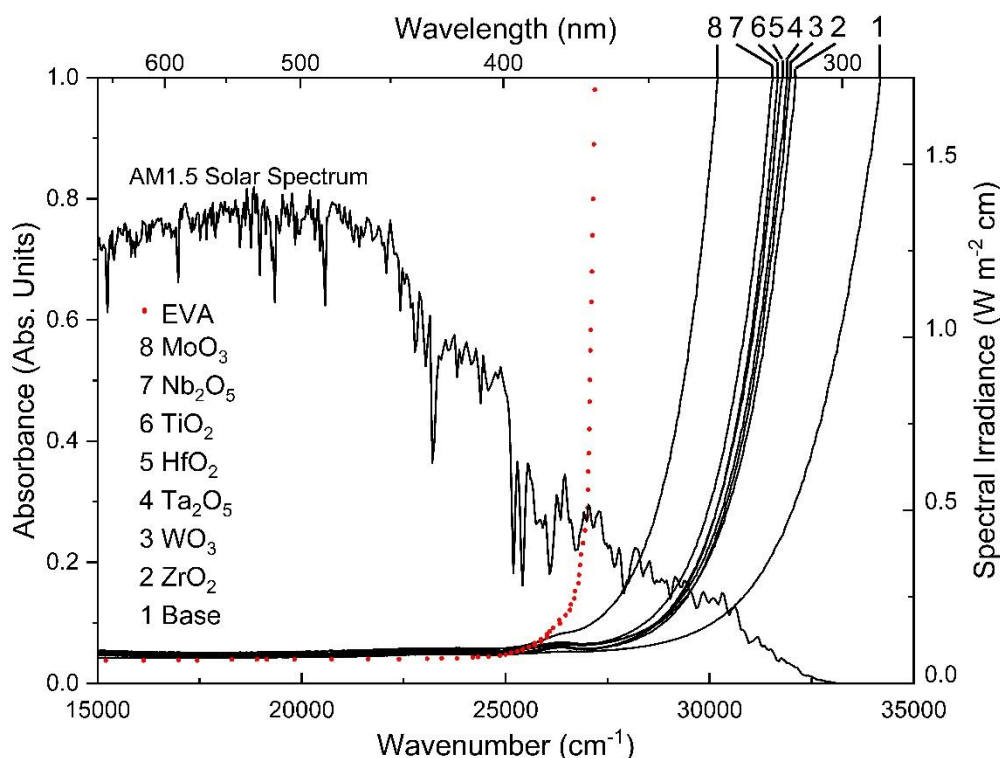
Figure 63 UV-Vis absorption of base and doped glasses (AM1.5 data from [18])

The AM1.5 solar spectrum shows that high energy photons (>25,000 cm^{-1}, <400 nm) have lower spectral irradiance, however these photons are particularly detrimental to the polymeric species within a PV module. The UV absorption profiles of the doped glasses absorb significant portions of these high energy, damaging, photons, particularly in the case of MoO_3. Higher energy photons do correspondingly more damage to the polymer layers and therefore absorption within the glass front sheet of these particularly deleterious photons is essential for the longevity of PV modules.
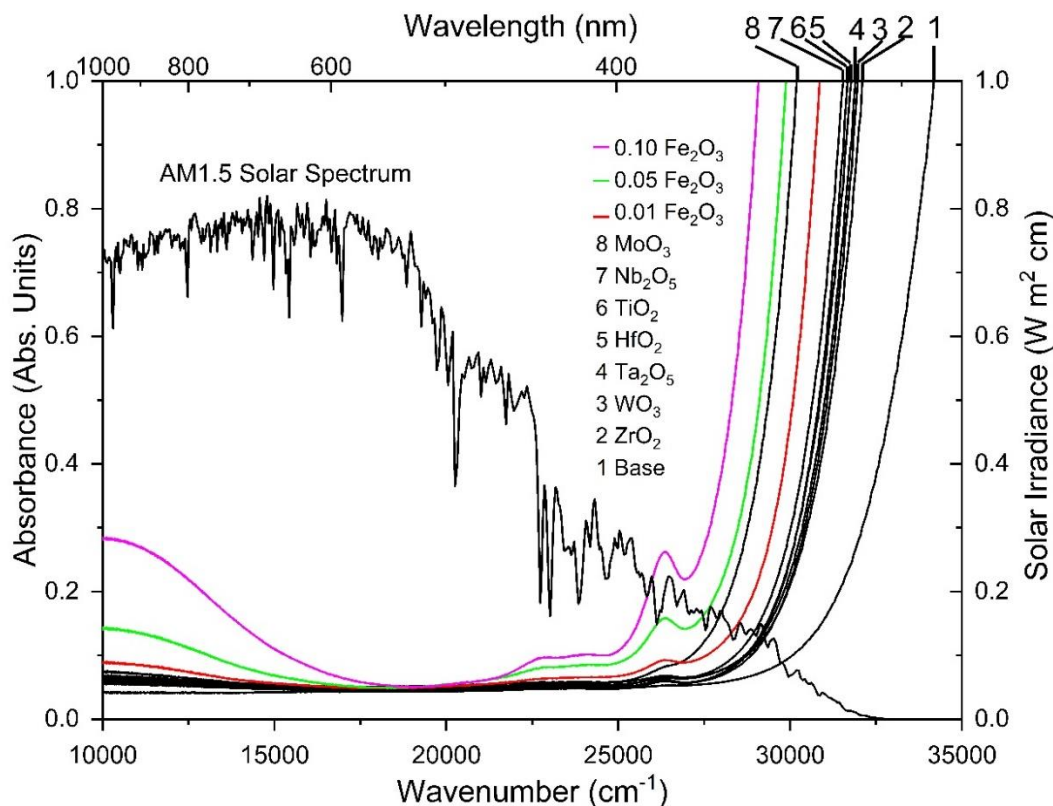
Figure 64 UV Vis IR absorbance of d^0 doped glasses and Fe_2O_3 doped glasses

Figure 64 shows UV Vis IR absorption spectra of the d^0 doped glasses along with Fe_2O_3 doped glasses. Although increasing quantities of Fe_2O_3 in silicate glasses shift the UV edge towards the visible there are visible and NIR absorption peaks within their absorption profiles. The prominent peak at 26,220 cm^{-1} (381 nm) corresponds to the $^6A_1(S) \rightarrow ^4E(D)$ transition of Fe^{3+} [56] which is present in all samples, a function of the chronic impurity of Fe_2O_3 in silicate glasses, in a lower intensity in the d^0 doped samples. MoO_3 doped SLS glass has a UV edge of similar position to that of 0.05mol% Fe_2O_3, with lower intensity of bands at 26,220 cm^{-1} (381 nm). Absorption in the IR region corresponds to Fe^{2+} [56] and prevents the transmission of photons close to the bandgap of c-Si solar cells, deleteriously impacting efficiency. All sample were 8.0±0.1 mm thickness and were normalised to 10 mm thickness.
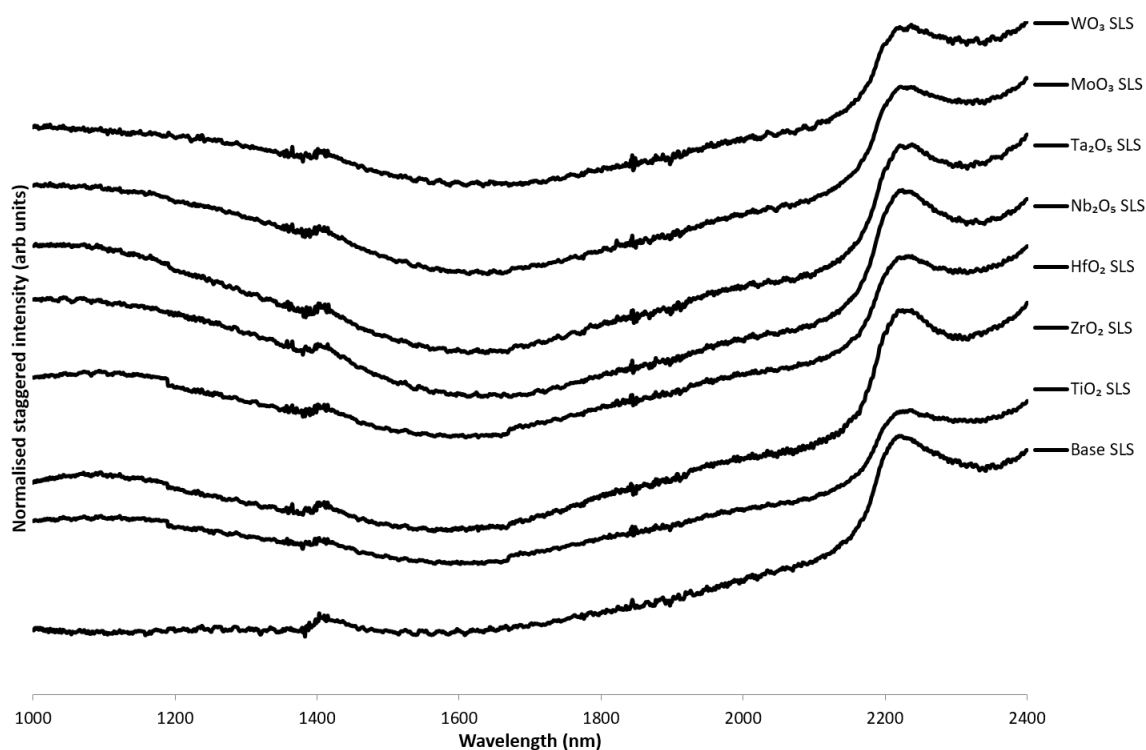
Figure 65 NIR absorption spectroscopy of d^0 doped SLS glasses

NIR absorption spectroscopy of d^0 transition metal doped glasses was undertaken to confirm no deleterious absorptions were occurring across the 1000-1200 nm range where c-Si panels can effectively absorb. As shown in Figure 65, the profile is flat across the range of 1000-2000 nm, with a small broadband centred at 2200 nm corresponding to H_2O content [273]. PV modules utilising c-Si have a strong absorbance near the band gap of Si (circa 1100 nm), as these glasses are not strongly absorbing within this region unlike Fe_2O_3 containing glasses, they may prove beneficial for the use as front sheets. There is little absorption corresponding to Fe^{2+} between 10,000 cm^{-1} – 7490 cm^{-1} (1000 nm – 1335 nm) [56] in Figure 65. Note there is a filter change at circa 1420 nm.

4.2.5 UV Vis Fluorescence Spectroscopy
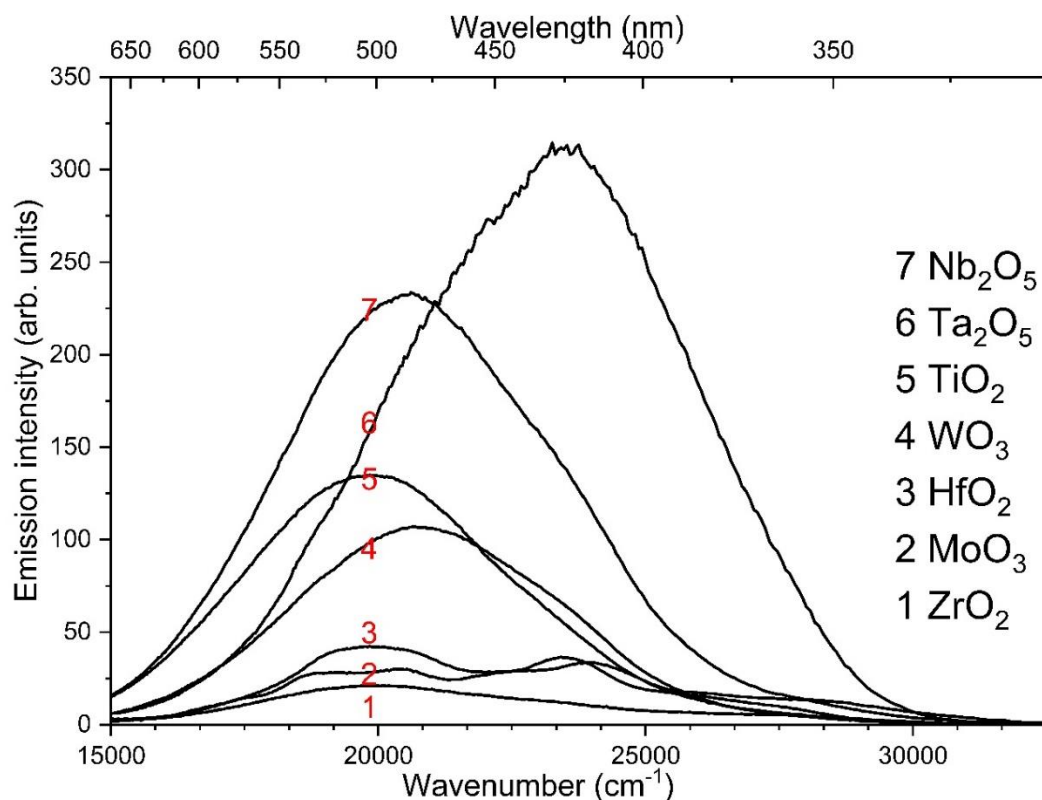
Figure 66 Fluorescence emission intensity under 41,666 cm^{-1} (240 nm) excitation (mercury discharge lamp)

The fluorescence emission spectra from 41,666 cm^{-1} (240 nm) excitation of d^0 doped glasses are presented in Figure 66. All glasses demonstrate broadband emission between 19,000 cm^{-1} and 25,000 cm^{-1} (400 nm to 525 nm) with a range of intensities. The colour photograph in Figure 67 shows the variation in colour and emission intensity upon UV excitation. ZrO_2 and MoO_3 doped glasses weakly emit visible photons at these excitation wavenumbers [74].
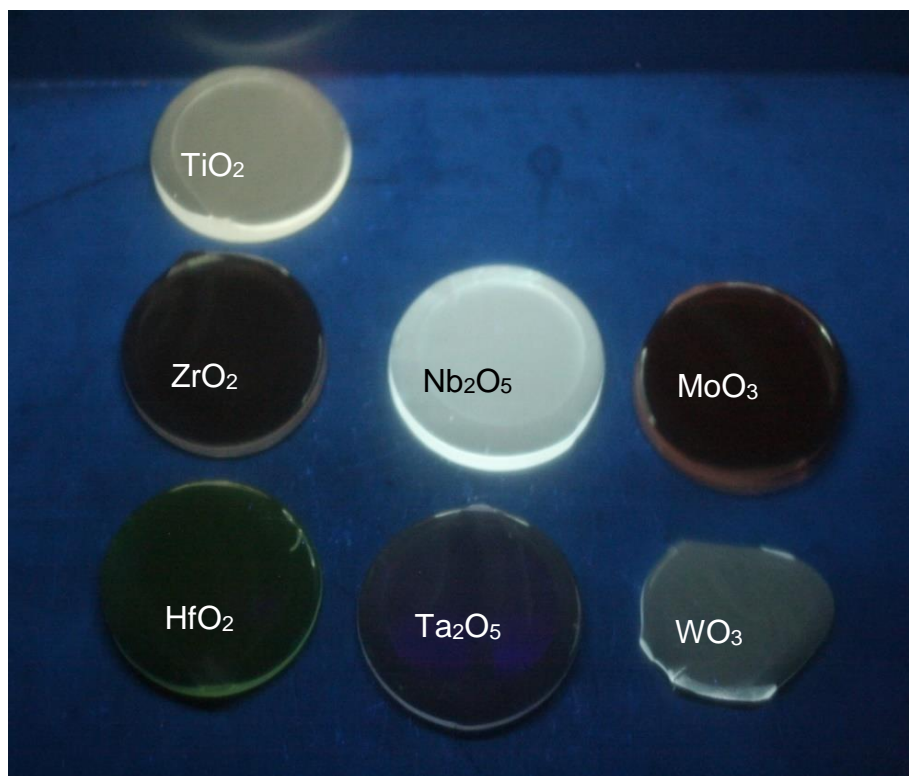
Figure 67 Visible fluorescence from d^0 doped SLS glasses. Photograph taken under 39,370 cm^{-1} (254 nm) UV light
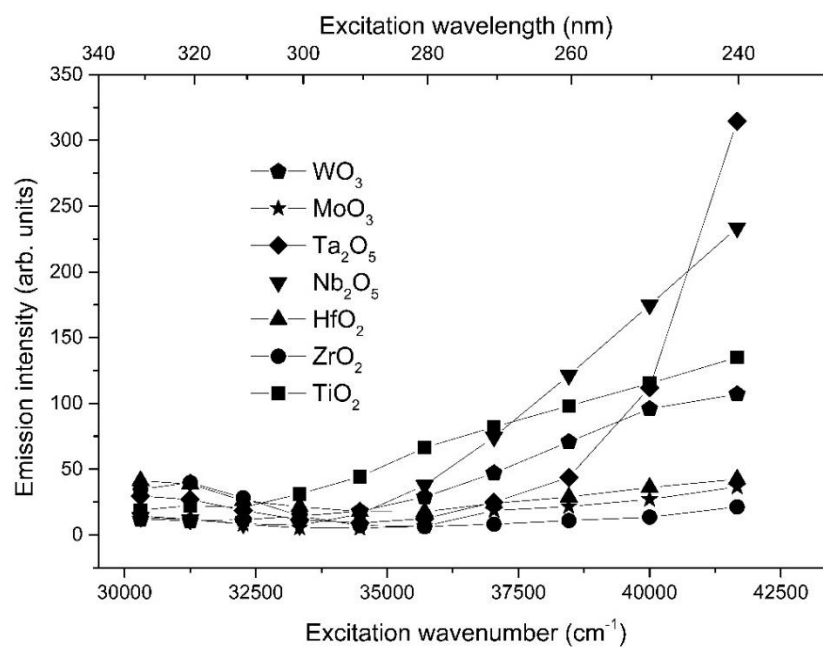
Figure 68 Variation of emission intensity as a function of excitation wavelength and dopant type

Figure 68 shows the maximum emission intensity at various excitation wavenumbers. All dopants have stronger emission at higher wavenumber excitation with a rapid decrease in emission intensity, however there is measurable emission at all measured wavenumbers. The glasses doped with Nb_2O_5 and Ta_2O_5 contain twice the quantity of active ions relative to TiO_2, ZrO_2, HfO_2, MoO_3 and WO_3. This may, in part, explain the greater emission intensity of the 0.20mol% doped SLS glasses with Nb_2O_5 and Ta_2O_5.

Modification of the host matrix positively affects the emission of TiO_2 as presented in Figure 69, with the addition of 5.00mol% Al_2O_3 into the glass in replacement of SiO_2 increasing the emission intensity by a factor of 2. The effect is also observed in Nb_2O_5 doped glasses with a modified glass matrix, the addition of 1.00mol% ZnO increases emission intensity by a factor of 2.5, as shown in Figure 70.
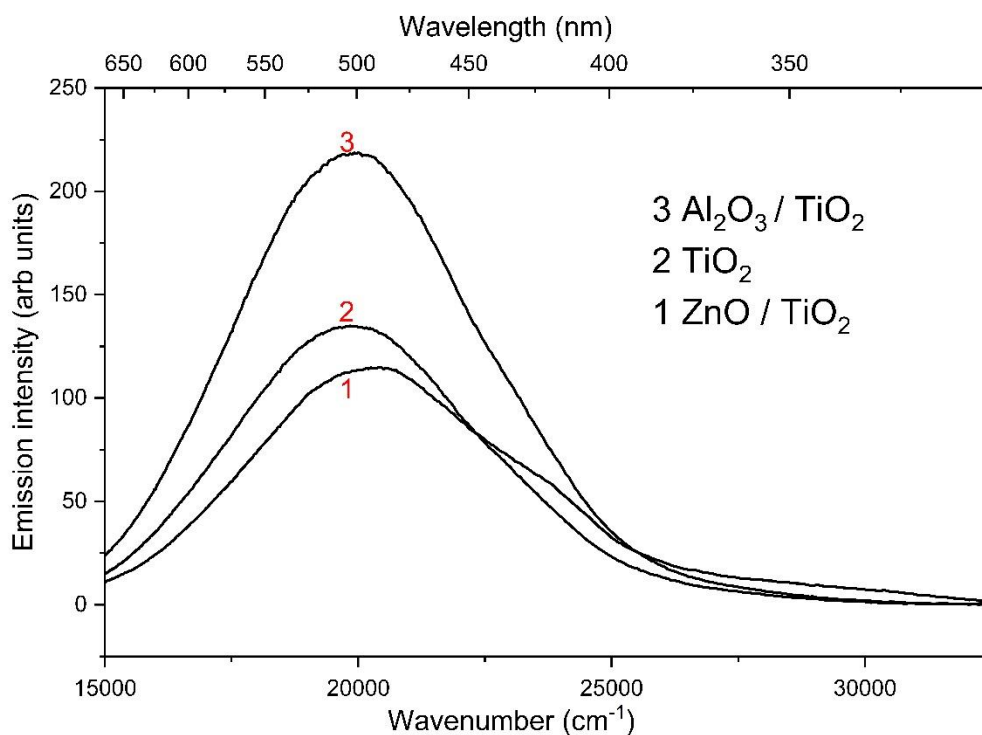
Figure 69 Fluorescence emission intensity of doped TiO₂ glasses
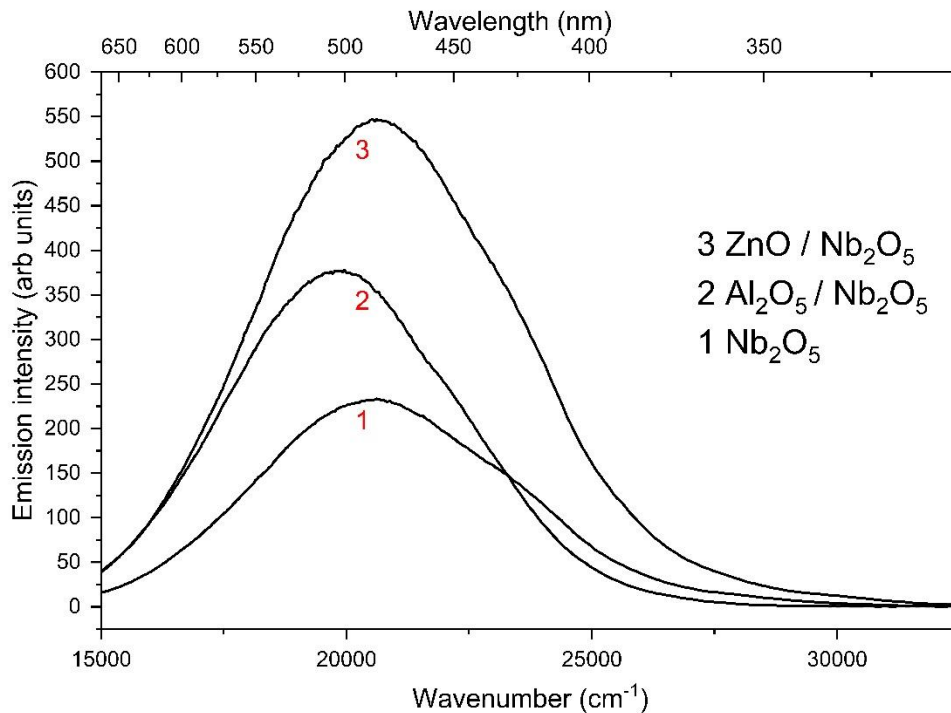
Figure 70 Fluorescence emission of doped Nb$_2$O$_5$ glasses

4.3 Discussion

The XRD patterns in Figure 56 show no sharp Bragg diffraction peaks indicating the presence of crystalline phases, thus confirming the amorphous nature of the representative samples considered. The diffraction patterns are consistent with other oxide glasses, showing the amorphous "hump" typical of silicate glasses [124]. Transition metal ions have been used as nucleating agents in lithium disilicate glasses [258,274]. While the transition metals may induce crystallisation in glass melts, the low doping concentrations in this study are below the thresholds observed in other studies [129,258]. Furthermore, soda lime silica glasses used in this study are less prone to nucleation than lithium disilicate glasses. Differences in XRD profiles are not readily resolved in SLS

glasses with the addition of Al_2O_3 below circa 7.0mol% Al_2O_3 [275], although with increasing Al_2O_3 content there may be an increase in the formation of Q^3 structural units [276].

Fluorescence emission intensity is lower in amorphous materials, but the bands are broader by comparison to crystalline equivalents [277]. Broader absorption and emission bands in the front sheet glass is advantageous for the protection of polymeric species. Both ZnO and Al_2O_3 demonstrate intermediate glass forming characteristics [124] they both can integrate and act as network formers. Densities are presented in section 3.1.1.1 and are consistent with both the Fluegel model [278] and other experimental values [261], indicating that glass compositions, for all samples, are close to their nominal compositions based on batch calculations under similar conditions.

The Raman spectra in Figure 57 show only small variations between the base and doped glasses, with only Nb_2O_5 and MoO_3 showing significant changes as indicated by the circle ● at 875 cm^{-1} and the square ■ at 925 cm^{-1} respectively. The six Raman bands in the base glass spectrum correspond to different structural configurations, the most intense band centred on 1093 cm^{-1} is due to the stretching mode of Si-O-Si in Q^3 arrangements [126,279–281] indicating a highly polymerised silicate network. The broad band centred at 990 cm^{-1} is consistent with the Si-NBO stretching mode (i.e. Q^2) [280,281]. The band centred at ca. 944 cm^{-1} is due to Q^2 speciation. The band centred at 796 cm^{-1} arises from Si-O-Si symmetric stretching modes between Si-O tetrahedra [127,279,281]. The bands at 450 cm^{-1} and 556 cm^{-1} correspond to Si-O-Si symmetric stretching of Q^4 and Q^3 species, respectively [282]. Deconvolution of these bands in base SLS and 0.20mol% Nb_2O_5 SLS show NBO comprise 36.1±2.5% and 36.4±2.5% respectively.

The SLS glass sample doped with 0.20mol% Nb_2O_5 exhibits an extra band relative to the base glass, at around 875 cm^{-1}. This is attributed to Nb-O symmetric vibrations in [NbO_6] octahedra [283]. [NbO_6] octahedra have high Raman cross sections and the peak at 875 cm^{-1} is detectable at low (>0.10mol%) concentrations in SLS glasses [263,264] and is present in Figure 57, Figure 58 and Figure 59. Deconvolution of Nb_2O_5 spectra along with base SLS through the program FitYK shown in Figure 61, give a BO:NBO ratio of circa 64:36 indicating high polymerisation and non-significant changes to the polymerisation with the incorporation of 0.20mol% Nb_2O_5 and are consistent with other similar glasses [262]. Molybdate tetrahedra likewise present strong Raman cross sections, thus giving rise to a stronger signal relative to the corresponding network [265] demonstrated in Figure 57. The peak at 925 cm^{-1} in Figure 57 corresponds to symmetric stretching of [MoO_4]$^{2-}$ tetrahedral motifs [266,267].

Bands associated with the d^0 transition metals, Ti^{4+} (937 cm^{-1} corresponding to internal vibrations of TiO_4 tetrahedra, and 1100 cm^{-1} to symmetric stretches of TiO_4) [284], Zr^{4+} (642 cm^{-1} tetragonal ZrO_2) [283], Hf^{4+} (680 cm^{-1} tetragonal HfO_2), Ta^{5+} (786 cm^{-1} octahedral TaO_6) [285] and W^{6+} (916 cm^{-1}, 958 cm^{-1}, 1017 cm^{-1} octahedral WO_6) [286], were also expected due to their high polarisability relative to Si. However, these were not observed even through a subtraction of the base glass spectrum from the doped glass' spectra. The high polarisability of the transition metals confer a higher Raman cross section relative to the silicate network, however, the low doping concentrations used in this study may result in low intensity peaks which are not readily observed.

EPR is used to detect unpaired electrons, and therefore d^0 dopants in their expected oxidation state are silent to this technique. Hence the two resonances at g=4.3 (1.6 T)

and g=2.0 (3.4T) shown in Figure 62 correspond to Fe^{3+} which occurs as a chronic impurity in the raw materials used to produce all sample glasses. Both resonances have been widely observed, even in spectra for glasses with very low (ppm) Fe^{3+} concentration [163]. The resonance at g=4.3 (1.6 T) corresponds to Fe^{3+} in an isolated environment [270,287]. The resonance at g=2.0 (3.4 T) is due to exchange-coupled Fe^{3+} ions [166,287,288]. It occurs even at impurity concentrations, but has also been attributed to octahedral Fe^{3+} [163,289].

Since EPR detects unpaired electrons and d^0 ions have no unpaired electrons, the lack of additional EPR peaks is commensurate with the dopants being present in the expected oxidation states of Ti^{4+}, Zr^{4+}, Hf^{4+}, Nb^{5+}, Ta^{5+}, Mo^{6+} and W^{6+} [74,246,247] . However, the EPR spectrum for the MoO_3 doped glass (Figure 62 and inset) shows an additional weak resonance at g=1.92 (3.7 T) which corresponds to Mo^{5+} [246]. Mo^{5+} (d^1) can give induce a yellow colour in silicate glasses due to $^4A_2$-$^4T_2$ absorption bands centred at 28,500 cm^{-1} (350 nm) and 22,700 cm^{-1} (440 nm) [77,246,290]. This may partly explain the shifted UV edge in the optical absorption spectra shown in Figure 63 and Figure 64 relative to other d^0 dopants. However, given the weakness of the Mo^{5+} EPR resonance in Figure 62, it can be concluded the concentration of Mo^{5+} is to be very low, and the majority of Mo is present as Mo^{6+}.

The oxidation state of Fe in soda lime silica glasses is affected by batch constituents, melting temperature, and any redox conditions during melting. The oxidation state or states of d^0 transition metal oxides in silicate glasses can be controlled by the redox conditions of the melt, ultimately affecting the absorbance and emission properties of the glasses [246]. Control of the redox conditions is crucial for any commercial glass

166

manufacture process. Typical $Fe^{2+}/\Sigma Fe$ redox ratios of ~0.2-0.3 are common in commercial float glass manufacturing processes [162]. Although the glasses prepared in this study did not utilise commercial glassmaking raw materials, and the melting atmosphere was more oxidising than within a commercial float glass furnace, the glasses were melted at similar temperatures and chemical proportions. Therefore, according to Van t'Hoff's law, it is estimated that the $Fe^{2+}/\Sigma Fe$ redox ratios in the glasses prepared in this work were not dissimilar to that found in commercial float glasses, albeit it is likely they were marginally more oxidised due to the furnace atmosphere [57,162].

While it was not possible to quantitatively measure the iron content from the EPR spectra as the measurements were made to qualitatively determine the oxidation state of the d^0 dopants, the weakness of the Fe^{3+} resonances are qualitatively consistent with Fe^{3+} contents in the ppm range [291]. Fe^{2+} cannot be measured though room temperature X-band EPR due to its short spin-lattice relaxation time and lack of unpaired electrons [163]. The Fe_2O_3 content was below the limit of detection for the program used for XRF (ca. 200 ppm).

For titanium doped glasses redox potentials developed by Schreiber et al [292,293] indicate that, under all but very strongly reducing conditions, these dopants will occur in soda-lime-silica glasses as Ti^{4+}. No comparable glass redox potential data was identified for the other dopants studied here, however, based on aqueous redox potentials it can reasonably be assumed that these dopants will occur in soda-lime-silica glasses prepared under oxidising melting conditions, predominantly as Nb^{5+}, Ta^{5+}, Zr^{4+}, Hf^{4+} and W^{6+}. The

results of this study are consistent with this view demonstrated in the EPR and absorbance measurements shown in Figure 62, Figure 63, and Figure 64.

Optical samples were polished to 8.0±0.1 mm thickness and normalised to 10 mm thickness and, as shown by the transmission spectra in Figure 63 and Figure 64, all are of high quality optical polishing as poor polishing leads to large amounts of diffuse scattering at the air-glass interface and results in poor transmission of light. The UV absorption edge is characterised by photons of an energy high enough to induce absorption of the silicate network [129]. Meng et al demonstrated that in broadly similar silicate glass compositions, 1mol% MoO_3 shifts UV absorption to lower wavenumbers (higher wavelengths) more strongly than other d^0 ions (Ti^{4+}, Zr^{4+}, Nb^{5+}, Ta^{5+} and W^{6+}) [74], this work shows a corresponding result.

It has been demonstrated that the local structure of MoO_3 has a strong influence on the absorption which can shift the absorption edge towards ca. 24,000 cm^{-1} (415 nm) [294]. However, as shown by our EPR results and the corresponding optical absorption spectra, in the Mo-doped sample studied here, a very small fraction of the molybdenum has been reduced to Mo^{5+} which could contribute to the shifted absorption. In Figure 64, Fe_2O_3 doped glasses are shown to shift the UV edge towards the visible region with increasing quantities of iron oxide. It has been demonstrated 0.01mol% Fe_2O_3 doped silicate glass as a PV encapsulant layer reduces module output by 1.1% due to the visible and IR absorptions at 26,220 cm^{-1} and 11,000 cm^{-1} (381 nm and 909 nm) of Fe^{3+} and Fe^{2+} [58]. Doping silicate glasses with 0.20mol% of d^0-ion oxide provides the solar protection, shown in Figure 63, without the deleterious bands shown in Figure 64.

EVA glues absorb strongly above 26,666 cm^{-1} (below 375 nm) [272] with photons of higher energy inducing greater damage. Yellowing index is a measure of transmission losses in polymers, with higher dimensionless numbers indicating a higher transmission loss [295]. An NREL study demonstrated in a c-Si based PV module with a front sheet of standard SLS glass, with a UV edge of 295 nm gave a yellowing index of 81.9. Identical PV modules with SLS glasses doped with CeO_2 to shift the UV edge to 325 nm and 330 nm had yellowing indexes of 23.8 and 17.8 respectively [28]. All modules underwent 35 weeks of accelerated aging to demonstrate the yellowing from UV degradation and no measures were undertaken to correlate this to an exposure time of modules in operation [28].

The glasses in the NREL study were doped with cerium oxide: we postulate that the d^0 doped glasses studied here may also be suitable to achieve similar UV protection. As shown in Figure 63, glasses with UV absorption closer to that of the EVA absorption line do not act as 100% effective bandpass filters. Shifting the absorption of the glasses to overlap the EVA absorption would induce a deleterious effect on the module efficiency by absorbing visible photons as the glass itself would be yellowed. Furthermore, the cost would be prohibitive and there would be potential for float glass furnace to have to change their melting regime with increasing the doping concentration further. An effective balance of the beneficial UV absorption against the negative visible absorption in the glass superstrate requires further study. Although a cost analysis would be required, along with a study investigating changes in melt chemistry, it is tentatively suggested a doping level between 0.20 and 0.50mol% may prove beneficial for the protection of polymeric species in PV modules [74,78].

As shown in Figure 68 under excitation from 41,666 cm^{-1} (240 nm) light, and visibly in Figure 67 with 39,370 cm^{-1} (254 nm) light, there is a large variation in emission intensity as a function of dopant type. The centre of the emission peaks vary up to 5,000 cm^{-1} (100 nm) between Ta_2O_5 and Nb_2O_5. At sea level there are few photons, as seen in the AM1.5 spectra in Figure 63 and Figure 64, with high photon energies in the UV (> ca. 33,300 cm^{-1}, < 300 nm), that would be required to induce the strong fluorescence emission from glasses containing the dopants described herein. The effect, although weaker, still occurs from excitation of photons of between 33,000 cm^{-1} to 30,300 cm^{-1} (300-330 nm). PV modules with front sheets with dopants such as these may be suitable for high UV locations such as Peru, Chile, Argentina and New Zealand, along with any higher altitude area in which UV photons are more intense, due to lower attenuation by the atmosphere, and of higher energies.

It has been suggested a possible origin of the emission are from defects in the silicate network induced by the addition of the various doped ions, especially Ta^{5+} [245], however, the EPR spectra only show Fe^{3+} impurity resonances. A more convincing mechanism is a ligand to metal charge transfer mechanism (LMCT) [296].

The excited state corresponds to nd^0 (n=3, 4, 5) of the transition metal ion, and the ground state is the $2p^6$ state of the oxide ions surrounding it, as shown in Figure 71. A photon of sufficient energy excites an electron from the $2p^6$ orbital of the oxygen atom surrounding a d^0 ion, which gets promoted to the empty nd^0 orbital, upon the electron falling to the ground state it releases a photon and a phonon. The energy loss between the excitation and emission photons corresponds to the energy of the phonon.
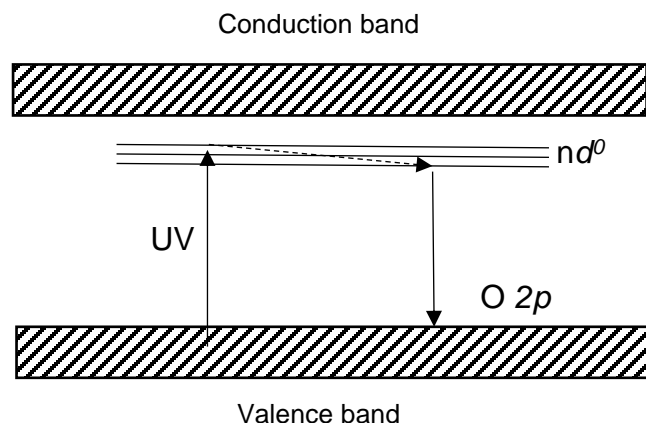
Figure 71 Schematic mechanism for nd^0 fluorescence emission n=3, 4, 5

In Figure 68 the variation of emission intensity as a function of excitation wavenumber (and wavelength) is shown. Although at 41,666 cm^{-1} (240 nm) excitation the Ta_2O_5 doped sample shows the strongest emission, Nb_2O_5 and TiO_2 were selected for codoping with Al_2O_3 and ZnO due to their low cost and high emission intensities over a wide range of excitation energies. Codoping was undertaken in an effort to increase emission intensity of the dopants. The levels of Nb_2O_5 and Ta_2O_5 added contained twice the quantity of active ions relative to the other singly doped systems. The emission intensity of both Nb_2O_5 and Ta_2O_5 is proportionally higher due, in part, to the effectively higher doping concentrations.

Codoped glasses were modified to contain 0.20mol% of d^0 ions TiO_2 or Nb_2O_5 and in conjunction contain 5.00mol% Al_2O_3 (replacing SiO_2), or 1.0 mol% ZnO (replacing MgO). Shown in Figure 69, the Al_2O_3 codoped TiO_2 sample exhibits enhanced fluorescence emission without changing λ_{max} due to the matrix having lower total phonon energy [297], i.e. the photon-phonon emission results in fewer non-radiative losses, and thus a higher fluorescence emission. ZnO codoped glasses induce a shoulder peak developing around

23,000 cm^{-1} (434 nm). This is attributed to the fluorescence emission of Zn^{2+}, it is understood the luminescence is due to interstitial zinc defects, involving a transition from the conduction band edge to a deep acceptor level [298]. It has been shown that codoping Nb$_2$O$_5$ with ZnO enhances the fluorescence emission relative to singularly-doped Nb$_2$O$_5$ samples as seen in Figure 70. Small modifications to the host glass matrix do not significantly change the structure, as evidenced by the XRD and Raman traces, but can have a significant effect on the emission intensity when excited under UV light. Differences in the Raman spectra reflect the high polarisability of the transition metal dopants and not significant structural changes of the Q^n silicate network.

4.4 Conclusions

A series of glasses doped with d^0 ions was prepared through a standard melt quench technique. Upon excitation by UV light all glasses demonstrate visible fluorescence of different magnitudes centred between 20,000 cm^{-1} and 25,000 cm^{-1} (400 nm – 500 nm), with the greatest intensity from 41,666 cm^{-1} (240 nm) excitation. A shift in the absorption spectra towards the visible region has been demonstrated in all doped samples, with MoO$_3$ doped glass having the strongest effect. A contributing factor may be a partial reduction in Mo^{6+} to Mo^{5+} shown by the peak at g=1.92 (3.7 T) through EPR spectroscopy. Silicate glasses doped with Nb$_2$O$_5$ and MoO$_3$ exhibit additional Raman peaks centred at 875 cm^{-1} and 925 cm^{-1}, respectively, attributed to Nb-O vibrations in [NbO$_6$] octahedra and Mo-O stretching modes in [MoO$_4$]$^{2-}$ tetrahedra. Through modification of the glass matrix with Al$_2$O$_3$ or ZnO, the fluorescence emission intensity can be enhanced in the case of TiO$_2$ and Nb$_2$O$_5$ up to a factor of 2.5. SLS glasses doped with d^0 ions confer several potential advantages for PV cover glass applications through absorption of

damaging UV light and re-emission as near-UV and visible light, which could simultaneously enhance both PV module lifetimes and efficiencies.

The glasses presented in this work are primarily suitable for absorption of damaging UV photons and hence for the protection of the EVA glue and backsheet layers. Further optimisation is required to fully overlap the absorption profile of the glass cover sheet to that of the EVA glue, whilst remaining transparent to visible photons in a technologically available manner. Modification of the excitation and emission properties of the dopants to more closely align with that of the particular solar cell is also required as this work primarily considered c-Si based PV modules which constitute the majority of installed PV worldwide. Increasing doping levels in the SLS front sheets without inducing visible absorption, or codoping effective UV absorbing dopants with efficient visible emitting dopants may prove more beneficial for increasing service lifetimes and efficiencies of PV modules. For clarity, doping of glasses is meant in the glass manufacture term rather than the semiconductor term. Doping of glasses within this thesis comprise of levels in the order of 0-0.50mol%.

5 Structural, Chemical and Optical Properties of Doping Silicate Glasses With S^2-Ion Oxide Post-Transition Metals for Photovoltaic Applications

5.1 Introduction

Photovoltaic modules primarily undergo critical failure through water ingress onto the conducting wires within [29]. This occurs due to the polymeric species becoming brittle after UV induced degradation after exposure in the field [19,211]. However, even before this critical failure conversion efficiency may drop up to 2.5% per year in high UV locations due to the polymer species discolouring to a yellow and ultimately brown colour [29,30]. The main photochemical processes involved in this degradation are the formation of unsaturated carbonyl groups and conjugated polyenes catalysed by UV photons [299]. This degradation hinders transmission of visible light and reduces the flux of photons available for conversion to electricity.

Bismuth oxide (Bi_2O_3) doped soda lime silica glasses have been demonstrated to absorb strongly in the UV, and confer an additional benefit of photoluminescence, depending on oxidation state, in the visible or NIR [88,300,301]. There are several interpretations within the literature of the source of the emission in the visible or NIR from Bi^+ [87], Bi^{2+} [302], Bi^{5+} [303], clusters of Bi_2 and Bi_2^- [304] in various glass matrices. Visible fluorescence centred around 22,200 cm^{-1} (450 nm) has been attributed to Bi^{3+} [218,305]. Absorption bands between 40,000 cm^{-1} and 25,000 cm^{-1} (250 nm – 400 nm) are ascribed to $^1S_0 \rightarrow {}^3P_0$ and $^1S_0 \rightarrow {}^3P_1$ transitions [218]. It is therefore postulated with the incorporation of bismuth in soda lime silica glass front sheets, crucially in the Bi^{3+} oxidation state, may confer UV protection to polymeric species whilst imparting a higher visible photon flux to

the PV module, and therefore, increase both the service lifetime of the PV module, and increase module efficiency.

As bismuth may be found in multiple valence states, 5, 4, 3, 2, 1, -1, -2, and -3, elucidation of the cause of visible and NIR luminescence has been extensively studied and debated within the literature [306–308]. Within silicate glasses such as the soda lime silica and borosilicate glasses similar to those studied within this research Bi^{3+} and metallic bismuth are considered to be the preponderant species, however the presence of Bi^{5+} has been elucidated [303]. Bi^{2+} [309], and Bi^+ are often observed in crystalline materials [218]. In general, the absorption and emission bands are broader in bismuth-doped glasses than a rare earth doped glass due to the unsheltered outer electrons [218]. Rare earth elements tend to show sharp absorption and emission lines which are not as beneficial for the protection of polymeric species as the broadband emission conferred with post-transition metal oxides.

The fluorescence emission of Bi^{3+} in phosphors has been studied at least from 1968 with work from Blasse et al [305]. Within recent years significant research on bismuth doped glasses has been undertaken for various applications such as luminescence in the visible and near-infrared wavebands for novel lasing sources [310] and for white light emitting LEDs [309]. However, careful control of the oxidation state of bismuth is required in silicate glasses, as lower oxidation states of bismuth such as Bi^{2+} in barium borates emits in the red region of the visible spectrum centred at 16,666 cm^{-1} (600 nm) [311]. Bi^+ complexes in pure silica fibres show three emission bands, at 8718 cm^{-1} (1147 nm) and 7127 cm^{-1} (1403 nm) caused by Bi_2O molecules and another centred at 6702 cm^{-1} (1492 nm) corresponding to SiOBi structures [312]. These emission bands are above the

bandgap of silicon resulting in inefficient absorption, they have absorption bands within the NIR centred between 12,500 cm^{-1} – 11,100 cm^{-1} (800 nm – 900 nm) which absorb photons of the energy suitable for efficient absorption, and do not confer the UV protection required for protection of polymer species.

Therefore, in oxidation states other than Bi^{3+} deleterious absorption bands are observed which parasitically absorb photons which may be converted to electricity within a PV module. Careful control of the oxidation state of bismuth is therefore essential for the protection of polymeric species with PV modules. A series of Bi$_2$O$_3$ doped silicate glasses has been prepared, and subsequently analysed by a suite of spectroscopic measurements to elucidate the oxidation state of the resultant bismuth molecules.

Lead oxide (Pb^{2+}) is isoelectronic to Bi^{3+} and therefore undergoes the same electronic transitions. Lead oxide has been used as a probe ion to aid in the understanding of optical basicity. This scale, developed by Duffy et al [228,313], measures shifts in the absorption of Pb^{2+} in the UV region. Shifts arise from differences in the composition of the glass host material and the electronegativities of the cations. All commercial glasses consist of metal silicates (oxyanions), upon the addition of a soluble ion into a glass network oxygen atoms donate some of their negative charge towards the metal ion. As lead is highly polarisable, it is particularly sensitive to its environment and therefore small changes in the electronegativity surrounding the ion are shown within the absorption spectra. In more basic solutions lead oxide has an absorption towards the visible region, and inversely in more acidic solutions the absorption tends towards the ultraviolet [228].

Lead oxide is unique in that it may form a glass with SiO$_2$ over a wide range up to 70mol% PbO [314]. Lead crystal glassware was invented by George Ravenscroft in 1654, which

extended the working time of the viscous glass and increased the refractive index up to an Rf of 1.9 relative to soda lime silica circa 1.5. Typically, lead crystal contains between 10 and 30% PbO by weight. The mechanical, optical, chemical and physical properties are modulated upon the addition of PbO to a SLS base glass. Density is increased dramatically, replacing CaO (RMM=40.1) with PbO (RMM=207.2) shifts the typical density of SLS glass of 2.4 g/cm^3 to between 3.1 g/cm^3 to 4.0 g/cm^3.

24wt% lead crystal glassware has a refractive index of circa 1.62, (note this value is measured with the sodium d-line at 17,000 cm^{-1} / 589 nm). This is similar to that of sapphire 1.77. The refractive index of lead crystal partially explains the brilliance; however, a small component of it arises from UV induced broad band fluorescence. This is centred at circa 24,000 cm^{-1} / 416 nm in 7.50mol% PbO SLS, and decreases to 26,000 cm^{-1} / 384 nm in 0.50mol% PbO SLS. This fluorescence effect is similar to that found in diamonds, where around 30% of diamonds fluorescence under UV excitation centred at 25,000 cm^{-1} / 400 nm.

As there is significant work on the optical transitions found within lead doped silicate glasses from the pioneering work of Duffy and Ingram [228] glasses containing PbO can be used as model glasses for Bi_2O_3 doped glasses. Furthermore, in float glass manufacture to attain flat and smooth sheets the molten glass is floated on molten tin. A small proportion of tin diffuses into the glass and oxidises to Sn^{2+}, which is also isoelectronic to Pb^{2+} and Bi^{3+}.

Sn^{2+}, also isoelectronic to both Pb^{2+} and Bi^{3+}, is found in float glass due to the manufacturing process, outlined in section 2.2.3.1.1. As the molten glass floats on the liquid tin bath, low quantities are diffused into the glass network, which oxidised to Sn^{2+}.

This leads to differences optically and chemically in the tin side and the air side of the glass. Absorption in the UV corresponding to an S→P transition of Sn^{2+} molecules [208]. The concentration of Sn^{2+} varies as a function of depth as it is a diffusion based process, and the total concentration is a function of the length of time the glass was floated on the tin bath [315]. As Sn^{2+} is isoelectronic to Bi^{3+} it undergoes visible fluorescence emission from UV excitation. This again corresponds to $^1S_0 \rightarrow {}^3P_0$ and $^1S_0 \rightarrow {}^3P_1$ transitions [218]. As the concentration of Sn^{2+} can vary through exposure time, temperature, and thickness of the glass, a model glass containing 0.20mol% SnO_2 was prepared and analysed optically to assist in the elucidation of the oxidation state of bismuth in the prepared glasses.

X-ray diffraction and Raman spectroscopy were done to understand structural changes associated with doping silicate glasses with post transition metals. Both XANES and EPR measurements on Bi_2O_3 doped silicate glasses were completed to elucidate the oxidation state of Bi. Density and XRF measurements were undertaken to confirm the composition was close to the nominal composition outlined in section 3.1.1.2, however, borosilicate glasses could not be measured through XRF due to the transparency of boron to X-Rays.

5.2 Results
5.2.1 X-Ray Diffraction

X-ray diffraction was carried out to confirm the samples were amorphous and displayed no crystalline phases. No samples were crystalline or showed crystalline phases corresponding to glass ceramics. Window glass compositions (circa 70% SiO_2, 10% CaO, 15% Na_2O with small modifier additions) used within this study readily form glasses under the standard melt quench technique outlined in the experimental methods section.

5.2.1.1 Bi$_2$O$_3$ – Soda Lime Silica Glasses
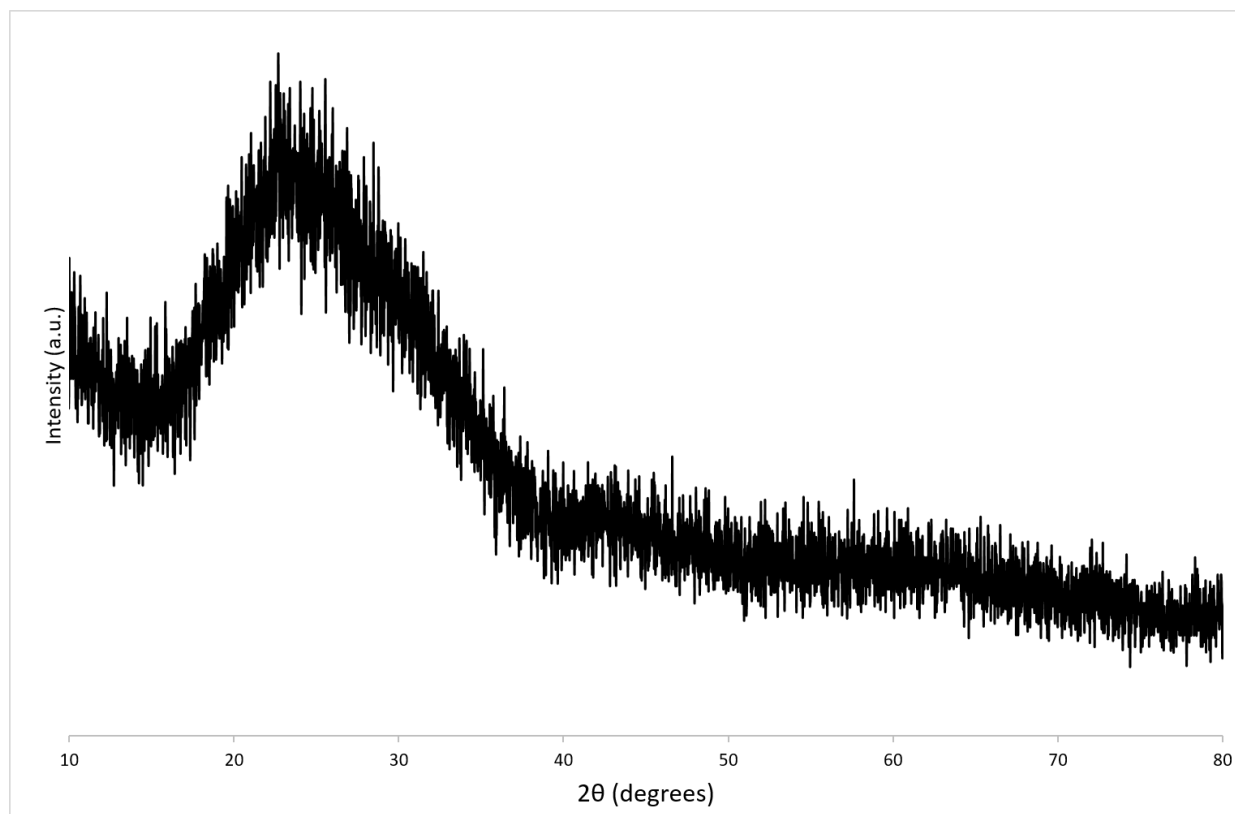
Figure 72 X-ray diffraction patterns of undoped (base) glasses

The XRD patterns shown in Figure 72 are consistent with other silicate glasses, showing the typical hump associated with oxide glasses [129]. Soda lime silica glass of similar composition (±1% of major constituents) display a hump at circa 25°2θ [316], this is commensurate with the broad hump in Figure 72. No crystallisation is observed in the base SLS glass as expected due to the low propensity for SLS glasses of this composition to spontaneously crystallise [121].

5.2.1.2 PbO – Soda Lime Silica Glasses
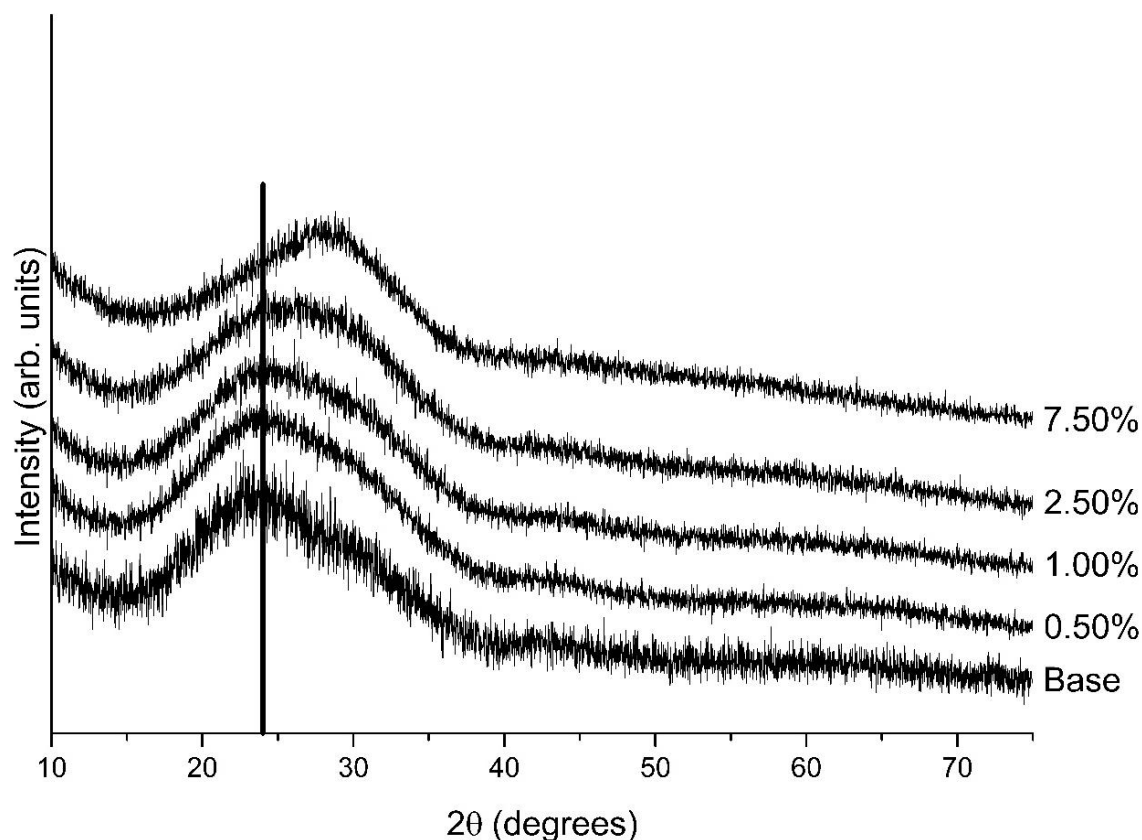
Figure 73 X-ray diffraction patterns of PbO doped SLS glasses

Shown in Figure 73 with increasing PbO content shifts to higher °2θ in the X-ray diffraction

patterns become apparent above 7.50mol% content. The shifts are towards higher

degrees 2θ indicating a less wide spread of O-Si-O bond angles, and potential differences

in the interatomic distances with increased scattering of X-rays due to the heavy lead

ions, a similar result has been shown in lithium lead borate glasses [230]. This is attributed

to the increasing proportion of Pb-O-Pb bonds, which are limited in the range of bond

angles due to the high ionic radius of the Pb^{2+} ion which sterically reduces the range

available. X-ray diffraction studies on $PbO-SiO_2$ binary glasses show Pb-O-Pb bond

angles between 107° and 109° [317]. At 2.50mol% PbO and lower concentrations, the XRD pattern is commensurate with that of the undoped SLS glass.

PbO is a network forming oxide, found as PbO_3 motifs within the glass structure [219]. As the concentration of PbO increases the average, interatomic bond-distance increases. PbO has two crystalline forms, a tetragonal structure (litharge or α-PbO) and an orthorhombic structure (massicot or β-PbO). In α-PbO (litharge), the Pb-O interatomic bond distance is 2.30 Å. In β-PbO (massicot) there are two Pb-O bond lengths, 2.21 Å corresponding to chain Pb-O bonds, and 2.49 Å for interlayer Pb-O bonds [318]. Furthermore, with increasing PbO content, there are fewer SiO_2 tetrahedra per volume. This is further exacerbated as the added PbO is in replacement of SiO_2 on a molar basis.

5.2.2 Raman Spectroscopy

5.2.2.1 Bi₂O₃ – Soda Lime Silica Glasses
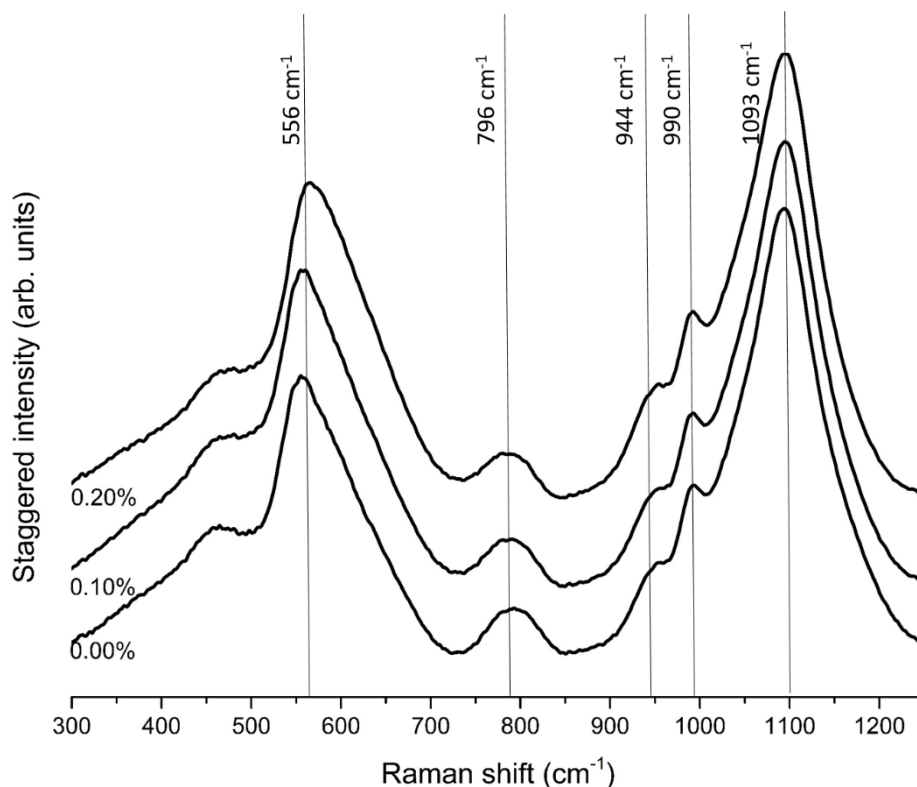
Figure 74 Normalised Raman spectra of base, 0.10mol% and 0.20mol% Bi₂O₃ SLS glasses

There are five bands shown in the Raman spectrum shown in Figure 74 which correspond to the amount of bridging and non-bridging oxygen atoms surrounding a central Si atom. The most intense band centred on 1093 cm^{-1} is due to the asymmetric stretching mode of Si-O-Si in a Q^3 configuration [279–281] indicating a highly polymerised silicate network. The broad band centred at 990 cm^{-1} is consistent with the Si-O-NBO stretching mode (i.e. Q^2) [280,281], however, it also includes a contribution from the n_1 symmetric S-O stretching mode in SO$_4^{2-}$ sulphate tetrahedra [261,319]. The band centred at ca. 944 cm^{-1} is due to Q^2 speciation. The band centred at 796 cm^{-1} arises from Si-O-Si symmetric

stretching modes between Si-O tetrahedra [127,279,281]. The bands at 450 cm^{-1} and 556 cm^{-1} correspond to Si-O-Si symmetric stretching of Q^4 and Q^3 species, respectively [282].
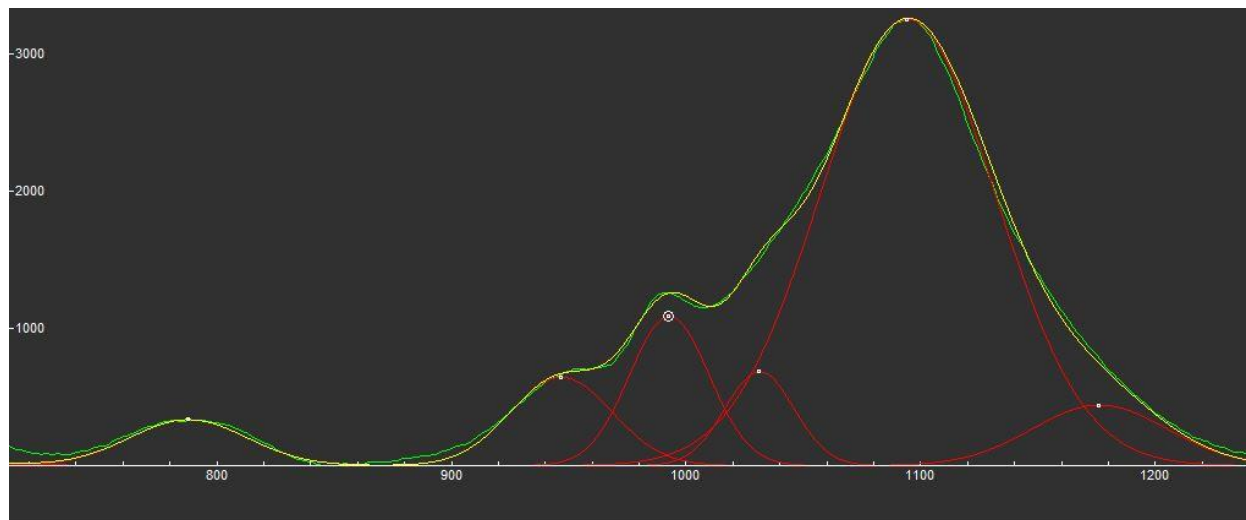
Figure 75 Deconvolution of Raman spectra of 0.00mol% Bi$_2$O$_3$ SLS

The ratio of bridging oxygen to non-bridging oxygen was calculated by fitting Gaussian peaks to the spectra of the base SLS, and 0.20mol% Bi$_2$O$_3$ SLS. A representative image is shown in Figure 75. Six peaks corresponding to Q^1 through Q^4 configuration were fitted using the FITYK program to minimise any residuals. Errors associated with this method were estimated to be ±2.5%, which include errors associated with any surface defects from the polishing regime, the optics within the Raman spectrometer and residuals from the fitted spectra to the data.

After the peaks were fitted corresponding to the various conformations of silicate tetrahedra the relative percentage areas of each peak were calculated in the FITYK program. The ratio of NBO to BO was then calculated, the undoped SLS has 36.1±2.5% NBO (and hence 63.9±2.5% BO), while 0.20mol% Bi$_2$O$_3$ SLS has 35.8±2.5% NBO (64.2±2.5% BO). As the difference between these samples is within the margin of error,

there is a 95% confidence that the addition of 0.20mol% of Bi_2O_3 does not change the polymerisation significantly in the SLS glasses prepared in this study.

5.2.2.2 PbO – Soda Lime Silica Glasses
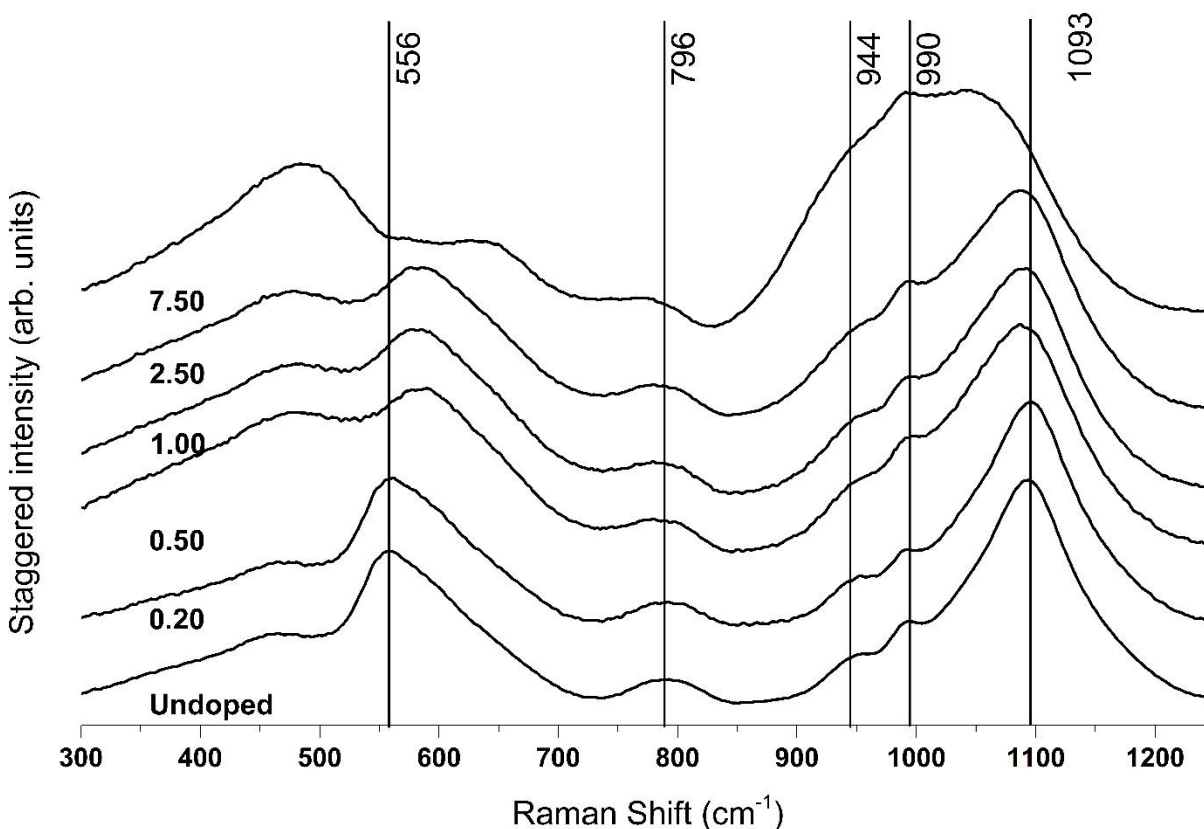
Figure 76 Normalised Raman spectra of base to 7.50mol% PbO SLS glasses

As shown in Figure 76 the 1093 cm^{-1} peak arises from a Si-O-Si stretching mode in Q^3 speciation. This Raman shift shifts to lower cm^{-1} with an increasing concentration of PbO shown in Figure 76, while the intensity of the band centred at 990 cm^{-1} increases. The band centred at 990 cm^{-1} corresponds to Q^2 configuration, indicating the average bond order is decreasing with increasing PbO content, depolymerising the glass network. This

is consistent with NBOs replacing BO. Traditionally PbO was added to glasses to lower viscosity, this effect occurs due to the increasing NBOs as a function of increasing PbO content.

5.2.2.3 Bi$_2$O$_3$ – Borosilicate Glasses
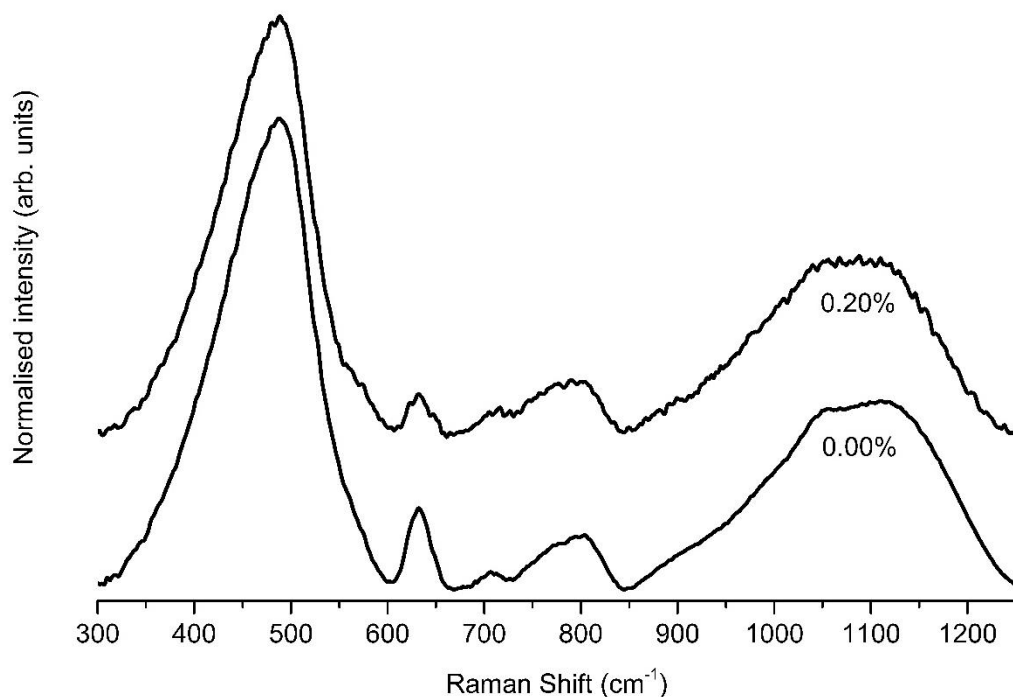
Figure 77 Normalised Raman spectra of base and 0.20mol% Bi$_2$O$_3$ borosilicate glasses
The structure of the Raman spectra of the undoped and 0.20mol% Bi$_2$O$_3$ doped borosilicate glasses is shown in Figure 77. The peak centred around 500 cm^{-1} is attributed to Si-O-Si bending modes [320] just as those found in soda lime silica glasses the Si-O-Si bending modes from Q^4 and Q^3 Si-O [282]. The small peak at ca. 630 cm^{-1} is attributed to BO$_3$ (danburite) units within the glass network [321]. The small peak centred at 700 cm^{-1} corresponds to the symmetric breathing modes of metaborate chains [322], and the shoulder peak at 760 cm^{-1} is related to the symmetric breathing mode of six membered

rings with a single BO_4^- in the ring [322]. The peak at 800 cm^{-1} corresponds to boroxol rings, i.e. $[B_3O_3]^{3-}$ structures [321], and the two overlapping peaks at 1050 cm^{-1} correspond to Si-O$^-$ stretching in Q^3 configuration and at 1130 cm^{-1} to fully polymerised $[SiO_4]^{2-}$ i.e. a Q^4 structure [320]. In the Raman spectra of borosilicate glasses, fluorescence of the sample is shown in the 0.20mol% Bi_2O_3 sample, evidenced by the greater level of noise relative to the undoped sample. This is not observed in the corresponding soda lime silica Bi_2O_3 doped glass as the total intensity was higher in this glass, resulting in a higher signal to noise.

5.2.3 Electron Paramagnetic Resonance Spectroscopy

5.2.3.1 Bi_2O_3 – Soda Lime Silica Glasses
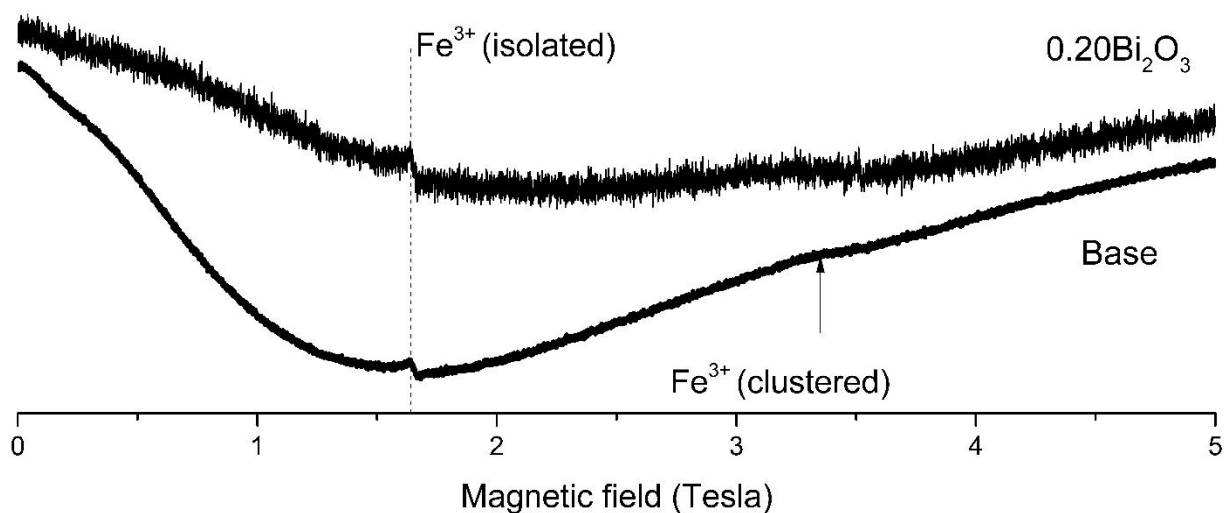
Figure 78 RT X-Band EPR of base and doped Bi_2O_3 Low Fe SLS

Figure 78 shows EPR spectra of powdered glass samples. The measurements were done in silica tubes at X-band frequencies. Two signals are present which are due to Fe^{3+} in

different environments. At g=4.3 (1.6 T) corresponds to isolated Fe^{3+} [166,287,288], and g=2.0 (3.4 T) of Fe^{3+} in an exchange coupled environment [270,287]. The resonance at g=2.0 has also been attributed to octahedral Fe^{3+} surrounded by oxygen ligands [163,289]. Although Fe_2O_3 was not added to these glasses intentionally, and the SiO_2 used had a specification of 10 ppm Fe_2O_3, impurities contained within the other raw materials give a resonances associated with Fe^{3+} in the order of 100 ppm as these are qualitatively consistent with other resonances found within the literature [163,291]. Resonances around g=2.0 are close to the free electron value [323], which may also be attributed to Ti^{3+} [324] or Mn^{2+} [270,271], Ti^{3+} is only found in heavily reducing glass melts [293,325]. As iron is the fourth most abundant element and is known to be a chronic impurity with glassmaking procedures these resonances have been assigned to be Fe^{3+}.

Control of the redox state of iron in glass is essential for any optical glass melting procedures. Typical Fe^{2+}/Fe^{3+} redox ratios of ca. 0.2 are common in commercial glasses and those prepared in a similar manner [162]. Van t'Hoffs law states the thermodynamic relationship between the heat of conversion (in this case between redox species) and the displacement of the equilibrium as a function of temperature change. As the temperature melted in this study was similar to that found in commercial glass melting furnaces it can be assumed the Fe^{2+}/Fe^{3+} redox ratios in the glasses in this study are similar to those found in commercial SLS glasses and other laboratory prepared glasses [56].

5.2.3.2 PbO – Soda Lime Silica Glasses
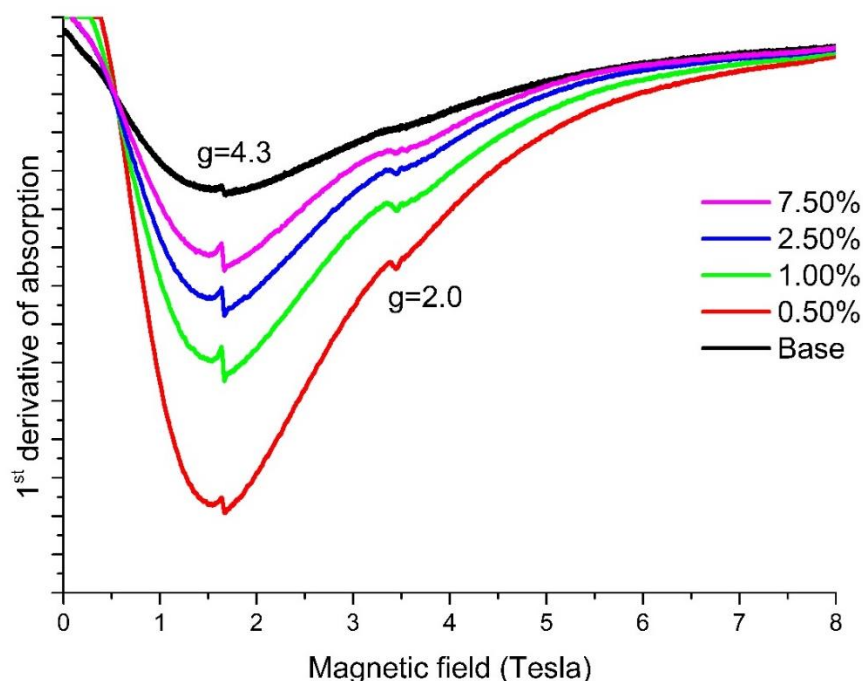
Figure 79 RT X-band EPR of base and PbO doped SLS glasses

In Figure 79 two resonances are observed, both from the contribution of Fe^{3+}. With increasing PbO content the resonance at both g=4.3 and g=2.0 increase, indicating additional impurity of Fe^{3+} from the PbO raw material. The resonances found in these glasses are of the same origin as those found in Figure 78.

5.2.3.3 Bi_2O_3 – Borosilicate Glasses

EPR spectra of borosilicate glasses shown in Figure 80, demonstrate the same EPR resonances of Fe^{3+} at g=2.0 (1.6 T) and g=4.3 (3.4 T) of those found in the comparable SLS glass shown in Figure 78. The intensity of the g=2.0 (3.4 T) resonance is lower, due to a lower total concentration of iron in the borosilicate system. This is also observed in the UV VIS IR spectra of borosilicate glasses relative to SLS glasses shown in Figure 81 and Figure 85.
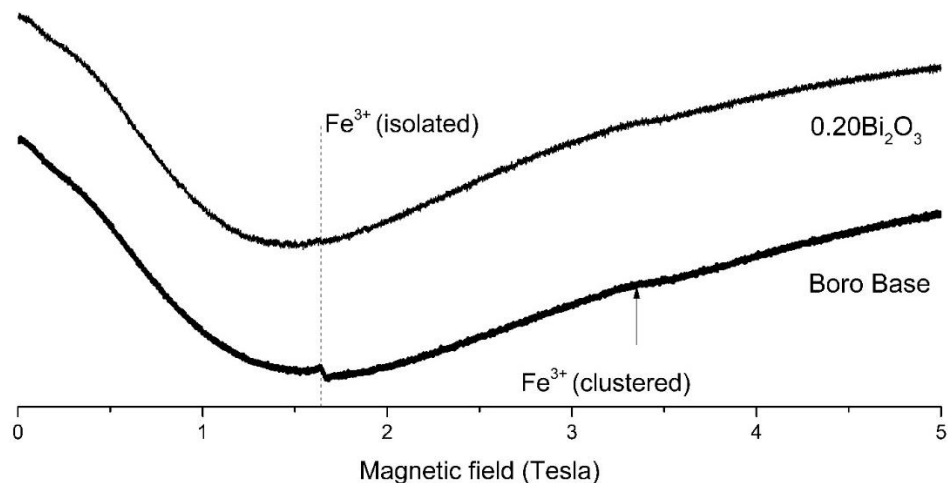
Figure 80 RT X-band EPR of base and Bi_2O_3 doped Borosilicate glasses

5.2.4 UV Vis NIR Absorption Spectroscopy

5.2.4.1 Bi_2O_3 – Soda Lime Silica Glasses

UV VIS IR absorption spectra of Bi_2O_3 doped and the corresponding undoped base glass are shown in Figure 81. These spectra all show a strong UV absorption edge arising from the Si-O network and network modifying cations. The Bi_2O_3 doped glasses shift the absorption towards the visible due to the attributed to $^1S_0 \rightarrow {}^3P_0$ and $^1S_0 \rightarrow {}^3P_1$ transitions, with increasing concentrations shifting towards the UV more strongly. 0.01mol% Bi_2O_3 shifts 1200 cm^{-1} (11 nm) closer to the visible than the base glass. The dotted line is reproduced from Yang et al [272] and extended with data from Fix *et al* [93], giving the absorbance of EVA glue. This value changes depending on the composition and age of the glue [28], with older, more irradiated glue having an absorption shifted towards the visible.
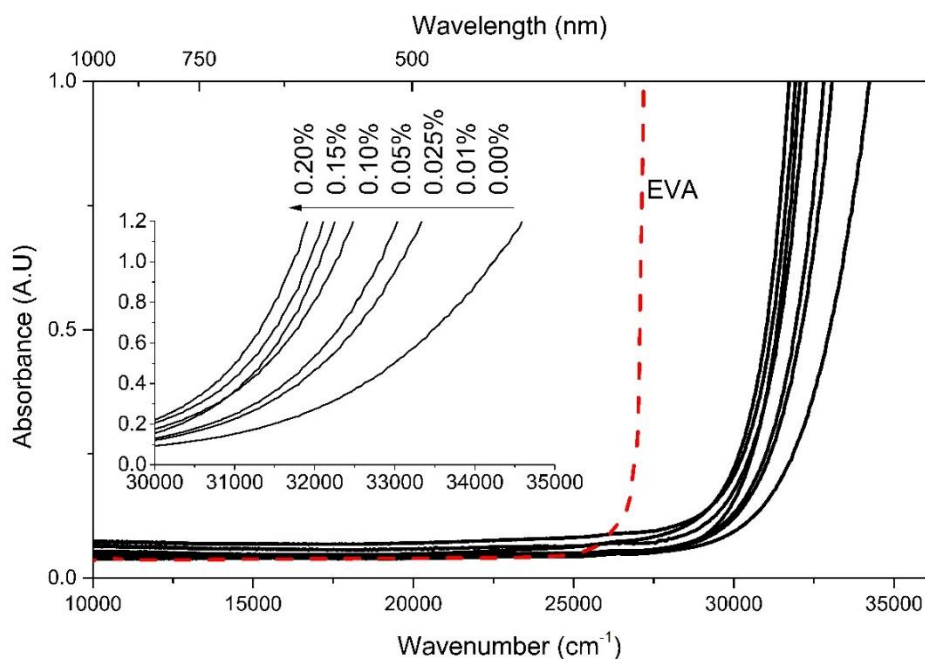
Figure 81 UV VIS IR absorption spectra of Bi$_2$O$_3$ doped and base SLS glasses, Red dotted line indicates the absorption of EVA glue.
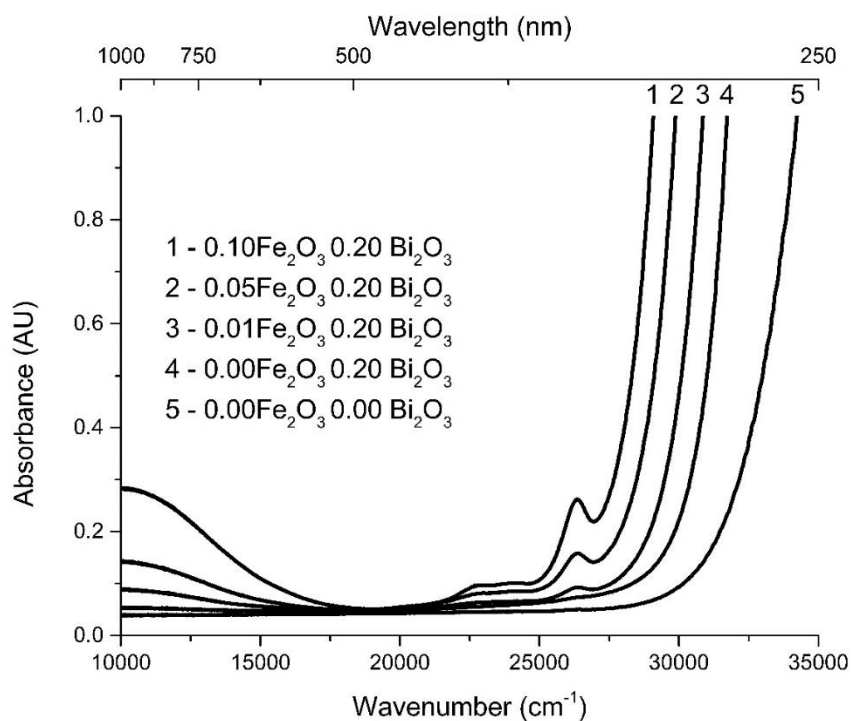
Figure 82 UV VIS NIR absorption spectra of Fe$_2$O$_3$ / Bi$_2$O$_3$ doped SLS glasses

Figure 82 shows the UV VIS NIR absorption of iron oxide and bismuth oxide doped silicate glasses, an undoped SLS is displayed for comparison. Increasing quantities of Fe_2O_3 shift the UV edge towards the visible. The prominent peak at 26,220 cm^{-1} corresponds to the $^6A_1(S) \rightarrow {}^4E(D)$ transition of Fe^{3+} [56]. Absorption in the IR region corresponds to Fe^{2+} corresponding to a $^5T_2(D) \rightarrow {}^5E(D)$ transition [56] and prevents the transmission of photons close to the bandgap of c-Si solar cells, deleteriously impacting efficiency.

5.2.4.2 SnO$_2$ – Soda Lime Silica Glasses
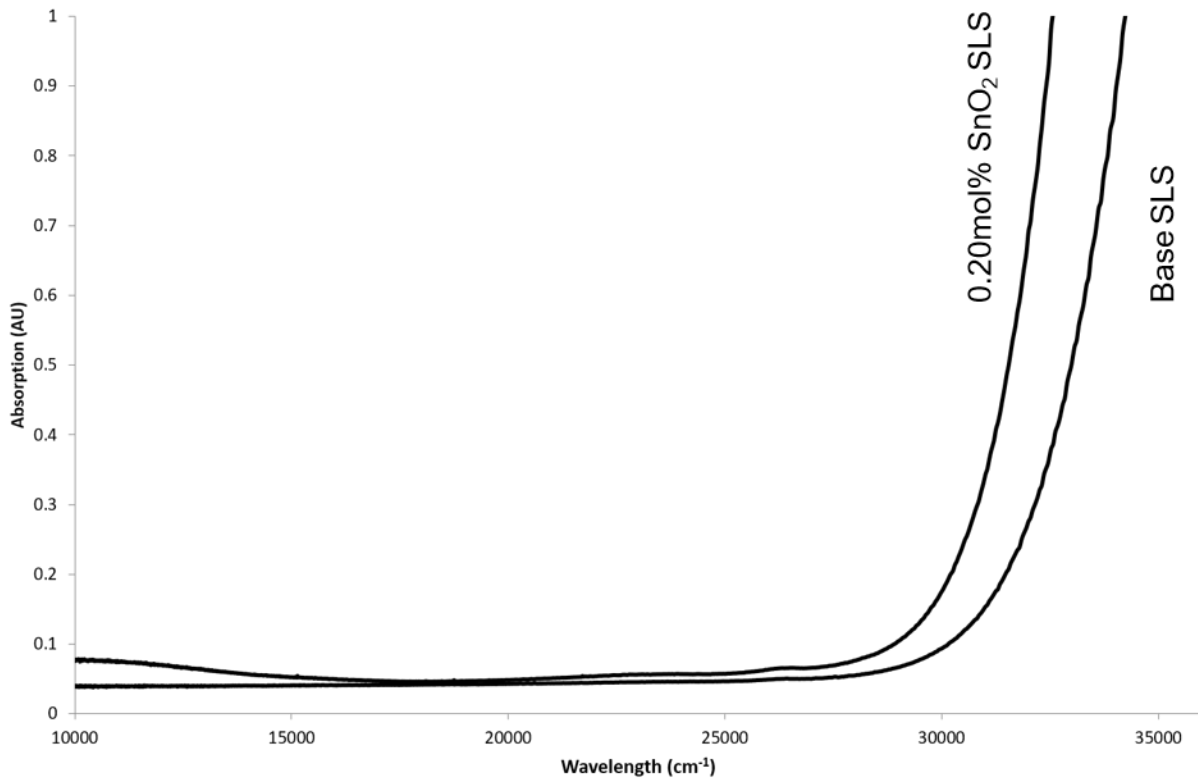
Figure 83 UV VIS NIR absorption spectra of 0.20mol% SnO$_2$ and Base SLS

The addition of 0.20mol% SnO$_2$ shifts the absorbance towards the visible relative to Base SLS. This corresponds to the same absorption as Bi_2O_3 and PbO, attributed to $^1S_0 \rightarrow {}^3P_0$

and $^1S_0 \rightarrow {}^3P_1$ transitions. There is an absorption towards the NIR increasing from 13,000 cm^{-1} to 10,000 cm^{-1} (750-1000 nm), likely from Fe_2O_3, as a band associated with Fe^{3+} is observed at ca. 26,200 cm^{-1}, which is of a higher magnitude than the corresponding base glass.

5.2.4.3 PbO – Soda Lime Silica Glasses
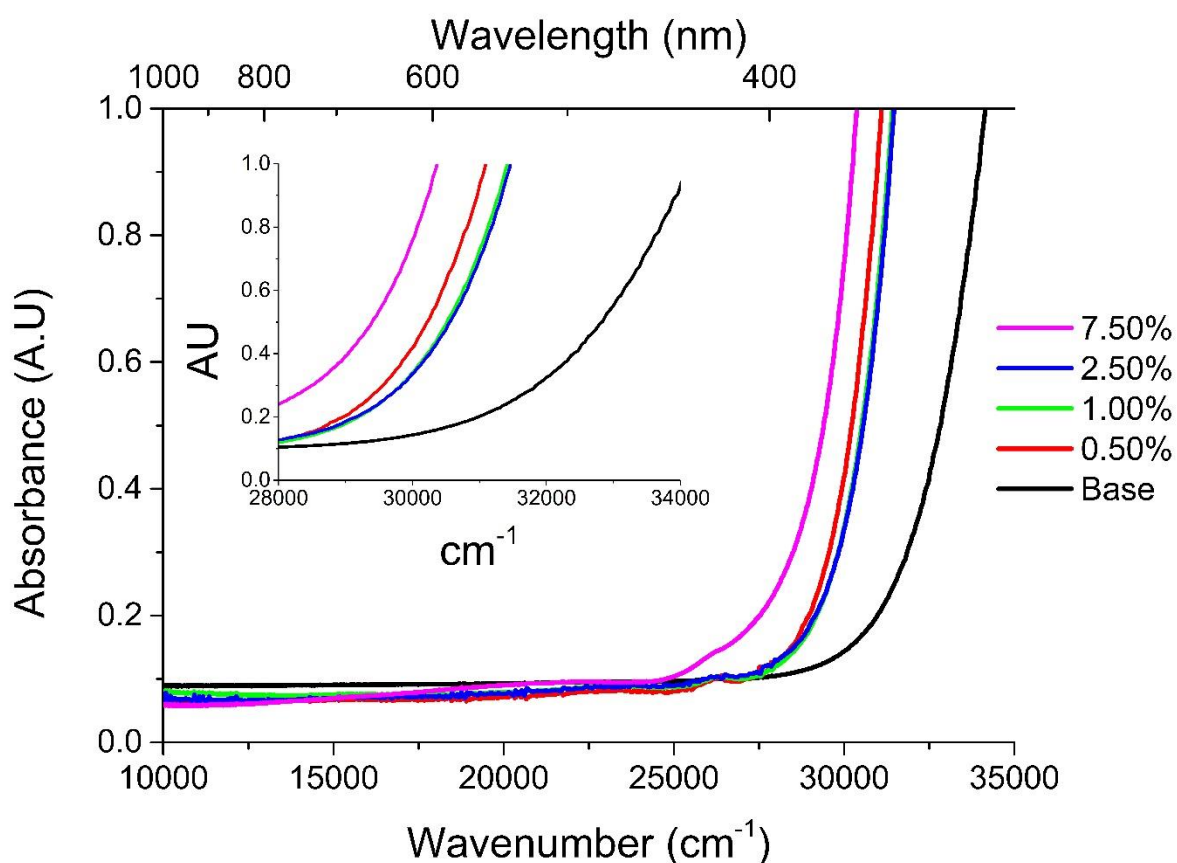
Figure 84 UV VIS IR absorption spectra of PbO doped SLS glasses

Figure 84 displays the UV VIS IR absorption spectra of PbO doped SLS glasses, as the glasses contained significant amount of residual bubbles from the Al_2O_3 crucible used in the melting procedure there is significant scattering and additional reflections. To partially

192

ameliorate this behaviour measurements were taken at five different spots on each sample, and subsequently averaged. The method showed clearly the absorbance of PbO doped glasses is distinct from that of the base glass (which was melted in ZGS-Pt, whereas the PbO glasses were melted in Al_2O_3) , which also was measured five times and averaged. Between 0.50mol% PbO SLS and 2.50mol% PbO SLS absorbance are within the error range (±2 nm) of the instrument and set up. With 7.50mol% PbO SLS the absorbance edge is shifted further towards the visible region by circa 4000 cm^{-1} (40 nm), due to the $^1S_0$ to $^3P_0 / ^3P_1$ transition [326].

5.2.4.4 Bi_2O_3 – Borosilicate Glasses
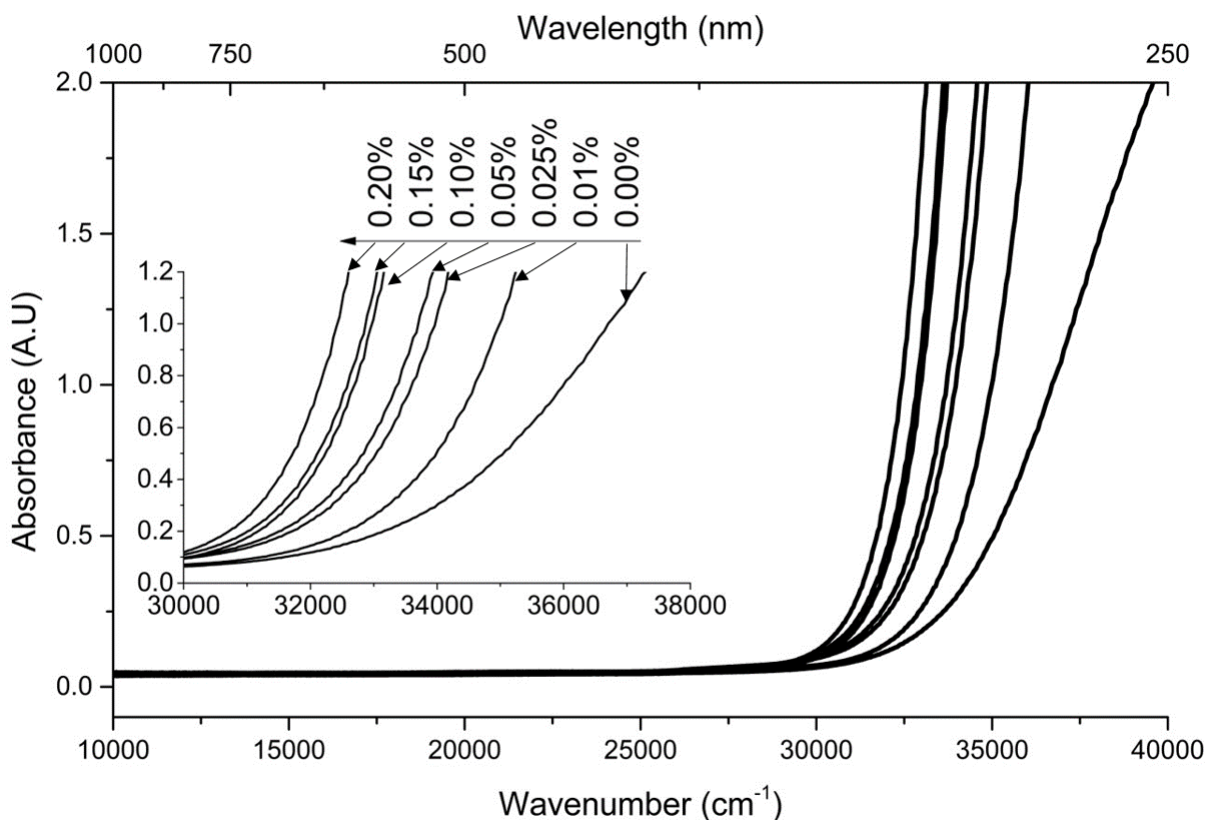
Figure 85 UV VIS IR absorption spectra of Bi_2O_3 doped Boro glasses

193

UV VIS IR absorption spectra of Bi_2O_3 doped and base Boro glasses are shown in Figure 85. As with the absorbance spectra in the corresponding SLS glasses shown in Figure 81 all glasses show a strong UV absorption edge from the Si-O network and modifying network cations. The shift from the base to doped glasses is attributed to $^1S_0 \rightarrow {}^3P_0$ and $^1S_0 \rightarrow {}^3P_1$ transitions, and with increasing concentration of Bi_2O_3 there are stronger shifts towards the visible relative to the base glass.

5.2.5 UV Vis Fluorescence Spectroscopy

5.2.5.1 Bi_2O_3 – Soda Lime Silica Glasses
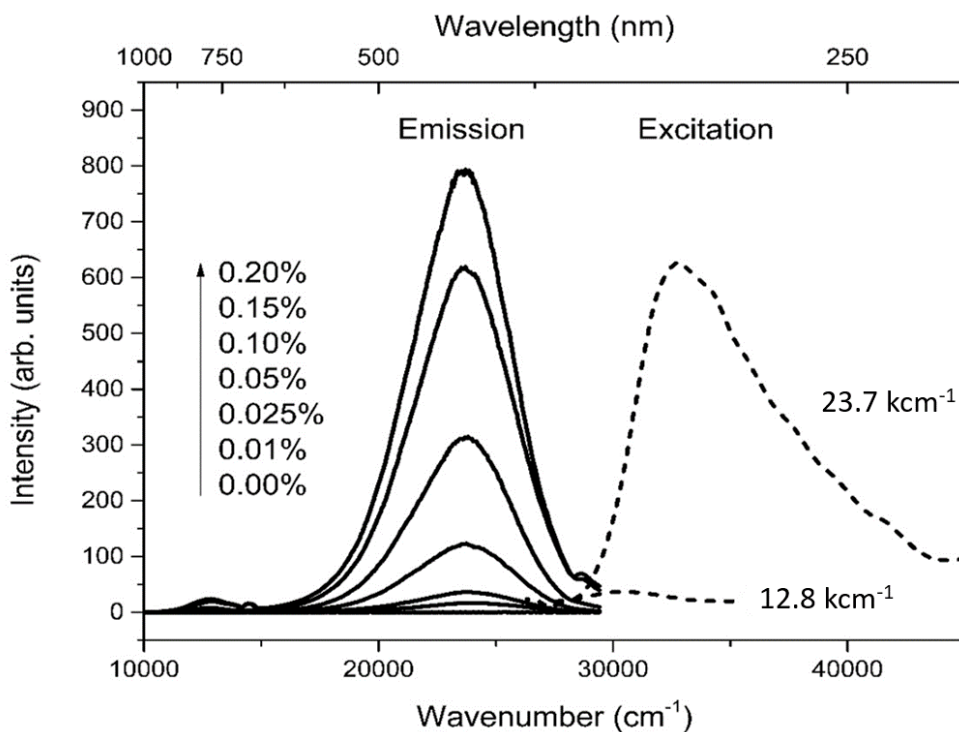
Figure 86 Excitation (dotted) and emission (solid) spectra of Bi_2O_3 doped SLS glasses

The fluorescence excitation and emission spectra of Bi_2O_3 doped SLS glasses are shown in Figure 86. The emission spectra are from excitation at 33,300 cm^{-1} (300 nm), and

shows with increasing doping concentration of Bi_2O_3 the emission intensity increases, concentration quenching was not observed in the doping range studied here. All emission profiles are broadband and featureless centred at 23,700 cm^{-1} (430 nm) and 12,800 cm^{-1} (780 nm). The excitation spectra (dotted) show which energies give the most emission intensity at 23,700 cm^{-1} and 12,800 cm^{-1}. The excitation spectra are attributed to $^1S_0 \rightarrow$ $^3P_0$ and $^1S_0 \rightarrow {}^3P_1$ and the emission spectra are attributed to $^3P_1 \rightarrow {}^1S_0$ [327]. The strongly forbidden transition $^3P_0 \rightarrow {}^1S_0$ [328] is not observed in the spectra due to the samples being measured at RT.
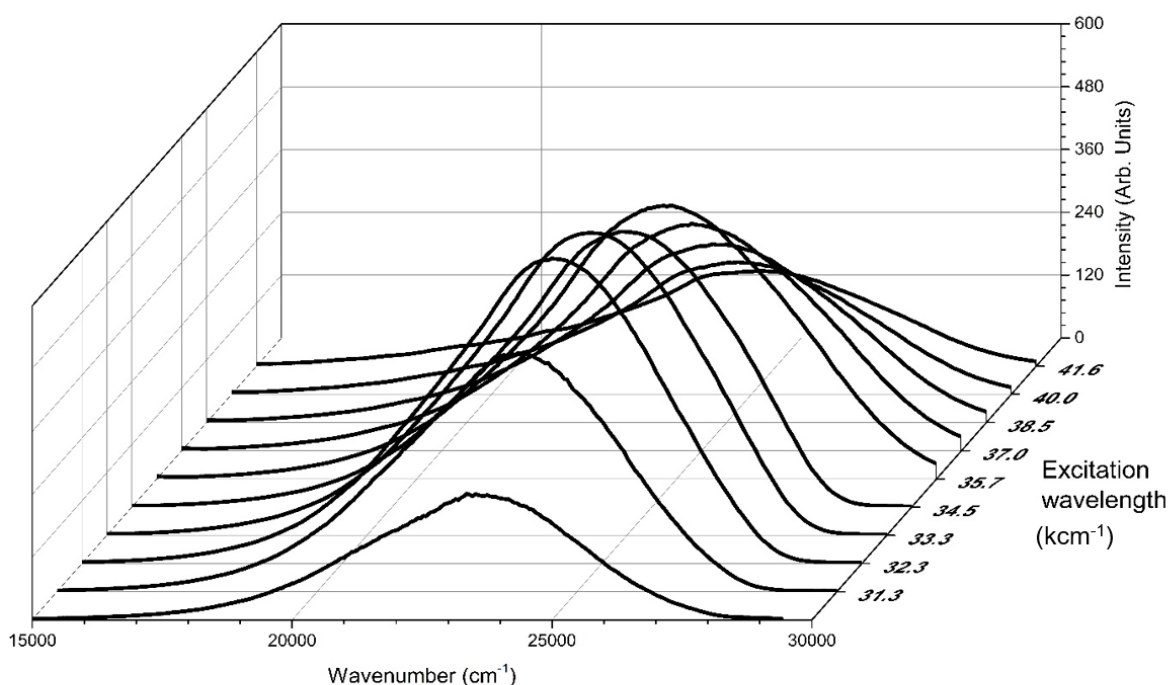
Figure 87 Emission spectra of 0.20mol% Bi_2O_3 SLS as a function of excitation wavenumber

The emission spectra shown in Figure 87 displays the emission spectra with different excitation wavenumbers. Within the deep UV there are inefficiencies of absorption due to

the photons having higher energy than the bandgap of Bi^{3+}, between 35,700 cm^{-1} (280 nm) and 33,300 cm^{-1} (300 nm) shows the greatest emission intensity. To maintain the total emission intensity below the saturation limit of the photomultiplier tube detector in the fluorescence spectrometer the emission slit width was reduced from 20 nm to 10 nm, and therefore the total counts of emission are lower than that given in Figure 86.

Figure 88 NIR fluorescence emission spectra of 0.20mol% Bi₂O₃ SLS (ex 12,500 cm⁻¹ 800 nm)

Bismuth in both Bi^{2+} and Bi^{3+} oxidation states do not emit in the IR at 7700 cm^{-1} (1300 nm) with 12,500 cm^{-1} (800 nm) excitation [329]. The band between 1170 nm and 1230 nm corresponds to an 3/2λ peak superimposed onto the spectra from the 800 nm excitation which had ±20 nm range. There is significant noise within the spectra in Figure

88 due to no signal being detected at 1300 nm. As the there is no peak at 1300 nm it suggests the oxidation state of Bi_2O_3 is in the Bi^{3+} oxidation state.
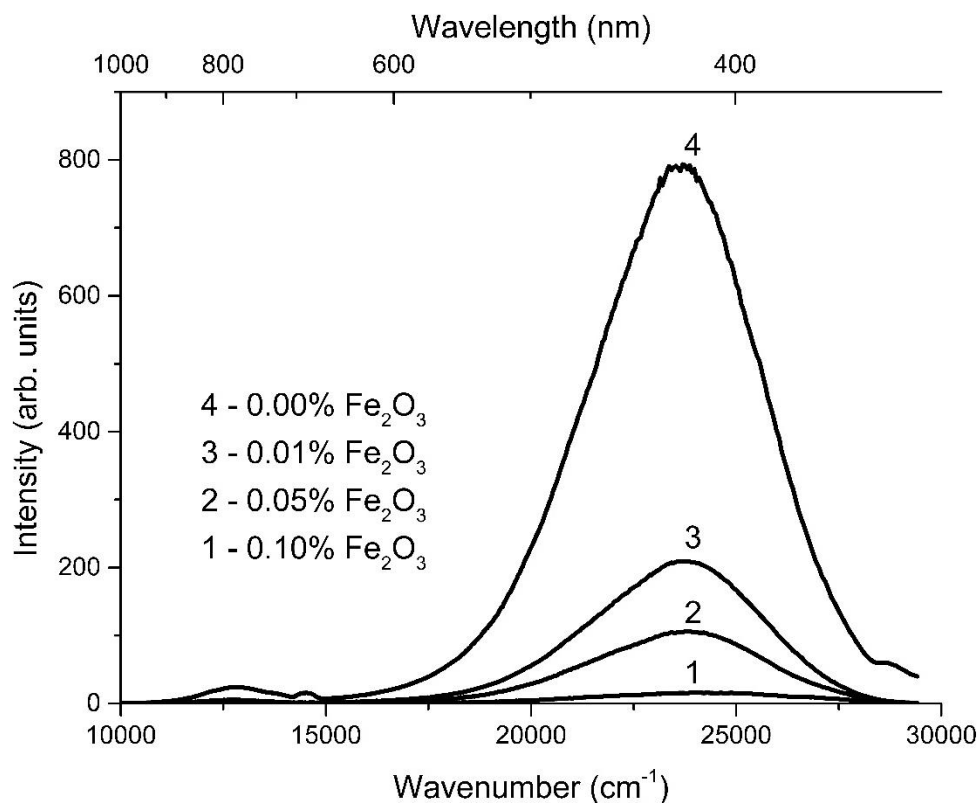
Figure 89 Fluorescence emission of 0.20mol% Bi_2O_3 (33,300 cm^{-1} / 300 nm excitation) with increasing Fe_2O_3 in mol%

Figure 89 shows the fluorescence emission spectra of 0.20mol% Bi_2O_3 in glasses with increasing quantities, in mol%, of Fe_2O_3. Through competitive absorption of UV photons as shown in Figure 82 and fluorescence quenching the total fluorescence emission intensity of Bi^{3+} decreases with increasing Fe_2O_3 concentration.

5.2.5.2 SnO$_2$ – Soda Lime Silica Glasses
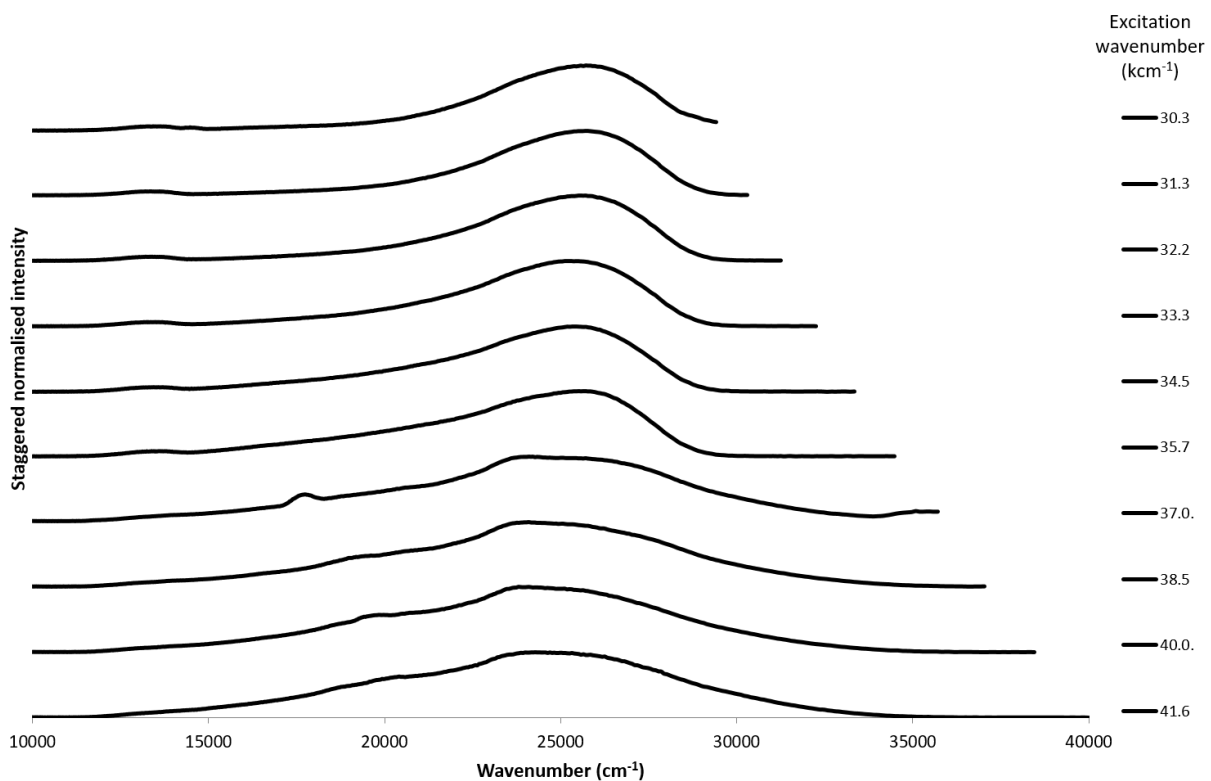
Figure 90 Fluorescence emission spectra of 0.20mol% SnO$_2$ SLS

Figure 90 shows the emission spectra of 0.20mol% SnO$_2$ SLS excited at various excitation wavenumbers. The emission profile is similar to that of glasses doped with Bi$_2$O$_3$ and PbO. The emission of SnO$_2$ can be used to identify which surface was in contact with the tin bath in float glasses [247].

5.2.5.3 PbO – Soda Lime Silica Glasses
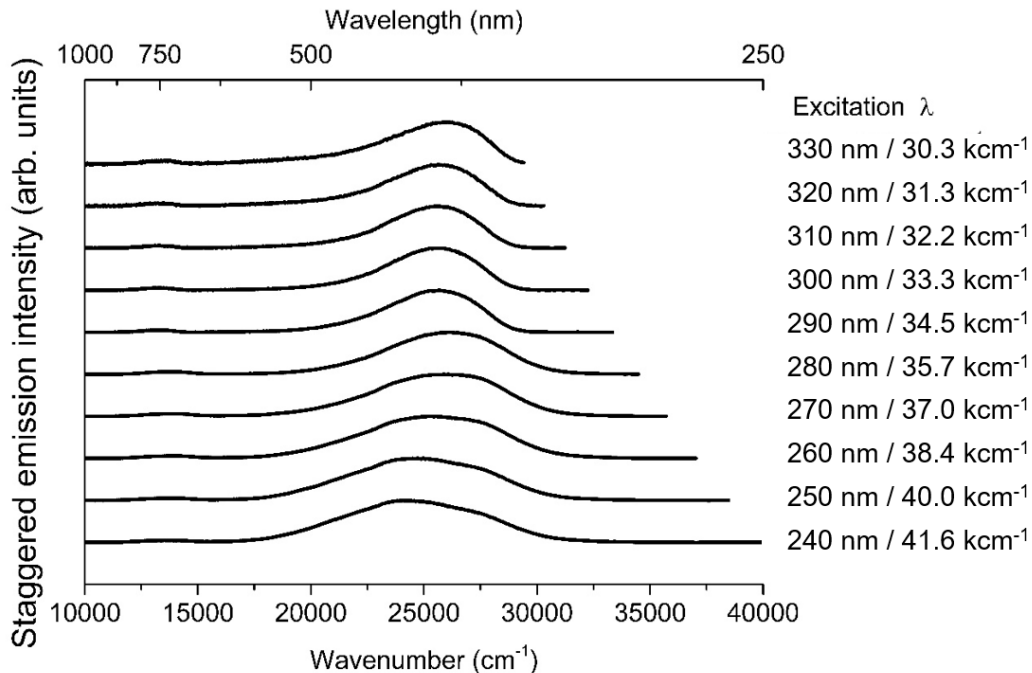
Figure 91 Fluorescence emission spectra of 0.50mol% PbO SLS

Between excitation at 35,700 cm^{-1} (280 nm) and 34,500 cm^{-1} (290 nm) a filter change was applied on the fluorescence spectrometer as shown by the non-Gaussian peak shapes in the emission spectra above this filter change. This is demonstrated in Figure 91, Figure 92, Figure 93, and Figure 94. The filter attenuated photons with energy higher than 35,700 cm^{-1} (lower than 280 nm), this was applied to remove secondary peaks superimposed onto the spectrum from the monochromator allowing light of 2λ through.
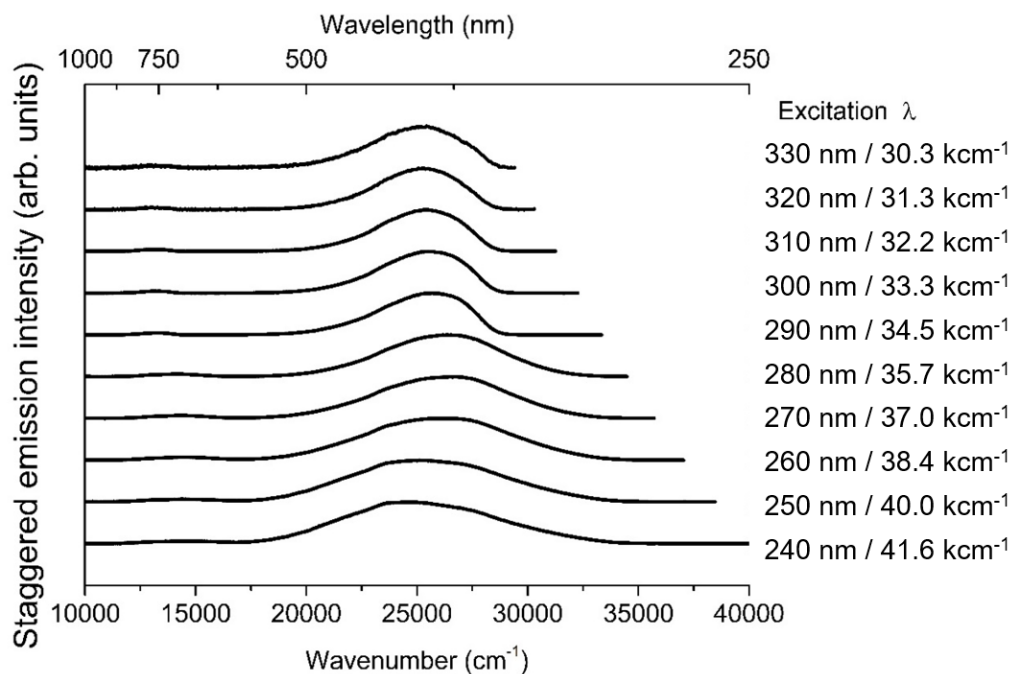
Figure 92 Fluorescence emission spectra of 1.00mol% PbO SLS
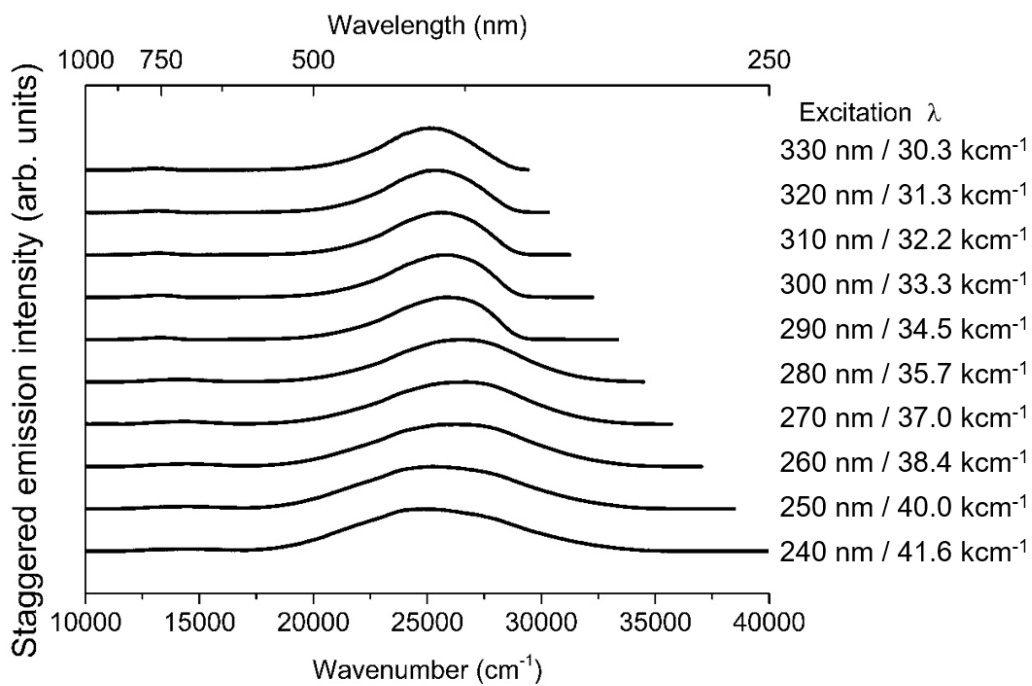
Figure 93 Fluorescence emission spectra of 2.50mol% PbO SLS
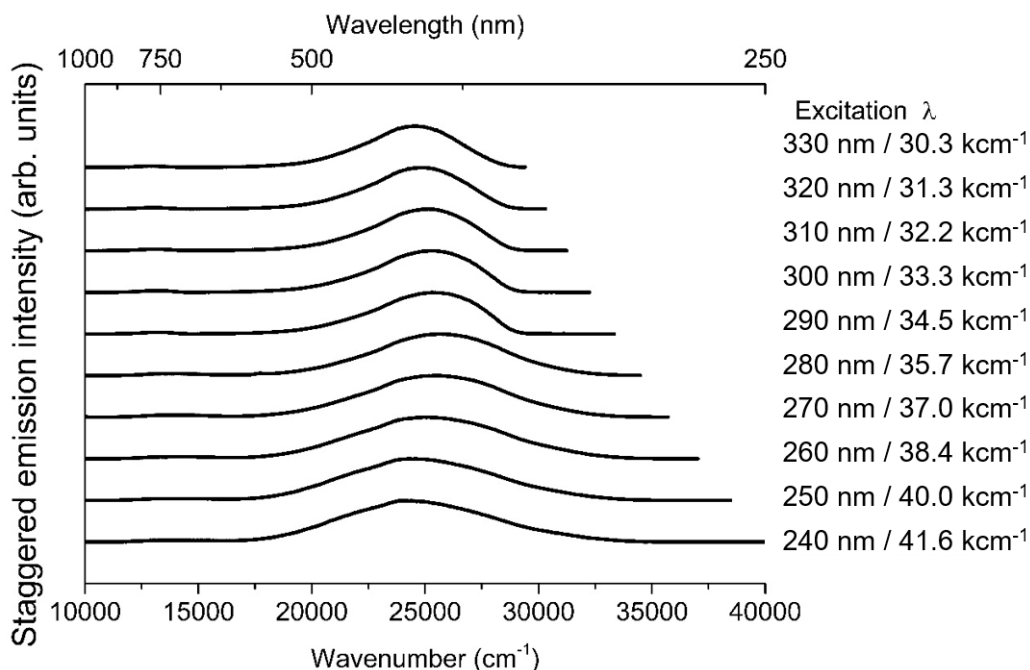
Figure 94 Fluorescence emission spectra of 7.50mol% PbO SLS

With increasing PbO content the emission shifts from 26,000 cm^{-1} (384 nm) for 0.50mol% (Figure 91) PbO SLS, to 24,000 cm^{-1} (416 nm) for 7.50mol% (Figure 94). This is attributed to the emission of a photon losing more energy to the creation of a phonon in glasses containing increasing quantities of PbO, and therefore emitting less energy in a radiative decay mechanism. The intensity of emission increases from between 0.50mol% PbO SLS to 2.50mol% PbO SLS before being less emissive in 7.50mol% PbO SLS as shown in Figure 95. The emission intensity between 0.50mol% PbO and 2.50mol% PbO is a function of concentration, but at 7.50mol% PbO there is a combination of concentration quenching and the phonon losses are greater resulting in a lower intensity of emission, this is displayed clearly in Figure 95.
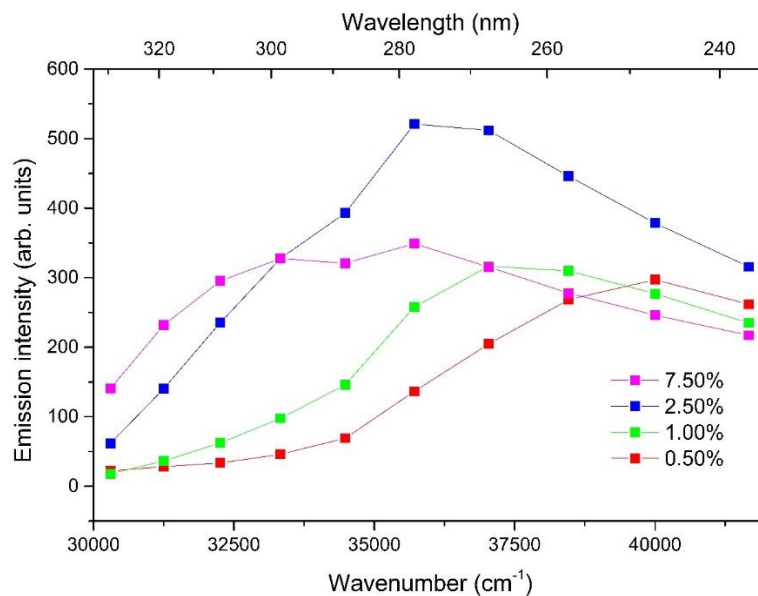
Figure 95 Emission intensity of PbO doped SLS glasses as a function of excitation energy

5.2.5.4 Bi$_2$O$_3$ – Borosilicate Glasses

The fluorescence excitation and emission spectra of Bi$_2$O$_3$ doped Boro glasses are shown in Figure 96. The emission spectra are from excitation at 33,300 cm^{-1} (300 nm). With increasing doping concentration, the emission intensity increases. There is no change in λ$_{max}$ as a function of doping concentration. The emission profiles are broadband and centred at 25,100 cm^{-1} (398 nm), and second minor peak centred at 13,400 cm^{-1} (746 nm). The excitation spectra (dotted lines) show the emission intensity at the highlighted wavenumber for the given excitation wavenumber, i.e. at 40,000 cm^{-1} excitation the emission at 25,100 cm^{-1} is in the order of 80 counts. The excitation spectra are attributed to $^1S_0 \rightarrow {}^3P_0$ and $^1S_0 \rightarrow {}^3P_1$ and the emission spectra are attributed to $^3P_1 \rightarrow {}^1S_0$ [327].
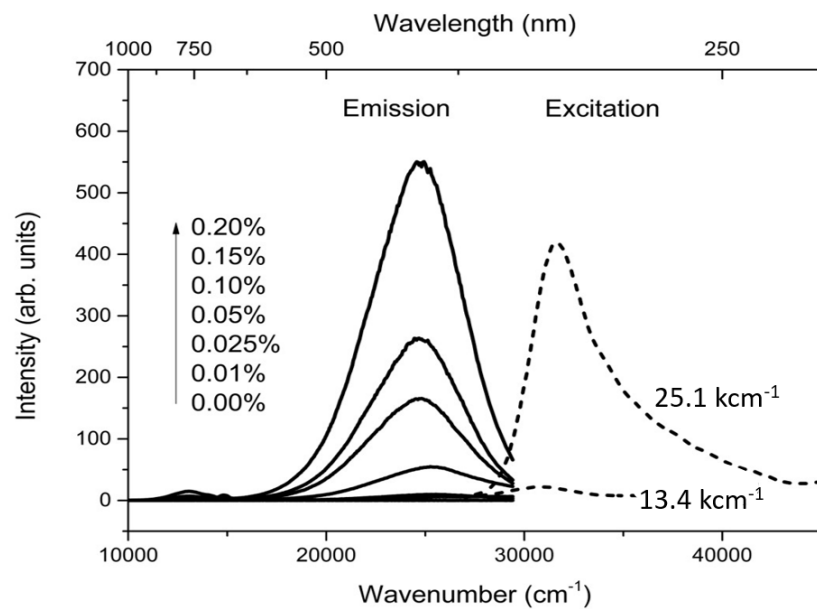
Figure 96 Excitation (dotted) and emission (solid) spectra of Bi_2O_3 doped Boro glasses
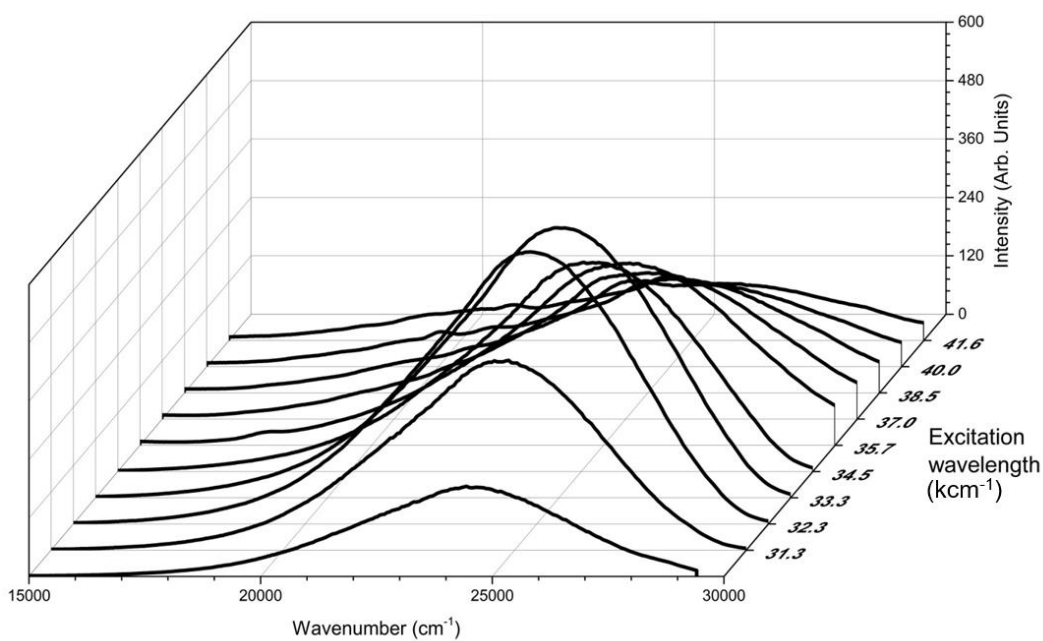
Figure 97 Emission spectra of 0.20mol% Bi_2O_3 Boro as a function of excitation wavenumber

5.2.6 X-Ray Absorption Near Edge Structure Spectroscopy

5.2.6.1 Bi_2O_3 – Soda Lime Silica Glasses

The oxidation state of bismuth in bismuth containing materials may be detected through XANES measurements. In Bi^{n+} containing samples, a characteristic hump is ascribed to transitions of $2p^{3/2}$ to 6s states [330]. Conventionally, standard materials of different oxidation states are used to define the edge position of those to be expected within the unknown samples. With increasing formal charge, the edge position shifts towards higher energy, as atoms with a higher formal oxidation state require a higher energy X-ray photon to excite the core electron due to the nucleus being less shielded. This shift to higher energy with increasing formal charge is shown in Figure 98.
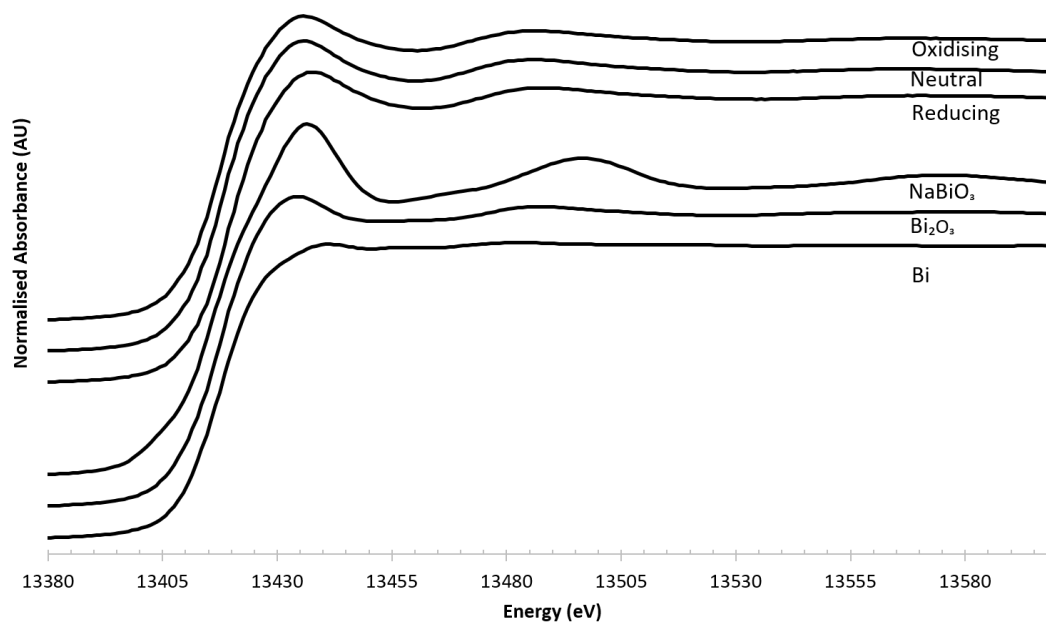
Figure 98 XANES absorption of bismuth standards and Bi_2O_3 doped SLS glasses

From Figure 98 there are clear differences between the absorbance of different bismuth containing standards. Bi metal shows a flat profile from after the absorption edge, while Bi_2O_3, with a formal charge of 3+ on the Bi atom shows a peak at 13,422 eV. This peak is larger in the $NaBiO_3$ sample with a second peak at circa 13,480 eV.

Bismuth oxide doped silicate glasses prepared in oxidising (the addition of Na_2SO_4), neutral (no additions) and reducing (the addition of C) all demonstrate a peak at 13,422 eV without a peak at 13,480 eV, shown in Figure 98, which indicates all are in Bi^{3+} oxidation state, as compared to the Bi containing standard materials.

5.2.7 Differential Scanning Calorimetry

5.2.7.1 Bi_2O_3 – Soda Lime Silica Glasses
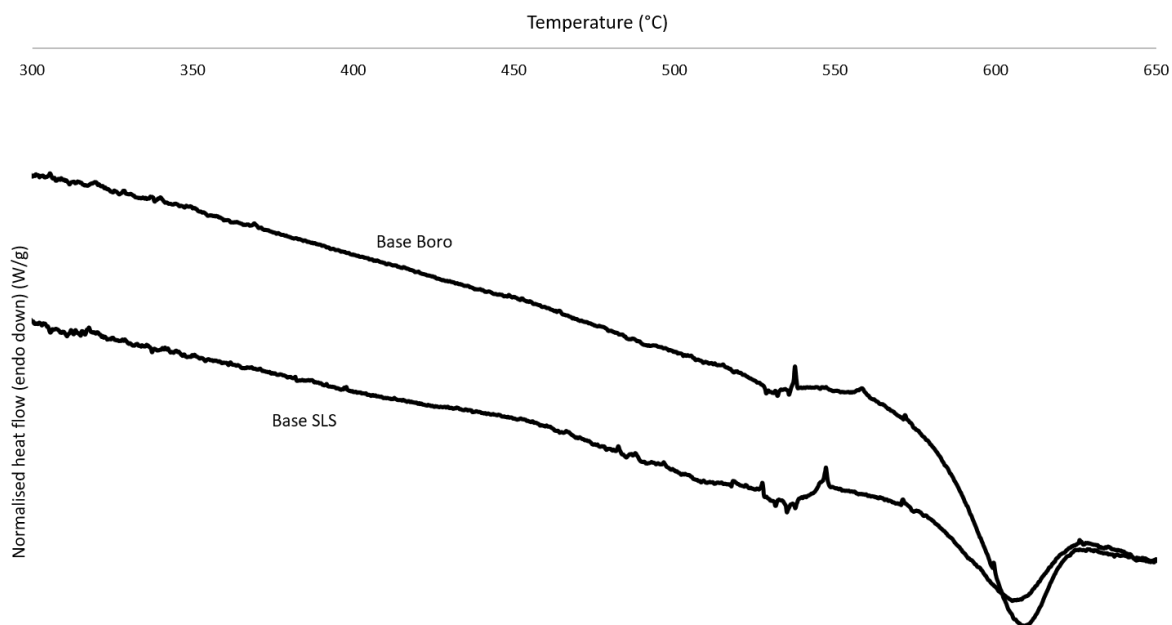
Figure 99 DSC of base SLS and Boro glasses

The DSC thermograph shows an endothermic glass transition temperature with an onset of ca. 570°C for both SLS and Borosilicate base glasses shown in Figure 99. The peaks superimposed onto the thermograph are instrumental in origin. The scan rate was 10°C/min.

5.2.6 X-Ray Fluorescence Spectroscopy

XRF of SLS base glasses are displayed in section 3.1.1.2. All samples are close to the nominal indicating little volatilisation during the melting procedure. In conjunction with the density measurements being within the range expected for glasses of this composition it is expected the samples are very close to the nominal composition. As expected doped glasses have a greater density, due to the more dense constituents Bi_2O_3 replacing SiO_2 within the melt [261,278,331].

To elucidate further the concentration of Bi_2O_3 within the glasses inductively coupled plasma – optical emission spectroscopy (ICP-OES) may be carried out which can readily detect ppm levels of Bi, whereas the XRF spectrometer used within this study was not sensitive enough below circa 0.5wt%. Boron is transparent to the X-rays used in the XRF spectrometer used and therefore an accurate concentration of B_2O_3 could not be achieved with this method. ICP-OES would be able to detect the concentration of boron remaining within the glass samples.

5.3 Discussion

The XRD patterns shown in Figure 72 and Figure 73 do not show Bragg diffraction peaks within the resolution of the instrument, confirming the amorphous nature of the glasses produced. These diffraction traces are similar to those shown in other SLS [124,316] and lead crystal type glasses [332]. There is a shift in °2θ between 2.50mol% PbO SLS and 7.50mol% PbO SLS, indicating a volume increase in this glass system. This is indicative of an increase in NBO, which increases the volume of a glass network [333]. Although incorporation of PbO into silicate glasses increases the proportion of NBO's, which lowers the viscosity of the melt, incorporation of isoelectronic Bi_2O_3 did not appreciably increase the proportion of NBOs within these glasses shown by the deconvolution of Raman spectra in Figure 74 and Figure 75. The base SLS glass, shown by deconvolution of the Raman spectra, has 36.1±2.5% NBO, while incorporation of 0.20mol% Bi_2O_3 has NBO corresponding to 35.8±2.5% of the silicate network. This small variation is within the error margins and is therefore unlikely the incorporation significantly modifies the glass network.

While Bi-O-Bi vibrations in distorted BiO_6 units may give Raman shifts ca. 575 cm^{-1}, and Bi-O-Bi stretching vibrations in the distorted BiO_6 unit are found at ca. 360 cm^{-1} [334], neither of these bands are shown in the Raman spectra of Bi_2O_3 doped glasses in Figure 74 or Figure 77. In Bi_2O_3-SiO_2 glasses with increasing concentration of Bi_2O_3 reduces the Q^4 proportion towards Q^1 speciation over the range 30mol% to 90mol% shown by ^{29}Si MAS-NMR [335]. With increasing Bi_2O_3 content a greater proportion of oxygen atoms are in a Bi-O-Bi or Si-O-Bi bonding configuration, which depolymerises the network. This effect has not been resolved in the Raman spectra shown in Figure 74, and after

deconvolution, indicating the concentration of bismuth is below the threshold for depolymerisation to be a critical and observed effect.

Within the Raman spectra of PbO doped SLS glasses shown in Figure 76 there is an increase in the intensity of the band centred at 990 cm^{-1} in 7.50mol% PbO SLS, which corresponds to a Q^2 conformation. This corresponds to an increase in the relative proportions of NBO within the network and a subsequent lowering of viscosity. The other peaks within Figure 76 correspond to the Q^n configurations outlined with Figure 74. Between 0.00mol% PbO SLS and 2.50mol% PbO SLS structural variations are not resolved clearly. Kacem et al demonstrated the increase of the Q^2 band with incorporation of 5mol% PbO in a silicate glass [336], a similar effect is observed here. With increasing PbO content the successive formation of Q^1 and Q^0 bands form at the loss of Q^4 speciation in agreement with Neuville et al [336,337], however the glasses prepared in this study were below the threshold of PbO content to observe this effect.

The structure of borosilicate glasses is commonly discussed within the literature [320]. The Raman spectra of base Boro and 0.20mol% Bi_2O_3 Boro is shown in Figure 77, the dominant peak centred at circa 500 cm^{-1} corresponds to Si-O-Si bending modes from Q^4 and Q^3 Si-O configurations [282,320]. The Raman profile shown in Figure 77 is similar to those found in the literature of similar borosilicate systems [320,321]. A small shoulder peak at ca. 575 cm^{-1} appears in the 0.20mol% Bi_2O_3 doped borosilicate Raman spectra in Figure 77, this is attributed to Bi-O-Bi vibrations in distorted BiO_6 octahedra [334]. A 0.20mol% addition of Bi_2O_3 in the borosilicate matrix shows no crystallinity according to the Raman spectra shown in Figure 77. None of the dopants added to either SLS or Boro type glasses induced crystallinity as shown by the XRD traces and Raman spectra.

Glasses of SLS and Boro type systems doped with up to 0.20mol% Bi_2O_3 may be applicable for the front sheet of PV modules as no crystallisation is observed.

DSC of SLS and Boro base glasses shows a broad endothermic peak with an onset of 570°C in Figure 99. No other peaks associated with crystallisation are on the thermograms, indicating both systems are amorphous. The T_g measured depends on heating rate, in Figure 99 the heating rate was at 10°C/min. No crystallisation peaks were observed and a T_g was similar to those found in the literature for SLS [261] and Boro type glasses [321]. The composition was close to the nominal value as shown through XRF and density measurements which are commensurate with those found in literature [261] and through the SciGlass database [338].

EPR was undertaken to assist in the elucidation of the oxidation state of bismuth. While Bi^+, Bi^{3+}, and Bi^{5+} are EPR silent as none have unpaired electrons, Bi^{2+} and Bi^{4+} would display a resonance. Two resonances from Fe^{3+} were expected and shown in Figure 78, Figure 79, and Figure 80. All display the characteristic resonances of Fe^{3+} at g=2.0 and g=4.3 [270,271,339] and no additional resonances indicating reduction or oxidation to Bi^{2+} and Bi^{4+} did not occur. Bi^{2+} resonances occur at g=1.54, g=1.38, and g=1.62 [301], while Bi^{4+} has a resonance at g=2.00 and ca. g=2.30 [340,341]. Although there is a peak at g=2.0 the second peak at g= 2.30 corresponding to Bi^{4+} was not observed, therefore these species are not present in detectable quantities. In lead containing glasses, with increasing PbO content the resonances at g=2.0 and g=4.3 also increase. This indicates the PbO raw material contained a larger proportion of Fe_2O_3 impurity than other raw materials, along with the higher concentration used i.e. 7.50mol% PbO to 0.20mol% Bi_2O_3, (37.5 times higher concentration). UV-VIS absorbance shows a Fe^{3+} absorption

peak at 26,220 cm^{-1} (381 nm) corresponds to the $^6A_1(S) \rightarrow ^4E(D)$ transition of Fe^{3+} [56], in Figure 84 this peak is most intense in 7.50mol% PbO SLS, indicating an increased concentration of Fe^{3+} species.

The aqueous electrochemical potential of Bi^{3+} to Bi^0 is +0.317 V while that of Fe^{3+} to Fe^{2+} is +0.771 V [342], therefore before Bi^{3+} would be reduced, Fe^{3+} would be fully reduced to Fe^{2+}. As Fe^{3+} is observed within all the glasses prepared in this study according to their UV VIS IR absorption spectra it can be concluded the reduction of Bi^{3+} is unlikely to have taken place. This is further shown in the EPR traces.

As shown through EPR measurements, the presence of Bi^{2+} and Bi^{4+} is not observed, therefore Bi^+, Bi^{3+} and Bi^{5+} are still possible candidates. XANES measurements require standard known oxidation states of standard materials to be analysed in conjunction with the sample of unknown valence. A core electron is excited with an X-ray of a particular energy, the energy relates to the element and valence. Higher oxidation states of elements require higher energy X-ray photons to excite the core electron due to higher nucleus shielding and electrostatic interactions. Figure 98 shows the XANES absorption of Bi metal, Bi_2O_3, and $NaBiO_3$, with characteristic absorption edges and post-absorption features. Bi metal shows a featureless absorption edge with no additional resonances, Bi_2O_3 has a resonance at the peak of the absorption at circa 13,422 eV, while $NaBiO_3$ shows this same resonance at 13,422 eV, and a second peak at circa 13,480 eV. The three SLS glasses analysed were prepared in oxidising (with 0.22mol% Na_2SO_4), neutral (with no redox reagents) and reducing (0.22mol% C). The XANES absorbance of these glasses are shown in Figure 98, and are most similar to the profile of Bi_2O_3 standard material. This is indicative that in the melt conditions the redox potential was not sufficient

to change the valence of Bi. The carbon added may have reduced the Bi^{3+}, which subsequently was oxidised again as the furnace atmosphere was in air. No measurements of concentration of Bi containing species were made in these glasses. Critically the oxidation state is not in Bi^{5+} as there are no peaks in Figure 98 at 13,480 eV in any of the Bi_2O_3 doped glasses.

EVA glue, the most commonly used glue polymer in PV modules [20], degrades under UV light. This process ultimately causes critical failure, therefore for effective protection of polymer species within a PV module, the front sheet must absorb these damaging UV photons, ideally to completely overlap the absorption of the EVA glue layer. The glass front sheet however must be low cost, and to prepared at large scale using existing infrastructure. Therefore significant changes to a SLS or Boro type glass would result in changes to the melt conditions and subsequently add cost to the module.

As shown in Figure 81 there is a shift of the UV edge of circa 2000 cm^{-1} (20 nm) from the base glass to 0.20mol% Bi_2O_3 SLS. UV photons of higher energy do more damage than lower energy photons and more rapidly degrades the polymers [28], therefore small shifts towards the visible may provide significant protection to the module. Low quantities of Fe_2O_3, even 0.01mol%, can reduce module output by 1.1% due to absorbance bands at 26,220 cm^{-1} and 11,000 cm^{-1} (381 nm and 909 nm) of Fe^{3+} and Fe^{2+} respectively [58] as shown in Figure 82. Adding Fe_2O_3 into the SLS glasses shifts the absorbance further towards the visible region, however there are two significant peaks in the visible and NIR which are deleterious for PV modules. The absorbance band in the NIR corresponds to Fe^{2+}, and within the UV-VIS region to Fe^{3+}. Replacing Fe_2O_3, with deleterious absorption bands, with Bi_2O_3 may protect the module without parasitically absorbing photons. The

absorption band associated with the shift in the UV edge is attributed to the $^1S_0 \rightarrow {}^3P_0$ and $^3P_1$ transition as shown schematically in Figure 100.
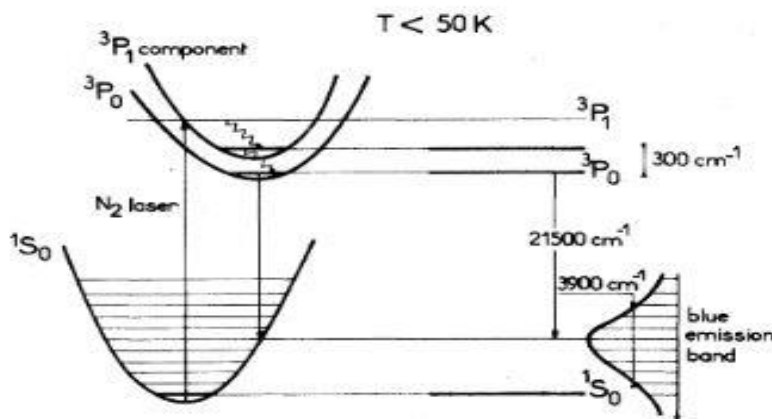
Figure 100 Coordinate diagram of the UV induced excitation and emission process [77]

A UV photon excites an electron from the ground state (designated as $^1S_0$ as the outermost orbital is a fully occupied ^6S orbital), to an empty P orbital, the excitation results in the electron residing in the $^3P_1$ orbital before thermally decaying to the $^3P_0$ orbital. The excited states of Bi^{3+} can be in a triplet state of $^3P_0, {}^3P_1,$ and $^3P_2$ or a singlet state of $^1P_1$. The absorption band as shown in Figure 81, Figure 82, and Figure 85 corresponds to the transition $^1S_0 \rightarrow {}^3P_1$, this transition is allowed due to a spin-orbital coupling. With increasing Bi_2O_3 content the shift towards the visible increases, the effect is observed with low doping concentrations of 0.01mol% Bi_2O_3 in both SLS and Boro systems.

Boro type glasses in this study transmit further into the UV than the corresponding SLS glass shown in Figure 85 and Figure 81 respectively. Where absorbance is equal to 1 (i.e. transmitting 10% of the incoming photons) for the base Boro glass this corresponds to circa 37,000 cm^{-1} (270 nm) while in base SLS this value is 34,500 cm^{-1} (289 nm). At maximum doping concentration this effect is less pronounced with the absorbance at 1

absorbance unit of 0.20mol% Bi_2O_3 Boro corresponding to 32,600 cm^{-1} (306 nm) and for 0.20mol% Bi_2O_3 SLS to 31,750 cm^{-1} (315 nm). For all doping concentrations studied within this work SLS absorbs at lower wavenumbers (higher wavelengths) than the corresponding Boro glass. It is worth noting Boro type glasses contained lower quantities of Fe^{3+} species as observed in the UV VIS region at ca. 26,200 cm^{-1} (380 nm), and in the EPR spectra. Fe^{3+} is known to strongly affect the UV edge in silicate glasses due to an absorbance corresponding to a $^6A_1(S) \rightarrow {}^4E(D)$ transition [56]. While Boro type glasses may confer additional chemical durability relative to a SLS glass, the SLS glass is more protective of UV photons for polymer species within PV modules. Glasses doped with CeO_2 which shift the UV absorbance towards the visible significantly reduce the yellowing index, a measure of degradation of polymer species within a PV module [28]. The dopants used in this study are of lower cost and of lower concentration but confer similar absorbance profiles and therefore will demonstrate similar protection.

PbO glasses were melted in Al_2O_3 crucibles, and after 5 hours melting at 1450°C retained significant residual bubbles. The bubbles came from the refractory material which the glass was slowly dissolving, therefore continually adding more bubbles while the glass was at elevated temperatures. The glass was polished the 1 µm CeO_2, as the SLS and Boro glasses were, and to obtain an absorbance measurement the glass was measured 5 times and averaged. This method did not reduce internal bubble reflection losses but minimised surface bubble reflection losses. Between 0.50mol% PbO SLS and 2.50mol% PbO SLS the absorbance is shifted from the base glass but shifts are of similar magnitude towards the visible. As PbO and SnO_2 are isoelectronic the absorbance transition also corresponds to $^1S_0 \rightarrow {}^3P_1$ absorbance [326,343].

Fluorescence spectroscopy shows a broadband featureless peak centred at 23,250 cm^{-1} (430 nm) or 25,000 cm^{-1} (400 nm) depending on the host glass (SLS or Boro respectively) shown in Figure 86, Figure 87, and Figure 89. This peak is attributed to $^1S_0 \rightarrow {}^3P_0$ and $^1S_0 \rightarrow {}^3P_1$ transitions [218], and may confer additional flux of visible photons to PV modules. Pb^{2+} is isoelectronic to Bi^{3+} and undergoes the same optical transitions with UV excitation and visible emission, this is demonstrated in the fluorescence spectra in Figure 91, Figure 92, Figure 93, and Figure 94.

With increasing Bi_2O_3 content the fluorescence emission intensity increases in both SLS and Boro type glasses. The excitation profile in SLS glasses is more broadband than the corresponding Boro glass, while the emission profile is shifted to lower wavenumbers (higher wavelengths). The ca. 2000 cm^{-1} shift (30 nm) in λ_{max} emission intensity between SLS and Boro type glasses confers a more beneficial flux of photons for c-Si PV modules, which more efficiently absorb these photons. Furthermore, in SLS glasses the intensity is higher in SLS than in Boro glasses of the same doping concentration. This is partially due to the Boro glasses having lower absorbance at the excitation wavenumber used as shown in Figure 85 and the excitation profile is less broad than in the SLS glass shown in Figure 86 and Figure 96. In different glass networks Bi^{3+} may be in multiple sites [344], and the broader the range of sites available, the broader the emission band. The emission intensity is lower at all excitation energies as shown in Figure 87 and Figure 97. Bi^{3+} does not emit in the NIR at 7700 cm^{-1} (1300 nm) from 12,500 cm^{-1} (800 nm) excitation. 0.20mol% Bi_2O_3 SLS is shown in Figure 88, without the characteristic of bismuth in lower oxidation states. This further indicates bismuth within the glasses prepared is in the Bi^{3+} oxidation state.

With increasing Fe_2O_3 content in SLS glasses the emission intensity of 0.20mol% Bi_2O_3 significantly reduces as shown in Figure 89 due to the competitive absorption of Bi^{3+} and Fe^{3+} centres. With increasing quantities of Fe^{3+} the probability of a charge transfer occurring between a Bi^{3+} to Fe^{3+} becomes more likely, which does not allow for radiative emission [345]. Concentration quenching was not observed in the prepared glasses over the doping concentration studied. For effective protection of polymer species while maintaining visible fluorescence the concentration of Fe^{3+} species must be kept to a minimum, as from circa 100 ppm to 0.01mol% Fe_2O_3 the emission intensity dropped by half as shown in Figure 89.

The fluorescence of lead oxide and tin oxide containing glasses is of the same profile as that of Bi_2O_3 containing glasses due to the identical transitions involved shown in the fluorescence emission spectra in Figure 90, Figure 91, Figure 92, Figure 93, and Figure 94. With increasing lead oxide content in SLS glasses the emission shifts to lower wavenumbers (higher wavelengths) due to higher phonon losses. Upon the radiative emission of a photon, a phonon is also emitted, this phonon non-radiatively releases some energy from the incident photon and therefore the photon emission is of lower energy.

5.4 Conclusions

Bismuth in SLS glasses may be in multiple valence states, however only Bi^{3+} confers the UV protective and visible emission beneficial for PV modules. This work through UV-Vis-NIR absorbance spectroscopy, fluorescence visible and NIR emission spectroscopy, EPR, and XANES show bismuth in the glasses prepared are in the Bi^{3+} oxidation state. Using PbO as a model glass shows the isoelectronic transitions in the UV to visible range. Significant structural changes are not observed through incorporation of Bi_2O_3 in both SLS and Boro glasses as shown through XRD, Raman spectroscopy, and DSC. No crystallinity is observed in any samples. Within all samples Fe^{3+} was observed in the UV VIS NIR absorption spectra, the electrochemical series shows Fe^{3+} would reduce to Fe^{2+} in preference to Bi^{3+} reducing to Bi^0. The presence of Fe^{3+} suggests no reduction of Bi^{3+} had occurred, further evidence supporting the EPR and XANES measurements.

Bi_2O_3 doped glasses may be particularly beneficial for the protection of polymeric species within c-Si PV modules due to their UV absorbance and visible emission. SLS type glasses are optically more beneficial for this purpose due to the absorbance profile being more towards the visible than the corresponding Boro glass. The emission profile is further into the visible in which c-Si can more effectively absorb whilst being more intense. The low doping concentration used within this study do not largely affect structural properties but confer critical optical properties for increasing the longevity of PV modules.

6 Photovoltaic Modules with Doped Soda Lime Silica Glasses

Glasses containing various proportions of Bi_2O_3 and Gd_2O_3, along with several base glasses were prepared by B. Allsopp and R. Orman at Johnson Matthey (JM), Sonning Common, Reading, UK. The glass monoliths were polished and sent to Solar Capture Technologies, Blyth (SCT), Newcastle, UK where they were prepared into PV modules corresponding to SCT's proprietary method. EVA glue was used as the polymeric species to glue the panel together. A float glass PV module is shown in Figure 101, the electroluminescence of before defined as string (left) and after lamination defined as module (right) is shown in Figure 102, and a typical I/V curve is shown in Figure 103.

Samples of glass were made as described in section 3.5. The strings were made from silicon with silver paste in the bus-bars, the backsheet was Tedlar® and the glue used was EVA. The exact details of the temperature, time and pressure for lamination of the PV modules are the propriety technology of Solar Capture Technologies and are not available within this manuscript. While efforts were made to prepare fully homogenous flat glasses, this proved difficult with the compositions of glass used for previous sample preparation. As the redox of the glass would be effected strongly by increasing the temperature to lower the viscosity for amenable pouring, it was decided to incorporate 2mol% Li_2O into the glass in replacement of Na_2O. This lowered the viscosity of the glass through two mechanisms, both the mixed alkali effect and the connectivity of a silica network is lowered during the replacement of Na_2O by Li_2O [346]. However, incorporation of Li_2O also affects the refractive index of the glass by increasing the polarizability of the

constituents relative to a glass containing the equivalent quantity of R_2O such as Na_2O or K_2O [347].

Several modules were prepared with the incorporation of Gd_2O_3. This was investigated as a dopant as part of the wider LIMES project but was not part of the work detailed in this manuscript. It is included within these results for comparison.
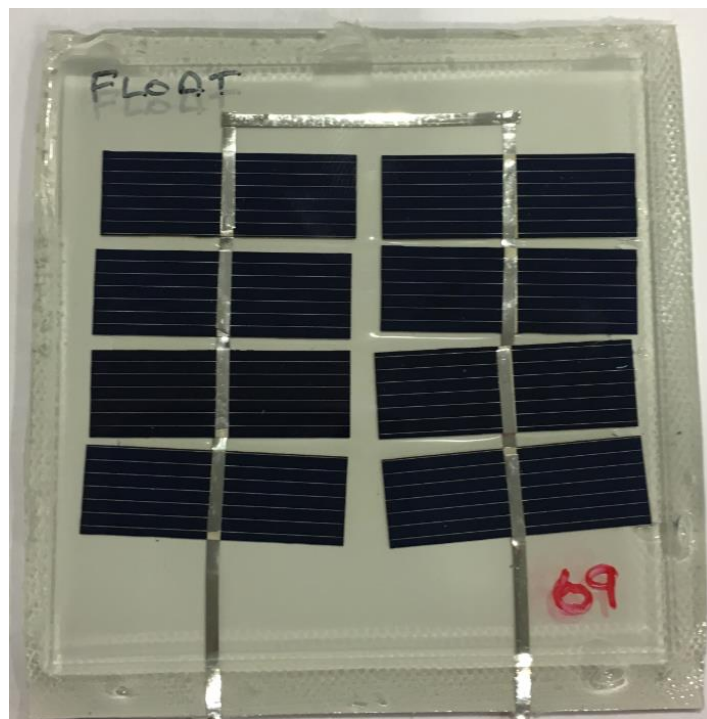
Figure 101 Float glass PV module prepared at SCT

Figure 102 Electroluminescence of string (left) and module (right) float glass PV module
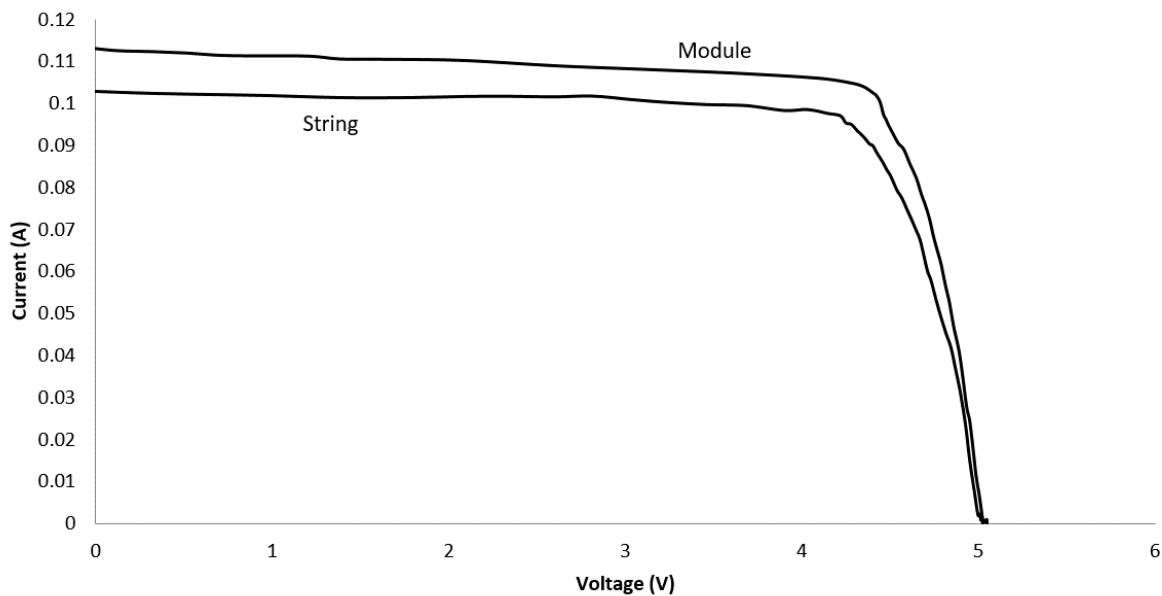
Figure 103 Typical I/V curve for PV modules prepared at SCT (float glass string and module)

There is an increase in the short circuit current between the string and module due to lower reflection losses, and a minor index matching corresponding to the EVA and glass layers. The difference in refractive indices is lower in the module than in the string, as the EVA glue acts as an index matching fluid when bonded together. There are several abbreviations in Table 17 which are explained below.

V_{OC} is the open-circuit voltage, the maximum voltage available from a PV module which occurs at zero current. On the I/V curve shown in Figure 103 this is where the curve touches the x-axis where the y-axis (current) is equal to zero.

I_{SC} is the short-circuit current, this is the maximum current available when the voltage across the PV module is zero. On the I/V curve shown in Figure 103 this is where the curve touches the y-axis where the x-axis (voltage) is equal to zero.

219

R_{SERIES} is the series resistance in a PV module. This is a measure of the movement of current across the emitter and base of the module, the resistance across the metal contacts and the silicon (or other PV active material) and the resistance of the top and rear contacts. This results in inefficiencies within the module and reduces the V_{OC} and I_{SC}.

R_{SHUNT} is the shunt resistance of a PV module. Low shunt resistance causes power loss in a module as the propagation of the current may follow an alternative path than that designed. Larger values therefore minimise the difference between theoretical maximum power output and realised power output of a PV module.

P_{MAX} is the maximum power (W) of a PV module, and is calculated by multiplying the V_{OC}, I_{SC} and fill factor of the module together.

V_{PM} is the voltage at maximum power of a PV module, similar to I_{PM} which is the current at maximum power within a PV module.

Fill factor is the maximum obtainable power of a PV module calculated from the dividing the maximum power point by the product of V_{OC} and I_{SC}. This is a measure of the quality of a given PV module.

Table 17 I_{sc} and I_{pm} data of PV modules

	Float	LIMES A	LIMES BG A	LIMES BG B	LIMES BG C	LIMES B2G A	LIMES B2G B	LIMES B2G2	LIMES B2
	Module								
Irradiance:	104.4	104.1	106.2	105.7	104.0	104.0	105.1	104.3	105.1
Corrected To:	100	100	100	100	100	100	100	100	100
Module Temp (°C)	23.4	24.0	24.0	23.8	21.8	22.2	23.1	23.2	22.9
Corrected To (°C)	25	25	25	25	25	25	25	25	25
Voc (V)	5.07	4.97	4.98	5.01	4.99	4.97	5.05	5.03	4.97
Isc (A)	0.113	0.062	0.070	0.113	0.115	0.114	0.117	0.111	0.115
Rseries (Ω)	45.20	7.06	85.16	11.18	6.18	15.51	14.37	18.50	5.59
Rshunt (Ω)	626.67	6460.12	4206.23	986.97	4838.96	504.53	1004.53	576.77	983.19
Pmax (W)	0.445	0.241	0.284	0.434	0.467	0.429	0.465	0.437	0.446
Vpm (V)	4.33	4.66	4.35	4.17	4.28	4.13	4.27	4.25	4.15
Ipm (A)	0.103	0.052	0.065	0.104	0.109	0.104	0.109	0.103	0.107
Fill Factor (%)	0.78	0.79	0.82	0.77	0.81	0.76	0.79	0.78	0.78

Table 18 I_{sc} and I_{pm} data for cell strings

	Float	LIMES A	LIMES BG A	LIMES BG B	LIMES BG C	LIMES B2G A	LIMES B2G B	LIMES B2G2	LIMES B2
	String								
Irradiance:	104.3	103.9	104.9	104.8	106.3	105.5	104.0	106.5	104.4
Corrected To:	100	100	100	100	100	100	100	100	100
Module Temp (°C)	25.0	24.9	24.6	24.2	24.2	24.5	25.4	25.3	23.8
Corrected To (°C)	25	25	25	25	25	25	25	25	25
Voc (V)	5.03	4.96	4.91	4.98	4.98	4.95	5.02	5.03	4.96
Isc (A)	0.102	0.098	0.097	0.100	0.100	0.099	0.102	0.104	0.099
Rseries (Ω)	12.67	8.60	12.86	9.85	8.06	14.66	12.51	11.46	24.19
Rshunt (Ω)	2274.31	1403.03	1249.74	1198.94	3304.78	2112.79	1012.15	1869.49	2448.08
Pmax (W)	0.405	0.381	0.376	0.391	0.394	0.380	0.398	0.405	0.384
Vpm (V)	4.22	4.38	4.13	4.18	4.18	4.11	4.19	4.22	4.15
Ipm (A)	0.096	0.087	0.091	0.094	0.094	0.093	0.095	0.096	0.093
Fill Factor (%)	0.79	0.78	0.79	0.78	0.79	0.78	0.78	0.78	0.78

Table 19 Change in I_{sc} and I_{pm} from string to module, and damage observations

	Float	LIMES A	LIMES BG A	LIMES BG B	LIMES BG C	LIMES B2G A	LIMES B2G B	LIMES B2G2	LIMES B2
Isc (A) % change	9%	-59%	-39%	11%	13%	14%	13%	7%	14%
Ipm (A) % change	7%	-68%	-39%	10%	14%	11%	13%	7%	14%
Observations		Cells cracked x2	Cells cracked x 2	Glass moved				Glass moved	Glass cracked

Table 20 Changes in Isc and Ipm relative to float glass module

	Float	LIMES A	LIMES BG A	LIMES BG B	LIMES BG C	LIMES B2G A	LIMES B2G B	LIMES B2G2	LIMES B2
					Module				
Irradiance:	104.3	104.1	106.2	105.7	104.0	104.0	105.1	104.3	105.1
Corrected To:	100	100	100	100	100	100	100	100	100
Module Temp (°C)	23.4	24.0	24.0	23.8	21.8	22.2	23.1	23.2	22.9
Corrected To (°C)	25	25	25	25	25	25	25	25	25
Voc (V)	5.07	4.97	4.98	5.01	4.99	4.98	5.05	5.04	4.97
Isc (A)	0.113	0.062	0.070	0.113	0.115	0.114	0.117	0.111	0.115
Rseries (Ω)	45.20	7.06	85.16	11.18	6.18	15.51	14.37	18.50	5.59
Rshunt (Ω)	626.68	6460.12	4206.23	986.97	4838.96	504.53	1004.53	576.76	983.19
Pmax (W)	0.445	0.241	0.284	0.435	0.467	0.429	0.465	0.437	0.446
Vpm (V)	4.33	4.66	4.35	4.17	4.28	4.13	4.28	4.25	4.15
Ipm (A)	0.103	0.052	0.065	0.104	0.109	0.104	0.109	0.103	0.107
Fill Factor (%)	0.78	0.79	0.82	0.77	0.81	0.76	0.79	0.78	0.78
Isc (A) % change	0.0%	-83.5%	-61.3%	-0.1%	1.9%	1.1%	3.8%	-1.3%	1.8%
Ipm (A) % change	0.0%	-98.9%	-57.3%	1.2%	5.7%	1.0%	5.4%	0.0%	4.3%

From Table 17-20, the I_{sc} and I_{pm} are shown, and the relative enhancement of the glass prepared at JM, and that of a commercially available float glass. Note in those samples in which the cells have cracked during lamination the total area available for photovoltaic conversion is lowered and therefore the relative enhancement appears to be lower. This is an artefact of the broken cells rather than being significantly lower efficiency. In samples

without significant damage to the cells there is an increase in I_{sc} and I_{pm} indicating higher efficiency from the dopants, graphed in Figure 104.

	Float	LIMES B	LIMES BG A	LIMES BG B	LIMES BG C	LIMES B2G A	LIMES B2G B	LIMES B2G2	LIMES B2 B
■ Isc (A)	0.0%	-83.5%	-61.3%	-0.1%	1.9%	1.1%	3.8%	-1.3%	1.8%
■ Ipm (A)	0.0%	-98.9%	-57.3%	1.2%	5.7%	1.0%	5.4%	0.0%	4.3%
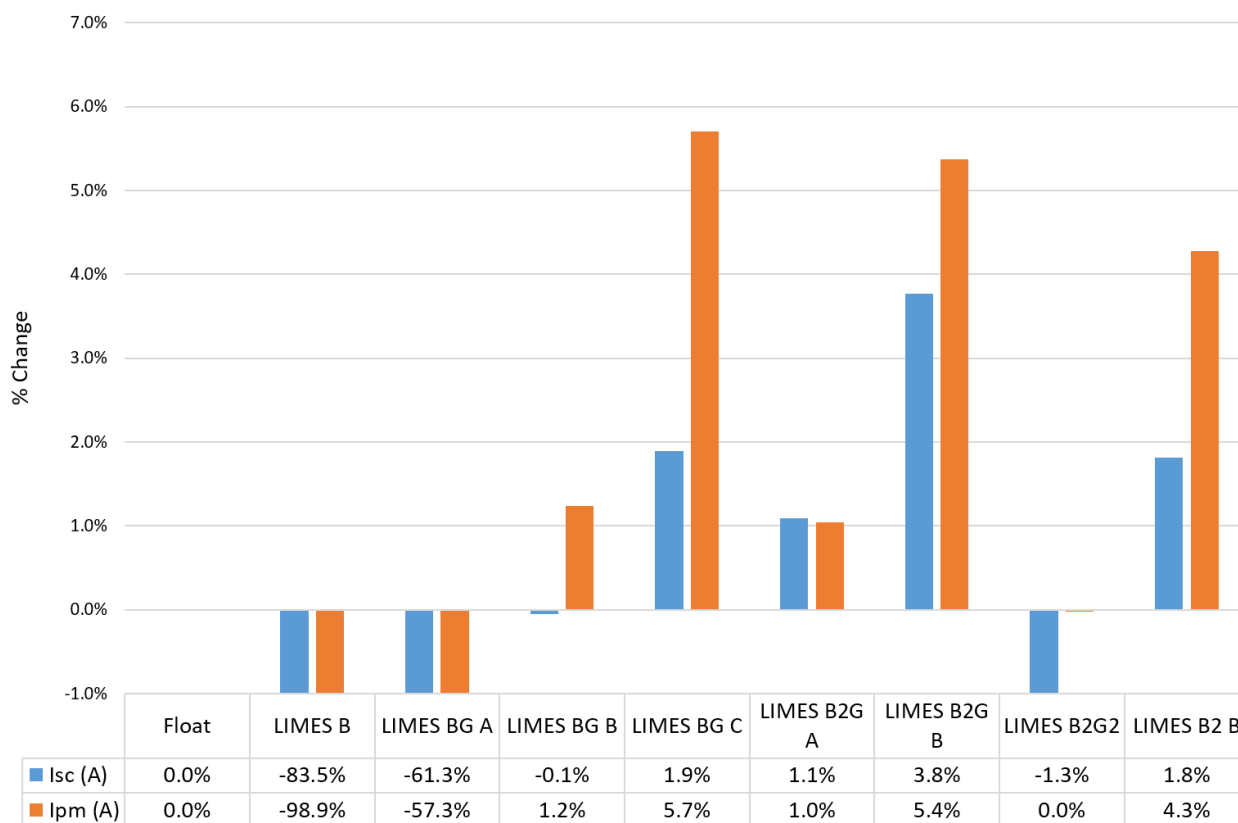
Figure 104 Relative enhancement of I_{sc} and I_{pm} relative to float glass

It is postulated the enhancement of the I_{sc} and I_{pm} is due to the addition of fluorescent dopants. The wide variation is due to slight sample differences, not all glasses were able to be prepared to the exact thickness, and slight wedging of all samples was observed. The variable thicknesses give rise to a longer path length, in which photons can be absorbed, however, the increased thickness gives a larger cross sectional area of fluorescent centres. Thicknesses were not recorded however. Critically all samples demonstrate higher module efficiency. A similar approach carried out by the National Renewable Energy Laboratory using CeO_2 as a dopant which absorbed within the UV

region and emitted within the visible showed a reduction in the yellowing index after 35 weeks of accelerated aging testing with UV irradiation [28]. A similar effect is proposed to occur within these doped glasses due to the shifted absorbance. Yellowing and ultimately browning of EVA has been shown to reduce module efficiency by up to 45% within 5 years of installation [19].

All doped samples within this study, d^0 and s^2, demonstrate an absorbance shifted towards the visible region, of between 2000 cm^{-1} and 4000 cm^{-1} (20-40 nm). This shifted absorbance is proposed to increase the service lifetimes of PV modules by reducing the rate of yellowing of EVA glues. As EVA glues comprise some 80% of c-Si based PV modules [68], and c-Si modules comprise some 87% of all installed capacity of PV modules worldwide [16], up to 158 GW of generated PV electricity is affected by yellowing from UV irradiation. Typically PV module manufacturers expect modules to last between 20 and 25 years, assuming between a 1.0 and 2.5% loss per year [348].

7 Cost of Dopant Additions, Further Work and Conclusions

7.1 Cost of Dopant Additions

To minimise the cost per Watt of PV modules dopant costs must be considered. A preliminary study of the costs associated with doping silicate glasses has been completed. However, this does not include any information regarding logistics of sourcing the materials, and any additional costs associated with processing and melting of the newly developed glasses.

The cost per tonne of the dopant oxides used in this study are listed in Table 21, note this is approximate and averaged from multiple commercial suppliers. Although PbO is the least costly per wt%, assuming 0.20mol% doping concentration, it is banned within the EU and therefore cannot be commercialised. The addition of 0.20mol% TiO_2 shifts the absorbance towards the visible by ca. 2000 cm^{-1} (20 nm), with strong broadband visible emission centred around 25,000 cm^{-1} (500 nm) and is the least costly dopant. ZrO_2 is also low cost and shifts the absorbance, but is weakly emitting relative to TiO_2.

Table 21 Prices per tonne of oxides, taken from IndMin.com and Metals-hub.com [349,350]

Oxide	Price per tonne (£)	Wt % in SLS glass (0.20mol%)	Cost per wt % (£)
TiO_2	3100	0.27	8.37
ZrO_2	2200	0.41	9.02
HfO_2	4400	0.71	31.24
Nb_2O_5	10,100	0.89	89.89
Ta_2O_5	11,150	1.47	163.91
MoO_3	16,400	0.48	78.72
WO_3	17,200	0.78	134.16
Bi_2O_3	11,700	1.55	181.35
PbO	900	0.81	7.29
SnO_2	12,500	0.51	63.75

Bi_2O_3 is the most costly dopant at 0.20mol%, however it has been shown to shift the UV absorbance with lower doping concentration of low as 0.01mol%. With this concentration the cost based on £11,700 per tonne is £9.36 which is on par with 0.20mol% TiO_2. PbO was included in this cost survey but incorporation into glasses for commercial use, except in the case of lead crystal ware, is banned within the EU due to health and environmental considerations, and therefore is not suitable for doping of glasses for PV modules.

Based on the cost survey, the UV VIS NIR absorption, and fluorescence emission data it is proposed doping with 0.20mol% TiO_2 may be the most cost effective dopant looked at within this study TiO_2 confers multiple advantages, such as visible emission centred at ca. 20,000 cm^{-1} (500 nm), strong UV absorption shifted 2000 cm^{-1} (20 nm) relative to the base glass to protect EVA glues and is significantly cheaper than other similarly performing dopants. Furthermore, TiO_2 already has supply chains and is a highly abundant material.

7.2 Further Work

This study was done to investigate doping silicate glasses to shift the absorbance within the UV region to protect polymeric compounds from irradiation damage. Secondary to this absorbance, a broadband visible emission would enhance module efficiency. This effect is observed in Figure 104 and Table 20. However, there is further work required to fully characterise and enhance these effects.

Firstly, shifting the absorbance of the glass front sheet to fully overlap the EVA glue, without any visible absorbance would further protect the polymeric species within the module. However, increasing the dopant concentration is not applicable due to increasing

the total cost. As observed with MoO_3 doped samples, the absorbance is shifted further towards the visible by 4000 cm^{-1} (40 nm) relative to the base glass sample, however the visible emission is weakly emitting. Through mixing of dopants within the glass, it is hypothesised a strongly shifted absorbance and strong emission could occur. However, there would be competitive absorption between the mixed dopants, and therefore it is required to control the concentration of each dopant.

Mixing dopants may reveal a sensitising effect between the two dopants, this has been observed with tungstate bismuth nanorods [351], niobium oxide modified bismuth oxide doped silicate glasses [352], in Bi doped tantalum silicate glasses [353] and between lanthanides and bismuth [97,354,355]. Utilising this effect lower doping concentration may be achieved, thus lowering the cost of the dopant whilst maintaining the strong absorbance and broadband visible emission. This would be essential to further lower the cost per watt of PV generated electricity.

Control of visible emission to better overlap the absorbance of the semiconductor within the PV module would further increase efficiency. Through controlling the emission profile of a particular doped front sheet for a specific type of PV module would confer greater efficiency than for a generic luminescent front sheet. Primarily the focus would be on silicon based PV modules with EVA glue layers, as these compromise circa 70% of installed capacity. Investigation into other types of PV modules may also prove highly beneficial, due to the market growth and efficiency increases within recent years shown in Figure 8.

A study to benchmark commercial front sheets for c-Si PV modules to allow for a deeper understanding of the effects of the dopants studied within this work is to be completed

next. Further to this, luminescent front sheets must be prepared on a small scale float system to produce flat sheets of glass with controlled thickness, and which do not require mechanical polishing. This will reduce the variability of the glasses prepared and allow for larger quantity of glass sheets to be prepared. Statistical analysis of improvements in efficiency and service lifetimes will therefore be possible on each of the dopants.

Accelerated aging testing of each doped front sheet assembled into a PV module will elucidate the increase in service lifetime. A calculation of the reduction in cost per watt produced from the luminescent front sheet will be possible through understanding the magnitude increase in service lifetime and efficiency increase.

7.3 Conclusions

The manuscript has detailed the effects of dopants on the optical effects in silicate glasses for the primary aim of absorption of UV photons for the protection of polymer layers within PV module. Transition metals of d^0 electronic configuration when incorporated into soda lime silica glasses of 0.20mol% concentration demonstrate a red-shifted absorption edge of between 20 to 40 nm relative to a corresponding undoped glass. Incorporation of post transition metal oxides such as Bi_2O_3 and SnO_2 also demonstrate a shifted UV absorbance indicating both are also suitable for the primary objective of protecting polymeric layers within a PV module from UV induced degradation.

The luminescence characteristics of these glasses were measured and the intensity of the emission is variable across the transition metal oxide dopants and post-transition metal oxides. The emissive properties of the glasses may confer additional flux of photons available for the photoelectric effect. However, due to the lower flux of UV photons and

the inefficient nature of the emission, as the energy is radiated in a sphere rather than directed towards the silicon, this effect has been difficult to prove. In Figure 104, the relative enhancement of I_{SC} and I_{PM} of doped and undoped glass front sheets on PV modules prepared at Solar Capture Technologies were shown, indicating an enhancement of these values due to the luminescence of the dopants.

8 References

[1]   Allsopp, B.L., Bingham, P.A., Booth, J., Johnson, S., Orman, R., Glass composition for solar energy applications, GB1700981.2, 2018.

[2]   Allsopp, B.L., Christopoulou, G., Brookfield, A., Forder, D., Bingham, P.A., Optical and structural properties of d^0 ion-doped silicate glasses for photovoltaic applications, Phys. Chem. Glas. Eur. J. Glas. Sci. Technol. Part B. (2018) 59,. doi:10.13036/17533562.59.4.003.

[3]   UNFCCC, Paris Agreement, 2015. doi:FCCC/CP/2015/L.9/Rev.1.

[4]   Krauter, S., Ruther, R., Considerations for the calculation of greenhouse gas reduction by photovoltaic solar energy, Renew. Energy. (2004) 29, 345–355. doi:10.1016/S0960-1481(03)00251-9.

[5]   Voss, A., Leitbilder und wege einer umwelt und kimavertaglichen energieversorgung, Springer, Berlin, 1997.

[6]   Tahara, K., Jojima, T., Inaba, A., Evaluation of CO_2 payback time of power plants by LCA, Energy Conserv. Manag. (1997) 38, 615–620.

[7]   International Renewable Energy Agency, Wind Power, 2012. doi:10.1016/B978-0-08-098330-1.00011-9.

[8]   International Renewable Energy Agency, Hydropower, 2012. http://www.irena.org/documentdownloads/publications/re_technologies_cost_analysis-hydropower.pdf.

[9]   International Renewable Energy Agency, Solar Photovoltaics, 2014. doi:10.1007/978-3-319-08512-8_7.

[10]   NREL, Best Research Cell Efficiencies, (2017). https://www.nrel.gov/pv/assets/images/efficiency-chart.png (accessed September 28, 2017).

[11]   O'Regan, B., Grätzel, M., A low cost, high efficiency solar cell based on dye sensitised colloidal TiO_2 films, Nature. (1991) 353, 737–740.

[12]   Akihiro Kojima, Kenjiro Teshima, Yasuo Shirai, and T.M., Organometal Halide Perovskites as Visible- Light Sensitizers for Photovoltaic Cells, J Am Chem Soc. (2009) 131, 6050–6051. doi:10.1021/ja809598r.

[13]   Chen, Y., Zhang, L., Zhang, Y., Gao, H., Yan, H., Large-area perovskite solar cells - A review of recent progress and issues, RSC Adv. (2018) 8, 10489–10508. doi:10.1039/c8ra00384j.

[14]   Haegel, N.M., Margolis, R., Buonassisi, T., Feldman, D., Froitzheim, A., Garabedian, R., Green, M., Glunz, S., Henning, H.-M., Holder, B., Kaizuka, I., Kroposki, B., Matsubara, K., Niki, S., Sakurai, K., Schindler, R.A., Tumas, W.,

Weber, E.R., Wilson, G., Woodhouse, M., Kurtz, S., Terawatt-scale photovoltaics: Trajectories and challenges, Science (80). (2017) 356,. doi:10.1126/science.aal1288.

[15] Lewis, N.S., Research opportunities to advance solar energy utilization, Science (80-.). (2016) 351,. doi:10.1126/science.aad5117.22.

[16] World Energy Council, World Energy Resources: Solar, 2016.

[17] ASTM, 2000 ASTM Standard Extraterrestrial Spectrum Reference E-490-00, 2000.

[18] Solar energy -- Reference solar spectral irradiance at the ground at different receiving conditions -- Part 1: Direct normal and hemispherical solar irradiance for air mass 1,5, (1992).

[19] Pern, F., Ethylene vinyl acetate (EVA) encapsulants for photovoltaic modules: Degradation and discoloration mechanisms and formulation modifications for improved, Die Angew. Makromol. Chemie. (1997) 252, 195–216. doi:10.1002/apmc.1997.052520114.

[20] Jentsch, A., Eichhorn, K.J., Voit, B., Influence of typical stabilizers on the aging behavior of EVA foils for photovoltaic applications during artificial UV-weathering, Polym. Test. (2015) 44, 242–247. doi:10.1016/j.polymertesting.2015.03.022.

[21] Liu, F., Jiang, L., Yang, S., Ultra-violet degradation behavior of polymeric backsheets for photovoltaic modules, Sol. Energy. (2014) 108, 88–100. doi:10.1016/j.solener.2014.06.027.

[22] de Wild, J., Meijerink, A., Rath, J.K., van Sark, W.G.J.H.M., Schropp, R.E.I., Upconverter solar cells: materials and applications, Energy Environ. Sci. (2011) 4, 4835. doi:10.1039/c1ee01659h.

[23] Badescu, V., De Vos, A., Badescu, A.M., Szymanska, A., Improved model for solar cells with down-conversion and down-shifting of high-energy photons, J. Phys. D-Applied Phys. (2007) 40, 341–352. doi:10.1088/0022-3727/40/2/009.

[24] Conibeer, G., Third-generation photovoltaics, Mater. Today. (2007) 10, 42–50. doi:10.1016/S1369-7021(07)70278-X.

[25] Creative Commons Attribution Share Alike 3.0 Unported Licence, Solar panels at Earth Rangers Centre, (n.d.). https://commons.wikimedia.org/wiki/File:EarthRangersCentre-ImageEnhancement.jpg.

[26] Louwen, A., van Sark, W., Schropp, R., Faaij, A., A cost roadmap for silicon heterojunction solar cells, Sol. Energy Mater. Sol. Cells. (2016) 147, 295–314. doi:10.1016/j.solmat.2015.12.026.

[27] Burrows, K., Fthenakis, V., Glass needs for a growing photovoltaics industry, Sol. Energy Mater. Sol. Cells. (2015) 132, 455–459. doi:10.1016/j.solmat.2014.09.028.

[28] Holley, W.W., Agro, S.C., Advanced EVA-Based Encapsulants, NREL Rep. (1998)

1–95.

[29] Kuitche, J.M., Pan, R., Tamizhmani, G., Investigation of dominant failure mode(s) for field-aged crystalline silicon PV modules under desert climatic conditions, IEEE J. Photovoltaics. (2014) 4, 814–826. doi:10.1109/JPHOTOV.2014.2308720.

[30] Jordan, D., Kurtz, S., Photovoltaic module stability and reliability, Elsevier Ltd., 2016. doi:10.1016/B978-1-78242-336-2.00003-3.

[31] Ojo, A.A., Dharmadasa, I.M., Progress in development of graded bandgap thin film solar cells with electroplated materials, J. Mater. Sci. Mater. Electron. (2017) 28, 6359–6365. doi:10.1007/s10854-017-6366-z.

[32] Dharmadasa, I.M., Advances in thin film solar cells, 1st ed., Pan Stanford Publishing Pte Ltd., Singapore, 2013.

[33] Green, M.A., Solar cells: operating principles, technology, and system applications, Prentice-Hall, Inc.,Englewood Cliffs, NJ, New Jersey, 1982.

[34] Markvart, T., Castañer, L., Principles of Solar Cell Operation, Elsevier Ltd, 2012. doi:10.1016/B978-0-12-385934-1.00001-5.

[35] Celik, Ilke, Phillips, A.B., Song, Z., Yan, Y., Ellingson, R., Heben, M., Apul, D., Environmental Analysis of Perovskites and Other Relevant Solar Cell Technologies in a Tandem Configuration, Energy Environ. Sci. (2017) 0–19. doi:10.1039/C7EE01650F.

[36] Khan, J., Yang, X., Qiao, K., Deng, H., Zhang, J., Liu, Z., Ahmad, W., Zhang, J., Li, D., Liu, H., Song, H., cheng, chun, Tang, J., Low Temperature-processed SnO_2-Cl for Efficient PbS quantum-dot solar cells via defect passivation, J. Mater. Chem. A. (2017). doi:10.1039/C7TA05366E.

[37] Dharmadasa, I.M., Madugu, M.L., Olusola, O.I., Echendu, O.K., Fauzi, F., Diso, D.G., Weerasinghe, A.R., Druffel, T., Dharmadasa, Ruvini Lavery, B., Jasinski, J.B., Krentsel, T.A., Sumanasekera, G., Electroplating of CdTe Thin Films from Cadmium Sulphate Precursor and Comparison of layers grown by 3-electrode and 2-electrode systems, Coatings. (2017) 7, 1–31. doi:10.3390/coatings7020017.

[38] Atapattu, H.Y.R., De Silva, D.S.M., Pathiratne, K.A.S., Dharmadasa, I.M., An investigation into the effect of rate of stirring of bath electrolyte on the properties of electrodeposited CdTe thin film semiconductors, J. Mater. Sci. Mater. Electron. (2018) 0, 0. doi:10.1007/s10854-018-8600-8.

[39] Ramanujam, J., Singh, U.P., Copper indium gallium selenide based solar cells – Review, Energy Environ. Sci. (2017) 0–41. doi:10.1039/C7EE00826K.

[40] Lutgens, F.K., Tarbuck, E.J., Essentials of Geology, 7th ed., Prentice Hall, 2000.

[41] Polman, A., Knight, M., Garnett, E.C., Ehrler, B., Sinke, W.C., Photovoltaic materials – present efficiencies and future challenges, Science (80-.). (2016) 352, 307. doi:10.1126/science.aad4424.

[42] Blakers, A.W., Wang, A., Milne, A.M., Zhao, J., Green, M.A., 22.8% Efficient Silicon Solar Cell, Appl. Phys. Lett. (1989) 55, 1363–1365. doi:10.1063/1.101596.

[43] Bagnall, D.M., Boreland, M., Photovoltaic technologies, Energy Policy. (2008) 36, 4390–4396. doi:10.1016/j.enpol.2008.09.070.

[44] Low, F.W., Lai, C.W., Recent developments of graphene-TiO_2 composite nanomaterials as efficient photoelectrodes in dye-sensitized solar cells: A review, Renew. Sustain. Energy Rev. (2018) 82, 103–125. doi:10.1016/j.rser.2017.09.024.

[45] Chouhan, A.S., Athresh, E., Ranjan, R., Raghavan, S., Avasthi, S., $BaBiO_3$: A potential absorber for all-oxide photovoltaics, Mater. Lett. (2018) 210, 218–222. doi:https://doi.org/10.1016/j.matlet.2017.09.038.

[46] Katagiri, H., Jimbo, K., Maw, W.S., Oishi, K., Yamazaki, M., Araki, H., Takeuchi, A., Development of CZTS-based thin film solar cells, Thin Solid Films. (2009) 517, 2455–2460. doi:10.1016/j.tsf.2008.11.002.

[47] Lin, Y., Xu, Z., Yu, D., Lu, L., Yin, M., Tavakoli, M.M., Chen, X., Hao, Y., Fan, Z., Cui, Y., Li, D., Dual-Layer Nanostructured Flexible Thin-Film Amorphous Silicon Solar Cells with Enhanced Light Harvesting and Photoelectric Conversion Efficiency, ACS Appl. Mater. Interfaces. (2016) 8, 10929–10936. doi:10.1021/acsami.6b02194.

[48] Zi, W., Ren, X., Xiao, F., Wang, H., Gao, F., Liu, S.F., Ag nanoparticle enhanced light trapping in hydrogenated amorphous silicon germanium solar cells on flexible stainless steel substrate, Sol. Energy Mater. Sol. Cells. (2016) 144, 63–67. doi:10.1016/j.solmat.2015.08.024.

[49] Renno, C., Petito, F., Experimental and theoretical model of a concentrating photovoltaic and thermal system, Energy Convers. Manag. (2016) 126, 516–525. doi:10.1016/j.enconman.2016.08.027.

[50] Daneshazarian, R., Cuce, E., Cuce, P.M., Sher, F., Concentrating photovoltaic thermal (CPVT) collectors and systems: Theory, performance assessment and applications, Renew. Sustain. Energy Rev. (2018) 81, 473–492. doi:10.1016/j.rser.2017.08.013.

[51] Kumavat, P.P., Sonar, P., Dalal, D.S., An overview on basics of organic and dye sensitized solar cells, their mechanism and recent improvements, Renew. Sustain. Energy Rev. (2017) 78, 1262–1287. doi:10.1016/j.rser.2017.05.011.

[52] McIntosh, K.R., Lau, G., Costnell, J.N., Hanton, K., Batzner, D.L., Bettiol, F., Richards, B.S., Increase in External quantum efficiency of encapsulated silicon solar cells from a luminescent down shifting layer, Prog. Photovolt Res. Appl. (2009) 17, 191–197. doi:10.1002/pip.

[53] van Sark, W.G., de Wild, J., Rath, J.K., Meijerink, A., Schropp, R.E., Upconversion in solar cells, Nanoscale Res. Lett. (2013) 8, 81. doi:10.1186/1556-276X-8-81.

[54] Strümpel, C., McCann, M., Beaucarne, G., Arkhipov, V., Slaoui, A., Švrček, V., del Cañizo, C., Tobias, I., Modifying the solar spectrum to enhance silicon solar cell

efficiency—An overview of available materials, Sol. Energy Mater. Sol. Cells. (2007) 91, 238–249. doi:10.1016/j.solmat.2006.09.003.

[55]   Shockley, W., Queisser, H.J., Detailed balance limit of efficiency of p-n junction solar cells, J. Appl. Phys. (1961) 32, 510–519. doi:10.1063/1.1736034.

[56]   Volotinen, T.T., Parker, J.M., Bingham, P.A., Concentrations and site partitioning of Fe^{2+} and Fe^{3+} ions in a soda-lime-silica glass obtained by optical absorbance spectroscopy, Phys. Chem. Glas. Eur. J. Glas. Sci. Technol. Part B. (2008) 49, 258–270.

[57]   Bingham, P. A., Parker, J.M., Searle, T., Williams, J.M., Fyles, K., Redox and clustering of iron in silicate glasses, J. Non. Cryst. Solids. (1999) 253, 203–209. doi:10.1016/S0022-3093(99)00361-0.

[58]   Vogt, M.R., Hahn, H., Holst, H., Winter, M., Schinke, C., Kontges, M., Brendel, R., Altermatt, P.P., Measurement of the optical constants of soda-lime glasses in dependence of iron content and modeling of iron-related power losses in crystalline si solar cell modules, IEEE J. Photovoltaics. (2016) 6, 111–118. doi:10.1109/JPHOTOV.2015.2498043.

[59]   Nolet, D.A., Optical absorption and Mössbauer spectra of Fe, Ti silicate glasses, J. Non. Cryst. Solids. (1980) 37, 99–110. doi:10.1016/0022-3093(80)90482-2.

[60]   Deubener, J., Helsch, G., Moiseev, a., Bornhöft, H., Glasses for solar energy conversion systems, J. Eur. Ceram. Soc. (2009) 29, 1203–1210. doi:10.1016/j.jeurceramsoc.2008.08.009.

[61]   Taxiarchou, M., Panias, D., Douni, I., Paspaliaris, I., Kontopoulos, A., Removal of iron from silica sand by leaching with oxalic acid, Hydrometallurgy. (1997) 46, 215–227. doi:10.1016/S0304-386X(97)00015-7.

[62]   Ren, T., He, J., Substrate-versatile approach to robust antireflective and superhydrophobic coatings with excellent self-cleaning property in varied environments, ACS Appl. Mater. Interfaces. (2017) 9, 34367–34376. doi:10.1021/acsami.7b11116.

[63]   Glaubitt, W., Löbmann, P., Antireflective coatings prepared by sol-gel processing: Principles and applications, J. Eur. Ceram. Soc. (2012) 32, 2995–2999. doi:10.1016/j.jeurceramsoc.2012.02.032.

[64]   Du, Y., Zhu, M., Sui, Z., Yi, K., Jin, Y., He, H., Porous antireflective coatings with controlled thickness and refractive index on glass, J. Non. Cryst. Solids. (2013) 363, 26–31. doi:10.1016/j.jnoncrysol.2012.11.043.

[65]   Megahed, A.A., Density of mixed alkali silicate glasses, Phys. Chem. Glas. (1999) 40, 130–134.

[66]   Carvalho, M. de O.M., Calculation of the Theoretical Energy Requirement for Melting Technical Silicate Glasses, J. Am. Ceram. Soc. (1998) 81, 3300–3306. doi:10.1111/j.1151-2916.1998.tb02771.x.

[67] Karlsson, S., Jonson, B., Stålhandske, C., The technology of chemical glass strengthening - A review, Glas. Technol. Eur. J. Glas. Sci. Technol. Part A. (2010) 51, 41–54.

[68] Jiang, S., Wang, K., Zhang, H., Ding, Y., Yu, Q., Encapsulation of PV Modules Using Ethylene Vinyl Acetate Copolymer as the Encapsulant, Macromol. React. Eng. (2015) 9, 522–529. doi:10.1002/mren.201400065.

[69] Marin, M.., Jimenez, A., Lopez, J., Vilaplana, J., Thermal degradation of ethylene vinyl acetate - Kinetic analysis of thermogravimetric data, J. Therm. Anal. (1996) 47, 247–258. doi:10.1007/BF01982703.

[70] Wang, D., Wright, M., Elumalai, N.K., Uddin, A., Stability of perovskite solar cells, Sol. Energy Mater. Sol. Cells. (2016) 147, 255–275. doi:10.1016/j.solmat.2015.12.025.

[71] Huang, J., Tan, S., Lund, P., Zhou, H., Impact of H_2O on organic-inorganic hybrid perovskite solar cells, Energy Environ. Sci. (2017) 0–53. doi:10.1039/C7EE01674C.

[72] Ayotunde, O., Cranton, W., Dharmadasa, I.M., Next generation multilayer graded bandgap solar cells, Springer, 2018. doi:10.1007/978-3-319-96667-0.

[73] Kim, N., Lee, S., Zhao, X.G., Kim, D., Oh, C., Kang, H., Reflection and durability study of different types of backsheets and their impact on c-Si PV module performance, Sol. Energy Mater. Sol. Cells. (2016) 146, 91–98. doi:10.1016/j.solmat.2015.11.038.

[74] Meng, X., Murai, S., Fujita, K., Tanaka, K., Intense visible emissions from d^0 ions-doped silicate glasses, J. Ceram. Soc. Japan. (2008) 116, 1147–1149. doi:10.2109/jcersj2.116.1147.

[75] Van De Craats, a. M., Blasse, G., The influence of d^{10} ions on the luminescence of bismuth(III) in solids, Mater. Res. Bull. (1996) 31, 381–387. doi:10.1016/0025-5408(96)00017-7.

[76] Srivastava, A.M., Comanzo, H.A., Camaradello, S.J., On the "Bi^{3+}–Ti^{4+}" charge transfer transition in the pyrochlore $Y_2Ti_2O_7$:Bi^{3+}, Opt. Mater. (Amst). (2015) 48, 31–35. doi:10.1016/j.optmat.2015.07.020.

[77] Boulon, G., Moine, B., Bourcet, J., Spectroscopic properites of $^3P_1$ and $^3P_0$ excited states of Bi^{3+} ions in germanate glass, Phys. Rev. B. (1980) 22, 1163–1169.

[78] Meng, X., Tanaka, K., Fujita, K., Murai, S., Intense greenish emission from d^0 transition metal ion Ti^{4+} in oxide glass, Appl. Phys. Lett. (2007) 90, 3–6. doi:10.1063/1.2437074.

[79] Quaranta, A., Cattaruzza, E., Gonella, F., Peruzzo, G., Giarola, M., Mariotto, G., Field-assisted solid state doping of glasses for optical materials, Opt. Mater. (Amst). (2010) 32, 1352–1355. doi:10.1016/j.optmat.2010.04.012.

[80] Cattaruzza, E., Mardegan, M., Pregnolato, T., Ungaretti, G., Aquilanti, G.,

Quaranta, a., Battaglin, G., Trave, E., Ion exchange doping of solar cell coverglass for sunlight down-shifting, Sol. Energy Mater. Sol. Cells. (2014) 130, 272–280. doi:10.1016/j.solmat.2014.07.028.

[81] Suzuki, T., Ohishi, Y., Bi-doped lithium alumino silicate glass for ultra-broadband near-infrared optical gain medium, Conf. Lasers Electro-Optics 2006 Quantum Electron. Laser Sci. Conf. CLEO/QELS 2006. (2006) 1–2. doi:10.1109/CLEO.2006.4627731.

[82] Sun, H.T., Yang, J., Fujii, M., Sakka, Y., Zhu, Y., Asahara, T., Shirahata, N., Ii, M., Bai, Z., Li, J.G., Gao, H., Highly fluorescent silica-coated bismuth-doped aluminosilicate nanoparticles for near-infrared bioimaging, Small. (2011) 7, 199–203. doi:10.1002/smll.201001011.

[83] Leonard, R.L., Gray, S.K., Albritton, S.D., Brothers, L.N., Cross, R.M., Eastes, A.N., Hah, H.Y., James, H.S., King, J.E., Mishra, S.R., Johnson, J.A., Rare earth doped downshifting glass ceramics for photovoltaic applications, J. Non. Cryst. Solids. (2013) 366, 1–5. doi:10.1016/j.jnoncrysol.2013.01.029.

[84] Murali Krishna, G., Gandhi, Y., Veeraiah, N., Luminescence spectroscopy of Ti ions in Li_2O-CaF_2-P_2O_5 glass ceramics, J. Lumin. (2008) 128, 631–634. doi:10.1016/j.jlumin.2007.10.034.

[85] Dumont, L., Benzo, P., Cardin, J., Yu, I.-S., Labbé, C., Marie, P., Dufour, C., Zatryb, G., Podhorodecki, A., Gourbilleau, F., Down-shifting Si-based layer for Si solar applications, Sol. Energy Mater. Sol. Cells. (2017) 169, 132–144. doi:10.1016/j.solmat.2017.05.011.

[86] Wohlgemuth, J.., Cunningham, D.., Nguyen, A.., Shaner, J., Ransome, S.., Artigao, A., Fernandez, J.., Increased energy collection using antireflective coated glass, 20th Eur. Photovolt. Sol. Energy Conf. (2005) 3–6.

[87] Qiu, J., Peng, M., Ren, J., Meng, X., Jiang, X., Zhu, C., Novel Bi-doped glasses for broadband optical amplification, J. Non. Cryst. Solids. (2008) 354, 1235–1239. doi:10.1016/j.jnoncrysol.2007.02.094.

[88] Parke, S., Webb, R.S., The optical properties of Thallium Lead and Bismuth in oxide glasses, J. Phys. Chem. Solids. (1973) 34, 85–95.

[89] Zhang, X., Guan, A., Zhou, L., Gong, M., Synthesis and luminescence study of $Zn_3V_2O_8$ Bi^{3+} yellow phosphor for solar spectral modification, Int. J. Appl. Ceram. Technol. (2017) 2–8. doi:10.1111/ijac.12663.

[90] Baumgartner, F., 5 – Photovoltaic (PV) balance of system components: Basics, performance, Elsevier Ltd., 2017. doi:10.1016/B978-1-78242-336-2.00005-7.

[91] Klampaftis, E., Ross, D., Seyrling, S., Tiwari, A.N., Richards, B.S., Increase in short-wavelength response of encapsulated CIGS devices by doping the encapsulation layer with luminescent material, Sol. Energy Mater. Sol. Cells. (2012) 101, 62–67. doi:10.1016/j.solmat.2012.02.011.

[92] Hosseini, Z., Diau, E.W.G., Mehrany, K., Taghavinia, N., Assessment of

luminescent downshifting layers for the improvement of light-harvesting efficiency in dye-sensitized solar cells, ChemPhysChem. (2014) 15, 3791–3799. doi:10.1002/cphc.201402505.

[93]   Fix, T., Nonat, A., Imbert, D., Di Pietro, S., Mazzanti, M., Slaoui, A., Charbonniere, L.J., Enhancement of silicon solar cells by downshifting with Eu and Tb coordination complexes, Prog. Photovolt Res. Appl. (2016). doi:10.1002/pip.

[94]   Hovel, H.J., Hodgson, R.T., Woodall, J.M., The effect of fluorescent wavelength shifting on solar cell spectral response, Sol. Energy Mater. (1979) 2, 19–29. doi:10.1016/0165-1633(79)90027-3.

[95]   Thomas, C.P., Wedding, A.B., Martin, S.O., Theoretical enhancement of solar cell efficiency by the application of an ideal "down-shifting" thin film, Sol. Energy Mater. Sol. Cells. (2012) 98, 455–464. doi:10.1016/j.solmat.2011.11.027.

[96]   Ho, W., Shen, Y.-T., Liu, J.-J., You, B.-J., Ho, C.-H., Enhancing Photovoltaic Performance Using Broadband Luminescent Down-Shifting by Combining Multiple Species of Eu-Doped Silicate Phosphors, Nanomaterials. (2017) 340. doi:10.3390/nano7100340.

[97]   Huang, C.., Chen, Y.., Hung, W.., Chen, T.., Sun, K.., Chang, W.., Enhanced light harvesting of Si solar cells via Luminenscent down shifting using YVO_4: Bi^{3+} Eu^{3+} nanophosphors, Prog. Photovoltaics. (2013) 21, 1507–1513. doi:10.1002/pip.

[98]   Klampaftis, E., Ross, D., Mcintosh, K.R., Richards, B.S., Enhancing the performance of solar cells via luminescent down-shifting of the incident spectrum : A review, Sol. Energy Mater. Sol. Cells. (2009) 93, 1182–1194. doi:10.1016/j.solmat.2009.02.020.

[99]   Williams, E., Lavery, N., Laser processing of bulk metallic glass: A review, J. Mater. Process. Tech. (2017) 247, 73–91. doi:10.1016/j.jmatprotec.2017.03.034.

[100]   Schönfeld, B., Zemp, J., Stuhr, U., Thermal vibrations in the metallic glass $Cu_{64}Zr_{36}$, J. Phys. Condens. Matter. (2017) 29, 015401. doi:10.1088/0953-8984/29/1/015401.

[101]   Mohammadi, M., Fazli, H., karevan, M., Davoodi, J., The glass transition temperature of PMMA: A molecular dynamics study and comparison of various determination methods, Eur. Polym. J. (2017) 91, 121–133. doi:10.1016/j.eurpolymj.2017.03.056.

[102]   Ma, M., Xue, T., Chen, S., Guo, Y., Chen, Y., Liu, H., Features of structural relaxation in diblock copolymers, Polym. Test. (2017) 60, 1–5. doi:10.1016/j.polymertesting.2017.02.027.

[103]   Zhu, L., Mimnaugh, B.R., Ge, Q., Quirk, R.P., Cheng, S.Z.D., Thomas, L., Lotz, B., Hsiao, B.S., Yeh, F., Liu, L., Hard and soft confinement effects on polymer crystallization in microphase separated cylinder-forming PEO- b -PS / PS blends, Polymer (Guildf). (2001) 42, 9121–9131.

[104]   Portier, J., Halogenide, chalcogenide and chalcohalogenide glasses: materials,

models, applications, J. Non. Cryst. Solids. (1989) 112, 15–22. doi:10.1016/0022-3093(89)90489-4.

[105] Zanotto, E.D., Mauro, J.C., The glassy state of matter: Its definition and ultimate fate, J. Non. Cryst. Solids. (2017) 471, 490–495. doi:10.1016/j.jnoncrysol.2017.05.019.

[106] Abo-Naf, S.M., Abdel-Hameed, S. A. M., Marzouk, M. A., Elwan, R.L., Sol–gel synthesis, paramagnetism, photoluminescence and optical properties of Gd-doped and Bi–Gd-codoped hybrid organo-silica glasses, J. Mater. Sci. Mater. Electron. (2015) 26, 2363–2373. doi:10.1007/s10854-015-2692-1.

[107] C.P. Scherer, C.G.P., Titania silica glasses using a colloidal sol gel process, J. Non. Cryst. Solids. (1986) 82, 340–345.

[108] Ren, J., Zhang, L., Eckert, H., Medium-Range Order in Sol − Gel Prepared Al_2O_3 − SiO_2 Glasses: New Results from Solid-State NMR, J. Phys. Chem. C. (2014) 4906–4917.

[109] Singh, Sadanand, M.D. Ediger, J. de P., Ultra stable glasses from in silico vapour deposition, Nat. Mater. (2013) 12, 139–144. doi:10.1038/nmat3521.

[110] Ballato, J., Dragic, P., Glass: The Carrier of Light - A Brief History of Optical Fiber, Int. J. Appl. Glas. Sci. (2016) 7, 413–422. doi:10.1111/ijag.12239.

[111] Hench, L.L., Bioglass : 10 milestones from concept to commerce, J. Non. Cryst. Solids. (2016) 432, 2–8.

[112] Jones, J.R., Brauer, D.S., Hupa, L., Greenspan, D.C., Bioglass and Bioactive Glasses and Their Impact on Healthcare, Int. J. Appl. Glas. Sci. (2016) 7, 423–434. doi:10.1111/ijag.12252.

[113] Bingham, P., Connelly, A J., Hyatt, N.C., Hand, R.J., Corrosion of glass contact refractories for the vitrification of radioactive wastes: a review, Int. Mater. Rev. (2011) 56, 226–242. doi:10.1179/1743280410Y.0000000005.

[114] Bingham, P. A., Vaishnav, S., Forder, S.D., Scrimshire, A., Jaganathan, B., Rohini, J., Marra, J.C., Fox, K.M., Pierce, E.M., Workman, P., Vienna, J.D., Modelling the sulfate capacity of simulated radioactive waste borosilicate glasses, J. Alloys Compd. (2017) 695, 656–667. doi:10.1016/j.jallcom.2016.11.110.

[115] Huang, X., Han, S., Huang, W., Liu, X., Enhancing solar cell efficiency: the search for luminescent materials as spectral converters, Chem. Soc. Rev. (2013) 42, 173–201. doi:10.1039/c2cs35288e.

[116] Morse, D.L., Evenson, J.W., Welcome to the Glass Age, Int. J. Appl. Glas. Sci. (2016) 4, 1–4. doi:10.1111/ijag.12242.

[117] Axinte, E., Glasses as engineering materials: A review, Mater. Des. (2011) 32, 1717–1732. doi:10.1016/j.matdes.2010.11.057.

[118] Gulbiten, O., Mauro, J.C., Guo, X., Boratav, O.N., Viscous flow of medieval

cathedral glass, J. Am. Ceram. Soc. (2017). doi:10.1111/jace.15092.

[119] Hunault, M.O.J.Y., Vinel, V., Cormier, L., Calas, G., Thermodynamic insight into the evolution of medieval glassworking properties, J. Am. Ceram. Soc. (2017) 1–5. doi:10.1111/jace.14819.

[120] Page, J.-A., The Art of Glass, 1st ed., Toledo Museum of Art, Toledo, 2006.

[121] Zanotto, E.D., Do cathedral glasses flow?, Am. J. Phys. (1998) 66, 392. doi:10.1119/1.19026.

[122] Goldschmidt, V.., Raumchemie der festen Stoffe, Naturwissenschaften. (1934) 22, 722–725.

[123] Zachariasen, W.H., The atomic arrangement in glass, J. Am. Chem. Soc. (1932) 54, 3841–3851. doi:doi:10.1021/ja01349a006.

[124] Jiang, Z.-H.H., Zhang, Q.-Y.Y., The structure of glass: A phase equilibrium diagram approach, Prog. Mater. Sci. (2014) 61, 144–215. doi:10.1016/j.pmatsci.2013.12.001.

[125] Heyde, M., Shaikhutdinov, S., Freund, H.J., Two-dimensional silica: Crystalline and vitreous, Chem. Phys. Lett. (2012) 550, 1–7. doi:10.1016/j.cplett.2012.08.063.

[126] Aguiar, H., Serra, J., González, P., León, B., Structural study of sol-gel silicate glasses by IR and Raman spectroscopies, J. Non. Cryst. Solids. (2009) 355, 475–480. doi:10.1016/j.jnoncrysol.2009.01.010.

[127] Yadav, A.K., Singh, P., A review of the structures of oxide glasses by Raman spectroscopy, RSC Adv. (2015) 5, 67583–67609. doi:10.1039/C5RA13043C.

[128] Vogel, W., Glass chemistry, Springer - Verlag, Berlin, 1992. http://refhub.elsevier.com/S0079-6425(13)00086-8/h0595.

[129] Wang, Z., Cheng, L., Effects of doping CeO_2/TiO_2 on structure and properties of silicate glass, J. Alloys Compd. (2014) 597, 167–174. doi:10.1016/j.jallcom.2014.01.232.

[130] Maekawa, H., Maekawa, T., Kawamura, K., Yokokawa, T., The structural groups of alkali silicate glasses determined from ^{29}Si MAS-NMR, J. Non. Cryst. Solids. (1991) 127, 53–64. doi:10.1016/0022-3093(91)90400-Z.

[131] Greaves, G.N., EXAFS and the structure of glass, J. Non. Cryst. Solids. (1985) 71, 203–217. doi:10.1016/0022-3093(85)90289-3.

[132] Greaves, G.N., Vaills, Y., Sen, S., Winter, R., Density fluctuations, phase separation and microsegregation in silicate glasses, J. Optoelectron. Adv. Mater. (2000) 2, 299–316.

[133] Varshneya, A.K., Fundamentals of Inorganic Glasses, 2nd ed., Society of Glass Technology, Sheffield U.K., 2012.

[134] Hench, L.L., Clark, D.E., Physical chemistry of glass surfaces, J. Non. Cryst. Solids.

(1978) 28, 83–105. doi:10.1016/0022-3093(78)90077-7.

[135] ISO 1776:1985 Glass -- Resistance to attack by hydrochloric acid at 100 degrees C -- Flame emission or flame atomic absorption spectrometric method, 1985.

[136] ISO 695:1991 Glass -- Resistance to attack by a boiling aqueous solution of mixed alkali -- Method of test and classification, 1991.

[137] ISO 719:1985 Glass -- Hydrolytic resistance of glass grains at 98 degrees C -- Method of test and classification, (1985).

[138] ISO 720:1985 Glass -- Hydrolytic resistance of glass grains at 121 degrees C -- Method of test and classification, (1985).

[139] Dathe, M., Roggendorf, H., Dissolution of sodium silicate glasses for the production of water glass – Part I Study of experimental parameters, Phys. Chem. Glas. Eur. J. Glas. Sci. Technol. Part B. (2018) 59, 241–250.

[140] Wassick, T.., Doremus, R.., Lanford, W.., Burman, C., Hydration of soda lime silicate glass, effect of alumina, J. Non. Cryst. Solids. (1983) 54, 139–151.

[141] Devreux, F., Barboux, P., Filoche, M., Sapoval, B., A simplified model for glass dissolution in water, J. Mater. Sci. (2001) 36, 1331–1340. doi:10.1023/A:1017591100985.

[142] Strachan, D., Glass dissolution as a function of pH and its implications for understanding mechanisms and future experiments, Geochim. Cosmochim. Acta. (2017) 219, 111–123. doi:10.1016/j.gca.2017.09.008.

[143] Richet, P., Water: An elusive component of silicate melts, Phys. Chem. Glas. (2005) 46, 333–339.

[144] Bocker, C., Rüssel, C., Percolation, phase separation and crystallisation, Phys. Chem. Glas. Eur. J. Glas. Sci. Technol. Part B. (2017) 58, 133–141. doi:10.13036/17533562.58.4.133.

[145] Brinks, H.W., Hauback, B.C., Jensen, C.M., Zidan, R., Synthesis and crystal structure of Na_2LiAlD_6, J. Alloys Compd. (2005) 392, 27–30. doi:10.1016/j.jallcom.2004.09.006.

[146] Liu, X., Wang, H., Lavina, B., Tu, B., Wang, W., Fu, Z., Chemical composition, crystal structure, and their relationships with the intrinsic properties of spinel-type crystals based on bond valences, Inorg. Chem. (2014) 53, 5986–5992. doi:10.1021/ic5002013.

[147] Shelby, J.E., Introduction to glass science and technology, 2nd editio, Royal Society of Chemistry, Cambridge, 2005.

[148] Fujimoto, Y., Nakatsuka, M., ^{27}Al NMR structural study on aluminum coordination state in bismuth doped silica glass, J. Non. Cryst. Solids. (2006) 352, 2254–2258. doi:10.1016/j.jnoncrysol.2006.02.047.

[149] Lezzi, P.J., Tomozawa, M., Effect of alumina on enthalpy of mixing of mixed alkali

silicate glasses, J. Non. Cryst. Solids. (2011) 357, 2086–2092. doi:10.1016/j.jnoncrysol.2010.12.074.

[150] Stebbins, J.F., Xu, Z., NMR evidence for excess non-bridging oxygen in an aluminosilicate glass, Nature. (1997) 390, 1996–1998. doi:10.1038/36312.

[151] Cormier, L., Ghaleb, D., Neuville, D.R., Delaye, J.M., Calas, G., Chemical dependence of network topology of calcium aluminosilicate glasses: A computer simulation study, J. Non. Cryst. Solids. (2003) 332, 255–270. doi:10.1016/j.jnoncrysol.2003.09.012.

[152] Neuville, D.R., Cormier, L., Flank, A.M., Briois, V., Massiot, D., Al speciation and Ca environment in calcium aluminosilicate glasses and crystals by Al and Ca K-edge X-ray absorption spectroscopy, Chem. Geol. (2004) 213, 153–163. doi:10.1016/j.chemgeo.2004.08.039.

[153] Cormier, L., Cuello, G.J., Mg coordination in a $MgSiO_3$ glass using neutron diffraction coupled with isotopic substitution, Phys. Rev. B - Condens. Matter Mater. Phys. (2011) 83, 1–8. doi:10.1103/PhysRevB.83.224204.

[154] Wilding, M.C., Benmore, C.J., Tangeman, J.A., Sampath, S., Evidence of different structures in magnesium silicate liquids: Coordination changes in forsterite- to enstatite-composition glasses, Chem. Geol. (2004) 213, 281–291. doi:10.1016/j.chemgeo.2004.08.055.

[155] Bechgaard, T.K., Scannell, G., Huang, L., Youngman, R.E., Mauro, J.C., Smedskjaer, M.M., Structure of MgO/CaO sodium aluminosilicate glasses: Raman spectroscopy study, J. Non. Cryst. Solids. (2017) 0–1. doi:10.1016/j.jnoncrysol.2017.05.014.

[156] Detcheva, A.K., Velinova, R.H., Manoylova, A.K., Ivanova, E.H., Study on the colouration of Bulgarian late-antique and medieval archaeological glass finds by a validated total reflection x-ray fluorescence procedure, Eur. J. Glas. Sci. Technol. Part B. (2017) 58, 217–225. doi:10.13036/17533562.58.5.014.

[157] Pascual, M.J., Durán, A., Pascual, L., Viscosity and thermal properties of glasses in the system R_2O-B_2O_3-SiO_2 , R=Li, K, Na, 2002.

[158] Erdem, İ., Guldiren, D., Aydin, S., Chemical tempering of soda lime silicate glasses by ion exchange process for the improvement of surface and bulk mechanical strength, J. Non. Cryst. Solids. (2017) 473, 170–178. doi:10.1016/j.jnoncrysol.2017.08.010.

[159] Sharaf, N.A., Ahmed, A.A., Abbas, A.F., Mixed alkali effect on density, refractive index and related properties of alkali borate glasses, Phys. Chem. Glas. (1998) 39, 76–82.

[160] Doweidar, H., A simple approach to the mixed alkali effect, Phys. Chem. Glas. (1999) 40, 345–349.

[161] Fluegel, A., Glass viscosity calculation based on a global statistical modelling approach, Glas. Technol. J. Glas. Sci. Technol. (2007) 48, 13–30.

http://www.ingentaconnect.com/content/sgt/gt/2007/00000048/00000001/art0000
3.

[162] Bingham, P.. A., Hand, R.. J., Hannant, O.. M., Forder, S.. D., Kilcoyne, S.. H., Effects of modifier additions on the thermal properties, chemical durability, oxidation state and structure of iron phosphate glasses, J. Non. Cryst. Solids. (2009) 355, 1526–1538. doi:10.1016/j.jnoncrysol.2009.03.008.

[163] Vercamer, V., Lelong, G., Hijiya, H., Kondo, Y., Galoisy, L., Calas, G., Diluted Fe^{3+} in silicate glasses: Structural effects of Fe-redox state and matrix composition. An optical absorption and X-band/Q-band EPR study, J. Non. Cryst. Solids. (2015) 428, 138–145. doi:10.1016/j.jnoncrysol.2015.08.010.

[164] Stalhandske, C., The impact of refining agents on glass colour, Glastek. Tidskr. (2000) 55, 65–71.

[165] Möncke, D., Ehrt, D., In : Materials Science Research Horizons Photoionisation of polyvalent ions 2007.

[166] Bingham, P. A., Parker, J.M., Searle, T., Williams, J.M., Smith, I., Novel structural behaviour of iron in alkali – alkaline-earth – silica glasses, C.R. Cnimie. (2002) 5, 787–796. doi:10.1016/S1631-0748(02)01444-3.

[167] Iwamoto, N., Hidaka, H., Makino, Y., State of Ti^{3+} Ti^{4+} redox reaction in reduced sodium silicate glasses, J. Non. Cryst. Solids. (1983) 58, 131–141.

[168] Min'ko, N, I; Binaliev, I, M., Role of sodium sulfate in glass technology, Glas. Ceram. (2013) 69, 361–365.

[169] Of, E., Sulfate, S., Of, F., Glass, F., The, O.N., Effect of sodium sulfate and temperature on the fining of float glass, J. Non. Cryst. Solids. (1986) 80, 630–636.

[170] Green, M.A., High-Efficiency Silicon Solar Cell Concepts, Second Edi, Elsevier Ltd, 2003. doi:10.1016/B978-185617390-2/50012-X.

[171] Llanos, C., Marcos, R., WO2001055040A1, 2001.Glass Composition for solar control

[172] Evans, T.C., Gavrilovich, E., Mihai, R.C. and Isbasescu, I., E.L., Thelen, D., Martin, J.A., Allen, S.M., SA, S., (12) Patent Application Publication (10) Pub . No .: US 2006 / 0222585 A1 Figure 1, (2017) 002, 354. doi:10.1037/t24245-000.

[173] Duffy, J. A., Redox equilibria in glass, J. Non. Cryst. Solids. (1996) 196, 45–50. doi:10.1016/0022-3093(95)00560-9.

[174] Iordanova, R., Gegova, R., Bachvarova-Nedelcheva, A., Dimitriev, Y., Sol-gel synthesis of composites in the ternary TiO_2 TeO_2 B_2O_3 system, Phys. Chem. Glas. Eur. J. Glas. Sci. Technol. Part B. (2015) 56, 128–138.

[175] Pilkington, Pilkington and the flat glass industry 2010, 2010. https://www.pilkington.com/resources/pfgi2010.pdf.

[176] Britist Glass Report., UK Glass Decarbonisation Roadmap 2050 March 2014, 2014.

[177] Inage, S.-I., Prospects for Large-Scale Energy Storage in Decarbonised Power Grids, 2009.

[178] Schaeffer, H. A., Stengel, M., Mecha, J., Dealkalization of glass surfaces utilizing HCl gas, J. Non. Cryst. Solids. (1986) 80, 400–404.

[179] Ehrt, D., Leister, M., Matthai, A., Polyvalent elements iron, tin and titanium in silicate, phosphate and fluoride glasses and melts, Phys. Chem. Glas. (2001) 42, 231–239.

[180] Benne, D., Rüssel, C., Diffusivity of tin in some soda silica and soda lime silica melts, Phys. Chem. Glas. Eur. J. Glas. Sci. Technol. Part B. (2008) 49, 160–165.

[181] August, C., Viscosity and viscometric fixed points of glass, Br. Stand. (1993) BS 7034-2:,.

[182] Rawlings, R.D., Wu, J.P., Boccaccini, A. R., Glass-ceramics: Their production from wastes-A Review, J. Mater. Sci. (2006) 41, 733–761. doi:10.1007/s10853-006-6554-3.

[183] Ghamsari, M.S., Gaeeni, M.R., Han, W., Park, H.-H., Highly stable colloidal TiO_2 nanocrystals with strong violet-blue emission, J. Lumin. (2016) 178, 89–93. doi:10.1016/j.jlumin.2016.05.036.

[184] Ruivo, A., Ferro, M.C., Andrade, S.M., Rocha, J., Pina, F., Antonio, C., Laia, T., Photoluminescent Nanocrystals in a Multicomponent Aluminoborosilicate Glass, J. Phys. Chem. C. (2016) 120, 24925–24931. doi:10.1021/acs.jpcc.6b04552.

[185] Iqbal, Y., Lee, W.E., Holland, D., James, P.F., Crystal nucleation in P_2O_5-doped lithium disilicate glasses, J. Mater. Sci. (1999) 34, 4399–4411.

[186] Aravindan, S., Rajendran, V., Rajendran, N., Influence of Ag_2O on crystallisation and structural modification of phosphate glasses, Phase Transitions. (2012) 85, 630–649. doi:10.1080/01411594.2011.639013.

[187] Stookey, S.D., Catalyzed crystallization of glass in theory and practice, Ind. Eng. Chem. (1959) 51, 805–808. doi:10.1021/ie50595a022.

[188] Paramesh, G., Varma, K.B.R., Mechanical properties of glasses and TiO_2 nanocrystal glass composites in BaO-TiO_2-B_2O_3 system, J. Non. Cryst. Solids. (2013) 380, 128–134. doi:10.1016/j.jnoncrysol.2013.09.010.

[189] Ananthanarayanan, A, Kumar, R., Bhattacharya, S., Shrikhande, V.K., Kothiyal, G.P., Some properties of lithium aluminium silicate (LAS) glass-ceramics used in glass-ceramic to metal compressive seal for vacuum applications, J. Phys. Conf. Ser. (2008) 114, 012042. doi:10.1088/1742-6596/114/1/012042.

[190] Llordés, A., Garcia, G., Gazquez, J., Milliron, D.J., Tunable near-infrared and visible-light transmittance in nanocrystal-in-glass composites., Nature. (2013) 500, 323–327. doi:10.1038/nature12398.

[191] Ehrt, D., Photoluminescence in glasses and glass ceramics, IOP Conf. Ser. Mater.

Sci. Eng. (2009) 2, 012001. doi:10.1088/1757-899X/2/1/012001.

[192] Alekseeva, I., Dymshits, O., Tsenter, M., Zhilin, A., Golubkov, V., Denisov, I., Skoptsov, N., Malyarevich, A., Yumashev, K., Optical applications of glass-ceramics, J. Non. Cryst. Solids. (2010) 356, 3042–3058. doi:10.1016/j.jnoncrysol.2010.05.103.

[193] Kjeldsen, J., Yue, Y., Bragatto, C.B., Rodrigues, A.C.M., Electronic conductivity of vanadium-tellurite glass-ceramics, J. Non. Cryst. Solids. (2013) 378, 196–200. doi:10.1016/j.jnoncrysol.2013.07.011.

[194] Nielsen, J.H., Olesen, J.F., Stang, H., The fracture process of tempered soda-lime-silica glass, Exp. Mech. (2009) 49, 855–870. doi:10.1007/s11340-008-9200-y.

[195] Gy, R., Ion exchange for glass strengthening, Mater. Sci. Eng. B Solid-State Mater. Adv. Technol. (2008) 149, 159–165. doi:10.1016/j.mseb.2007.11.029.

[196] Mochel, E.., US Patent 3,451,769 Corning Glass Works, 1969.

[197] Varshneya, A.K., The physics of chemical strengthening of glass: Room for a new view, J. Non. Cryst. Solids. (2010) 356, 2289–2294. doi:10.1016/j.jnoncrysol.2010.05.010.

[198] Hand, R.J., Tadjiev, D.R., Mechanical properties of silicate glasses as a function of composition, J. Non. Cryst. Solids. (2010) 356, 2417–2423. doi:10.1016/j.jnoncrysol.2010.05.007.

[199] Varshneya, A.K., Stronger glass products: Lessons learned and yet to be learned, Int. J. Appl. Glas. Sci. (2018). doi:10.1111/ijag.12341.

[200] Firstov, S. V, Khopin, V.F., Velmiskin, V. V, Firstova, E.G., Bufetov, I. a, Guryanov, A.N., Dianov, E.M., Anti-Stokes luminescence in bismuth-doped silica and germania-based fibers., Opt. Express. (2013) 21, 18408–13. doi:10.1364/OE.21.018408.

[201] Ceglia, A., Nuyts, G., Meulebroeck, W., Cagno, S., Silvestri, A., Zoleo, A., Nys, K., Janssens, K., Thienpont, H., Terryn, H., Iron speciation in soda-lime-silica glass: a comparison of XANES and UV-vis-NIR spectroscopy, J. Anal. At. Spectrom. (2015) 30, 1552–1561. doi:10.1039/C5JA00046G.

[202] Weyl, W.A., Coloured Glasses, 1st ed., Dawsons of Pall Mall, London, 1959.

[203] Dimitrov, V., Komatsu, T., Optical basicity and chemical bonding of Bi_2O_3 containing glasses, J. Non. Cryst. Solids. (2013) 382, 18–23. doi:10.1016/j.jnoncrysol.2013.10.005.

[204] Jia, H., Chen, G., Wang, W., Refractive index and absorption spectra changes induced by UV irradiation in lead silicate glasses, J. Non. Cryst. Solids. (2004) 347, 220–223. doi:10.1016/j.jnoncrysol.2004.08.242.

[205] Pettit, R.B., Brinker, C.J., Ashley, C.S., Sol-sel double-layer antireflection coatings for silicon solar cells, Sol. Cells. (1985) 15, 267–278.

[206] Arabatzis, I., Todorova, N., Fasaki, I., Tsesmeli, C., Peppas, A., Li, W.X., Zhao, Z., Photocatalytic, self-cleaning, antireflective coating for photovoltaic panels: Characterization and monitoring in real conditions, Sol. Energy. (2018) 159, 251–259. doi:10.1016/j.solener.2017.10.088.

[207] Jimenez-Solano, A., Delgado-Sanchez, J.-M., Calco, M.E., Miranda-Munoz, J.M., Lozano, G., Shancho, D., Sanchez-Cortezon, E., Miguez, H., Design and realization of transparent solar modules based on luminescent solar concentrators integrating nanostructured photonic crystals, Prog. Photovoltaics Res. Appl. (2015).

[208] Ehrt, D., UV-absorption and radiation effects in different glasses doped with iron and tin in the ppm range, Comptes Rendus Chim. (2002) 5, 679–692. doi:10.1016/S1631-0748(02)01432-7.

[209] Abdel-Baki, M., El-Diasty, F., Optical properties of oxide glasses containing transition metals: Case of titanium- and chromium-containing glasses, Curr. Opin. Solid State Mater. Sci. (2006) 10, 217–229. doi:10.1016/j.cossms.2007.08.001.

[210] Das Mohapatra, G.K., A spectroscopic study of Ce^{3+} ion in calcium metaphosphate glass, Phys. Chem. Glas. (1998) 39, 50–55.

[211] King, D.E., Pern, F.J., Pitts, J.R., Bingham, C.E., Czanderna, A.W., Optical changes in cerium containing glass as a result of accelerated exposure testing.pdf, Conf. Rec. IEEE Photovolt. Spec. (1997) 1117–1120.

[212] W, Schropp, Solar Spectrum Conversion for Photovoltaics Using Nanoparticles, in: Third Gener. Photovoltaics, 2012.

[213] Trupke, T., Green, M.A., Würfel, P., Improving solar cell efficiencies by down-conversion of high-energy photons, J. Appl. Phys. (2002) 92, 1668–1674. doi:10.1063/1.1492021.

[214] Trupke, T., Green, M.A., Würfel, P., Improving solar cell efficiencies by up-conversion of sub-band-gap light, J. Appl. Phys. (2002) 92, 4117–4122. doi:10.1063/1.1505677.

[215] PerkinElmer, An Introduction to fluorescence spectroscopy, Microchem. J. (2000) 65, 353. doi:10.1016/S0026-265X(00)00048-5.

[216] Trueba, A., Garcia-Fernandez, P., García-Lastra, J.M., Aramburu, J.A., Barriuso, M.T., Moreno, M., Spectrochemical series and the dependence of racah and 10 Dq parameters on the metal-ligand distance: Microscopic origin, J. Phys. Chem. A. (2011) 115, 1423–1432. doi:10.1021/jp110586e.

[217] Maeder, T., Review of Bi_2O_3 based glasses for electronics and related applications, Int. Met. Rev. (2012) 58, 3–40. doi:10.1179/1743280412Y.0000000010.

[218] Sun, H.-T., Zhou, J., Qiu, J., Recent advances in bismuth activated photonic materials, Prog. Mater. Sci. (2014) 64, 1–72. doi:10.1016/j.pmatsci.2014.02.002.

[219] Miyaji, F., Yoko, T., Jin, J., Sakka, S., Fukunaga, T., Misawa, M., Neutron and X-ray diffraction studies of $PbO-Ga_2O_3$ and $Bi_2O_3-Ga_2O_3$ glasses, J. Non. Cryst.

Solids. (1994) 175, 211–223. doi:10.1016/0022-3093(94)90013-2.

[220] Bliokh, K.Y., Niv, A., Kleiner, V., Hasman, E., Spin-orbit interaction of light, SPIE Newsroom. (2009) 2–4. doi:10.1117/2.1200906.1711.

[221] Nazarov, M., Brik, M.G., Spassky, D., Tsukerblat, B., Crystal Field Splitting of 5d States and Luminescence Mechanism in $SrAl_2O_4:Eu^{2+}$ Phosphor, J. Lumin. (2016) 182, 79–86. doi:10.1016/j.jlumin.2016.10.015.

[222] Reisfeld, R., Boehm, L., Optical properties of bismuth in germanate borax and phosphate glasses, J. Non. Cryst. Solids. (1974) 16, 83–92.

[223] Montenero, A., Friggeri, M., Giori, D.C., Belkhiria, N., Pye, L.D., Iron-soda-silica glasses: Preparation, properties, structure, J. Non. Cryst. Solids. (1986) 84, 45–60. doi:10.1016/0022-3093(86)90761-1.

[224] Zhou, Y., Dynamic Jahn – Teller effect in the near-infrared spectra of Fe^{2+} ions in ZnS, J. Appl. Phys. (2012) 6870, 2–5. doi:10.1063/1.1669270.

[225] Bingham, P. A., Hannant, O.M., Reeves-Mclaren, N., Stennett, M.C., Hand, R.J., Selective behaviour of dilute Fe^{3+} ions in silicate glasses: An Fe K-edge EXAFS and XANES study, J. Non. Cryst. Solids. (2014) 387, 47–56. doi:10.1016/j.jnoncrysol.2013.12.034.

[226] Fix, T., Nonat, A., Imbert, D., Di Pietro, S., Mazzanti, M., Slaoui, A., Charbonniere, L.J., Enhancement of silicon solar cells by downshifting with Eu and Tb coordination complexes, Prog. Photovoltaics. (2016) 24, 1251–1260. doi:10.1002/pip.

[227] Tai, Y., Li, X., Pan, B., Efficient near-infrared down conversion in Nd^{3+} -Yb^{3+} co-doped transparent nanostructured glass ceramics for photovoltaic application, J. Lumin. (2018) 195, 102–108. doi:10.1016/j.jlumin.2017.10.051.

[228] Duffy, J. A., Ingram, M.D., An interpretation of glass chemistry in terms of the optical basicity concept, J. Non. Cryst. Solids. (1976) 21, 373–410. doi:10.1016/0022-3093(76)90027-2.

[229] Kitamura, N., Fukumi, K., Nakamura, J., Hidaka, T., Ikeda, T., Hashima, H., Nishii, J., Optical properties of fluorine-substituted zinc bismuth phosphate glasses, J. Non. Cryst. Solids. (2011) 357, 1188–1192. doi:10.1016/j.jnoncrysol.2010.10.029.

[230] Dahiya, M.S., Dalal, S., Khasa, S., Lead modified properties of molybdenum doped lithium borate glasses, J. Non. Cryst. Solids. (2018) 485, 24–33. doi:10.1016/j.jnoncrysol.2018.01.024.

[231] Zotov, N., Ebbsjö, I., Timpel, D., Keppler, H., Calculation of Raman spectra and vibrational properties of silicate glasses: Comparison between $Na_2Si_4O_9$ and SiO_2 glasses, Phys. Rev. B. (1999) 60, 6383–6397. doi:10.1103/PhysRevB.60.6383.

[232] Bamford, C.., Control of Colours and Generation in Glass, Elsevier-North Holland Publications, Amsterdam, 1977.

[233] Schreiber, H.D., Schreiber, C.W., Polyselenide formation in borosilicate glasses, J.

Non. Cryst. Solids. (1993) 155, 209–220. doi:10.1016/0022-3093(93)91255-2.

[234] Lakowicz, J.R., Principles of Fluorescence Spectroscopy, 3rd ed., Springer - Verlag US, 2006. doi:10.1007/978-0-387-46312-4.

[235] Creative Commons Attribution Share Alike 3.0 Unported Licence Qwerty123uiop, Schematic view of a photomultiplier coupled to a scintillator, illustrating detection of gamma rays, (2013).

[236] Dai, N., Luan, H., Liu, Z., Sheng, Y., Peng, J., Jiang, Z., Li, H., Yang, L., Li, J., Broadband NIR luminescence of Bi-doped $Li_2O-Al_2O_3-SiO_2$ glass-ceramics, J. Non. Cryst. Solids. (2012) 358, 2970–2973. doi:10.1016/j.jnoncrysol.2012.07.024.

[237] Ravel, B., Newville, M., ATHENA, ARTEMIS, HEPHAESTUS: data analysis for X-ray absorption spectroscopy using IFEFFIT, J. Sychrotron Radiat. (2005) 12, 537–541. doi:https://doi.org/10.1107/S0909049505012719.

[238] Façanha, M.X., do Nascimento, J.P.C., Silva, M. A S., Filho, M.C.C., Marques, A. N.., Pinheiro, A. G., Sombra, A. S.B., Up-conversion emission of Er^{3+}/Yb^{3+} co-doped $BaBi_2Nb_2O_9$ (BBN) phosphors, J. Lumin. (2017) 183, 102–107. doi:10.1016/j.jlumin.2016.08.011.

[239] Rambabu, U., Han, S.-D., Synthesis and luminescence properties of broad band greenish-yellow emitting $LnVO_4:Bi^{3+}$ and $(Ln1, Ln2)VO_4:Bi^{3+}$ (Ln=La, Gd and Y) as down conversion phosphors, Ceram. Int. (2013) 39, 701–708. doi:10.1016/j.ceramint.2012.06.081.

[240] Jamalaiah, B.C., Jayasimhadri, M., Reddy, G.V.L., Blue emitting $YAl_3(BO_3)_4:Tm^{3+}$ single-phase phosphors under UV excitation, Phys. Chem. Glas. Eur. J. Glas. Sci. Technol. Part B. (2016) 57, 68–70. doi:10.13036/17533562.57.2.008.

[241] Ahrens, B., Löper, P., Goldschmidt, J.C., Glunz, S., Henke, B., Miclea, P.T., Schweizers, S., Neodymium-doped fluorochlorozirconate glasses as an upconversion model system for high efficiency solar cells, Phys. Status Solidi Appl. Mater. Sci. (2008) 205, 2822–2830. doi:10.1002/pssa.200880452.

[242] Bingham, P. A., Parker, J.M., Searle, T.M., Smith, I., Local structure and medium range ordering of tetrahedrally coordinated Fe^{3+} ions in alkali-alkaline earth-silica glasses, J. Non. Cryst. Solids. (2007) 353, 2479–2494. doi:10.1016/j.jnoncrysol.2007.03.017.

[243] Reddy, S.L., Endo, T., Reddy, G.S., Electronic (Absorption) Spectra of 3d Transition Metal Complexes, Adv. Asp. Spectrosc. (2012) 3–48. doi:10.5772/50128.

[244] Jordan, D.C., Kurtz, S.R., Photovoltaic Degradation Rates — an Analytical Review, (2013) 12–29. doi:10.1002/pip.

[245] Meng, X., Murai, S., Fujita, K., Tanaka, K., Intense blue emission from tantalum-doped silicate glass, Appl. Phys. Lett. (2006) 89, 11–14. doi:10.1063/1.2335394.

[246] Möncke, D., Ehrt, D., Photoinduced redox reactions in Zr, Nb, Ta, Mo, and W doped

glasses, Phys. Chem. Glas. Eur. J. Glas. Sci. Technol. Part B. (2007) 48, 317–323.

[247] Ehrt, D., Photoluminescence in the UV–VIS region of polyvalent ions in glasses, J. Non. Cryst. Solids. (2004) 348, 22–29. doi:10.1016/j.jnoncrysol.2004.08.121.

[248] Ehrt, D., Phosphate and fluoride phosphate optical glasses — properties , structure and applications, Phys. Chem. Glas. Eur. J. Glas. Sci. Technol. B. (2015) 56, 217–234. doi:10.13036/17533562.56.6.217.

[249] Wiegel, M., Blasse, G., Feigelson, R., Luminescence of stoichiometric lithium niobate crystals, Mater. Res. Bull. (1993) 28, 1025–1028.

[250] Wiegel, M., Blasse, G., Ouwerkerk, M., Luminescence of potassium lithium niobate compositions, Mater. Res. Bull. (1992) 27, 617–621.

[251] Wiegel, M., Middel, W., Blasse, G., Influence of $_ns^2$ ions on the luminescence of niobates and tantalates, J. Mater. Chem. (1995) 5, 981–983. http://dx.doi.org/10.1039/JM9950500981.

[252] Schipper, W.J., Piet, J.J., De Jager, H.J., Blasse, G., On the luminescence of hafnium compounds, Mater. Res. Bull. (1994) 29, 23–30. doi:10.1016/0025-5408(94)90101-5.

[253] Wiegel, M., Hamoumi, M., Luminescence and nonlinear niobates and titanates optical properties of perovskite like niobates and titanates, Mater. Chem. Phys. (1994) 36, 289–293.

[254] Mondal, S., Basak, D., Defect controlled tuning of the ratio of ultraviolet to visible light emission in TiO_2 thin films, J. Lumin. (2016) 179, 480–486. doi:10.1016/j.jlumin.2016.07.046.

[255] Lin, C.C., Xu, K.Y., Wang, D., Meijerink, A., Luminescent manganese-doped $CsPbCl_3$ perovskite quantum dots, Sci. Rep. (2017) 7, 45906. doi:10.1038/srep45906.

[256] Hsiao, Y.J., Fang, T.H., Lin, S.J., Shieh, J.M., Ji, L.W., Preparation and luminescent characteristic of Li_3NbO_4 nanophosphor, J. Lumin. (2010) 130, 1863–1865. doi:10.1016/j.jlumin.2010.04.023.

[257] Maeda, K., Yasumori, A., Effect of molybdenum and tungsten oxides on nucleation and crystallization behaviors of $MgO–Al_2O_3–SiO_2$ glasses, J. Non. Cryst. Solids. (2015) 427, 152–159. doi:10.1016/j.jnoncrysol.2015.07.040.

[258] Ghaebi Panah, N., Eftekhari Yekta, B., Marghussian, V., Mohaghegh, E., Effects of TiO_2 and P_2O_5 on solarization and crystallisation of photosensitive lithium silicate glass, J. Non. Cryst. Solids. (2015) 430, 25–30. doi:10.1016/j.jnoncrysol.2015.09.018.

[259] Thieme, K., Avramov, I., Rüssel, C., The mechanism of deceleration of nucleation and crystal growth by the small addition of transition metals to lithium disilicate glasses, Sci. Rep. (2016) 6, 1–16. doi:10.1038/srep25451.

[260] Komatsu, T., Design and control of crystallization in oxide glasses, J. Non. Cryst. Solids. (2015) 428, 156–175. doi:10.1016/j.jnoncrysol.2015.08.017.

[261] Kilinc, E., Hand, R.J., Mechanical properties of soda–lime–silica glasses with varying alkaline earth contents, J. Non. Cryst. Solids. (2015) 429, 190–197. doi:10.1016/j.jnoncrysol.2015.08.013.

[262] Woelffel, W., Claireaux, C., Toplis, M.J., Burov, E., Barthel, É., Shukla, A., Biscaras, J., Chopinet, M.H., Gouillart, E., Analysis of soda-lime glasses using non-negative matrix factor deconvolution of Raman spectra, J. Non. Cryst. Solids. (2015) 428, 121–131. doi:10.1016/j.jnoncrysol.2015.08.016.

[263] Kaur, A., Khanna, A., Sathe, V.G., Gonzalez, F., Ortiz, B., Optical, thermal, and structural properties of Nb_2O_5 –TeO_2 and WO_3 –TeO_2 glasses, Phase Transitions. (2013) 86, 598–619. doi:10.1080/01411594.2012.727998.

[264] Caixeta, F.J., Aquino, F.T., Pereira, R.R., Gonsalves, R.R., Broad and intense NIR luminescence from rare earth doped SiO_2-Nb_2O_5 glass and glass ceramic prepared by a new sol gel route, J. Lumin. (2016) 171, 63–71. doi:10.1016/j.jlumin.2015.08.054.

[265] McKeown, D.A., Gan, H., Pegg, I.L., Stolte, W.C., Demchenko, I.N., X-ray absorption studies of chlorine valence and local environments in borosilicate waste glasses, J. Nucl. Mater. (2011) 408, 236–245. doi:10.1016/j.jnucmat.2010.11.035.

[266] Chouard, N., Caurant, D., Majérus, O., Guezi-Hasni, N., Dussossoy, J.L., Baddour-Hadjean, R., Pereira-Ramos, J.P., Thermal stability of SiO_2-B_2O_3-Al_2O_3-Na_2O-CaO glasses with high Nd_2O_3 and MoO_3 concentrations, J. Alloys Compd. (2016) 671, 84–99. doi:10.1016/j.jallcom.2016.02.063.

[267] Chouard, N., Caurant, D., Majerus, O., Dussossoy, J.L., Klimin, S., Pytalev, D., Baddour-Hadjean, R., Pereira-Ramos, J.P., Effect of MoO_3, Nd_2O_3, and RuO_2 on the crystallization of soda lime aluminoborosilicate glasses, J. Mater. Sci. (2015) 50, 219–241. doi:10.1007/s10853-014-8581-9.

[268] Pushpa, N., Kokila, M.K., Effect of cobalt doping on structural, thermo and photoluminescent properties of ZnO nanopowders, J. Lumin. (2017) 190, 100–107. doi:10.1016/j.jlumin.2017.05.032.

[269] Xiong, G., Pal, U., Serrano, J.G., Correlations among size, defects, and photoluminescence in ZnO nanoparticles, J. Appl. Phys. (2007) 101,. doi:10.1063/1.2424538.

[270] Griscom, D.L., Electron spin resonance in glasses, J. Non. Cryst. Solids. (1980) 40, 211–272. doi:10.1016/0022-3093(80)90105-2.

[271] Kliava, J., EPR of Impurity Ions in Disordered Soilds, Phys. Stat. Sol. B. (1986) 134, 411–455. doi:10.1002/pssb.2221340202.

[272] Yang, J., Lee, D., Baek, D., Kim, D., Nam, J., Huh, P., Effect of various encapsulants for frameless glass to glass Cu(In,Ga)(Se,S)$_2$ photovoltaic module, RSC Adv. (2015) 5, 51258–51262. doi:10.1039/C5RA03663A.

[273] Leschik, M., Heide, G., Frischat, G.H., Behrens, H., Wiedenbeck, M., Wagner, N., Heide, K., Geißler, H., Reinholz, U., Determination of H_2O and D_2O contents in rhyolitic glasses, 2004.

[274] Dittmer, M., Ritzberger, C., Holand, W., Rampf, M., Controlled precipitation of lithium disilicate, lithium niobate, or lithium tantalate in glass ceramics, J. Eur. Ceram. Soc. (2018) 38, 263–269.

[275] Fujimoto, Y., Local structure of the infrared bismuth luminescent center in bismuth-doped silica glass, J. Am. Ceram. Soc. (2010) 93, 581–589. doi:10.1111/j.1551-2916.2009.03419.x.

[276] Kamitsos, E.I., Kapoutsis, J.A., Jain, H., Hsieh, C.H., Vibrational study of the role of trivalent ions in sodium trisilicate glass, J. Non. Cryst. Solids. (1994) 171, 31–45. doi:10.1016/0022-3093(94)90030-2.

[277] Duffy, J.A., Bonding, energy levels and bands in inorganic solids, Harlow : Longman Scientific and Technica, 1990.

[278] Fluegel, A., Global Model for Calculating Room-Temperature Glass Density from the composition, J. Am. Ceram. Soc. (2007) 2625, 2622–2625. doi:10.1111/j.1551-2916.2007.01751.x.

[279] Wang, M., Cheng, J., Li, M., He, F., Raman spectra of sodalimesilicate glass doped with rare earth, Phys. B Condens. Matter. (2011) 406, 3865–3869. doi:10.1016/j.physb.2011.07.014.

[280] González, P., Serra, J., Liste, S., Chiussi, S., León, B., Pérez-Amor, M., Raman spectroscopic study of bioactive silica based glasses, J. Non. Cryst. Solids. (2003) 320, 92–99. doi:10.1016/S0022-3093(03)00013-9.

[281] Galeener, F.L., Band limits and the vibrational spectra of tetrahedral glasses, Phys. Rev. B. (1979) 19, 4292–4297. doi:10.1103/PhysRevB.19.4292.

[282] Deschamps, T., Martinet, C., Bruneel, J.L., Champagnon, B., Soda-lime silicate glass under hydrostatic pressure and indentation: a micro-Raman study., J. Phys. Condens. Matter. (2011) 23, 035402. doi:10.1088/0953-8984/23/3/035402.

[283] Möncke, D., Ehrt, R., Palles, D., Efthimiopoulos, I., Kamitsos, E.I., Johannes, M., A multi technique study of a new lithium disilicate glass-ceramic spray-coated on ZrO_2 substrate for dental restoration, Biomed. Glas. (2017) 3, 41–55. doi:10.1515/bglass-2017-0004.

[284] Richter, S., Möncke, D., Zimmermann, F., Kamitsos, E.I., Wondraczek, L., Tünnermann, A., Nolte, S., Ultrashort pulse induced modifications in ULE - from nanograting formation to laser darkening, Opt. Mater. Express. (2015) 5, 1834. doi:10.1364/OME.5.001834.

[285] De Pietro, G.M., Pereira, C., Gonçalves, R.R., Ribeiro, S.J.L., Freschi, C.D., Cassanjes, F.C., Poirier, G., Thermal, Structural, and Crystallization Properties of New Tantalum Alkali-Germanate Glasses, J. Am. Ceram. Soc. (2015) 98, 2086–2093. doi:10.1111/jace.13555.

[286] Bih, L., Azrour, M., Manoun, B., Graça, M.P.F., Valente, M.A., Raman spectroscopy, X-Ray, SEM, and DTA analysis of alkali-phosphate glasses containing WO_3 and Nb_2O_5, J. Spectrosc. (2013) 1,. doi:10.1155/2013/123519.

[287] Castner Jr., T., Newell, G.S., Holton, W.C., Slichter, C.P., Note on the paramagnetic resonance of iron in glass, J. Chem. Phys. (1960) 32, 668–673. doi:10.1063/1.1730779.

[288] Dowsing, R.D., Electron Spin Resonance of High-Spin d^5 Systems, J. Chem. Phys. (1970) 52, 2795. doi:10.1063/1.1673393.

[289] Camara, B., Oel, H.J., Behaviour and effect of iron in X-ray irradiated silicate glass, J. Non. Cryst. Solids. (1984) 65, 161–176. doi:10.1016/0022-3093(84)90363-6.

[290] Parke, S, Gomolka, S, Sandoe, J.N, Effect of composition and temperature on the absorption and emission spectra of molybdenum in glasses, J. Non. Cryst. Solids. (1976) 20, 1–14.

[291] Elvers, A., Weismann, R., ESR spectroscopy - an analytical tool for the glass industry, Glas. Sci. Technol. Glas. Berichte. (2001) 74,.

[292] Schreiber, H.D., Wilk, N.R., Schreiber, C.W., Comprehensive electromotive force series of redox couples in soda-lime-silicate glass, J. Non. Cryst. Solids. (1999) 253, 68–75. doi:10.1016/S0022-3093(99)00344-0.

[293] Schreiber, H.D., Redox processes in glass-forming melts, J. Non. Cryst. Solids. (1986) 84, 129–141. doi:10.1016/0022-3093(86)90770-2.

[294] Weber, R.S., Effect of Local Structure on the UV-Visible Absorption Edges of Molybdenum Oxide Clusters and Supported Molybdenum Oxides, J. Catal. (1995) 151, 470–474. doi:http://dx.doi.org/10.1006/jcat.1995.1052.

[295] Fairbrother, A., Boyd, M., Lyu, Y., Avenet, J., Illich, P., Wang, Y., Kempe, M., Dougherty, B., Bruckman, L., Gu, X., Differential degradation patterns of photovoltaic backsheets at the array level, Sol. Energy. (2018) 163, 62–69. doi:10.1016/j.solener.2018.01.072.

[296] Rack, P.D., Potter, M.D., Kurinec, S., Park, W.H., Penczek, J., Wagner, B.K., Summers, C.J., Luminescence properties of thin film $Ta_2Zn_3O_8$ and Mn doped $Ta_2Zn_3O_8$, J. Appl. Phys. (1998) 84, 4466–4470. doi:10.1063/1.368672.

[297] Zhao, J., Zheng, X., Schartner, E.P., Ionescu, P., Zhang, R., Nguyen, T.-L., Jin, D., Ebendorff-Heidepriem, H., Upconversion Nanocrystal-Doped Glass: A New Paradigm for Photonic Materials, Adv. Opt. Mater. (2016) 1–11. doi:10.1002/adom.201600296.

[298] Irimpan, L., Nampoori, V.P.N., Radhakrishnan, P., Deepthy, A., Krishnan, B., Size dependent fluorescence spectroscopy of nanocolloids of ZnO, J. Appl. Phys. (2007) 102,. doi:10.1063/1.2778637.

[299] Peike, C., Kaltenbach, T., Weiß, K.A., Koehl, M., Non-destructive degradation analysis of encapsulants in PV modules by Raman Spectroscopy, Sol. Energy

Mater. Sol. Cells. (2011) 95, 1686–1693. doi:10.1016/j.solmat.2011.01.030.

[300] Bulatov, L.I., Mashinsky, V.M., Dvoirin, V. V., Kustov, E.F., Dianov, E.M., Sukhorukov, A. P., Structure of absorption and luminescence bands in aluminosilicate optical fibers doped with bismuth, Bull. Russ. Acad. Sci. Phys. (2008) 72, 1655–1660. doi:10.3103/S1062873808120174.

[301] De Jong, M., Meijerink, A., Gordon, R.A., Barandiarán, Z., Seijo, L., Is Bi^{2+} responsible for the red-orange emission of bismuth-doped SrB_4O_7?, J. Phys. Chem. C. (2014) 118, 9696–9705. doi:10.1021/jp502996t.

[302] Ren, J., Yang, L., Qiu, J., Chen, D., Jiang, X., Zhu, C., Effect of various alkaline-earth metal oxides on the broadband infrared luminescence from bismuth-doped silicate glasses, Solid State Commun. (2006) 140, 38–41. doi:10.1016/j.ssc.2006.07.023.

[303] Fujimoto, Y., Nakatsuka, M., Infrared luminescence from bismuth-doped silica glass, Japanese J. Appl. Physics, Part 2 Lett. (2001) 40, 3–6. doi:10.1143/JJAP.40.L279.

[304] Dianov, E.M., Nature of Bi-related near IR active centers in glasses: state of the art and first reliable results, Laser Phys. Lett. (2015) 12, 095106. doi:10.1088/1612-2011/12/9/095106.

[305] Blasse, G., Investigations on Bi^{3+}-Activated Phosphors, J. Chem. Phys. (1968) 48, 217. doi:10.1063/1.1667905.

[306] Ren, J., Qiu, J., Chen, D., Hu, X., Jiang, X., Zhu, C., Luminescence properties of bismuth-doped lime silicate glasses, J. Alloys Compd. (2008) 463, 5–8. doi:10.1016/j.jallcom.2007.09.026.

[307] Xu, W., Peng, M., Ma, Z., Dong, G., Qiu, J., A new study on bismuth doped oxide glasses, Opt. Express. (2012) 20, 15692. doi:10.1364/OE.20.015692.

[308] Torrengo, S., Paul, M.C., Halder, A., Das, S., Dhar, A., Sahu, J.K., Jain, S., Kir'Yanov, A. V., D'Acapito, F., EXAFS studies of the local structure of bismuth centers in multicomponent silica glass based optical fiber preforms, J. Non. Cryst. Solids. (2015) 410, 82–87. doi:10.1016/j.jnoncrysol.2014.11.027.

[309] Peng, M., Da, N., Krolikowski, S., Stiegelschmitt, A., Luminescence from Bi^{2+} -activated alkali earth borophosphates for white LEDs, Opt. Express. (2009) 17, 2885–2887.

[310] Romano, V., Ryser, M., Bi doped Optical Fibers and Fiber Lasers, IEEE J. Sel. Top. Quantum Electron. (2014) 20, 2–3.

[311] De Jong, M., Meijerink, A., Color tuning of Bi^{2+} luminescence in barium borates, J. Lumin. (2016) 170, 240–247. doi:10.1016/j.jlumin.2015.10.036.

[312] Jia, B., Lu, P., Peng, Z., Yan, B., Yang, B., Wang, Y., Peng, G., Near-IR luminescence characteristics of monovalent bismuth in Bi-doped pure silica optical fiber : First-principle study, J. Lumin. (2018) 198, 384–388.

doi:10.1016/j.jlumin.2018.02.060.

[313] Duffy, J. A., Optical Basicity: A Practical Acid-Base Theory for Oxides and Oxyanions, J. Chem. Educ. (1996) 73, 1138. doi:10.1021/ed073p1138.

[314] Jak, E., Degterov, S., Wu, P., Hayes, P.C., Pelton, A.D., Thermodynamic Optimization of the Systems PbO-SiO$_2$, PbO-, Metall. Mater. Trans. B. (1997) 28, 1011–1018.

[315] Yang, B., Townsend, P.D., Holgate, S.A., Cathodoluminescence and depth profiles of tin in float glass, J. Phys. D. Appl. Phys. (1994) 27, 1757–1762. doi:10.1088/0022-3727/27/8/026.

[316] Chakraborty, R., Dey, A., Mukhopadhyay, A.K., Loading rate effect on nanohardness of soda-lime-silica glass, Metall. Mater. Trans. A Phys. Metall. Mater. Sci. (2010) 41, 1301–1312. doi:10.1007/s11661-010-0176-8.

[317] Tse, J.S., Wang, X.D., Jiang, D.T., Chen, N., Jiang, J.Z., High energy synchrotron X-ray diffraction study of lead oxide silicate glasses at the Canadian light source, Nucl. Instruments Methods Phys. Res. Sect. A Accel. Spectrometers, Detect. Assoc. Equip. (2011) 626–627, 144–146. doi:10.1016/j.nima.2010.10.088.

[318] Trinquier, G., Hoffmann, R., Lead monoxide. Electronic structure and bonding, J. Phys. Chem. (1984) 88, 6696–6711. doi:10.1021/j150670a038.

[319] Konijnendijk, W.L., Buster, J.H.J.M., Raman-scattering measurements of silicate glasses containing sulphate, J. Non. Cryst. Solids. (1977) 23, 401–418. doi:10.1016/0022-3093(77)90123-5.

[320] Manara, D., Grandjean, A., Neuville, D.R., Advances in understanding the structure of borosilicate glasses: A raman spectroscopy study, Am. Mineral. (2009) 94, 777–784. doi:10.2138/am.2009.3027.

[321] Angeli, F., Villain, O., Schuller, S., Charpentier, T., de Ligny, D., Bressel, L., Wondraczek, L., Effect of temperature and thermal history on borosilicate glass structure, Phys. Rev. B. (2012) 85, 1–15. doi:10.1103/PhysRevB.85.054110.

[322] Padmaja, G., Kistaiah, P., Infrared and Raman Spectroscopic Studies on Alkali Borate Glasses: Evidence of Mixed Alkali Effect, J. Phys. Chem. A. (2009) 11, 2397–2404. doi:10.1021/jp809318e.

[323] Fuxi, G. A N., Huimin, L.I.U., ESR study on glass, J. Non. Cryst. Solids. (1987) 96, 61–70.

[324] Lombard, P., Ollier, N., Boizot, B., EPR study of Ti^{3+} ions formed under beta irradiation in silicate glasses, J. Non. Cryst. Solids. (2011) 357, 1685–1689. doi:10.1016/j.jnoncrysol.2010.12.015.

[325] Schreiber, H.D., Jr, N.R.W., Schreiber, C.W., A comprehensive electromotive force series of redox couples in soda - lime - silicate glass, J. Non. Cryst. Solids. (1999) 253, 68–75.

[326] Folkerts, H.F., Ghianni, F., Blasse, G., Search for D-level emission of Pb^{2+} in alkaline-earth aluminates and gallates, J. Phys. Chem. Solids. (1996) 57, 1659–1665. doi:10.1016/0022-3697(96)00041-8.

[327] Srivastava, A.M., Camardello, S.J., Concentration dependence of the Bi^{3+} luminescence in $LnPO_4$ (Ln = Y^{3+}, Lu^{3+}), Opt. Mater. (Amst). (2015) 39, 130–133. doi:10.1016/j.optmat.2014.11.011.

[328] Vandecraats, A M., Blasse, G., The Quenching of Bismuth(III) Luminescence in Yttrium-Oxide (Y_2O_3), Chem. Phys. Lett. (1995) 243, 559–563. doi:10.1016/0009-2614(95)00897-D.

[329] Dianov, E.M., Bismuth-doped optical fibers: a challenging active medium for near-IR lasers and optical amplifiers, Light Sci. Appl. (2012) 1, e12. doi:10.1038/lsa.2012.12.

[330] Sardar, K., Walton, R.I., Hydrothermal synthesis map of bismuth titanates, J. Solid State Chem. (2012) 189, 32–37. doi:10.1016/j.jssc.2012.01.017.

[331] Limbach, R., Karlsson, S., Scannell, G., Mathew, R., Edén, M., Wondraczek, L., The effect of TiO_2 on the structure of Na_2O-CaO-SiO_2 glasses and its implications for thermal and mechanical properties, J. Non. Cryst. Solids. (2017) 471, 6–18. doi:10.1016/j.jnoncrysol.2017.04.013.

[332] Karczewski, J., Miruszewski, T., Bochentyn, B., Kusz, B., Determination of ionic conductivity in the Bi-Si-O and Pb-Si-O glasses, Mater. Sci. Pol. (2017) 35, 681–686. doi:10.1515/msp-2017-0102.

[333] Abdel-Wahab, F.A., Fayad, A.M., Abdel-Baki, M., Abdel-Maksoud, H., Role of non-bridging oxygen defect in the ionic conductivity and associated oxygen trap centers in lead-borate oxide glass: Effect of structural substitution of PbO for Ag_2O and Li_2O modifiers, J. Non. Cryst. Solids. (2018) 500, 84–91. doi:10.1016/j.jnoncrysol.2018.06.033.

[334] Suneel Kumar, A., Narendrudu, T., Suresh, S., Sambasiva Rao, M. V., Chinna Ram, G., Krishna Rao, D., Role of titanium ions on the physical and structural properties of calcium zinc bismuth phosphate glass ceramics, J. Non. Cryst. Solids. (2016) 434, 62–70. doi:10.1016/j.jnoncrysol.2015.12.010.

[335] Todea, M., Turcu, R.V.F., Vasilescu, M., Trandafir, D.L., Simon, S., Structural characterization of heavy metal SiO_2–Bi_2O_3 glasses and glass–ceramics, J. Non. Cryst. Solids. (2015) 432, 271–276. doi:10.1016/j.jnoncrysol.2015.10.021.

[336] Kacem, I. Ben, Gautron, L., Coillot, D., Neuville, D.R., Kacem, I. Ben, Gautron, L., Coillot, D., Structure, D.R.N., Structure and properties of lead silicate glasses and melts, Chem. Geol. (2017) 461, 104–114.

[337] Neuville, D.R., de Ligny, D., Henderson, G.S., Advances in Raman Spectroscopy Applied to Earth and Material Sciences, Rev. Mineral. Geochemistry. (2014) 78, 509–541. doi:10.2138/rmg.2013.78.13.

[338] SciGlass v7 - Glass Property Information System., (n.d.).

[339] Griscom, D.L., Stapelbroek, M., Electron spin resonance studies of iron group impurities in beryllium fluoride glasses, J. Non. Cryst. Solids. (1980) 41, 329–345. doi:10.1063/1.3075988.

[340] Aleksandrov, A.I., Bubnov, N.N., Prokof'ev, A.I., Stabilization of elements in unusual oxidation states and temperature-reversible dynamics of electron pairs in oxide glasses. EPR-investigation, Appl. Magn. Reson. (1995) 9, 251–266. doi:10.1007/BF03162045.

[341] Agulo-Lopez, F., Insulating Materials for Optoelectronics: New Developments, 1995. doi:https://doi.org/10.1142/2720.

[342] Housecroft, C., Constable, E., Chemistry, 4th ed., Pretince Hall, 2009.

[343] Reisfeld, R., Lieblich, N., Absorption and fluorescence of lead in germanate, borate and phosphate glasses, J. Non. Cryst. Solids. (1973) 12, 207–212. doi:10.1016/0022-3093(73)90070-7.

[344] Ren, J., Dong, G., Xu, S., Bao, R., Qiu, J., Inhomogeneous broadening, luminescence origin and optical amplification in bismuth-doped glass, J. Phys. Chem. A. (2008) 112, 3036–3039. doi:10.1021/jp709987r.

[345] Awater, R.H.P., Dorenbos, P., Towards a general concentration quenching model of Bi^{3+} luminescence, J. Lumin. (2017) 188, 487–489. doi:10.1016/j.jlumin.2017.05.011.

[346] Wright, B.M., Shelby, J.E., Phase separation and the mixed alkali effect, Phys. Chem. Glas. (2000) 41, 192–198.

[347] Duffy, J.A., Ultraviolet transparency of glass: A chemical approach in terms of band theory, polarisability and electronegativity, Phys. Chem. Glas. (2001) 42, 151–157.

[348] Czanderna, A.W., Jorgensen, G.J., Service Lifetime Prediction for Encapsulated Photovoltaic cells/Minimodules, AIP Conf. Proc. (1997) 295–312. doi:10.1063/1.52899.

[349] https://www.indmin.com/, (2018). https://www.indmin.com/.

[350] https://www.metals-hub.com, (n.d.). https://www.metals-hub.com (accessed August 20, 2011).

[351] Zhao, M., Liu, Y., Liu, D., Ma, S., Wang, K., Effects of Bi^{3+} ions on luminescence properties of $ZnWO_4$:Eu^{3+}, Sm^{3+}, Bi^{3+} nanorods, J. Mater. Sci. (2018) 53, 11512–11523. doi:10.1007/s10853-018-2329-x.

[352] Li, J., Liao, L., Chu, Y., Liu, P., Li, H., Peng, J., Dai, N., Effect of cerium oxide and niobium oxide addition on absorption and emission properties of bismuth doped silicate glasses, J. Non. Cryst. Solids. (2015) 431, 22–26. doi:10.1016/j.jnoncrysol.2015.02.026.

[353] Peng, J., Cao, J., Tan, L., Peng, M., Glass-forming region and enhanced Bi NIR emission in sodium tantalum silicate laser glass, J. Am. Ceram. Soc. (2018) Article

In, jace.16121. doi:10.1111/jace.16121.

[354] Li, M., Wang, L., Ran, W., Ren, C., Song, Z., Shi, J., Enhancing Sm^{3+} red emission via energy transfer from $Bi^{3+} \rightarrow Sm^{3+}$ based on terbium bridge mechanism in $Ca_2Al_2SiO_7$ phosphors, J. Lumin. (2017) 184, 143–149. doi:10.1016/j.jlumin.2016.12.014.

[355] Lu, J., Mu, Z., Zhu, D., Wang, Q., Wu, F., Luminescence properties of Eu^{3+} doped $La_3Ga_5GeO_{14}$ and effect of Bi^{3+} co-doping, J. Lumin. (2018) 196, 50–56. doi:10.1016/j.jlumin.2017.12.017.